Studies of Ion Molecule Reactive Processes, Electron Impact Ionisation, and Inelastic Collisions in State Selected Molecular Beams

A thesis submitted in partial fulfilment of
the requirements for the degree of

Doctor of Philosophy in Chemistry

at the
University of Canterbury,
Christchurch,
New Zealand.

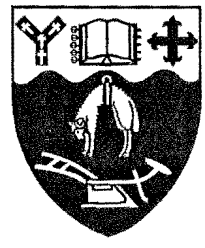

Sean Anthony Harris

1997

Abstract

Alkali metal ion sources have been designed for the production of Li^+, Na^+ and K^+ ion beams. The thermionic emission of alkali metal ions from heated synthetic zeolites is utilised to produce the alkali ions. As a precursor to crossed beam studies of the reactions of the alkali metal ions with spatially oriented symmetric top alkyl halides, the ion molecule chemistry of K^+ with CH_3X and tertiary C_4H_9X where X = Cl or Br has been examined for collision energies up to 5 eV using a Drift Tube Mass Spectrometer.

The electron impact ionisation cross sections for the inert gases, H_2, N_2, SF_6, CCl_3H and the molecules CH_3X where X = H, F, Cl, Br, I, have been measured. The ionisation efficiency curves for Ar, CH_4, CH_3F, CH_3Cl and CH_3Br from threshold up to 200 eV have been determined.

The cross sections for the loss of hexapole focused upper Stark state molecules from $|JKM\rangle$ rotational state selected molecular beams of CH_3F, CH_3Cl and CF_3H have been measured. The upper Stark state molecules are defocused from the beam in rotationally inelastic collisions with a scattering gas introduced to the hexapole. The long range attractive van der Waals interaction between the colliding species has been used to account for the magnitude of the cross sections from consideration of rotational transitions of the $|JKM\rangle$ state selected beam molecules where $\Delta M = \pm 1$ or $\Delta J = \pm 1$. The seeded beam technique has been used to determine the velocity dependence of the defocusing cross sections.

Acknowledgements

I would like to thank my supervisor, Dr. Peter Harland, for his guidance and friendship over the last 5 years. His invaluable advice and experience kept this research going when otherwise chaos would reign.

Without the support of the Chemistry Department technical staff this research would not be possible. I would like to thank Wayne Mackay for his electrical expertise, willingness to have a beer at the Dux at the drop of a hat and most importantly his great friendship. I would also like to thank Dave Macdonald and Rob McGregor of the glassblowing workshop for their humour and friendship. Thanks to the mechanical workshop and in particular Barrie Wood for his machining talents constantly put to good use by our never ending list of jobs. Thanks also to Sandy Ferguson and Derek Williams of the electronics workshop for keeping our electronic equipment running after entropy had done its best.

Thanks to my colleagues who have been a constant source of advice, friendship and humour throughout this research. In particular I would like to thank David Blunt for introducing me to the importance of a good Single Malt and Claire Vallance for her friendship.

Financial support from the Chemistry Department and the University of Canterbury is gratefully acknowledged.

Finally, but most importantly, thank you to my parents, family and friends for their continued support.

Contents

List of Figures

List of Tables

Chapter 1

Introduction

Recent experiments in this laboratory have successfully investigated the effect of molecular orientation on electron impact ionisation using hexapole state selected spatially oriented molecular beams crossed by an ionising electron beam [Aitken, 1994; Aitken, 1995b]. To further study the orientation asymmetry of collisions between oriented molecules and charged particles, the investigation of the ion molecule chemistry of alkali metal ions with alkyl halides has been proposed. The first section of this thesis describes the preliminary work for the design of the ion sources and the investigation of the ion molecule chemistry. Ion sources have been designed utilising the thermionic emission of alkali ions from heated zeolites as a source for the alkali metal ion beam. The sources must produce an ion beam of adequate intensity for the crossed beam studies, and high purity so the chemistry is not complicated by interfering reactions with the unwanted alkali ions. The various alkali metal ion containing zeolites have been prepared and purified using ion exchange techniques. The chemistry of the alkali ion K^+ with CH_3X and tertiary C_4H_9X where X = Cl or Br has been studied at collision energies up to 5 eV.

The ionisation studies with the oriented molecules showed there is a lack of experimental values for the electron impact ionisation cross sections for the symmetric top alkyl halides in the literature. The second section of this thesis details the design and optimisation of an apparatus to measure the absolute total electron impact ionisation

cross sections for atomic and molecular species. The cross sections are determined by passing an electron beam through a region of known path length containing the gas to be ionised and recording the resulting ion and electron electrical currents on suitable collection electrodes.

It has been noticed that the orientation asymmetry effects shown by the ionisation studies with hexapole state selected spatially oriented beams, disappear when the background pressure in the hexapole increases. This has been attributed to rotationally inelastic collisions between the hexapole focused upper Stark states and the background gas leading to the upper Stark states being defocused and lost from the beam. To further investigate this, experiments have been carried out in the third part of this thesis to measure the cross section for the loss of the focused upper Stark states. The cross sections are determined by measuring the attenuation of the upper Stark state signal transmitted by the hexapole due to the addition of a scattering gas in the hexapole region. The dependence of the cross section on the focusing conditions of the hexapole and hence on the transmitted rotational state distribution of the beam has been examined.

Each of the three experiments outlined above are discussed separately in this thesis. A brief summary of each chapter is given below.

In chapter 2 the experimental apparatus used to characterise the alkali ion sources is described. Background information is given on the theory of operation of the drift tube which is used to study the ion molecule chemistry of the alkali ions with symmetric top alkyl halides. The operation of the quadrupole mass filter and the channeltron electron multiplier detector is described.

The ion exchange methods used to produce the Li^+, Na^+ and K^+ zeolites are described in chapter 3 followed by a section on the ion source used to test the various alkali ion emitting materials. In the last section some ion source designs are presented. The main part of the chapter presents the results of the ion molecule chemistry which was observed in the drift tube for the reactions of K^+ ions with CH_3X and t-C_4H_9X

where X = Cl or Br. Appendix A provides background information on the materials used as thermionic alkali metal ion emitters. The preparation and synthesis of these materials is discussed with emphasis on the ion exchange techniques used to produce the various alkali ion zeolites.

Chapter 4 provides information on the electron impact ionisation process and describes the experimental quantities required for cross section measurements. The major experimental techniques for the determination of ionisation cross sections are discussed.

Chapter 5 describes the vacuum and electrical apparatus used in the determination of the electron impact ionisation cross sections. The optimisation of the ionisation chamber is presented.

Chapter 6 describes the cross section experimental process. SIMION calculations are used to determine the effective ionising path length of the electron beam. The maximum electron impact ionisation cross sections are presented for the inert gases and various alkyl halides and compared to literature values. A simple electrostatic model is used to relate the cross sections to the polarisability and ionisation potential of the gases used.

The theory behind the formation of effusive and supersonic molecular beams is presented in chapter 7. The operation of the hexapole is described and the transmission of upper Stark states of symmetric top molecules are discussed. Attenuation of the molecular beam by inelastic scattering is described also. The upper Stark state defocusing cross sections are modelled using the long range attractive van der Waals potential.

Chapter 8 describes the molecular beam machine used to measure the upper Stark state defocusing cross sections. The important experimental components including the hexapole, various beam sources and detectors are discussed.

In chapter 9 the upper Stark state defocusing cross sections are presented. A discussion of the experimental analysis is given including velocity and angular resolution aspects. The cross sections are compared to the $|JKM\rangle$ state distribution of the hexapole focused beam to examine the correlation between the cross section and the $|JKM\rangle$ rotational states present. The velocity dependence of the cross sections is examined and the van der Waals interaction potential is used to determine the processes responsible for the defocusing of the upper Stark states.

Finally, in chapter 10 a brief overview of the future work to be done on the alkali ion-alkyl halide chemistry and the upper Stark state defocusing cross sections is given.

Chapter 2

Drift Tube Mass Spectrometer

In order to investigate the orientation dependence for reactions between alkali metal ions and spatially oriented symmetric top molecules, a method for producing the alkali ion beam must be developed and the products of the ion molecule reactions must be identified. A drift tube mass spectrometer (DTMS) [Harland, 1984] has been used in this work as a test bed for the design of the alkali metal ion sources and as an environment for the study of their ion molecule reactions with symmetric top alkyl halide molecules. The integral components of the DTMS to be discussed are:

- The vacuum system
- Gas handling
- Ion source linear motion feedthrough
- Drift tube
- Mass spectrometer.

2.1 Vacuum System

The vacuum system comprises two Varian 8" OD 4 way stainless steel crosses, one to house the drift tube and the other the mass spectrometer (Fig. 2.1). The division between the two chambers is made by a gold plated skimmer of 2 mm orifice mounted in a stainless steel top-hat on an 8" flange bolted between the two chambers. All vacuum seals are made using conflat knife edges with copper gaskets for the vacuum chambers and Viton o-rings for the pumping system.

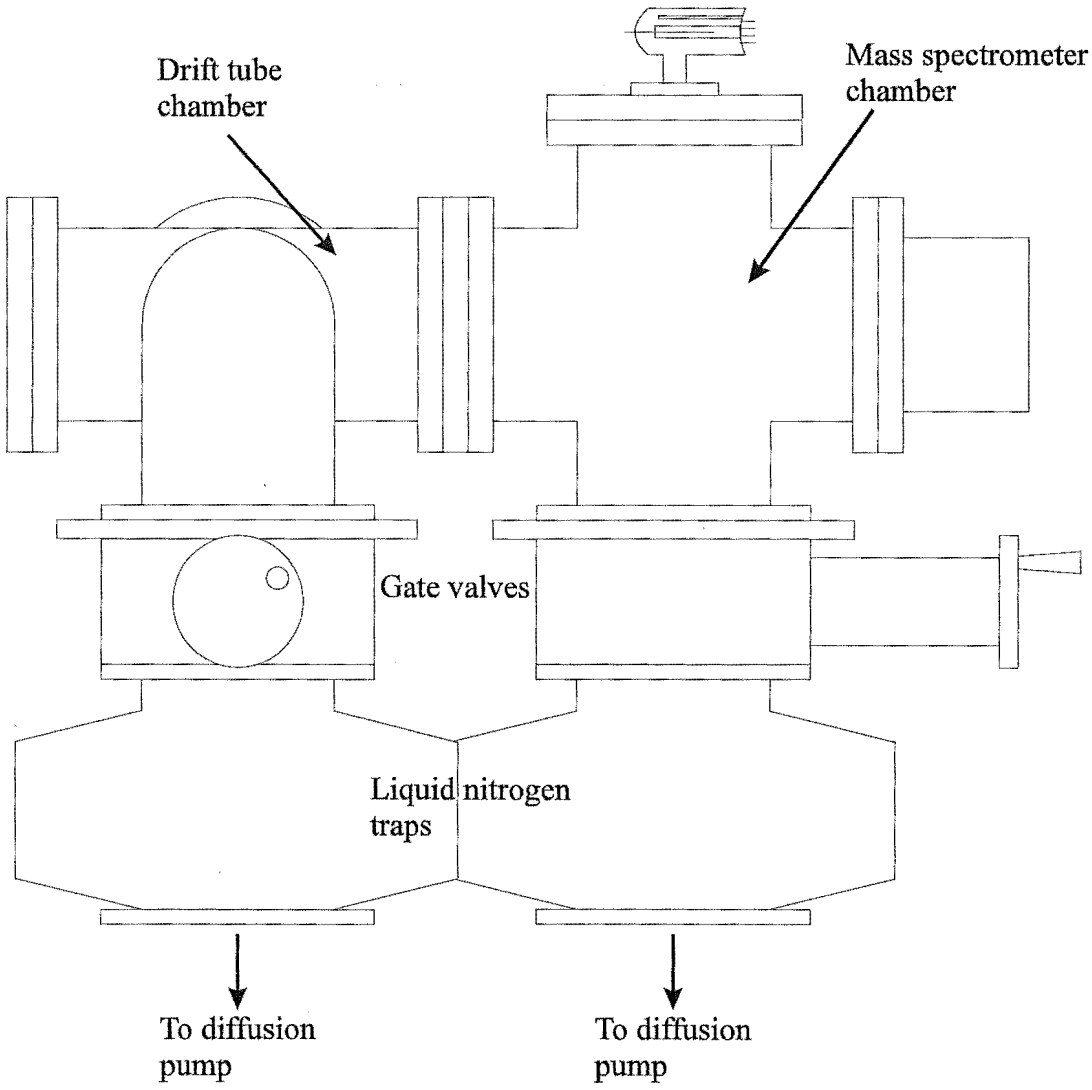

Fig. 2.1. The drift tube mass spectrometer vacuum system, scale 1:6.

2.1.1 Drift Tube Chamber

The drift tube chamber is mounted with the 4 way cross horizontal. The drift tube is mounted on an 8" flange attached to the cross opposite the flange connected to the mass spectrometer chamber. The drift tube flange incorporates all of the electrical feedthroughs to supply voltage to the drift tube rings as well as connections to thermocouples and heating elements in the drift tube jacket. $^1/_4$" stainless steel tubing carries coolant water to the jacket through two brass o-ring Swagelock fittings screwed into the flange. The gas inlet for the drift tube is also mounted this way while the gas outlet is a $^3/_8$" copper tube welded in place. The centre of the flange has a 50 mm hole machined into it through which a 83 mm OD flange containing the movable ion source feedthrough is mounted. A tin wire gasket is sandwiched between the flange and the ion source feedthrough to provide the necessary vacuum seal. Pressure monitoring for the chamber is via a Varian 843 ionisation gauge controller connected to a MKS Bayard-Alpert type ion gauge mounted on a $2^3/_4$" flange attached to the centre of an 8" flange bolted to one of the remaining ports on the cross. Attached to the last port is an 8" stainless steel elbow (Varian) leading to the pumping system.

The drift tube chamber is pumped by a 2000 Ls^{-1} Varian VHS-4 oil diffusion pump, backed by a two stage Dynavac D330 rotary mechanical pump. A Varian 362-4 4.7 L donut shaped liquid nitrogen cold trap is mounted on top of the diffusion pump to prevent oil backstreaming and to improve the vacuum in the drift tube chamber. Isolation of the pumping system from the vacuum chamber is via a Airco Temescal 4" 5010-R gate valve. Varian 1251 $1^1/_8$" bellows valves are used to bypass the diffusion pump for rough pumping of the drift tube chamber by the mechanical pump. Pressure is monitored in the diffusion pump foreline and just above the mechanical pump using 531 thermocouple gauges. Operating pressure for the chamber with 0.2 torr gas pressure in the drift tube is in the range 10^{-6} torr.

2.1.2 Mass Spectrometer Chamber

The mass spectrometer chamber is mounted with the 4 way cross vertical. The top flange is occupied by a MKS Bayard-Alpert type ion gauge mounted on a $2^3/_4$" flange mounted onto the 8" flange to monitor pressure. This is monitored by a Veeco RG-830 ionisation gauge controller Attached to the end port is the quadrupole mass spectrometer, an Extranuclear 4-270-9. The bottom flange leads to the pumping system. The liquid nitrogen trap, gate valve and foreline valves are identical to those used on the drift tube chamber {2.1.1}. The oil diffusion pump is a Bendix PMCS 4B which is backed by a 158 $Lmin^{-1}$ two stage Edwards Speedivac ES150. A pressure of 10^{-8} torr is maintained in the chamber, for operating pressures in the drift tube around 0.2 torr.

2.1.3 Protection System

Sensitive equipment such as the mass spectrometer needs to be protected from damage in case of a vacuum or pumping system failure. The protection is triggered by any one of:

- Vacuum failure in the mass spectrometer chamber
- Temperature increase of a diffusion pump
- Increase of a diffusion pump foreline pressure.

Full scale deflection of the reading from the mass spectrometer chamber ion gauge will result in the shutdown of both diffusion pumps and any electronics drawing power from the protected supply. Appropriate setting of the range on the Veeco ion gauge controller sets the full scale trigger to any pressure from 10^{-7} torr up to 10^{-3} torr, 10^{-5} torr being the normal trip point. Usually the ion source is protected to prevent burn out of the filaments at high pressure. The mass spectrometer is always protected to avoid rf discharge between the quadrupole rods and to prevent high voltage discharge across the surface of the channeltron electron multiplier.

A reduction in the flow rate of the diffusion pump water cooling supply can result in damage to the diffusion pump oil. If the temperature registered by thermocouples attached to the water lines on the diffusion pumps exceeds a preset limit the protection is triggered and all protected equipment and the diffusion pumps are switched off. The diffusion pumps can be manually turned back on once the temperature has dropped back to acceptable levels.

In a similar manner, failure of a mechanical pump results in high foreline pressure to the connected diffusion pump. If the foreline pressure increases above a preset value the protection is triggered as normal but only the diffusion pump with the high foreline pressure is turned off. The pump may be turned back on when the foreline has dropped below the preset pressure.

2.2 Gas Handling

Gas mixtures for admission to the drift tube are prepared and stored in a glass array of gas lines and storage bulbs (Fig. 2.2). The central manifold is divided into two independent sections and consists of fixed and removable storage bulbs, connections to the pressure monitoring and pumping system and gas inlets to the drift tube. A $^1/_4$" copper gas line is also attached to one end of the manifold for easy connection to regulated gas cylinders. All valves are high vacuum teflon barrelled taps. The gas handling system is pumped by a water cooled oil diffusion pump backed by a 75 $Lmin^{-1}$ Alcatel 1004A single stage mechanical pump. The vacuum established is typically of the order of 10^{-3} torr and is monitored by a 531 thermocouple gauge connected to a Duniway Stockroom Corp thermocouple gauge display. For the preparation of gas mixtures the pressure is monitored using a 1000 torr MKS 122AD differential capacitance manometer, the reference side pumped by the gas line diffusion pump. The mixtures from these bulbs are admitted to the drift tube using a Varian 951-5106 variable leak valve. If necessary gases are purified for use by passing through molecular sieve, liquid nitrogen traps or both. Liquids can be vacuum distilled by similar methods.

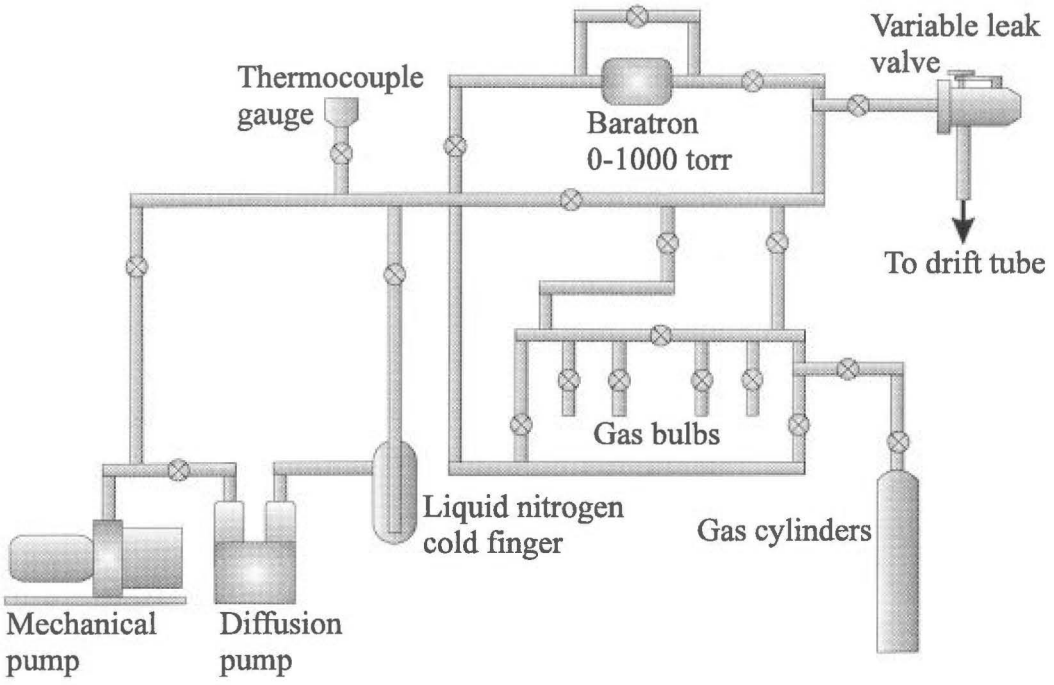

Fig. 2.2. The drift tube gas handling system.

2.3 Ion Source Linear Motion Feedthrough

The drift tube ion source is mounted on the end of a linear motion feedthrough (Fig. 2.3) which allows positioning of the ion source at any point along the drift tube length to an accuracy better than 0.1 mm. A stainless steel bellows retains the vacuum and allows the feedthrough to be extended and contracted. A GKH variable speed motor connected to a GKH S-10 motor controller is used to drive the feedthrough. To prevent damage from over extension or contraction while driving the feedthrough, two microswitches, set to trip out the motor, limit the extremes of the motion so the ion source is kept safely within the length of the drift tube. The feedthrough is supported on an 83 mm stainless steel flange sealed against the drift tube flange with a tin wire gasket. The shaft passes through a 50 mm hole in the centre of the drift tube flange. The centre of the feedthrough shaft is hollow and acts as a gas inlet directly into the ion source. A sapphire glass window attached to the end of the shaft allows a He/Ne laser to be aimed down the hollow shaft for alignment of the drift tube, skimmer and mass

spectrometer to the ion source feedthrough axis. Ion sources are mounted on the end of the feedthrough and are electrically isolated from the support by a glass ceramic disc. Electrical connections are made with a rod and sleeve arrangement to allow for extension of the feedthrough. The sleeves are attached to electrical feedthroughs passing through the linear motion feedthrough support flange and the rods are fixed at the other end to the glass ceramic disc to allow electrical connections to be made to the ion source elements.

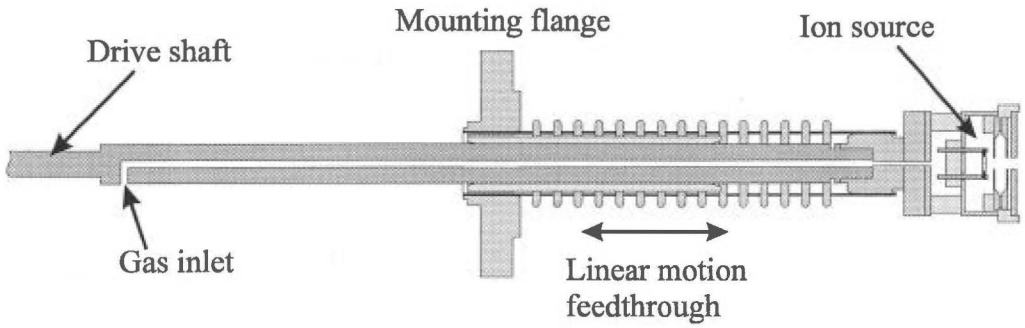

Fig. 2.3. The drift tube ion source mounted on the linear motion feedthrough, scale 1:3.

2.4 Drift Tube

2.4.1 Drift Tube Apparatus

The drift tube comprises eleven 1 cm wide interlocking gold plated stainless steel rings of internal diameter 5 cm. The rings are separated by precision ground glass ceramic insulators and are connected electrically by vacuum compatible 100 kΩ resistors. The drift tube endplate is also gold plated stainless steel. A 1.5 cm diameter molybdenum disc is mounted in the middle of the end plate containing a conical exit aperture drilled through the disc of minimum diameter 0.25 mm. The drift tube is surrounded by a stainless steel jacket which acts as a water cooled vacuum envelope to thermostat the drift tube environment. The jacket contains four 150 W cartridge heaters

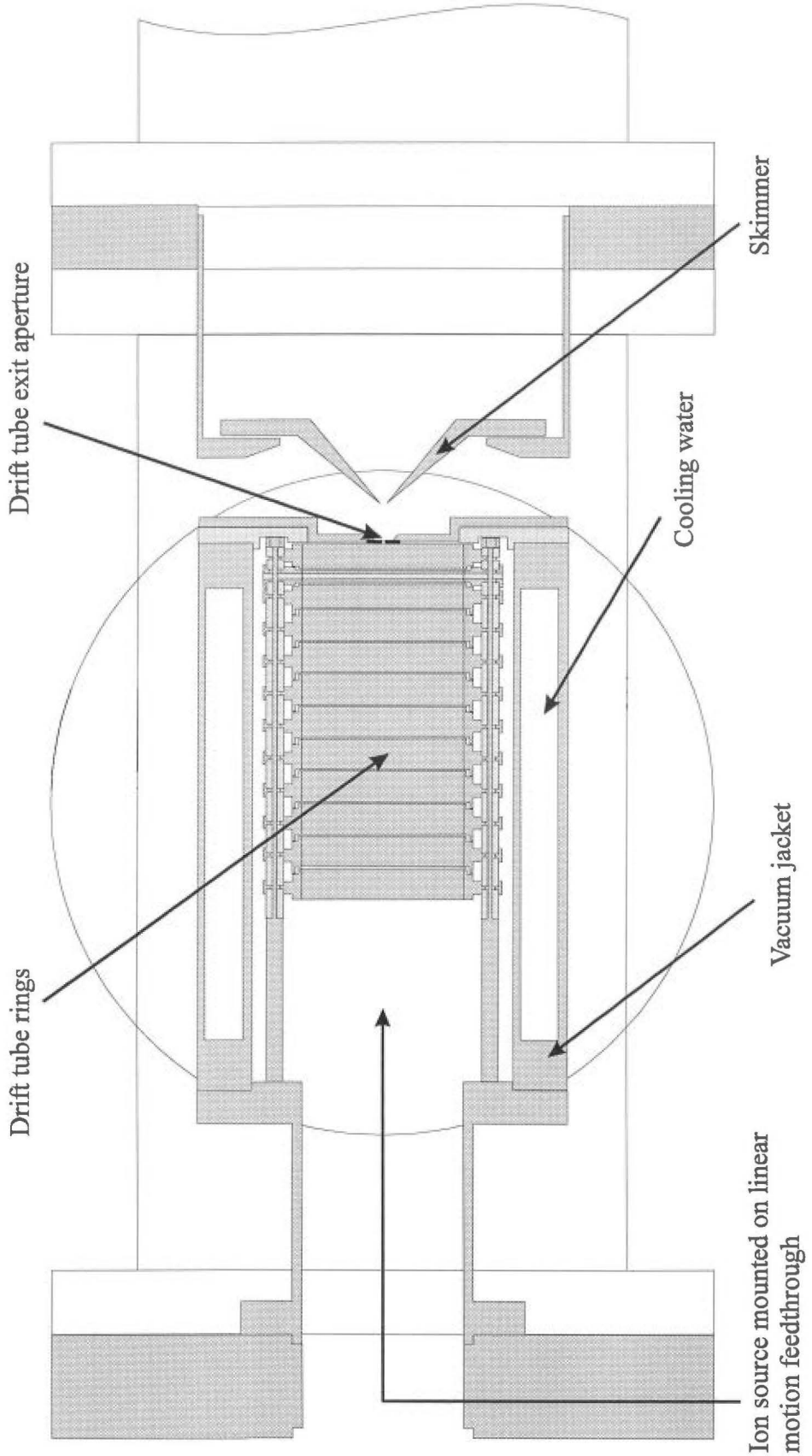

Fig. 2.4. The drift tube rings and thermostated vacuum jacket, scale 1:2.

for baking the drift tube to facilitate degassing from the surfaces. Fig. 2.4 details the drift tube and vacuum jacket design.

Temperature is monitored with iron-constantan thermocouples positioned; on the third and ninth drift rings (numbered from the ion source feedthrough end), in the space between the rings and the vacuum jacket, and a fourth on the envelope. During typical operation the temperature is maintained at about 298 K by regulating the water flow through the vacuum jacket. The heat generated in the ion source by the hot filament results in a temperature increase of 1-2 K in the immediate drift tube vicinity over the average background temperature.

Gas samples are admitted to the drift tube via gas inlets through the shaft of the linear motion feedthrough and through the vacuum jacket into the space near the middle drift ring. The pressure is monitored with a gas outlet passing through the vacuum jacket opposite the gas inlet. This line can also be used to quickly evacuate the drift tube. The pressure is measured by a 310CH-10 MKS capacitance manometer with a 10 torr head. This is connected to a 170M-6C MKS electronics unit which displays the pressure on a MKS 250B controller.

The entire drift tube vacuum jacket assembly is mounted on a stainless steel spigot attached in turn to an 8" flange. All electrical connections, gas lines and water lines pass through the flange to keep the removal of the drift tube for maintenance as simple as possible.

2.4.2 Theory

Ions produced in the ion source exit the source and are accelerated by the electric field E (Vcm^{-1}) in the drift tube. The potential difference (V) applied across the rings is

$$V = 10.5E. \tag{2.1}$$

The electric field must be kept constant for various positions of the ion source along the drift tube axis. To ensure this is the case the ion source end plate is electrically biased at a potential V_z according to the distance z (drift distance) from the ion source end plate to the drift tube exit plate

$$V_z = Ez. \tag{2.2}$$

Two opposing forces act on the ions as they travel down the drift tube. They are accelerated by the drift tube electric field and decelerated by elastic and inelastic collisions with the gas species present in the drift tube. The ions will reach a terminal velocity when these forces are balanced, termed the drift velocity (v_d) [Ellis, 1976; McDaniel, 1984].

$$v_d = KE. \tag{2.3}$$

The proportionality constant K is called the mobility of the ion and is a property of both the ion and the gas through which it is drifting. The mobility is usually reported as a reduced mobility (K_0) defined at STP such that

$$v_d = N_0 K_0 \left(\frac{E}{N}\right) \tag{2.4}$$

where N_0 is the gas number density at STP. Equation 2.4 shows the drift velocity is a function of both the drift tube electric field and the gas pressure.

Wannier [Wannier, 1953] showed that the total energy (E_k) of an ion in the drift tube is given by

$$E_k = \frac{mv_d^2}{2} + \frac{Mv_d^2}{2} + \frac{3k_bT}{2} \tag{2.5}$$

where m is the ion mass, M is the neutral species mass, T is the gas temperature and k_b is the Boltzmann constant. The first term is the electric field energy due to the drift motion of the ions, the second term is due to the random part of the field energy and the

final term is the thermal energy. The centre of mass relative kinetic energy (E_{rel}) for the ion molecule collisions will be

$$E_{rel} = \frac{3k_bT}{2} + \frac{Mv_d^2}{2}. \tag{2.6}$$

2.5 Mass Spectrometer

The quadrupole mass spectrometer detector is an Extranuclear model 4-270-9. The mass spectrometer is mounted on an 8" flange and aligned to the drift tube axis. Ions exiting the drift tube pass through a skimmer with a 2 mm diameter orifice before being focused by an Einzel lens into the quadrupole mass filter. The mass selected ions are detected by a Galileo 4816 channeltron electron multiplier. A schematic of the complete mass spectrometer system is given in Fig. 2.5.

2.5.1 Quadrupole Mass Filter

The quadrupole mass filter [Dawson, 1976] uses a high frequency transverse electric field to permit transmission of ions on the basis of their mass to charge ratio (m/z). The quadrupole consists of four parallel rods spaced evenly about the axis. Ideally rods with hyperbolic cross section are used but due to machining difficulties rods of circular cross section are more common. For circular rods the ratio of the quadrupole inscribed radius r_0 to the rod radius r is set to 0.871 to closely match the electric field generated by hyperbolic rods (Fig. 2.6). DC potentials and radio frequency (rf) potentials are simultaneously applied to the rods with opposite rods connected together. The rods in the x-z plane have an applied potential of $+(U + V\cos(2\pi ft))$ and the rods in the y-z plane $-(U + V\cos(2\pi ft))$. U is the dc voltage and V is the peak rf amplitude of

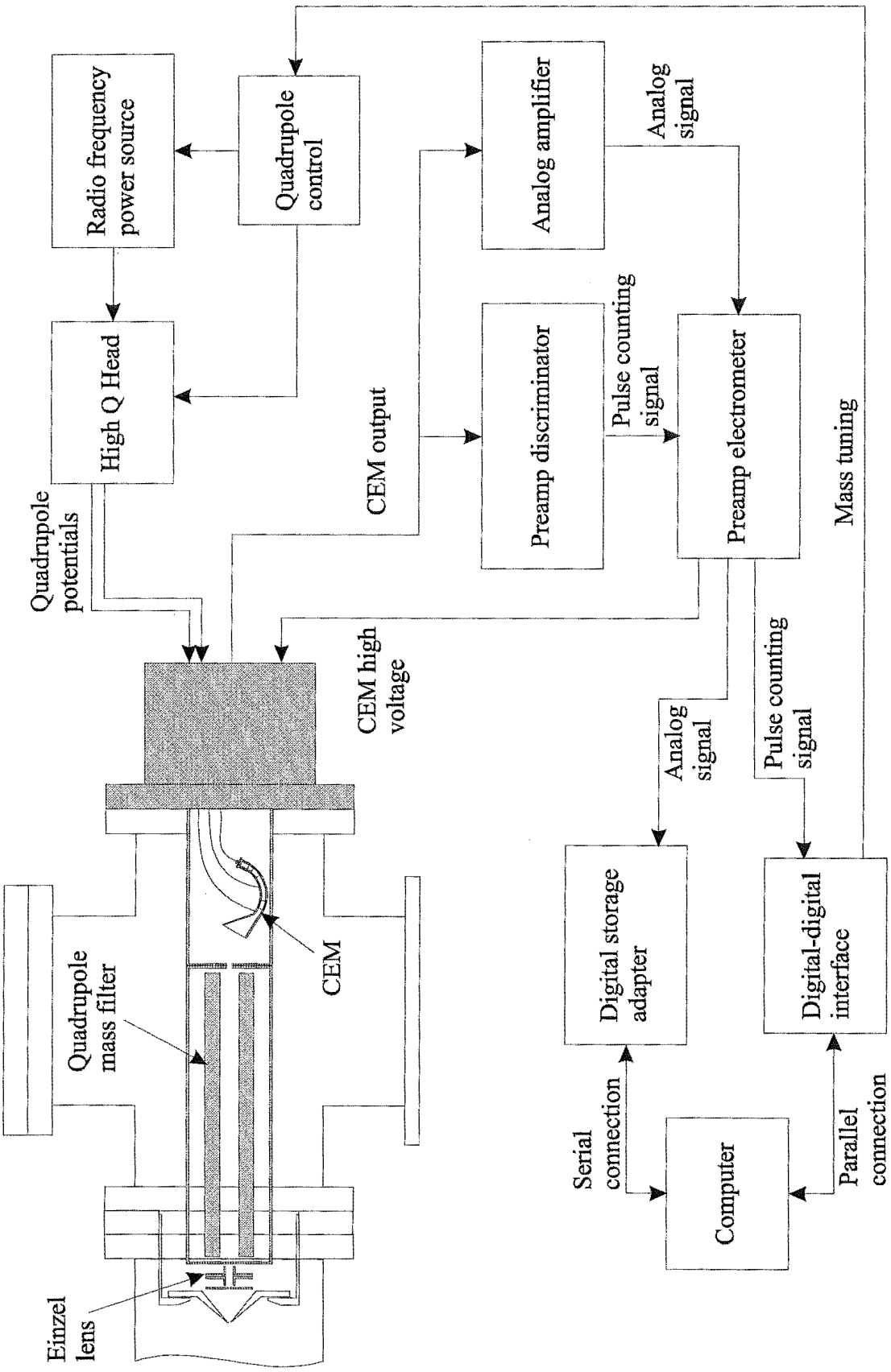

Fig. 2.5. Schematic of the Extranuclear mass spectrometer, scale 1:5. Includes analog and pulse counting data collection schemes.

frequency *f*. The rf potential applied to the x-z rods is out of phase by 180° with the rf on the rods in the y-z plane.

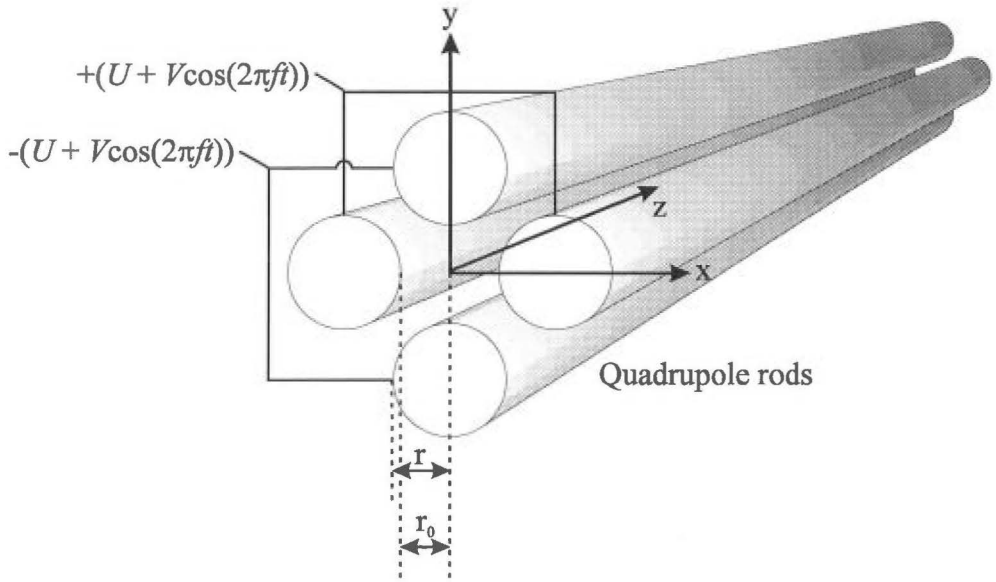

Fig. 2.6. Quadrupole mass filter.

The oscillatory motion of the ions in the quadrupole electric field is complex and is described by the Mathieu equations [Dawson, 1976]. Positive ions entering the field on axis will experience a repulsive dc potential in the x-z plane coupled with a rf field inducing oscillations in the ion trajectories. The amplitude of this oscillation increases with decreasing ion mass. Simultaneously the ions will be subjected to an attractive dc field in the y-z plane with the superimposed rf field tending to guide the lighter ions towards the axis. The amplitudes U and V are adjusted so that only ions with a single m/z will follow stable trajectories through the quadrupole field. Lighter ions will be lost to the rods in the x-z plane, heavier ions will be lost to the rods in the y-z plane. The transmission of the quadrupole is described by the stability plot of the parameters a and q functions of U and V respectively in Fig. 2.7.

The quadrupole is scanned along a line where the ratio a/q is constant, that is the ratio of the dc and rf amplitudes is fixed. Only ions with masses falling within the stable area will be transmitted by the quadrupole. The points at which the scan line crosses the stability region boundaries determines the band width Δm of the quadrupole.

Increasing the slope of the scan line a/q = const brings the line closer to the apex of the stable region, hence a narrower band of masses (Δm) are transmitted. The quadrupole resolution is increased at the cost of reduced transmission. The resolution can also be increased by increasing the rf frequency or increasing the quadrupole length. The resolution is decreased for high energy or divergent ion beams. Hence the ion energy is typically kept in the range 2-50 eV and the use of an Einzel lens to focus ions into the quadrupole reduces the divergence.

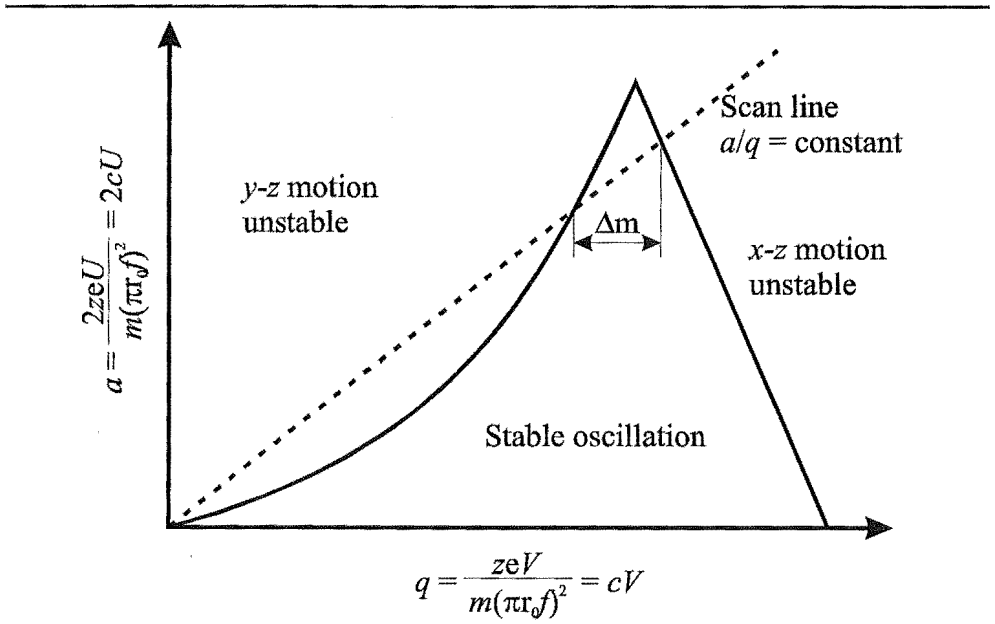

Fig. 2.7. Stability diagram for the quadrupole mass filter.

2.5.2 Channeltron Electron Multiplier

The simplest method to detect an ion beam is to use a Faraday cup, however lack of gain means the sensitivity of the Faraday cup is poor. Instead channeltron electron multipliers (CEM) (or particle multipliers) are used which have a sensitivity many orders of magnitude greater than a Faraday cup.

The CEM (Fig. 2.8) is constructed of a heavily lead doped glass, the inside is coated with a semiconductive layer of very low work function. The front end forms a

cone for collection of the ions and has a large negative potential (1.5-2.5 kV) applied to it to attract the positive ions. The cone tapers to a hollow curved tube which is grounded at a point part way along its length. Ions striking the inside of the cone will cause the emission of at least one secondary electron from the semiconductor surface. This electron is accelerated down the CEM by the electric field until it hits the surface, where if it has gained enough energy, it will cause the emission of more than one secondary electron. These electrons in turn will be accelerated down the tube striking the walls resulting in more secondary electrons being released. Repetition of this pattern along the length of the CEM produces a cascade of electrons, perhaps 10^8 for each individual ion impacting in the cone. The electrons exiting the end of the CEM are collected on a small metal cup and measured. The gain from the electron multiplying effect means an ion signal of a few femtoamps is converted to an easily measured current of a few hundred nanoamps.

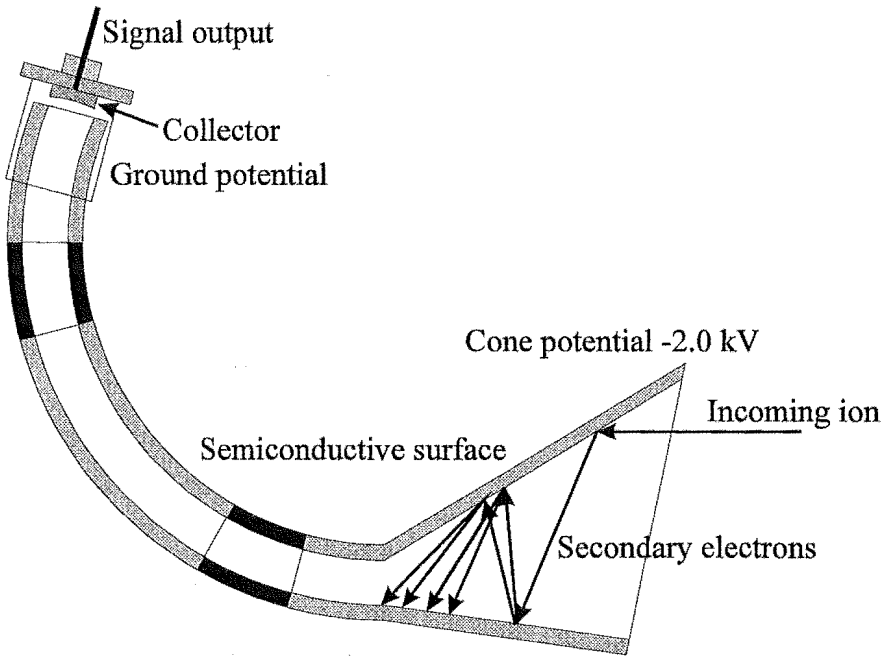

Fig. 2.8. Channeltron electron multiplier.

CEM's can be operated in two modes; pulse counting or analog. The electron pulses exiting the CEM from individual ion impacts have a duration of around 10 ns. These electron pulses are amplified by a preamp discriminator which converts the current pulses to voltage pulses of height 5 V and width 250 ns. These amplified pulses

can be individually counted only if they can be distinguished in time from other pulses. For ion impact rates of less than 1 MHz on the CEM cone the pulses are completely resolved and individual pulses can be counted, this is pulse counting mode. For higher ion intensities where overlap of successive pulses is significant, pulse counting fails and analog amplification is necessary. The time averaged output from the CEM is amplified typically to 0-10 V with a time constant around 50 μs.

CEM's are very sensitive and must be used with care. Exposure to pump oil corrupts the semiconductor surface and lowers the gain resulting in a reduced operational lifetime. Cleaning of the CEM with solvents can only partially restore the gain. Operation of the CEM at pressures in excess of 10^{-4} torr can cause electrical discharging across the semiconductor surface effectively destroying the CEM.

Chapter 3

Alkali Ion Chemistry Results

3.1 Zeolite Ion Exchange

Type A zeolite [Breck, 1956], available commercially as Linde 4A molecular sieve was initially used as the thermionic alkali ion emitter. Emission intensities greater than 1 μA were attained. Mass analysis of the emission showed a mixture of K^+ and Na^+ ions present. The potassium was dominant with both the isotopes 39 and 41 distinguishable, lower levels of sodium were observed. After a number of hours of operation the Na^+ signal had decreased to about 5-10% of the total emission. The K^+ emission was measured with the mass spectrometer as a function of the filament current and is graphed in Fig. 3.1. The graph shows the zeolite emission reaches a maximum value probably limited by diffusion of the alkali ions through the zeolite matrix.

The purity of the alkali ion emission from the commercial type A zeolite is poor and if it is to be used as an ion source will need to be improved. Ion exchange of the commercial zeolite with appropriate solutions needs to be used to produce materials with pure emission of one of the alkali metals with only trace levels of the others. The zeolite can be ion exchanged by either the column or batch methods as described in {A.2.1}.

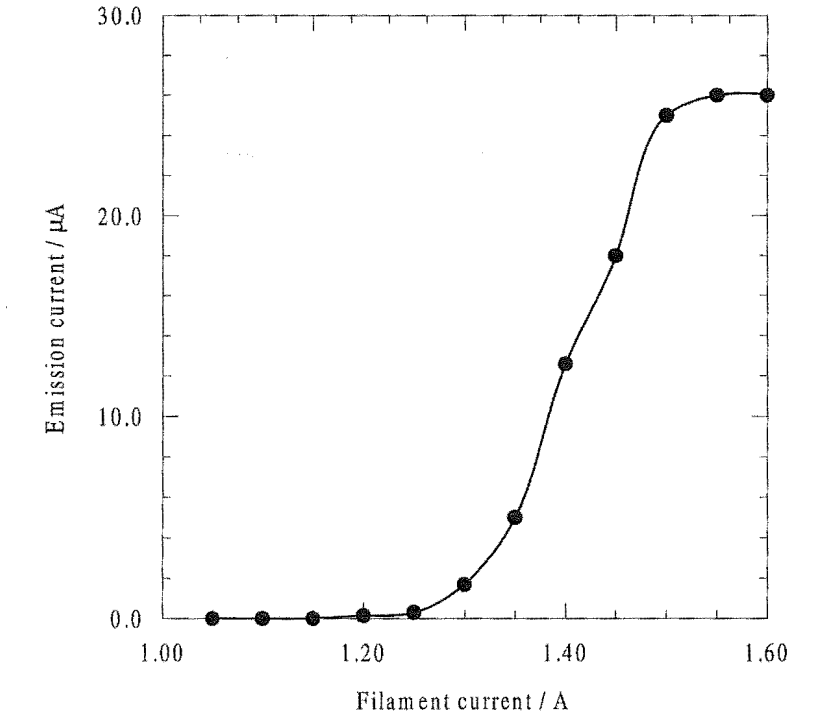

Fig. 3.1. K^+ emission from the crude type A zeolite.

3.1.1 Column Exchange

Columns for the exchange of the type A zeolite with Li^+, Na^+ and K^+ were setup as shown in Fig. 3.2. Heating tape was wrapped around the Li^+ column so the column could be run at 80°C [Satoh, 1987]. Type A zeolite was ground to a fine powder and placed into the column trapped between glass wool plugs. The zeolite bed height was around 7-8 cm with a diameter of 1 cm. The columns were left overnight with 1 M solutions of the alkali chloride (analytical grade) salt solutions to run through them. Unfortunately the flow resistance of the columns was extremely high and only a couple of millilitres of solution had passed through. The problem is the binder used to produce the zeolite pellets. When this is finely powdered it forms a paste with the aqueous solution introduced to the top of the column resulting in blockage. The columns were stripped and fresh type A zeolite was added but not as finely ground as the first attempt. This time the column flow resistance was low enough to allow the required flow rate of 0.5 $mLmin^{-1}$ to be attained. 2 L of the 1 M alkali ion solutions were passed through the

columns over a period of three days to ensure a large excess of the exchanging alkali cation was added.

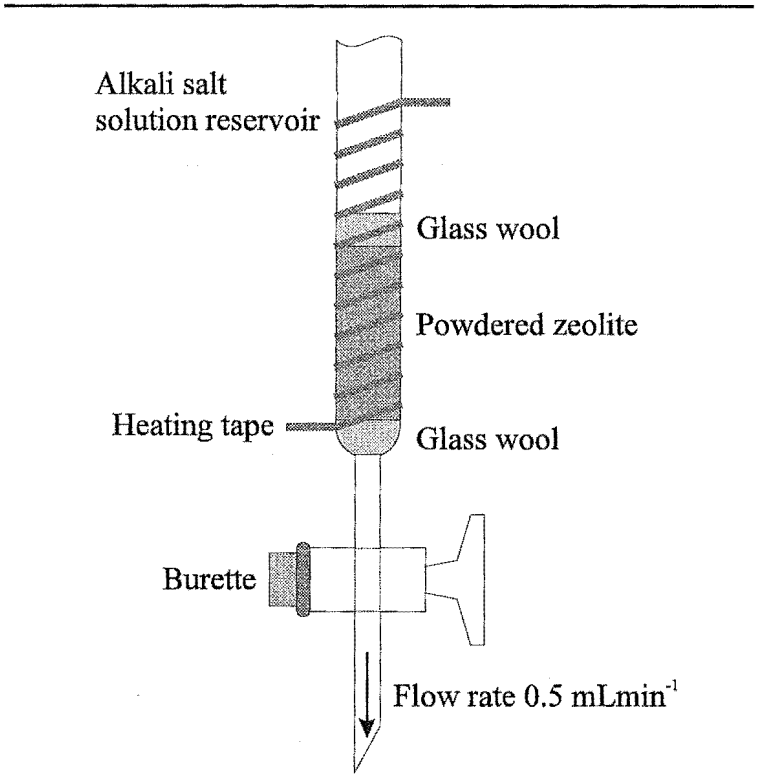

Fig. 3.2. Ion exchange column.

Samples of the ion exchanged zeolite were removed from the tops of the ion exchange columns, dried, finely ground and mounted on filaments. The emission showed the column exchange had only been partially successful. The K^+ source was the purest, only a trace percentage of Na^+ was observed which decreased with time as the filament was aged. Initially the Na^+ zeolite emission showed about a 50:50 ratio of Na^+:K^+. After running the filament for around 10 hours the Na^+ emission had become dominant, the Na^+:K^+ ratio had increased to about 8:1. Certainly ageing the filament improves the emission purity but a 10% level of impurities is still too high. The Li^+ exchanged zeolite was the least successful of all the ion exchanges. The initial emission was dominated by K^+ with a few percent of Na^+, there was no Li^+ seen. Leaving the source running overnight reduced the ratio of K^+:Na^+, the Li^+ signal which was now observable was still only a fraction of the total emission.

The ion exchange appears to be incomplete, especially in the case of the Li^+ emitter. This is probably due to the use of less finely ground zeolite. The irregular sizes of the zeolite particles packed into the column can lead to channelling of the solution as it will flow easier and faster through the less densely packed regions of the column. Hence the flow is favoured in volumes containing the larger zeolite particles, which, because of their size have less efficient ion exchange kinetics. In the dense parts of the column where the zeolite is finely ground the flow resistance is very high due to the binder from the zeolite. The finely ground zeolite will have very little exposure to the alkali ion solution and hence will have not undergone substantial ion exchange.

In order to improve the efficiency of the ion exchange column the powdered form of the type A zeolite [Weber, 1966] which does not contain the binder present in the pellets is required. On the other hand the problem can be avoided if the finely ground zeolite is ion exchanged by the batch method rather than by the use of a column.

3.1.2 Batch Exchange

Finely ground type A zeolite was stirred in excess 1 M alkali metal ion salt solutions to produce the Li^+, Na^+ and K^+ emitters (Fig. 3.3). Approximately 10 g of the zeolite in a 500 mL beaker, was stirred on a magnetic stirrer/hotplate with around 170 mL of the alkali solution for 12 hours. The zeolite was filtered and fresh solution was added for a further 12 hours exchange. This was repeated twice for a total of 500 mL of the 1 M alkali cation solution. The Li^+ exchange was run at 80°C as suggested by Satoh *et al* [Satoh, 1987] in a covered beaker to minimise evaporation. The final ion exchanged zeolite was washed in distilled water and thoroughly dried overnight in an oven at 120°C.

The K^+ emitter gave very pure emission. There was no detectable Na^+ present after a couple of hours ageing. The Na^+ emitter initially did not look very successful, the ratio of Na^+:K^+ was 0.6, definitely not what was required. After 5 hours running however the ratio had increased dramatically and the Na^+ accounted for over 90% of the

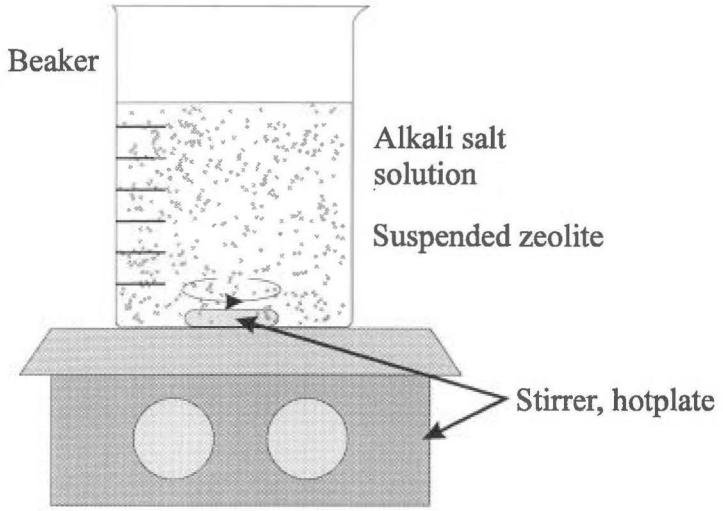

Fig. 3.3. Batch method for ion exchange.

total emission. Further ageing overnight reduced the K^+ impurity to 0.1%, an acceptable level. The decrease in the K^+ signal followed a roughly exponential decay shown in Fig. 3.4. The Na^+ emission is shown as a function of the filament current in Fig. 3.5.

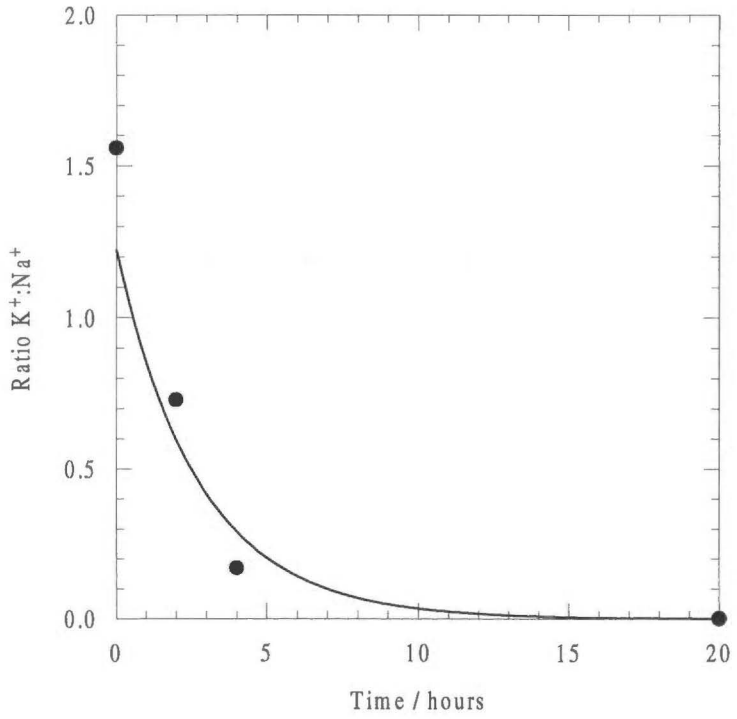

Fig. 3.4. Decay of the K^+ impurity in the Na^+ type A zeolite emitter.

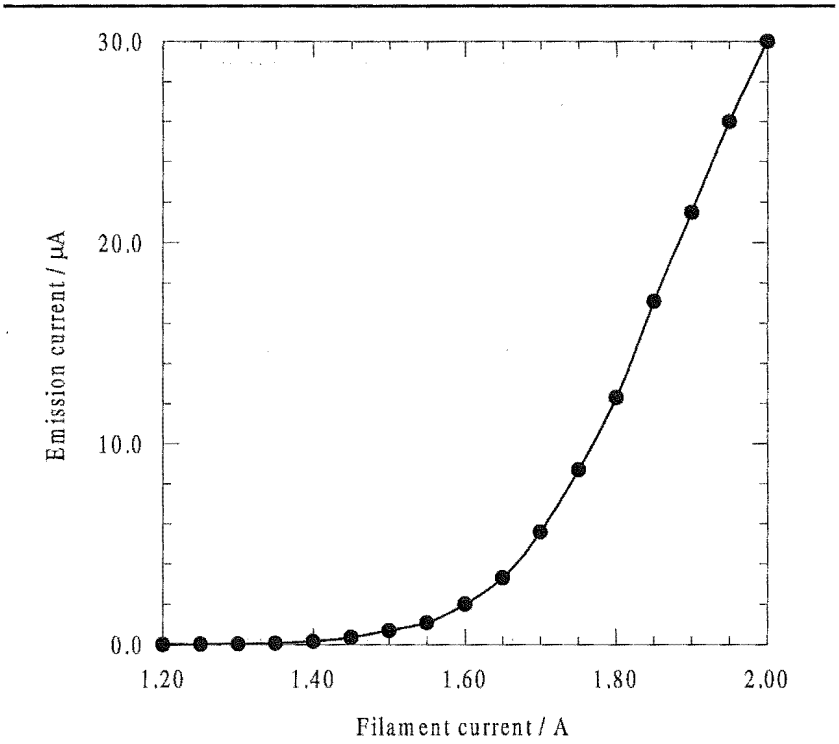

Fig. 3.5. The Na^+ emission from the Na^+ type A zeolite as a function of the filament current.

The Li^+ also looked poor initially. The emission was dominated by K^+ and Na^+ with almost no Li^+ observed. Ageing the filament at high current (1.9 A) gave around 50 μA emission of Na^+ and K^+. After 10 hours the K^+ signal had decreased to a fraction of a percent of the total emission, the Na^+ signal accounted for 5-10% of the emission and the Li^+ for greater than 90%. This is an enormous improvement over the results obtained from the ion exchange column. Further ageing of the filament did not reduce the Na^+ impurity to much less than 5%. This is probably due to sodium present in the lithium salt used in the ion exchange.

A sample of type Y zeolite was obtained in the Na^+ form. It gave highly pure Na^+ emission for filament currents similar to those used for the type A zeolites. The filament current threshold measured for the Na^+ type Y zeolite was lower than the threshold for the Na^+ type A zeolite. This is due to the lower work function for removal of Na^+ from the type Y zeolite [Satoh, 1987]. The emission characteristics of the type Y zeolite are shown in Fig. 3.6.

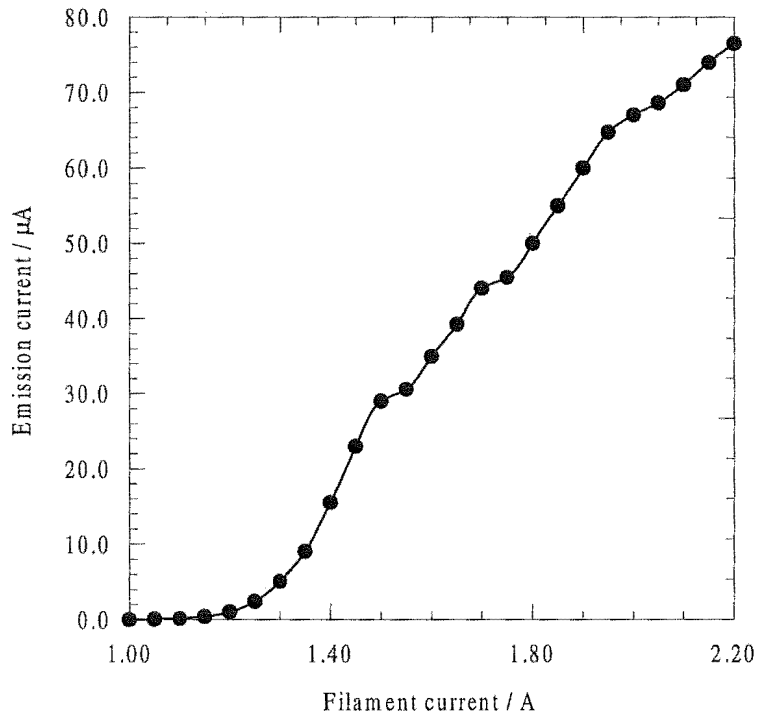

Fig. 3.6. The Na^+ emission from the type Y zeolite.

3.2 Ion Source

The drift tube electron impact ionisation source was used for the alkali metal ion source. The electron impact source incorporates twin rhenium filaments mounted in a shielded case with a two element extraction, focusing lens system. For conversion to use as an alkali ion source, the filament assembly was removed and replaced with a single filament for the production of alkali metal ions (Fig. 3.7). The filament is spot welded to molybdenum rods and clamped in a glass ceramic mount.

To ensure a reasonable lifetime for the alkali filament, the rhenium wire was coiled into a tube of 2 mm internal diameter by 6 mm long. The zeolite emitters were finely ground and mixed with amyl acetate to form a slurry which is painted onto the filament and dried by passing a current through the filament under a nitrogen atmosphere. Repeated applications of the slurry and thorough heating result in a solid glassy plug of the zeolite supported within and about the coiled wire. This proved to be

very satisfactory, all of the filaments used showed only a slight depletion of the emission after many days of operation. After extended use the filament wire tended to burn out, as the sources were operated in an environment containing reactive gases at pressures up to 0.2 torr. This occurred well before the depletion of the zeolite became a problem. As well as the zeolite sources several Spectra-mat 250 sources [Heinz, 1968] are available including the Li^6, Li^7, K and Cs. The Spectra-mat sources can be mounted easily into the existing ion source.

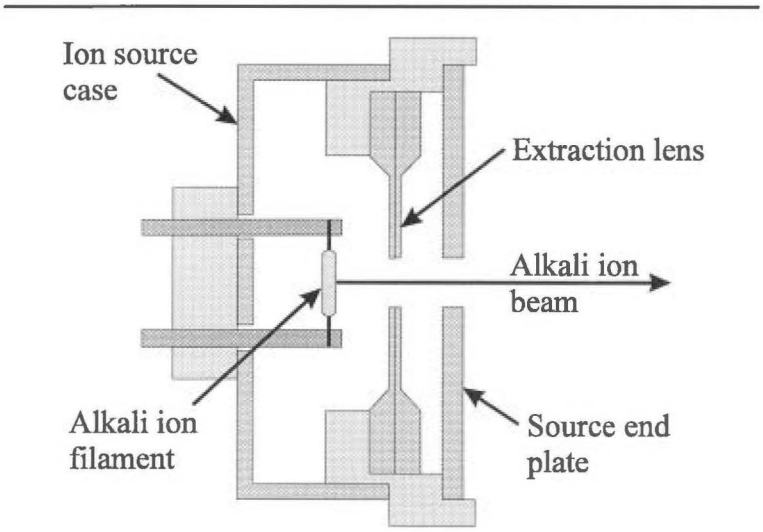

Fig. 3.7. Alkali metal ion source.

An intense alkali ion beam can be generated from the source by a combination of appropriate filament current and ion lens voltages. For the zeolite to emit ions it must be heated by the filament so that the temperature is high enough to overcome the work function for the emission of ions from the zeolite. Coupled with this are the ion extraction optics which must be at potentials suitable to extract the alkali ions from the vicinity of the filament and focus them into an ion beam. For use in energy dependent experiments involving the drift tube the ion energy is very important so the potential gradient between the filament and ion source end plate is matched to the gradient in the drift tube. The extraction lens immediately in front of the filament is then used as needed to produce an ion beam of the desired intensity. Similarly, for the production of an ion beam in a crossed beam reaction with a neutral species, the energy of the beam is determined by the potential gradient between filament and source end plate. The extraction lens again controls the beam intensity and focusing. SIMION 6.0 [Dahl,

1995] an electrostatic lens design and analysis program, was used to calculate the trajectories of the alkali ions generated by the source for typical ion source electrical potentials. The results are given in Fig. 3.8.

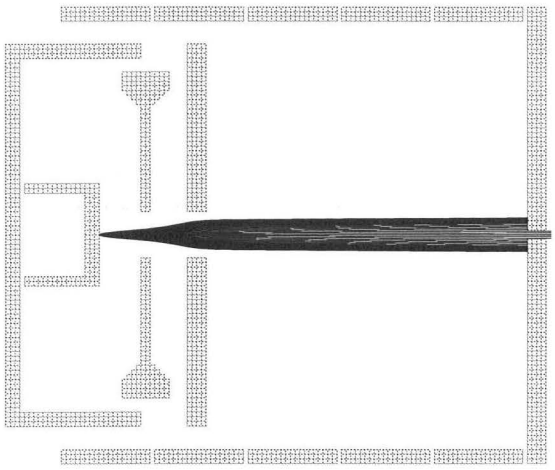

Fig. 3.8. Trajectories through the drift tube for K^+ ions generated in the ion source.

3.3 Drift Velocities

The measurement of the alkali ion drift velocities {2.4.1} in the drift tube is necessary to determine the ion energy for reactive collisions of the alkali ions with any gas species introduced to the drift tube. To measure the drift velocity of the alkali ions in a specific gas, the ion source must be operated in a pulsed fashion to enable the arrival time distribution (ATD) of the ions to be collected.

The ion source is pulsed by the application of a blocking bias potential to one of the source lenses to prevent alkali ions from exiting the source. Pulsing this potential for a short period to a value which allows alkali ions to pass, will admit a short burst of ions into the drift tube. The time dependent signal received by the mass spectrometer can be collected and digitised by a storage oscilloscope triggered by the switching of the ion source blocking potential. The flight time of the ions through the region beyond the end of the drift tube and end effects due to distortions at the end of the drift tube can be

eliminated by recording ATD's at multiple positions of the ion source in the drift tube. The ion drift velocity is then taken as the slope of the resultant plot of ion source position verses the time for the maximum point of the ATD's.

ATD's were measured for K^+ ions in Ar by pulsing the ion source extraction lens with an open time of 5 μs. The ATD's produced were broad and of low intensity and hence the uncertainty in the position of the distribution maximum is large. The emission from the filament was obviously affected by the electric field changes imposed by the pulsing lens. To avoid this problem and hence improve the ATD shape, a third lens was added to the ion source to provide the pulsed blocking potential (Fig. 3.9). The SIMION calculations illustrating the effect of the pulsed blocking potential are shown in Fig. 3.10.

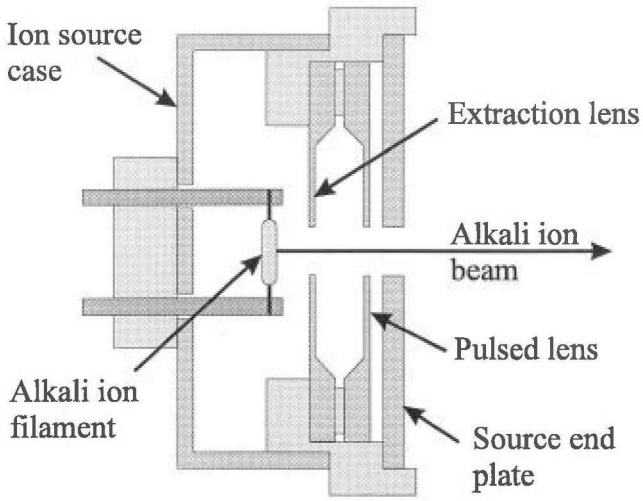

Fig. 3.9. Alkali metal ion source containing an extra lens to pulse the source.

The results of experiments to measure the drift velocities of Na^+ and K^+ in the inert gases He and Ar were successful in reproducing the literature values. However, because large drawout voltages were used in the ion source the ions take time to reach equilibrium with the gas in the drift tube. For this reason, measurements of the drift time for the pulsed ions could not be made with the ion source positioned within 3-4 cm of the drift tube exit plate, as for these short distances the alkali ions had not attained the terminal drift velocity. For longer drift distances the ions have time to reach equilibrium

before they exit the drift tube and measurements can be made to determine the drift velocity.

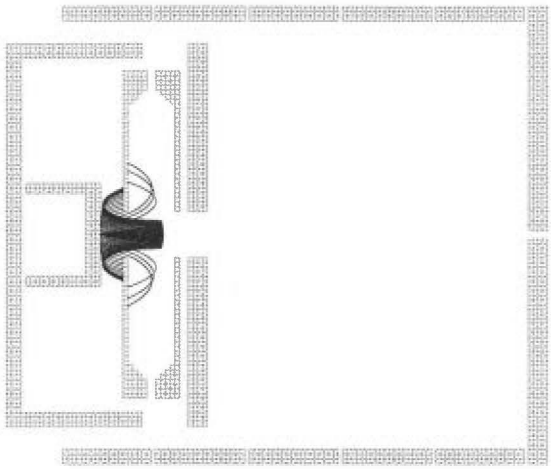

Fig. 3.10. K^+ ion trajectories prevented from entering the drift tube by the blocking potential applied to the pulsed lens.

3.4 Alkali Ion Chemistry

3.4.1 Background

The chemistry of the alkali metal ions with alkyl halides and alcohols has been studied using ion cyclotron resonance (ICR) [Allison, 1979; Larrivee, 1990; Staley, 1977; Wieting, 1975] and crossed molecular beams [Creasy, 1985; Creasy, 1986; Creasy, 1987a; Creasy, 1987b] since the mid seventies. The reactions reported were mostly dehydration of the alcohols and dehydrohalogenation of the alkyl halides. In some cases where the reaction enthalpy was exothermic, such as when M = Li and RX = t-C_4H_9Br [Staley, 1977], the halide transfer reaction 3.1 was observed.

$$M^+ + RX \rightarrow MX + R^+ \qquad (3.1)$$

Generally the enthalpy for this reaction is endothermic due to the greater affinity of the halide for the alkyl cation than for the alkali ion. For the alkyl halides used in this work the enthalpy changes for reaction 3.1 are given in Table 3.1. The endothermicity is especially large in the cases of the CH_3X molecules, up to 452 $kJmol^{-1}$ for the reaction of K^+ with CH_3Cl. Obviously at the thermal energies used in the (ICR) experiments [Larrivee, 1990] there is not enough energy available to activate the halide transfer reaction channel, but if high energy (1-5 eV) alkali ions are used there may be enough collisional energy available from the fast ions to induce the reaction. In the drift tube which was used here to study the reactions of the alkali ions, the acceleration of the ions to high drift velocities by the drift tube electric field {2.4.1} provides the means to increase the collision energy to activate reaction 3.1. With pure alkyl halide gases present in the drift tube at pressures of about 0.1 torr the alkali ions can be accelerated up to energies around 2 eV. If dilute mixtures of the alkyl halide in light inert buffers such as He are used, the increase in the ion drift velocity allows even higher collision energies to be accessed.

	Li^+	Na^+	K^+
CH_3Cl	298.8	389.6	452.3
CH_3Br	297.4	384.4	442.4
t-C_4H_9Cl	1	92.1	153.7
t-C_4H_9Br	-2.1	84.4	142.9

Table 3.1. The enthalpy changes ($kJmol^{-1}$) for the halide transfer reaction 3.1 for the symmetric top alkyl halides used in this work. All enthalpies for these and reactions 3.2-3.36 were calculated using heats of formation tabulated by Lias *et al* [Lias, 1988].

Based on the enthalpies in Table 3.1, the reactivity is expected to follow the trend $Li^+ > Na^+ > K^+$ and increase for increasing substitution of the alkyl halide. This is also expected of the dehydrohalogenation reaction

$$M^+ + RHX \rightarrow MR^+ + HX \qquad (3.2)$$

and the elimination reaction

$$M^+ + RHX \rightarrow MHX^+ + R \qquad (3.3)$$

which have both been observed for numerous systems [Allison, 1979; Creasy, 1987a; Creasy, 1987b; Staley, 1977; Wieting, 1975].

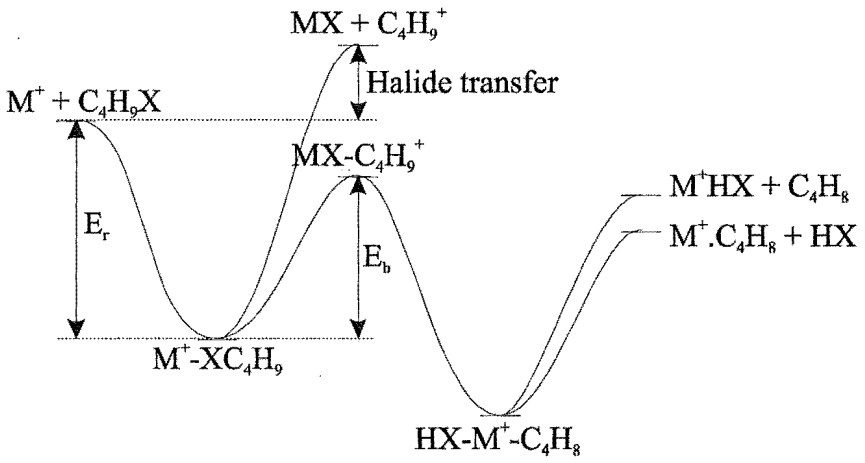

Fig. 3.11. Potential energy curve for the reactions of M^+ with t-C_4H_9X.

Allison and Ridge [Allison, 1979] observed the dehydration reaction for Li^+ reacting with t-C_4H_9OH (reaction 3.2 where X = O) but did not observe any reaction for Li^+ with i-C_4H_9OH even though the dehydration of i-C_4H_9OH is 42 kJmol^{-1} more exothermic than the dehydration of the t-C_4H_9OH. Similarly the dehydrohalogenation of t-C_4H_9Cl with Na^+ was observed but reaction with i-C_4H_9Cl wasn't, although dehydrohalogenation of i-C_4H_9Cl is 25 kJmol^{-1} more exothermic. The reactivity agrees with the trend due to increasing substitution shown in Table 3.1 but does not agree with the enthalpies of the dehydrohalogenation reactions. The important factor controlling the reactivity is the difference in the heterolytic bond strengths $D(R^+\text{-}X^-)$ - $D(M^+\text{-}X^-)$ which corresponds to the enthalpy change for the halide exchange reaction 3.1. This suggests a reaction mechanism involving transfer of the halide to the alkali metal ion and generation of charge on the alkyl fragment. The schematic potential energy surface for this is shown in Fig. 3.11. Reaction will occur when the energy of the reactants (E_r) exceeds the barrier height (E_b) which is related to the halide transfer enthalpy.

Wieting *et al* [Wieting, 1975] proposed the mechanism in Fig. 3.12 for the reaction of alkali cations with alkyl halides. The halide transfer products are ejected

from the collision complex before isomerisation of the complex occurs. The isomerisation corresponds to crossing the barrier E_b shown in Fig. 3.11. The elimination products are produced from the rearranged intermediate. Allison and Ridge [Allison, 1979] observed various reaction sequences for different combinations of alkali ions and alkyl halides. Generally, the products of the primary halide transfer and elimination reactions reacted further with the alkyl halide RHX by dehydrohalogenation or elimination of the R fragment.

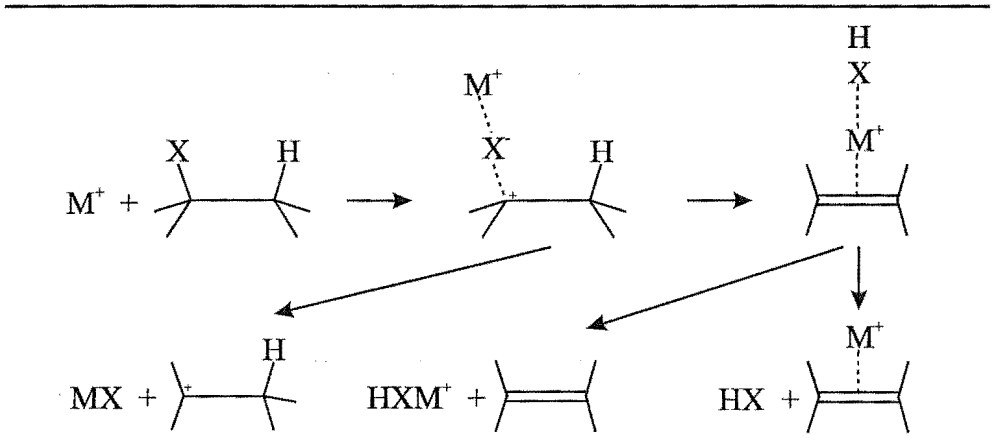

Fig. 3.12. Reaction mechanism for M^+ with an alkyl halide.

In this work mass spectra are recorded using the drift tube mass spectrometer by passing high energy K^+ ions through the drift tube which is pressurised to 0.1 torr with either CH_3Cl, CH_3Br, t-C_4H_9Cl or t-C_4H_9Br. The reactions of these systems have not been reported in the literature, although similar reactions of Li^+ and Na^+ with alkyl halides have been previously reported. The spectra recorded are dominated by the K^+ ion signal. In some cases the K^+ ion accounts for more than 95% of the total ion flux reaching the mass spectrometer. Because of this the resolution of the quadrupole is reduced, so the signal level is high enough to detect the low intensity peaks. The low resolution means the signals are broadened so it is difficult to allocate the peaks to a particular m/z value especially at high mass. The structure due to the 79 and 81 isotopes of Br and the 35 and 37 isotopes of Cl is not resolved at this reduced resolution.

Without the ability to measure the drift velocities of the alkali ions {3.3} in the pure alkyl halide gases the energy of the K^+ ions initiating the reactions is unknown.

However, product ions are only seen when the drift tube electric field or the ion source field gradient is high. This suggests that the initiating K^+ reactions are endothermic and the enthalpies can be used to approximate a lower limit to the K^+ ion translational energy. In most cases this was in the range 2-5 eV.

The reactions that are observed in the drift tube for K^+ ions with CH_3Cl, CH_3Br, t-C_4H_9Cl or t-C_4H_9Br are presented in the following sections.

3.4.2 CH_3X Reactions

The mass spectra recorded for K^+ reacting with CH_3Cl are dominated by the K^+ signal. The reaction product ions only accounted for a few percent of the total ion signal. At very high energy the CH_3Cl reactivity was poor. There is no evidence for the occurrence of the elimination reactions 3.2 and 3.3 and these have not been observed previously for this system. However, the mass spectra contained signals at m/z = 15 and 89 which suggest the primary reaction processes that are occurring are the halide transfer

$$K^+ + CH_3Cl \rightarrow CH_3^+ + KCl \qquad (3.4)$$

and the association reaction,

$$K^+ + CH_3Cl \rightarrow K^+.CH_3Cl \qquad (3.5)$$

which have not been observed previously in the literature.

The halide transfer reaction is endothermic by 451.3 $kJmol^{-1}$ and hence requires the K^+ to be accelerated to energies around 4.5 eV for initiation. For this reason the reaction was not observed for low electric fields in the drift tube as there is only enough energy available for the reaction to occur at higher drift tube fields. The association reaction forming the complex product $K^+.CH_3Cl$ at mass 89 occurs as the halide transfer

process is so highly endothermic the barrier E_b to rearrangement in the reaction mechanism shown in Fig. 3.11 will be large. Hence the initial complex formed may well be stable enough to exist for a long enough time to be detected. For low collision energies reaction 3.5 is the exclusive reaction channel. At higher collision energies the endothermic halide transfer reaction is activated and the two reaction paths compete with the halide transfer becoming dominant as the collision energy is raised. From the reaction scheme of Allison and Ridge for reactions with Li^+ ions, further collisions of the complex may induce the following

$$K^+.CH_3Cl + CH_3Cl \rightarrow K^+ + 2CH_3Cl \tag{3.6}$$

$$K^+.CH_3Cl + CH_3Cl \rightarrow K^+.(CH_3Cl)_2 \tag{3.7}$$

$$K^+.CH_3Cl + CH_3Cl \rightarrow K^+.C_2H_5Cl + HCl. \tag{3.8}$$

Product ions are not observed for either reactions 3.7 or 3.8. The K^+ ion signal is not observed to continually decrease with increasing drift distance and hence increasing reaction time through the drift tube. This suggests that dissociation reactions releasing the K^+ ion bound in complexes such as $K^+.CH_3Cl$ are occurring. Therefore reaction 3.6 is expected to proceed as the $K^+.CH_3Cl$ complex is not tightly bound in a deep potential well and the acceleration of the complex ion by the drift tube field should provide more than enough energy to cause the dissociation in collisions with CH_3Cl.

The fragment CH_3^+ generated by reaction 3.4 only appears in the mass spectra for short drift distances and therefore short reaction times. The reactive CH_3^+ is quickly lost for longer drift distances by further reactions to give:

$$CH_3^+ + CH_3Cl \rightarrow (CH_3)_2Cl^+ \tag{3.9}$$

$$CH_3^+ + CH_3Cl \rightarrow CH_2Cl^+ + CH_4 \tag{3.10}$$

$$CH_3^+ + CH_3Cl \rightarrow CH_3Cl^+ + CH_3 \tag{3.11}$$

$$CH_3^+ + CH_3Cl \rightarrow C_2H_5^+ + HCl \tag{3.12}$$

$$CH_3^+ + CH_3Cl \rightarrow C_2H_3^+ + HCl + H_2. \quad (3.13)$$

The product of reaction 3.9 at mass 65 is observed and the enthalpy is calculated to be -291 kJmol^{-1}. Both or either of the next two reactions are occurring in the drift tube. The mass spectra show a signal which due to the low resolution is difficult to accurately allocate to a particular mass. It appears most likely to be the CH_2Cl^+ ion at mass 49 produced in 3.10. The enthalpy change for this reaction is -128.1 kJmol^{-1} whereas it is 133.9 kJmol^{-1} for the reaction 3.11 which produces the ion at mass 50. The exothermicity of reaction 3.10 as opposed to the less favourable enthalpy change for reaction 3.11 suggests that reaction 3.10 is the favoured of the two processes. Similarly, the mass spectra do not differentiate between the products of reactions 3.12 and 3.13 at m/z = 29 and 27. Reaction 3.12 is exothermic by 202.2 kJmol^{-1} but reaction 3.13 is slightly endothermic by 6.3 kJmol^{-1}. Hence on an energetic basis reaction 3.12 is the favoured path.

The only further product ion seen in the mass spectra is a signal around mass 99 due to either the $C_2H_4Cl_2^+$ ion or to the $C_2H_5Cl_2^+$ ion. Possible reactions to produce these are:

$$CH_2Cl^+ + CH_3Cl \rightarrow C_2H_4Cl_2^+ + H \quad (3.14)$$

$$CH_2Cl^+ + CH_3Cl \rightarrow C_2H_5Cl_2^+ \quad (3.15)$$

$$(CH_3)_2Cl^+ + CH_3Cl \rightarrow C_2H_4Cl_2^+ + CH_3 + H_2 \quad (3.16)$$

$$(CH_3)_2Cl^+ + CH_3Cl \rightarrow C_2H_5Cl_2^+ + CH_4 \quad (3.17)$$

$$K^+.CH_3Cl + CH_3Cl \rightarrow C_2H_4Cl_2^+ + KH_2 \quad (3.18)$$

$$K^+.CH_3Cl + CH_3Cl \rightarrow C_2H_5Cl_2^+ + KH. \quad (3.19)$$

The enthalpy changes for reactions 3.14 and 3.16 are 276.1 kJmol^{-1} and 440.1 kJmol^{-1} respectively. Without knowledge of the enthalpies for all of the other reactions it is difficult to say which, if any, are occurring and whether the product ion is $C_2H_4Cl_2^+$, $C_2H_5Cl_2^+$ or both.

The mass spectra of CH_3Br with the K^+ ion were measured to compare to the CH_3Cl reactions that are observed. All of the product ions observed for the reactions with CH_3Br can be produced by the same series of reactions that are occurring for CH_3Cl, that is:

$$K^+ + CH_3Br \rightarrow CH_3^+ + KBr \quad (3.20)$$

$$K^+ + CH_3Br \rightarrow K^+.CH_3Br \quad (3.21)$$

$$K^+.CH_3Br + CH_3Br \rightarrow K^+ + 2CH_3Br \quad (3.22)$$

$$CH_3^+ + CH_3Br \rightarrow (CH_3)_2Br^+ \quad (3.23)$$

$$CH_3^+ + CH_3Br \rightarrow CH_2Br^+ + CH_4 \quad (3.24)$$

$$CH_3^+ + CH_3Br \rightarrow C_2H_5^+ + HBr. \quad (3.25)$$

The enthalpy changes for the reactions are calculated to be 442.5 $kJmol^{-1}$ for 3.20, -312.1 $kJmol^{-1}$ for 3.23, -198.8 $kJmol^{-1}$ for 3.24 and -189.6 $kJmol^{-1}$ for 3.25. A broad signal is also present in the mass spectra around mass 187 to mass 191, this is either the $C_2H_4Br_2^+$ or $C_2H_5Br_2^+$ ion produced by one or more of reactions 3.14-3.19. Without an increase in the resolution of the mass spectra the identity of the peak cannot be established.

3.4.3 Tertiary C_4H_9X Reactions

The extent of the reactions between K^+ and tertiary C_4H_9X (t-C_4H_9X), where X = Cl or Br observed in the drift tube, are greater than those seen for CH_3X. In some instances the intensities of product ions surpassed the K^+ signal. There is no indication that the elimination reaction 3.3 is occurring, but unlike CH_3X the dehydrohalogenation reaction 3.2 does appear. The presence of ion signals in the mass spectra at m/z = 57, 95 and 131 suggest that the primary reaction processes occurring are:

$$K^+ + t\text{-}C_4H_9Cl \rightarrow C_4H_9^+ + KCl \quad (3.26)$$

$$K^+ + t\text{-}C_4H_9Cl \rightarrow K^+.C_4H_8 + HCl \quad (3.27)$$

$$K^+ + t\text{-}C_4H_9Cl \rightarrow K^+.C_4H_9Cl. \quad (3.28)$$

The halide exchange reaction 3.26 is 153.7 kJmol^{-1} endothermic and hence is only activated when the K^+ ions are accelerated to around 1.5 eV by the drift tube electric field. This is much more energetically favoured than the corresponding reaction with CH_3Cl or CH_3Br (3.4, 3.20) where collision energies of 4-5 eV are required. The enthalpy of formation for $K^+.C_4H_8$ is unknown but cannot exceed 500 kJmol^{-1} (calculated from the binding of K^+ to C_4H_8). The enthalpy for reaction 3.27 can therefore not be greater than about 80 kJmol^{-1} endothermic, in fact it should be near to thermoneutral. For low collision energies the formation of the association complex in reaction 3.28 is the dominant reaction path and the $K^+.C_4H_9Cl$ ion signal is ten times larger than the signals due to the other primary ions. For increasing collision energies the endothermic halide transfer reaction competes favourably with reaction 3.28 and becomes the dominant reaction path at very high collision energies. The reactivity of the dehydrohalogenation reaction is greatest at low collision energies where it occurs to an extent similar to the halide exchange reaction. For higher collision energies very little of the $K^+.C_4H_8$ ion is observed.

The hydrocarbon ion $C_4H_9^+$ reacts further with t-C_4H_9Cl to produce:

$$C_4H_9^+ + t\text{-}C_4H_9Cl \rightarrow C_6H_{13}^+ + C_2H_5Cl \quad (3.29)$$

$$C_4H_9^+ + t\text{-}C_4H_9Cl \rightarrow C_8H_{17}^+ + HCl. \quad (3.30)$$

Both of these ions are observed at masses 85 and 113 respectively. The structures of the hydrocarbon ions produced in reactions 3.29 and 3.30 are unknown so only approximate enthalpies can be calculated for the reactions. The enthalpy changes for the two reactions are about 18 kJmol^{-1} and -22 kJmol^{-1}, so they should both occur favourably with the high energy $C_4H_9^+$ ions in the drift tube. The product ion $C_8H_{17}^+$ at mass 113 can also be produced by reaction of the $K^+.C_4H_8$ complex produced in reaction 3.27

$$K^+.C_4H_8 + t\text{-}C_4H_9Cl \rightarrow C_8H_{17}^+ + KCl \quad (3.31)$$

which is approximately 50 $kJmol^{-1}$ endothermic.

Using the reaction sequence observed by Allison and Ridge [Allison, 1979] for reactions of Li^+ with $t\text{-}C_4H_9Cl$ and applying it to the K^+ chemistry with $t\text{-}C_4H_9Cl$ gives the following series of reactions:

$$K^+.C_4H_8 + t\text{-}C_4H_9Cl \rightarrow K^+.C_4H_9Cl + C_4H_8 \quad (3.32)$$

$$K^+.C_4H_8 + t\text{-}C_4H_9Cl \rightarrow K^+.(C_4H_8)_2 + HCl \quad (3.33)$$

$$K^+.C_4H_9Cl + t\text{-}C_4H_9Cl \rightarrow K^+.C_8H_{17}Cl + HCl \quad (3.34)$$

$$K^+.C_4H_9Cl + t\text{-}C_4H_9Cl \rightarrow K^+.(C_4H_9Cl)_2 \quad (3.35)$$

$$K^+.(C_4H_8)_2 + t\text{-}C_4H_9Cl \rightarrow K^+.C_8H_{17}Cl + C_4H_8 \quad (3.36)$$

$$K^+.C_8H_{17}Cl + t\text{-}C_4H_9Cl \rightarrow K^+.(C_4H_9Cl)_2 + C_4H_8. \quad (3.37)$$

The product ions for reactions 3.32-3.37 are all observed; $K^+.C_4H_9Cl$ at mass 131, $K^+.(C_4H_8)_2$ at 151, $K^+.C_8H_{17}Cl$ at 187 and $K^+.(C_4H_9Cl)_2$ at 223. It is expected that these high mass complex ions can also dissociate in energetic collisions to produce the parent K^+ ion or smaller hydrocarbon fragments such as $C_4H_9^+$.

For the reactions of K^+ with $t\text{-}C_4H_9Br$ the ions $C_4H_9^+$, $C_6H_{13}^+$, $K^+.C_4H_8$, $C_8H_{17}^+$ and $K^+.C_4H_9Br$ at m/z = 57, 85, 95, 113 and 175 are all observed but the ion at mass 151, $K^+.(C_4H_8)_2$ is not. The large complex ions of K^+ with $t\text{-}C_4H_9Br$ (similar to those produced in reactions 3.33-3.37 with $t\text{-}C_4H_9Cl$) are not observed, mainly due to the poor signal to noise at masses above m/z = 200 in the mass spectra. The chemistry of $t\text{-}C_4H_9Br$, although not as complete as is observed for $t\text{-}C_4H_9Cl$, does show the same overall reaction scheme as observed for $t\text{-}C_4H_9Cl$ in reactions 3.26-3.32.

3.5 Conclusions

From the mass spectra recorded as a result of the ion molecule reactions of K^+ with CH_3Cl, CH_3Br, t-C_4H_9Cl and t-C_4H_9Br, it is apparent that reactions, none of which have been previously observed in the literature for these systems are occurring. The primary reactions observed are halide transfer and association for the CH_3X species and halide transfer, association and dehydrohalogenation for the C_4H_9X species. Secondary reactions including association and dissociation processes are also observed. The reactions that are observed for the CH_3X species with K^+ are summarised in the following scheme:

$$K^+ + CH_3X \rightarrow CH_3^+ + KX$$

$$K^+ + CH_3X \rightarrow K^+.CH_3X$$

$$K^+.CH_3X + CH_3X \rightarrow K^+ + 2CH_3X$$

$$CH_3^+ + CH_3X \rightarrow (CH_3)_2X^+$$

$$CH_3^+ + CH_3X \rightarrow CH_2X^+ + CH_4$$

$$CH_3^+ + CH_3X \rightarrow C_2H_5^+ + HX.$$

At low collision energies the favoured primary process is the association reaction producing $K^+.CH_3X$, but for higher collision energies the endothermic halide transfer reaction is activated and both primary reaction channels occur to a similar extent. Furthermore the product ion $C_2H_4X_2^+$ or $C_2H_5X_2^+$, which cannot be identified with the resolution used, is observed. The reaction or reactions which produce either or both of these ions are not clear, but some possibilities are listed in reactions 3.14-3.19.

The ion molecule chemistry of K^+ with t-C_4H_9X that is observed, is summarised by the following:

$$K^+ + t\text{-}C_4H_9X \rightarrow C_4H_9^+ + KX$$

$$K^+ + t\text{-}C_4H_9X \rightarrow K^+.C_4H_8 + HX$$

$$K^+ + t\text{-}C_4H_9X \rightarrow K^+.C_4H_9X$$

$$C_4H_9^+ + t\text{-}C_4H_9X \rightarrow C_6H_{13}^+ + C_2H_5X$$

$$C_4H_9^+ + t\text{-}C_4H_9X \rightarrow C_8H_{17}^+ + HX$$

$$K^+.C_4H_8 + t\text{-}C_4H_9X \rightarrow C_8H_{17}^+ + KX$$

$$K^+.C_4H_8 + t\text{-}C_4H_9X \rightarrow K^+.C_4H_9X + C_4H_8.$$

As was seen for the CH_3X reactions, the association reaction is the favoured primary reaction path at low collision energies and the halide transfer only occurs favourably for higher collision energies. The dehydrohalogenation reaction does not occur to a great extent and only accounts for a small fraction of the product ions from the primary processes. No further reactions are observed with $t\text{-}C_4H_9Br$ but for $t\text{-}C_4H_9Cl$ the product ions from reactions 3.33-3.37 are observed.

It is expected that the use of either Li^+ or Na^+ in place of K^+ will produce even richer ion molecule chemistry than what has been observed here, due to the greater reactivity of Li^+ and Na^+ over K^+.

The versatility of the alkali ion sources used means they can easily be integrated into a crossed molecular beam apparatus to provide ion beams of adequate intensity and energy spread for scattering reactions with symmetric top alkyl halide molecules. Ultimately the orientation dependence for the approach of the alkali metal cation to the alkyl halide can be probed for the reactive processes. Collision energies of up to 5 eV will be necessary if the endothermic halide transfer reactions with CH_3X are to be activated in the crossed beam studies. However, the endothermicity of the halide transfer reactions with $t\text{-}C_4H_9X$ are much less and it is expected that collision energies of less than 1.5 eV will be adequate for the crossed beam reactions.

Chapter 4

Electron Impact Ionisation

The electron impact ionisation of gases is of great importance in many fields of research such as planetary atmospheres, plasmas and mass spectrometry. The measurement of absolute ionisation cross sections for molecules have not been very extensive. Since the early measurements made in the 1920's and 1930's [Bleakney, 1929; Compton, 1925; Jones, 1927; Smith, 1930; Tate, 1932] very few new systems have been examined, most studies being refinements of earlier experiments. The currently available cross section data are limited to atomic species and a relatively few small stable molecules. This work describes and presents results for an apparatus designed to measure the absolute electron impact ionisation cross sections for atomic and molecular gaseous species.

4.1 Theory

Elastic collisions occur between electrons and atomic or molecular targets when the electron's translational energy is less than the energy difference between the targets ground state and first electronic excited state. However if the electron energy is increased above this, electronic excitation of the neutral target can occur. When the energy of the electron is above the ionisation potential of the neutral, enough energy

may be transferred in the collision to cause one or more electrons to be ejected. This process is called electron impact ionisation. The probability that an electron with energy E will be involved in an ionising collision while passing along a path l (cm) through a gas of particle density n (cm^{-3}) is equal to $\sigma(E)nl$ [Massey, 1952]. $\sigma(E)$ (cm^2) is the total ionisation cross section. If the ratio of the positive ion current generated in this manner to the electron current is small, that is, the electrons undergo at most one collision in passing through the gas, then

$$\sigma(E) = \frac{I^+}{I^e nl} \tag{4.1}$$

where I^+ is the positive ion current and I^e is the electron beam current. If the electron energy E is sufficiently large the possibility of multiple ionisation arises

$$X + e^- \rightarrow X^{z+} + ze^- + e^-$$

where $z > 1$. The total positive ion current will then be equal to

$$I^+ = I^e nl(\sigma_1(E) + 2\sigma_2(E) + \ldots + z\sigma_z(E)) \tag{4.2}$$

where the charge weighted sum of the partial ionisation cross sections $\sigma_z(E)$ is equal to the total ionisation cross section $\sigma(E)$ given in (4.1). The threshold energy for the occurrence of multiple ionisation collisions increases with the degree of ionisation and the partial ionisation cross sections rapidly decrease as a function of the degree of ionisation. Hence at any electron energy above the ionisation potential the partial ionisation cross section for single ionisation will dominate the multiple ionisation terms.

4.2 Experimental Quantities

In order to measure an ionisation cross section the experimental variables I^+, I^e, n and l in equation (4.1) need to be determined. Although this appears to be inherently

simple, the experimental conditions that must be met to enable accurate determination of the above quantities ensure that it is not [Kieffer, 1966].

To collect the positive ion current I^+ the total number of ions produced by ionisation within a region of known path length must be collected. Any positive ions produced outside of the collection region, such as those that will reflect off the electron collector, must not impact on the positive ion collector. The ion current must also be free of any secondary electron current generated by the electron beam striking the electron collector or scattering off the edges of the ion and electron optics. Finally, if partial ionisation cross sections are to be measured, mass identification of the ions is required.

Similarly, for the electron current I^e the entire electron beam causing the ionisation of the gas must be collected, there must be no reflection of electrons from the collector surface. Any secondary electron emission caused by the electron beam travelling through the focusing optics, and the electrons produced in the ionising collisions, must not be collected. However if the ratio of the positive ion current to the electron beam current is kept small then the collection of either the electrons or ions produced in the ionisation of the gas will introduce only a very small error to the electron beam current.

For experiments involving ionisation of a static gas sample in a collision cell the number density of the gas must be determined from accurate measurement of the pressure. In the case of beam experiments, the total neutral beam flux must be measured and the velocity of the neutral beam must be known.

For the collision cell experiments, the path length of the electrons through the volume of gas from which the positive ion current is generated must be determined. If magnetic collimation of the electron beam is used the electrons will follow helical paths along the magnetic field lines. This may introduce an increase in the path length which will be limited by the maximum transverse velocity the electrons attain depending on the beam collimation. Hence an upper limit to the path length can be found. For

crossed beam experiments, the overlap between the electron and neutral beams must be calculated from measurement of the spatial distributions of the two beams.

4.3 Experimental Methods

The experimental apparatus used to measure the ionisation cross sections fall into two main areas

- Gas collision chambers
- Crossed neutral and electron beams.

In both cases total ionisation cross sections may be measured, but modification to include mass selection by the use of mass spectrometers is needed in order to determine the partial ionisation cross sections.

4.3.1 Gas Collision Chambers

Early experiments carried out in the 1920's and 1930's measured total ionisation cross sections by a variety of different methods. The most successful experimental apparatus was that designed by Jones [Jones, 1927], which was also used in the experiments of Smith and Tate [Smith, 1930; Tate, 1932] and more recently in a number of studies [Asundi, 1963b; Briglia, 1965; Rapp, 1965a; Rapp, 1965b; Schram, 1964]. The results of Rapp and Englander-Golden [Rapp, 1965b] have been accepted as the current de facto standard.

A schematic for the apparatus used by Rapp *et al* is shown in Fig. 4.1. The electron beam is produced by the heated cathode (F) and accelerated to the ionising energy by the electron optics (1,2,3). The centre slit in the second collimating lens is

only 0.36 mm in width and acts to keep the pressure near the cathode at a fraction of the ionisation chamber pressure. The electron beam passes through the collision chamber and then through the electron collector shield (ECS) before entering the electron collector cylinder (ECC) where the electron current is measured on the electron collector plate (ECP). A 500 G magnetic field is used to confine the electrons to a narrow beam down the centre of the apparatus. To ensure that the entire electron beam was being collected the current was measured as a function of the collector plate voltage. Above 200 V the electron current became constant with increasing plate potential, indicating that all electrons were being collected. Under these conditions the largest electron current to any other electrode was to the electron collector cylinder which was less than 0.1% of the signal measured at the plate. Hence the measured electron current was saturated to better than 0.1%.

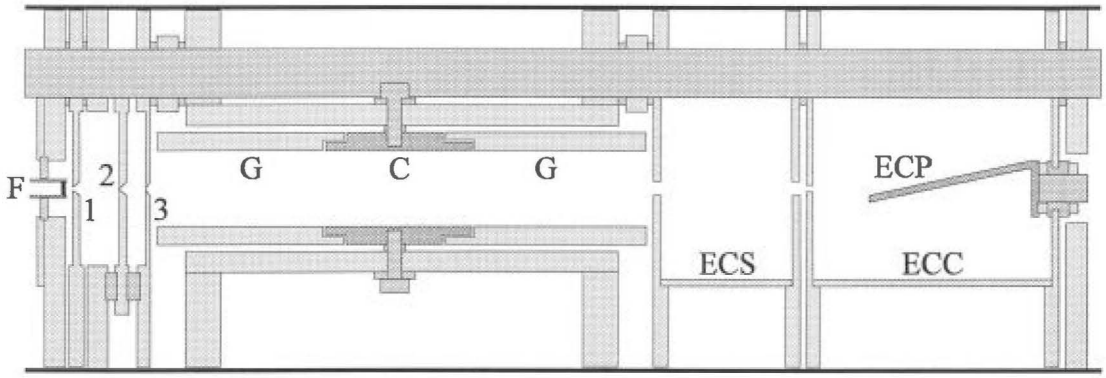

Fig. 4.1. Total ionisation apparatus of Rapp *et al* [Rapp, 1965a].

Ions produced in the ionisation chamber are detected by the application of an electric field across the two parallel plates sufficiently large to collect all the ions formed in a fixed path length on the ion collector (C). The guard plates (G) flanking the ion collector serve to keep the field uniform throughout the collection region. Again, it is necessary to show that the positive ion current from ionisation of the gas along a path length equal to the length of the ion collector plate is independent of the chamber field. For atomic gases the ion current saturated for electric fields greater than 5 Vcm^{-1}. However the fields required to collect all the ions from ionisation of molecules were higher. This is due to the production of energetic fragments generated by dissociative ionisation. These fragments which may have kinetic energy up to a few eV (3 - 15 eV

fragments have been recorded for the production of H^+ from H_2) require a stronger field to ensure complete collection. Typically fields around 20 - 25 Vcm^{-1} were adequate to produce saturated ion collection for diatomic and small polyatomic molecules.

The path length l is nominally determined as being equivalent to the length of the ion collection plate. However, as a magnetic field is used to confine the electron beam, the electrons will follow helical paths about the direction of the magnetic field, effectively increasing the ionising path length to a value L greater than l. Assuming the diameter of the helical motion is defined by a collimating aperture of diameter d the path length L is approximated by [Massey, 1952]

$$L = l(1 + 1.10 \times 10^{-4} \frac{d^2 H^2}{V}) \tag{4.3}$$

where H is the magnetic field strength in gauss and V is the electron energy in volts. For typical experimental values of d, H and V used by Smith [Smith, 1930] and Tate and Smith [Tate, 1932] equation 4.3 predicts an increase in the electron path length of up to 77% at 20 V and 19% at 80 V. Asundi [Asundi, 1963b] repeated the work of Tate and Smith using conditions where the path length correction from equation 4.3 was around 1% and reproduced the data of Tate and Smith within experimental uncertainties. This would indicate that equation 4.3 is not valid. Instead it was assumed that the maximum diameter of the electron helices was limited by the maximum energy available to the electrons perpendicular to the magnetic field [Asundi, 1963a] rather than by the diameter of the final beam collimator. This was found to be about a thousandth of the electron energy parallel to the magnetic field. From this the path length corrections were calculated to be only a few percent, even at low electron energies.

Rapp and Englander-Golden [Rapp, 1965b] found that at high magnetic fields even the corrections calculated by Asundi could be neglected as the magnetic field is strong enough to confine the electrons to the limiting case of exactly linear trajectories. They illustrated this by calculating the ionisation cross section as a function of the magnetic field. At high magnetic field (> 300 G) the cross section was independent of the field and hence the electron path length is assumed to be the geometrical path l. An

estimate was also made for the increase in the path length due to elastic scattering of the electrons off the neutral gas molecules. For near threshold electron energies the correction was found to be about 0.1% and for higher energies even less. Hence no path length correction needed to be made due to elastic scattering.

The pressure in the ionisation chamber is measured with a McLeod gauge. If the gauge is connected to the chamber via tubing of diameter smaller than the mean free path of the gas molecules then molecular flow [Holland, 1974] conditions are met and the relationship between the pressures and temperatures in the gauge (P_g, T_g) and chamber (P_c, T_c) is given by [Kieffer, 1966]

$$\frac{P_c}{P_g} = \left(\frac{T_c}{T_g}\right)^{1/2}. \tag{4.4}$$

Hence the number density of the gas in the ionisation chamber in particles per cubic centimetre (n) will be given by

$$n = 9.656 \times 10^{18} \frac{P_g}{(T_c T_g)^{1/2}}. \tag{4.5}$$

The McLeod gauges are highly accurate but the use of cold traps between the gauge and the ionisation chamber to prevent mercury vapour from contaminating the chamber, can cause departure from the thermal transpiration law (4.4). The stream of mercury vapour between the gauge and the trap can act like a diffusion pump, affecting the molecular flow enough to give large inaccuracies in the pressure measurement. Rapp and Englander-Golden used an effusive flow technique [Rapp, 1965b] to find the pressures for gases other than H_2, O_2 and NO relative to an absolute measurement for H_2 made using the McLeod gauge. It was estimated that the uncertainty in the pressure measurements was ±7% and as such is the source of greatest error in the determination of the ionisation cross sections. The recent availability of 0.1 torr full scale capacitance manometers [Straub, 1995] capable of measuring the pressure accurately down to 10^{-6} torr, provides a more reliable way of measuring the pressure accurately.

To measure partial ionisation cross sections the ion current must be mass analysed [Bleakney, 1929; Tate, 1932]. Because of the difficulty in finding the collection efficiency of the mass spectrometers used to mass filter the ions, most partial cross sections are measured as relative values and then normalised to the total ionisation cross sections measured in the normal way. For accurate partial ionisation cross section measurements, the collection efficiency of the mass spectrometer must be independent of m/z and the electron energy, that is, multiply charged ions and fragment ions must be collected with the same efficiency as the singly charged molecular ion.

4.3.2 Crossed Neutral and Electron Beams

New experimental methods were required to measure the ionisation cross sections for inherently unstable species such as atomic hydrogen, nitrogen, oxygen and the alkali metals, due to the unsuitability of the collision cell apparatus for such work. Of the new methods used [Boyd, 1958; Brook, 1978; Fite, 1958; Hayes, 1987; Stephan, 1980; Straub, 1995; Tate, 1934; Wetzel, 1987] the most successful was the technique of crossed beams.

A general crossed beam experiment Fig. 4.2, consists of a fast neutral particle beam crossed at right angles by an electron beam with detection of the electron beam current, the neutral beam intensity and the mass selected ion beam current. Because of the directional nature of the neutral beam and the negligible momentum transfer in collisions between the electrons and the neutral species, the positive ions produced by electron impact ionisation will have essentially the same direction as the neutral beam. This makes it easier to separate the ions from the neutral beam and focus them into the mass analyser for detection.

The appreciable velocity of the neutral beam combined with the non homogeneous electron and neutral beam profiles, means equation 4.1 for the ionisation cross section will not be valid. A corrected equation for the crossed beam situation when the two beams are perpendicular is given by [Wetzel, 1987]

$$\sigma(E) = \frac{I^+(E)v_e v_n}{I^e(E)RF(v_e^2 + v_n^2)^{1/2}} \tag{4.6}$$

where v_e and v_n are the electron and neutral beam velocities respectively, $I^e(E)$ and $I^+(E)$ are the electron and ion currents respectively, R is the neutral beam flux and F is a measure of the overlap between the two beams. E is the relative kinetic energy of the electron and neutral beams and is approximated by

$$E \sim E_e + \left(\frac{m_e}{m_n}\right)(E_e + E_n) \tag{4.7}$$

where E_e and E_n are the translational energies of the electron and neutral beams respectively and m_e and m_n are the masses of the electron and neutral particles respectively.

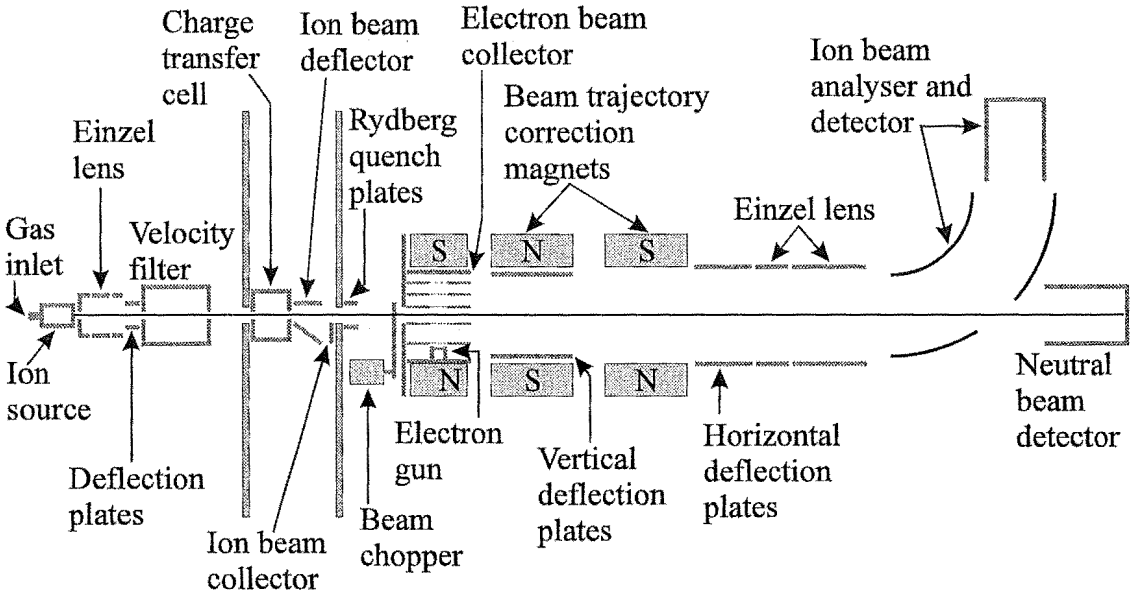

Fig. 4.2. Crossed beam ionisation experiment.

The accurate measurement of the electron and ion currents is subject to the same consistency checks required for the collision cell experiments. Essentially all charged particles must be collected with minimal losses to other components in the system. The velocity of the electron beam is easily calculated from knowledge of the electron energy in the beam crossing region. The neutral beam velocity can be measured by time of flight analysis, or in the case of Wetzel *et al* [Wetzel, 1987], the neutral beam velocity

was assumed to be the same as the velocity of the fast velocity selected ion beam from which it was produced by resonant charge transfer.

The total flux of the neutral beam R is measured with a detector placed on the neutral beam axis which must detect every beam particle. This is especially difficult for low energy neutral beams. Fast neutral beams can be detected by measuring the current from the secondary electron emission (I_{sec}) generated by the beam molecules striking a metal surface [Brook, 1978; Wetzel, 1987]. For each neutral impact on the detector surface an average number of secondary electrons γ will be ejected, all of which must be collected to give an accurate measurement of the beam flux. The neutral flux is then given by

$$R = \frac{I_{\text{sec}}}{\gamma}. \tag{4.8}$$

Therefore the absolute measurement of the beam flux requires the secondary electron yield γ to be determined accurately. Both Brook *et al* and Wetzel *et al* used pyroelectric detectors for this purpose. For the detection method to be useful the energy of the neutral beam must be greater than the work function of the collecting surface for secondary electron emission to occur. Materials with suitably low work functions and beams with high energies must be used.

Finally, the overlap F between the neutral and electron beams

$$F = \frac{\int j_n(r) j_e(r) \mathrm{d}r}{\int j_n(r) \mathrm{d}r \int j_e(r) \mathrm{d}r} \tag{4.9}$$

is measured by recording the beam profiles $j_n(r)$ and $j_e(r)$, that is the beam intensity j as a function of r the distance from the centre of the beam.

4.4 Electron Energy

Due to the voltage drop across the cathode, contact potential differences between electrodes and surface potentials on electrodes, the nominal electron energy defined by the potential difference between the cathode and the ionisation region may be quite different from the true value. At low electron energies where the ionisation efficiency curves rapidly change with energy this can have a serious effect. Therefore absolute calibration of the electron energy scale is required [Kieffer, 1966]. This is usually done by shifting the measured ionisation efficiency curve by an appropriate amount so the ionisation potential agrees with accurately measured spectroscopic values.

Chapter 5

Experimental Design

Over the course of the ionisation cross section measurements two different vacuum and electronics systems were used to house and run the ionisation apparatus. Both experimental arrangements will be described here. The changes made to the ionisation apparatus to improve electron and ion collection efficiencies will also be discussed.

5.1 Vacuum Systems

Initially the ionisation apparatus was setup in the vacuum chamber shown in Fig. 5.1. The chamber was custom made in the departmental mechanical workshop from 20 mm stainless steel plate. $2^3/_4$" and 8" OD conflat flange faces are machined into the chamber walls. The chamber is pumped by a 300 Ls^{-1} Alcatel 5400 turbomolecular pump backed by a 345 $Lmin^{-1}$ Alcatel 2021 mechanical pump. A vacuum of better than 5×10^{-8} can be attained. Chamber pressure is monitored with a Bayard-Alpert type ionisation gauge (Duniway Stockroom T-100-K) mounted on a $2^3/_4$" stainless steel flange and the turbomolecular pump foreline is monitored with a 531 thermocouple gauge. A pneumatically operated VAT 8" gate valve isolates the vacuum chamber from the 5400 turbomolecular pump which in turn is isolated from the mechanical pump by a

high vacuum bellows valve. Rough pumping of the chamber is facilitated by a $^1/_4$" stainless steel gas line attached to the turbo foreline and connected to the chamber by way of a $^1/_4$" brass Nupro JN needle valve.

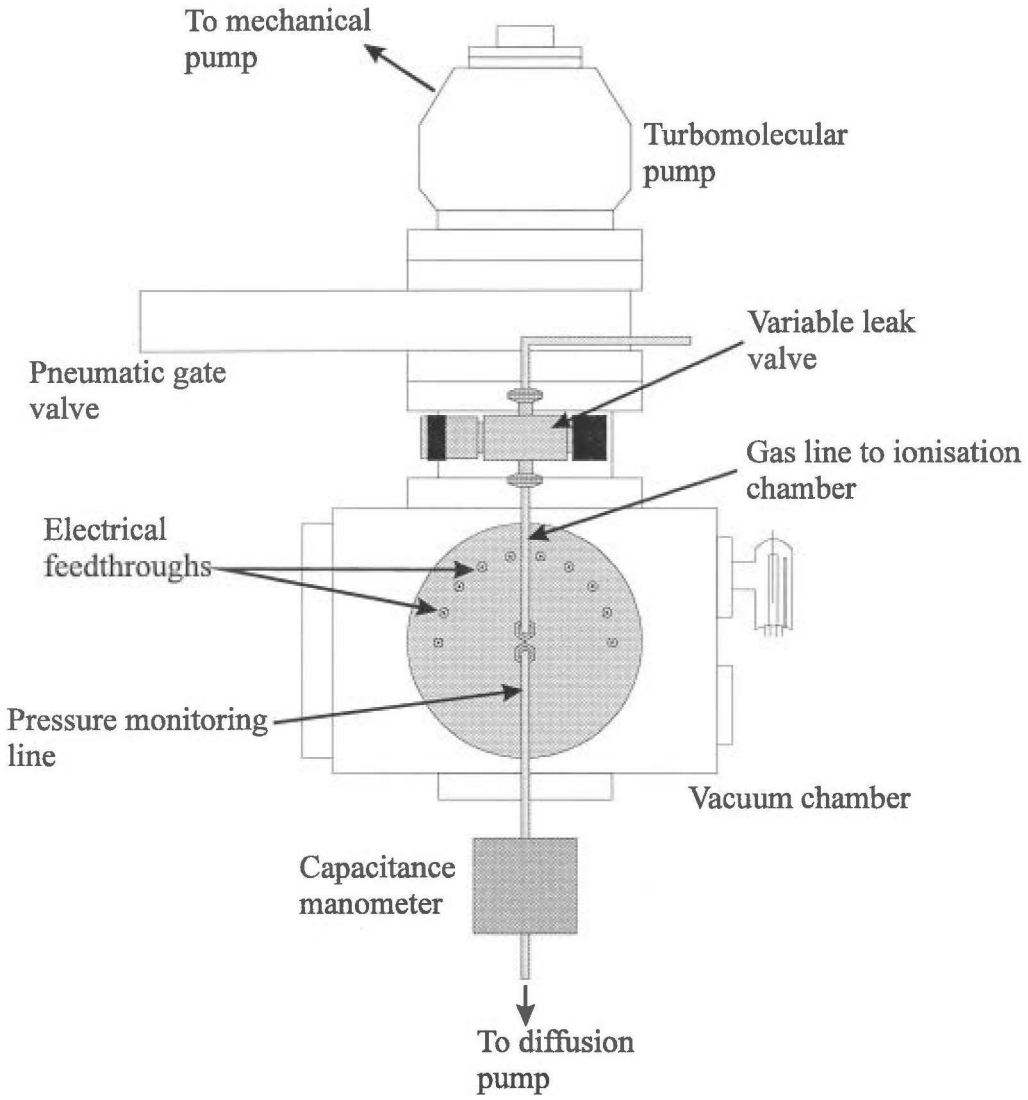

Fig. 5.1. Initial vacuum system for the ionisation experiment, scale 1:6.5. The ionisation apparatus is mounted on the 8" flange on the front of the vacuum chamber.

After the electron impact ionisation experiment had been optimised it was reinstalled in a different vacuum system. The new vacuum chamber has already been described {2.1.1} but essentially consists of a Varian 8" OD 4 way stainless steel cross, pumped by a 2000 Ls^{-1} Varian VHS-4 oil diffusion pump backed by a Dynavac D330 mechanical pump. The chamber has been separated from the mass spectrometer

chamber {2.12} and the drift tube has been removed and replaced with an ion gauge for vacuum monitoring. The ionisation apparatus is mounted on an 8" flange attached to the side of the 4 way cross (Fig. 5.2).

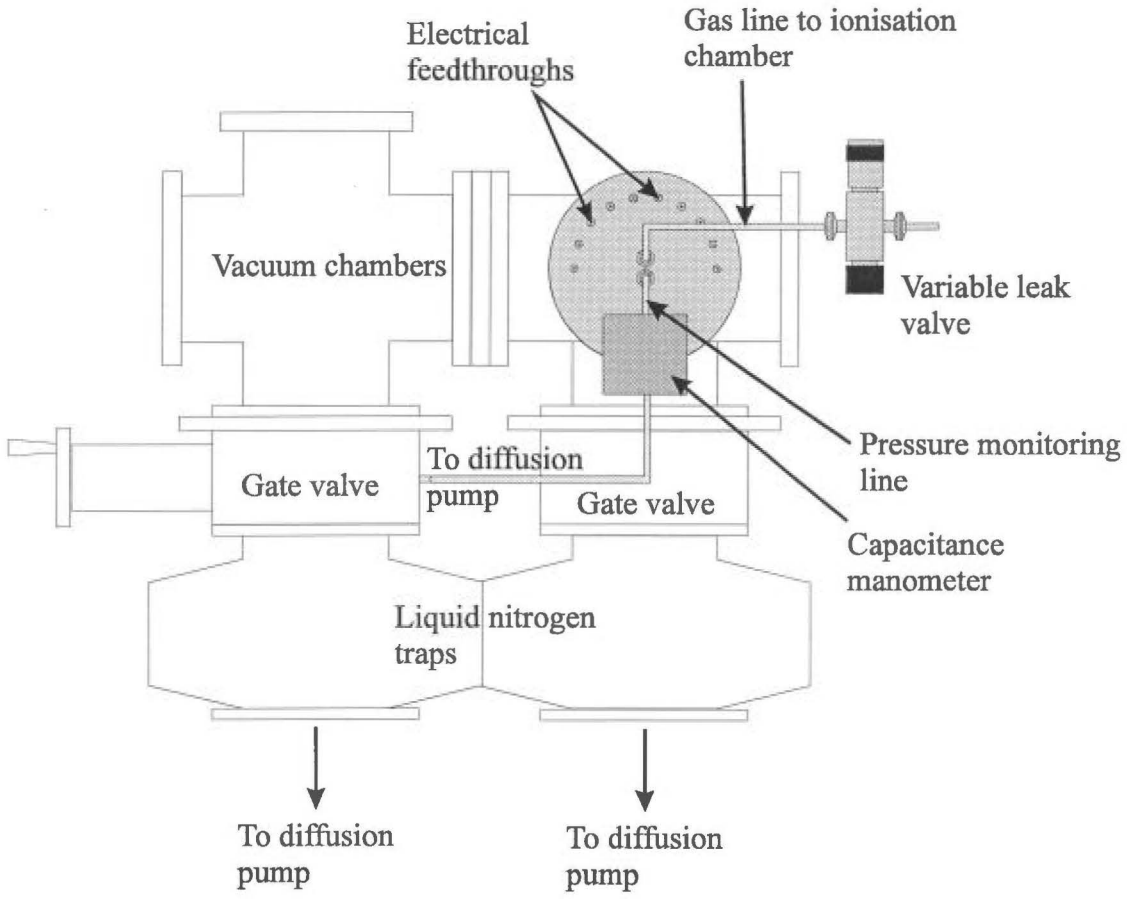

Fig. 5.2. Final vacuum system used for the ionisation experiment, scale 1:8.

5.2 Ionisation Apparatus Components

The ionisation apparatus is mounted on an 8" flange which incorporates all the electrical feedthroughs for connection to the ionisation apparatus, including connections for all of the electrodes, thermocouples, filament, and electron and ion current measurement. $^1/_4$" brass o-ring sealing Swagelock pipe fittings are used for the gas line connection to the ionisation chamber and pressure monitoring line.

The ionisation experiment consists essentially of three main parts:

- Electron gun and magnetic collimation
- Electron collector
- Ionisation chamber.

5.2.1 Electron Gun

The electron gun consists of a 0.007" rhenium filament spot welded to molybdenum posts. The filament is coated with a mixture of $BaZrO_3$ (90.1%), $BaCO_3$ (5.6%) and $SrCO_3$ (4.3%) to reduce the work function for electron emission. The filament assembly is supported by a ceramic block within a stainless steel shield which is usually held 15 V negative of the filament potential. The filament is typically run at 2.6 A which is supplied by custom built electronics and it is floated up to 200 V negative by an externally applied cathode potential. This potential is the nominal electron energy of the beam.

The electron beam is formed by a three element lens system which defines both the energy and collimation for the beam. The lenses are made of 1 mm thick stainless steel shim containing 1 mm apertures and are spaced 2 mm apart. All lens voltages are established using custom built floatable 200 V dc supplies. The final lens is held at ground potential and defines the front end of the ionisation chamber as well as the reference for the electron energy of the beam. Collimation of the electron beam along the beam axis is ensured by the use of an axial magnetic field of no less than 600 G. The magnetic field is generated by two rare earth cobalt magnets rated at 8200 G positioned at either end of the ionisation apparatus and held in place by a steel yoke.

5.2.2 Electron Collector

The electron beam is collected by a faraday cup after passing through the ionisation chamber. The faraday cup is made from stainless steel and is covered in colloidal graphite to reduce electron scattering. To ensure complete collection of the electron beam and to prevent the loss of secondary electrons from the surface, the collector is usually held at 60 V. The electron current is measured by a Keithley 160B multimeter which is referenced to the faraday cup potential. Typical operating beam currents are of the order of 1 μA, which is low enough to minimise the degradation of the beam divergence and energy distribution due to space charge effects.

5.2.3 Ionisation Chamber

The cylindrical ionisation chamber of 1 cm internal diameter is made from stainless steel and is coated in colloidal graphite to minimise the scattering of positive ions off the surface. The chamber is held at -20 V to attract the ions formed by electron impact ionisation of the gas near the axis of the cell. This voltage is adequate to ensure the collection of all ions formed in the collision region including the energetic charged products from dissociative ionisation processes. The ion current collected on the chamber is measured by a Keithley 486 picoammeter and is typically of the order of 10 nA, about 1% of the ionising electron beam current.

Gas is admitted to the chamber via a 3 mm diameter hole through the middle of the chamber. The pressure is regulated to between 1 x 10^{-5} and 1 x 10^{-3} torr by a Leybold-Heraeus 283-41 DN 10 KF variable leak valve. The pressure is monitored through a 3 mm gas outlet opposite the gas inlet, connected by $^1/_4$" stainless steel pipe to a 310CH-10 10 torr head MKS baratron capacitance manometer. In the first vacuum system used the reference side of the differential baratron is pumped down to better than 10^{-7} torr with a 100 Ls^{-1} Edwards oil diffusion pump backed by a 345 Ls^{-1} Alcatel 2021 mechanical pump. In the second vacuum system a $^1/_2$" gas line from the reference side

of the baratron led to an Edwards E04 diffusion pump backed by a 158 $Lmin^{-1}$ Edwards Speedivac ES150 mechanical pump which produced a vacuum of the order of 10^{-8} torr. The differential baratron was replaced after the initial experiments with an absolute 0.05 torr head MKS 627 baratron, which allows the pressure to be measured with greater accuracy. To minimise pressure gradients in the ionisation chamber the electrodes defining the ends of the chamber were sealed against the chamber with teflon or ceramic insulators. The insulators have large internal diameters to keep them isolated from the electron beam.

The baratron head used to measure the chamber pressure is regulated to 45°C and calibrated to measure the pressure of gas at 298 K. The chamber temperature is monitored by a thermocouple embedded near the gas line into the chamber. The thermocouple response was linear in the thermal temperature region. The chamber temperature was found to not vary by more than ±2°C from 298°C and therefore no corrections for thermal transpiration {4.3.1} are required for the pressure P_g measured by the baratron. The particle density in the chamber at 298 K is

$$n = 2.970 \times 10^{16} P_g . \tag{5.1}$$

5.3 Ionisation Apparatus Optimisation

5.3.1 Chamber Design

The original design for the ionisation experiment is shown in Fig. 5.3. The stainless steel collision chamber has an internal diameter of 10 mm and a length of 27 mm. The electron beam is collimated by the 1 mm diameter holes in the lenses of the electron gun and exits the ionisation chamber through a grounded lens made of 1 mm stainless steel shim containing a 4 mm axial hole. Insulated from this is the faraday cup electron collector. Initial experiments with this apparatus indicated a large electron current reaching the collision chamber, probably due to a combination of elastic

scattering off the gas, scattering of the electron beam off the exit lens and secondary electron emission from the lens surface. The electron current measured on the exit lens was a substantial fraction of the current measured by the faraday cup and as such had to be added to the collector current to get the total electron beam signal. Due to the large amount of scattered electron flux collected by the chamber the total measured electron current was in error.

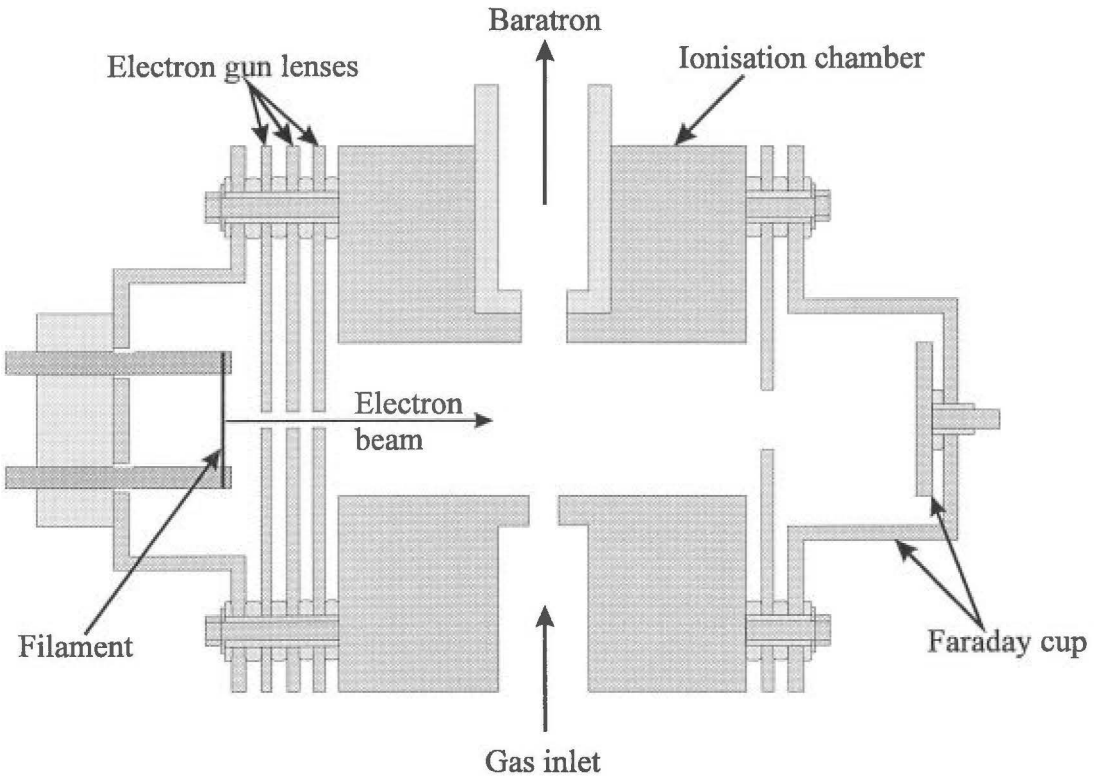

Fig. 5.3. Original ionisation apparatus using the 27 mm long chamber, scale 2:1.

To reduce the scattering and hence improve the determination of the electron beam current, the exit lens was replaced by a mesh electrode made of 95% transmitting gold electroformed mesh (Fig. 5.4). The mesh shields the ionisation chamber from the electric field generated by the faraday cup while at the same time allowing passage of the electron beam. This reduced the scattered electron current to the chamber to less than 10% of the previous amount. The electron current measured on the exit lens gold mesh was found to be less than 1% of the signal measured by the faraday cup and was not included in the determination of the total ionising electron current. The same gold mesh was also attached across the 1 mm diameter entrance hole in the lens on the front

end of the chamber. This was done to stop field penetration into the chamber and hence to reduce the probability that ions produced outside of the chamber would enter and be detected.

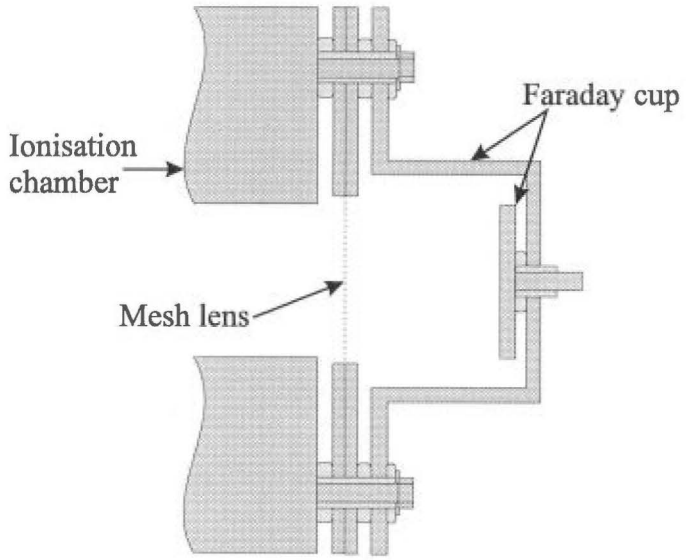

Fig. 5.4. The electroformed mesh exit lens on the ionisation chamber, scale 2:1.

The scattering of the electron beam off the exit lens has been minimised by the introduction of the mesh lens. The scattered electron current still reaching the chamber walls is due mostly to elastic scattering of electrons off the gas present in the chamber. The amount of elastic scattering of the electron beam is dependent on the gas pressure and hence would be best reduced by using lower gas pressure in the chamber. However, at this time the 310CH-10 baratron was used to measure the pressure and this is only accurate down to 1 x 10^{-5} torr so the lowest usable pressure in the chamber is limited by this. Instead, to minimise the electron scattering, the path length of the electrons through the gas was reduced. This was done by installing a new ionisation chamber which decreased the chamber length from 27 mm down to 10 mm, still with 10 mm internal diameter. The geometric path length for the electron beam through this chamber is defined by the entrance and exit lenses and was calculated to be 12.5 mm.

To reduce the possibility of the formation of pressure gradients at the ends of the ionisation chamber which would change the particle density over the ionising path

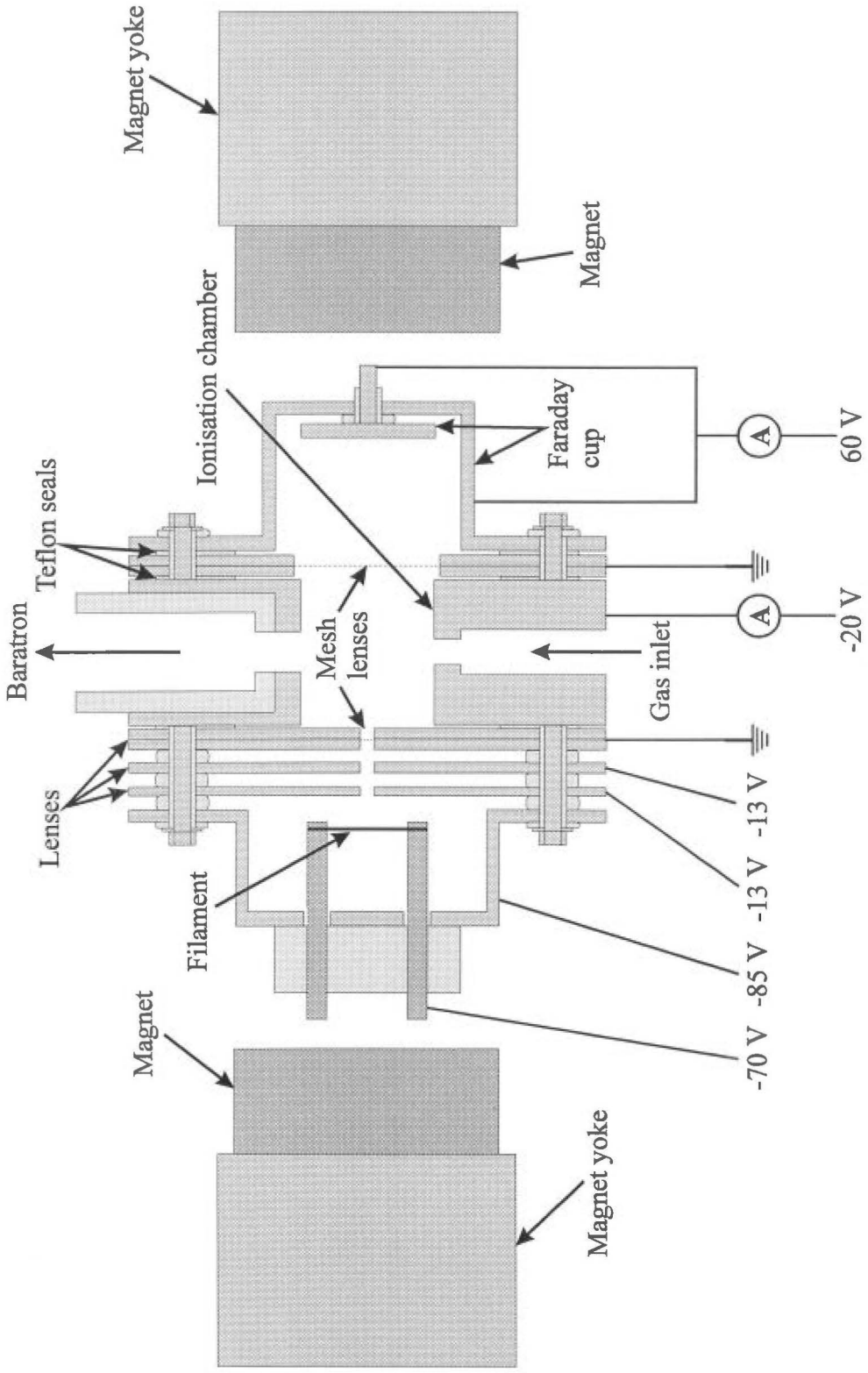

Fig. 5.5. The final ionisation apparatus used incorporating the 10 mm long chamber and the magnetic collimation of the electron beam, scale 2:1.

length, the ceramic insulators between the chamber and adjacent lenses and faraday cup were replaced by teflon sheet. The teflon is sandwiched between the lenses around the full circumference and effectively seals the chamber so that gas admitted to the chamber in an experiment can only leak out through the centre of the front lens. Since the conductance of gas out of the chamber is drastically reduced the pressure gradients will be minimised and variation of the pressure along the chamber axis can be disregarded.

5.3.2 Magnetic Collimation

Any further reduction of the scattered electron current to the chamber cannot be achieved by more changes to the ionisation region geometry. Magnetic collimation of the electron beam was first proposed by Compton and Voorhis [Compton, 1925] and successfully applied by Jones [Jones, 1927]. The magnetic field causes the electrons to follow helical paths in the field direction thus increasing the path length of the electrons through the ionising region {4.3.1}. Rapp and Englander-Golden [Rapp, 1965b] pointed out that the electron motion would approach linear trajectories if the magnetic field strength is above 300 G, therefore making the path length correction zero. In this work 20 mm diameter rare earth cobalt magnets rated at 8200 G at the pole face were used in the later experiments to confine the electron beam. The magnets are positioned at either end of the ionisation apparatus and the axial magnetic field they generated was measured with a Hall probe and found to be no less than 600 G along the electron beam path length. Fig. 5.5 shows the final ionisation apparatus including the magnetic collimation and typical operating voltages.

Chapter 6

Ionisation Cross Section Results

6.1 Electron Impact Ionisation Cross Section Measurement

6.1.1 Data Collection

For the ionisation cross section to be measured accurately the positive ion current generated from electron impact ionisation must be small relative to the electron current. This means that the pressure of the gas in the ionisation chamber must be low. Two baratrons have been used in this work to measure the chamber pressure. The initial experiments used a 10 torr full scale head which has a linear pressure response over 5 orders of magnitude, that is, 10 torr down to 10^{-4} torr. Hence the lowest pressure that may be used is 1 x 10^{-4} torr, although at this range the baratron reading is subject to large uncertainty. For these experiments the pressure used in the ionisation chamber is maintained between 1 x 10^{-4} torr and 1 x 10^{-3} torr which produces a positive ion current around a few percent of the intensity of the electron beam. For the final results reported here two modifications were made to the experimental arrangement. The collimating magnets were installed and these greatly reduced the electron current scattered to the chamber wall. Secondly, a 0.05 torr head baratron became available and this was

installed to replace the 10 torr baratron. Since the new baratron is accurate down to around 1 x 10^{-6} torr lower pressures can be used in the ionisation chamber. Typically the pressure was maintained from high 10^{-5} torr up to low 10^{-4} torr in the experiments.

Due to the less than perfect electrical isolation of the chamber and faraday cup there are small leakage currents present which introduce a zero error in the reading of the ion and electron signals. The Keithley 486 picoammeter used to measure the positive ion current can be rezeroed in the absence of gas in the chamber to remove the offset due to leakage. The electron beam collector must also be corrected for the leakage current present in the absence of the electron beam.

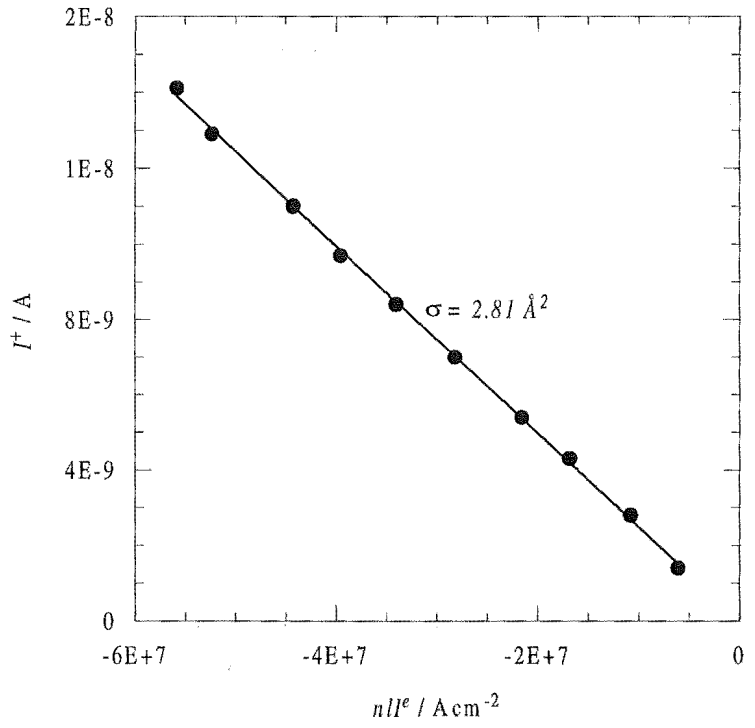

Fig. 6.1. Experimental plot of I^+ verses nlI^e for 70 eV ionisation of Ar. The ionisation cross section σ is found from the linear least squares fit to the data.

A typical experiment involves setting the electron beam intensity such that the collected electron current is about 1-2 μA. Gas is then bled into the chamber in approximately 1 x 10^{-4} torr steps (less for the final experiments with the 0.05 torr baratron) and the positive ion and electron currents (corrected for zero errors) recorded at each pressure. At each point a few seconds is all that is required for the pressure and

currents to stabilise. The temperature of the chamber is monitored so the baratron pressure readings can be converted to number densities in the ionisation chamber (equation 5.1). Plotting the positive ion current verses the electron current times the path length times the number density, will give a line whose slope is the ionisation cross section for the electron energy and gas used. A typical plot is shown in Fig. 6.1 for ionisation of Ar with 70 eV electrons using the length of the chamber; 1.25 cm, as the ionisation path length.

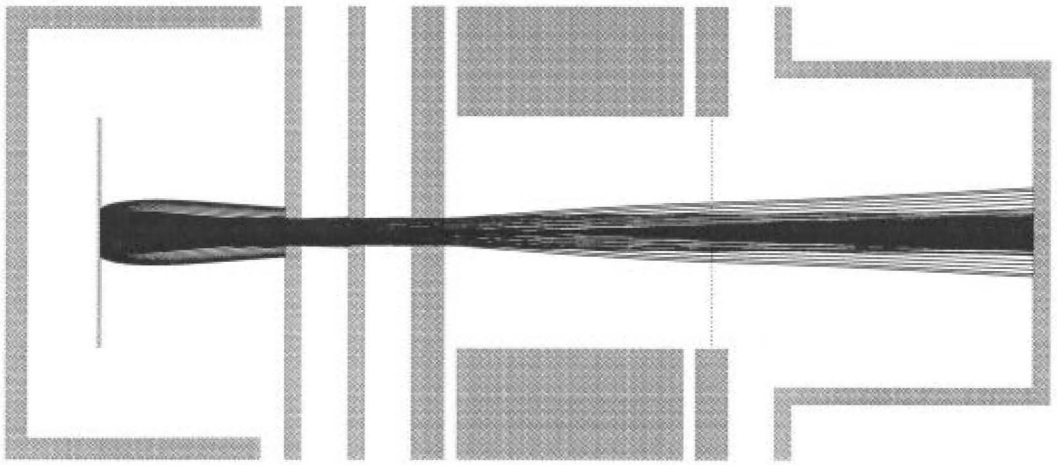

Fig. 6.2. 70 eV electron beam passing through the ionisation chamber.

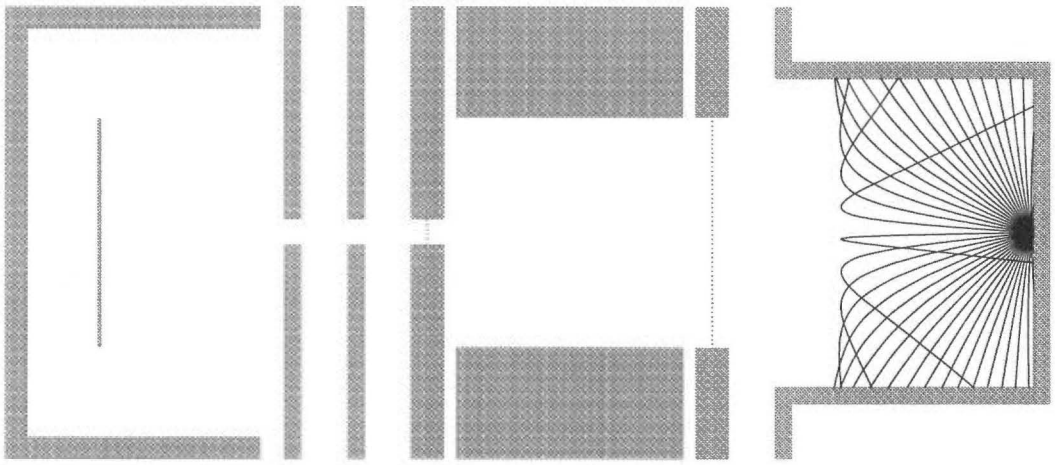

Fig. 6.3. Secondary electron emission from the electron beam collector.

The ionisation apparatus used to measure the cross sections is depicted in Fig. 5.5. Using the geometry and voltages given here the apparatus was modelled using

SIMION [Dahl, 1995]. Fig. 6.2 shows the electron beam for 70 eV acceleration. There is only slight divergence of the beam through the ionisation chamber which suggests any electron pickup on the chamber can only be due to secondary electron emission or elastic scattering. The magnets used in the later experiments ensure this is minimised. The impact of the fast beam electrons on the collector can cause secondary electron emission. The secondary electrons generally have an energy of 2-3 eV but may have up to a few tens of volts energy independent of the impacting electron energy [Massey, 1952]. It is important that these electrons do not escape the collector as this will affect the measurement of the electron beam current. Fig. 6.3 shows the trajectories of 10 eV secondary electrons emitted by the collector and shows that under the experimental conditions (60 V on collector) these will all return to the collector causing no net effect on the electron beam current determination. This is supported by Fig. 6.4, a plot of the

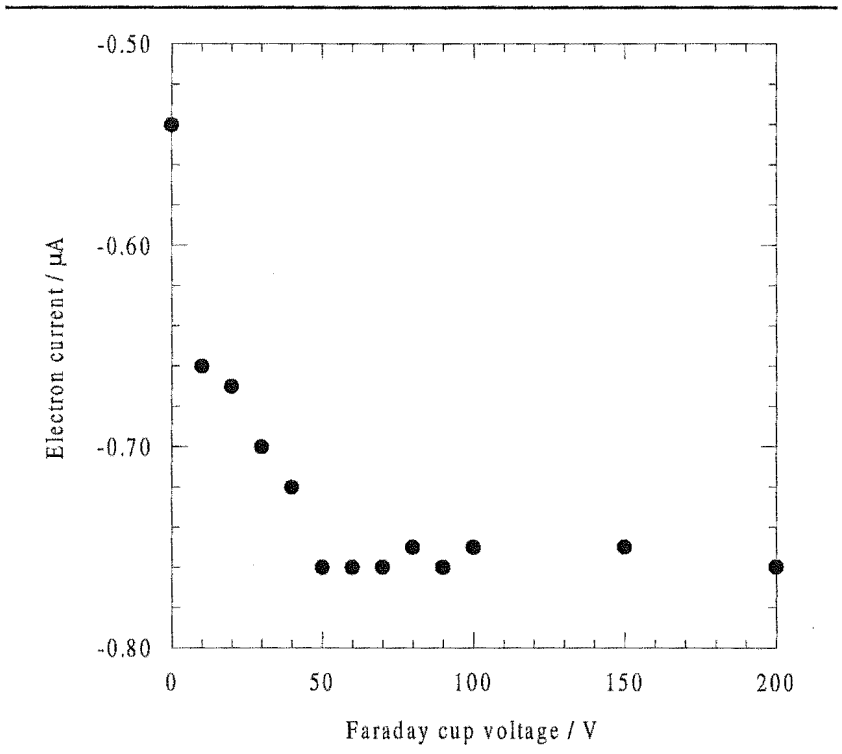

Fig. 6.4. Electron beam signal as a function of the faraday cup collector potential without magnetic collimation.

collector potential verses the electron beam current in the absence of magnetic collimation, which shows the measured electron current is independent of the collector voltage above 50 V, that is the entire electron beam is collected and secondary emission

is negligible. In the presence of the magnetic collimation voltages as low as 10 V were adequate to ensure complete collection of the electron beam.

6.1.2 Ionising Path Length

The geometry of the ionisation chamber defines a path length for the electron beam through the chamber as 1.25 cm, the distance from the lens on the front end to the mesh lens on the back end. It may be possible for positive ions formed in the spaces before and after the chamber to be attracted into the ionisation region by the electric fields where they can impact on the chamber wall and contribute to the ion current. If this is the case the choice of path length must necessarily include all areas from which ions will be detected. SIMION was used to determine the ion trajectories for thermal Ar^+ ions produced by ionisation at all points along the axis of the electron beam. For the production of thermal positive ions at all points within the ionisation chamber through which the electron beam passes (ignoring electron scattering), the calculated ion trajectories (Fig. 6.5) all terminated with collision of the Ar^+ ions with the chamber walls. That is all ions are successfully collected.

At the mesh grids at the limits of the chamber region the collection efficiency decreases from 100% as some ions are lost through the mesh to other electrodes. At the front end of the chamber the electric fields are not very strong, so ions produced with velocity vectors pointing away from the ionisation chamber are generally lost through the mesh to the beam extraction lenses. Conversely those ions with velocity vectors pointing towards the ionisation chamber will mostly be collected on the chamber wall. Fig. 6.6 shows the SIMION Ar^+ ion trajectories originating from the point slightly to the chamber side of where the mesh lens intersects the electron beam axis. Roughly half the ion produced at this point are successfully collected by the chamber wall. Moving the point of origin for the ion trajectories back up the electron beam axis rapidly reduces the fraction of ions collected. The mesh completely prevents any ions produced in the region outside of the chamber from reaching the chamber wall. Hence using SIMION, the cut off point for the beginning of the electron impact ionisation path length through

the gas is taken as the point where half of the ions will be measured. In this case the point is 0.1 mm on the chamber side of the mesh lens.

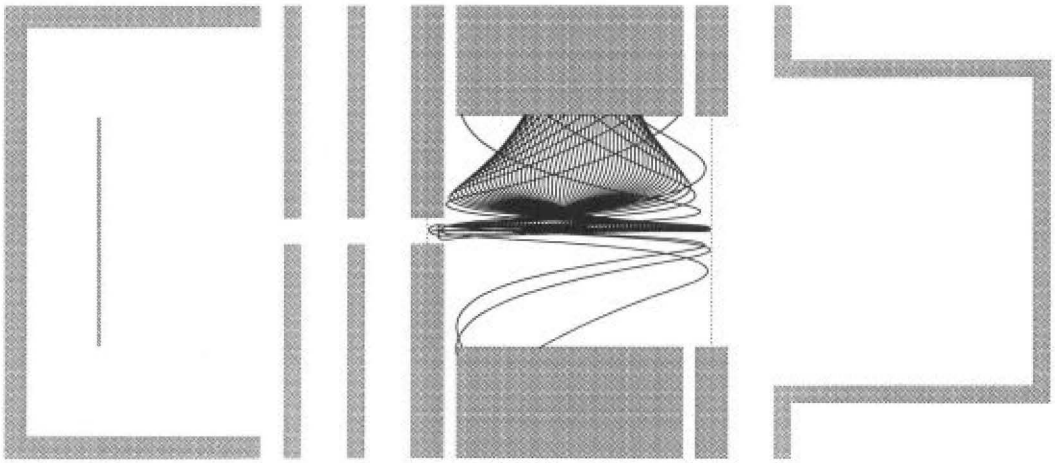

Fig. 6.5. Trajectories for Ar^+ ions created along the ionisation chamber axis.

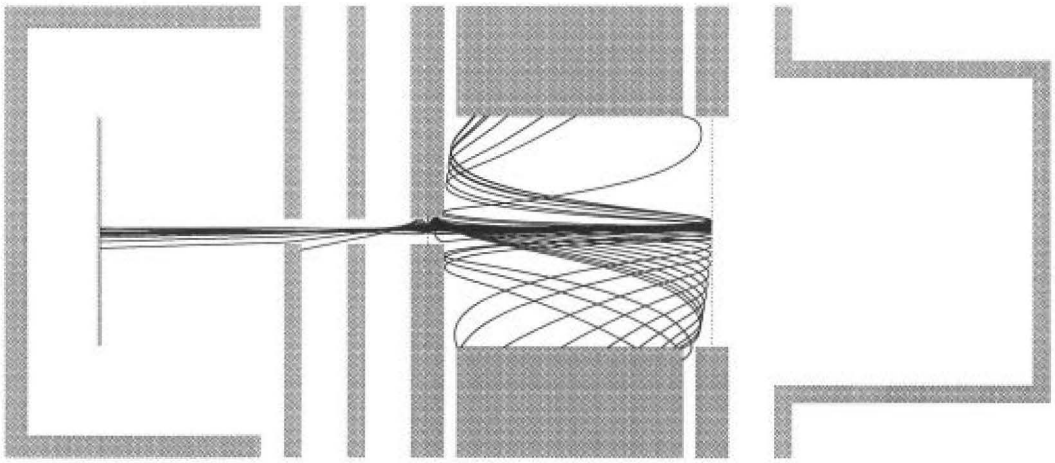

Fig. 6.6. Ar^+ trajectories for ions created at the front lens.

The determination of the end of the electron path length through the chamber is not as easy to find as it was for the front end. Due to the slight divergence of the electron beam ions can be formed up to 2 mm away from the axis. These ions will sample substantially different fields from the ions produced on the axis and hence will have different trajectories. Ions generated in the faraday cup can gain energy up to the potential of the collector which is typically at 60 V. As the ion energy increases the deviation of the ions from the axial trajectories they gain from the faraday cup will

decrease. Hence most ions produced in this region will pass back through the ionisation chamber where they will either hit the lens on the front of the chamber or carry on further up the electron beam axis towards the cathode. The collections of ions by the chamber generally appeared to be favoured for ions produced at increasing displacement from the axis and decreasing distance beyond the mesh electrode. Fig. 6.7 shows the Ar^+ trajectories for ions produced at a point 0.1 mm beyond the mesh lens at the back of the ionisation chamber and 0.75 mm off the axis. This position best represents the point where half of the ions produced will be measured by the chamber. Moving towards the faraday cup or moving towards the beam axis from this position will decrease the percentage of ions collected by the chamber, moving further from the axis to the limit of the electron beam profile will increase the collection efficiency.

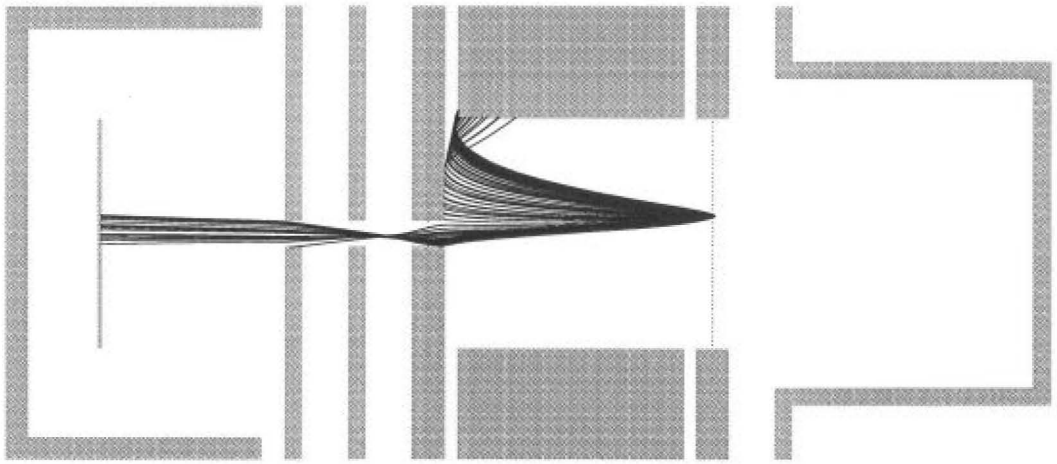

Fig. 6.7. Ar^+ trajectories for ions created at the back mesh lens.

From the results in Fig. 6.6 and Fig. 6.7 SIMION predicts the ionising path length will be 1.25 cm. That is, the same as the geometrical distance between the two mesh lenses. Hence no correction to the path length for the cross section calculations needs to be made.

6.2 Results

6.2.1 Initial Results

Using the 10 torr full scale baratron and with no magnetic collimation of the electron beam, ionisation cross sections were measured for various gas species with a 70 eV electron beam. Table 6.1 shows the results of the current work for the gases used and compares them to the literature values where available. The uncertainties for the experimental data are quoted as one standard deviation. The agreement of the data for the inert gases between the two sets of measurements is reasonable except for the Kr cross section. However the agreement for the higher mass polyatomic species such as SF_6 and CH_4 is not very good.

The conductance of gas out of the ionisation chamber has been minimised by the use of teflon sheet insulators to seal the gaps between the chamber, adjacent lenses and faraday cup collector. Since the rate of gas flow out of the ionisation chamber is inversely proportional to the square root of the mass of the gas, any pressure gradients still present in the chamber would be expected to most severely effect the determination of the ionisation cross sections for the light gases such as H_2 and He. The cross sections would underestimate the true ionisation cross sections. If this is the case then the differences between the data sets in Table 6.1 should be maximised at low mass and minimal for the ionisation cross sections for the higher mass species. Table 6.1 shows that if anything the opposite is true, the experimental ionisation cross sections for the high mass molecular gases are too low while the agreement with the literature is good for the lighter gases. Hence the difference between the effusive flow rate of gas into the chamber and the flow rate out of the chamber must be high enough to ensure the number density of the gas is homogeneous throughout the chamber and the pressure measured by the baratron is in equilibrium with the chamber pressure. The low experimental values for the ionisation cross sections for the large polyatomic gases in Table 6.1 must therefore be due to other factors resulting in the underestimation of the positive ion current measured at the ionisation chamber wall.

Species	Ionisation cross section (Å^2)	
	Experimental	Literature
He	0.37 ± 0.04	0.32[a,b,e]
Ne	0.61 ± 0.03	0.49[e], 0.51[a,b]
Ar	2.53 ± 0.05	2.77[a], 2.81[b], 2.91[e], 2.96[d]
Kr	3.51 ± 0.08	4.18[e], 4.21[a], 4.27[b]
Xe	5.1 ± 0.1	5.12[a], 5.24[c], 5.75[e]
H_2	1.17 ± 0.04	0.97[a]
N_2	2.09 ± 0.04	2.33[a]
SF_6	5.1 ± 0.1	5.65[a]
CH_4	3.06 ± 0.05	3.66[a]
CH_3F	3.26 ± 0.07	-
CH_3Cl	6.1 ± 0.1	-
CCl_3H	9.0 ± 0.2	-

Table 6.1. The ionisation cross sections measured at 70 eV without magnetic collimation, with comparison to the literature values. [a] [Rapp, 1965b], [b] [Stephan, 1980], [c] [Stephan, 1984], [d] [Straub, 1995], [e] [Wetzel, 1987].

For the molecular species, ionisation by electron impact can cause the molecule to dissociate. The resulting charged fragments can typically gain between 1-15 eV from the ionising impact as they are formed from dissociation of a repulsive state of the parent molecular ion [Kieffer, 1966; Rapp, 1965a]. In general the angular distribution of the fragment ions will be anisotropic with respect to the electron beam and the production of the fragments will be dependent on the ionising electron energy. For high energy electron beams the fragments can gain a lot more energy than is available from ionisation by low energy electrons. Because of both the high kinetic energy and nonisotropic distribution of the fragment ions, they will require much higher electric fields to ensure they are all collected by the chamber. Failure to collect all of the

fragment ions produced in such a manner will result in the underestimation of the positive ion current and hence give ionisation cross sections that are too low.

To check if the fragment ions are all being collected by the ionisation chamber, the ion current as a function of chamber potential was recorded for a 70 eV electron beam ionising diatomic N_2 in the absence of magnetic collimation of the electron beam. The results of this are graphed in Fig. 6.8 which shows the ion current remains constant with the negative chamber potential greater than -15 V. That is, the ion current is saturated as all of the N_2^+ and fragment N^+ ions are collected. The cross section for N_2 was measured as 2.09±0.04 $Å^2$ which compared to 2.33±0.16, the value of Rapp and Englander-Golden. The values agree very nearly within experimental uncertainties.

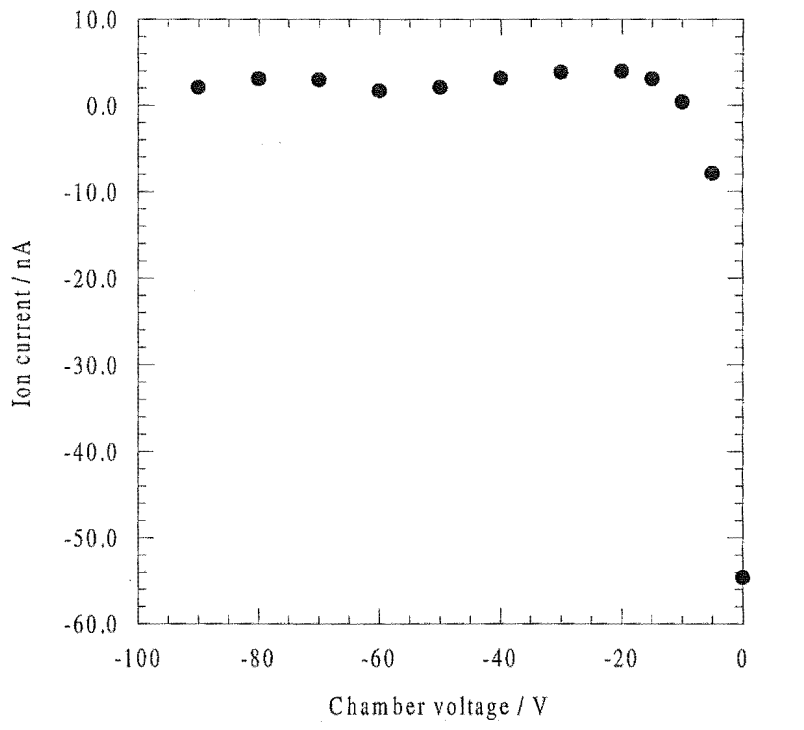

Fig. 6.8. Positive ion current for 70 eV ionisation of N_2 as a function of the ionisation chamber potential without magnetic collimation.

For the larger molecules CH_4 and SF_6 the differences between the experimental and literature cross sections are greater and cannot be accounted for by uncertainties. Two possibilities exist to account for the differences. A chamber potential of -20 V was used for all of the different gases but it may be that for the larger molecular species such

as CH_4, SF_6 and the methyl halides, the positive ion collecting field is not strong enough to ensure collection of all of the high energy fragments. Hence larger collecting fields may be required. The second possibility is that for the polyatomic species the cross section for elastic scattering of electrons is large resulting in a substantial electron current being collected on the chamber wall which will interfere with the measurement of the positive ion current. For the later experiments where magnetic collimation of the electron beam is incorporated, the scattered electron current that reaches the chamber wall will be greatly reduced and the cross sections measured for the polyatomic species are expected to be the true values.

To try and improve the fragment ion collection efficiency the chamber voltage can be increased to higher negative potentials. The problem with this is the chamber voltage creates an electric field along the axis of the collision region which is proportional to the voltage. This field must be kept to a minimum as the energy of the electron beam travelling along the axis will be changed by the field. If the field is too great the energy spread of the electrons that are involved in the ionisation of the gas will be large. This means cross sections quoted at a particular electron energy will actually be the average result of ionisation by electrons whose maximum energy will be bounded by the nominal electron energy but whose average energy will be substantially lower. This could be a serious problem in the region of the ionisation efficiency curve between threshold and the maximum where the cross section changes rapidly with electron energy.

SIMION was used to calculate the axial electric field in the chamber for the conditions used in all of the experiments. Fig. 6.9 shows the result for the field between the two mesh bounding lenses. The path length is divided up into three areas defined by the mesh lenses and the edge of the chamber. That is, area *A* is the length 1.3 mm from the front mesh to the front of the chamber, *B* is the length of the chamber 9.9 mm and *C* is the length 1.3 mm from the end of the chamber to the back mesh lens. Each area was fitted with a two degree polynomial with a fitting coefficients being better than 0.9999. The polynomial best fits were integrated over the electron path length through the chamber and the average axial voltage in the region was calculated as -10 V. This

means for a beam of electrons accelerated to 70 eV, the average energy of an electron involved in an ionising collision with a gas molecule will be: 70 - 10 = 60 eV. The cross section data in Table 6.1 should therefore be quoted at 60 eV rather than the nominal 70 eV. From the data used in Fig. 6.9 the standard deviation of the axial voltage was calculated to be ±7 eV so the energy spread of the beam is rather high. For the measurement of ionisation efficiency curves, the electron energy spread will introduce a large uncertainty in the determination of the ionisation potential and will smooth out the curve shape. The maximum in the ionisation curve will be poorly defined. No attempt was made to determine the effect of contact potentials {4.4} on the electron beam energy as no ionisation curves were measured down to the ionisation threshold. The large energy spread of the electron beam would make a comparison between an experimentally determined threshold potential and the accurately known literature value very difficult to make. Hence scaling the energy scale for the ionisation efficiency curves to account for contact potentials will be open to a high degree of uncertainty.

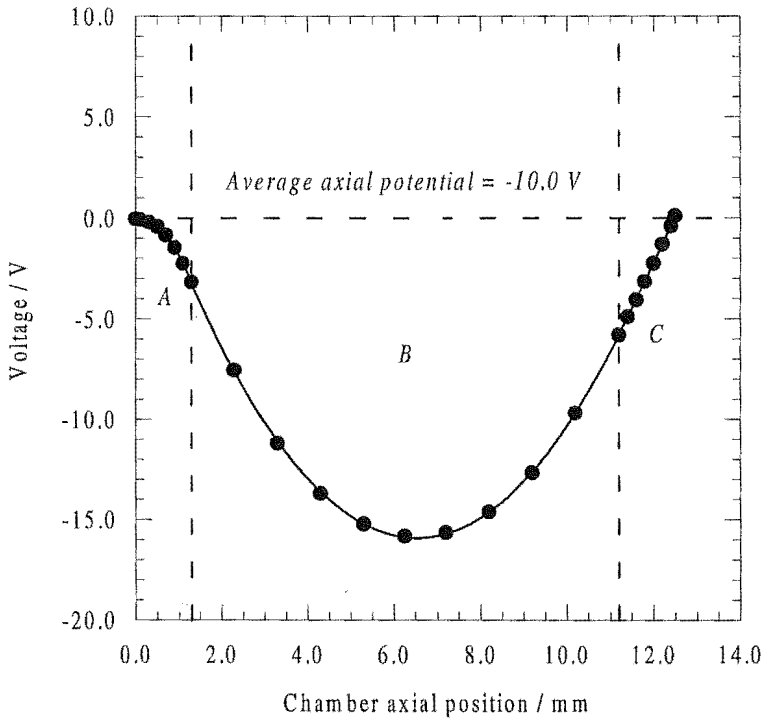

Fig. 6.9. The electric field along the ionisation chamber with the chamber at -20 V and the lenses at the ends of the chamber grounded.

6.2.2 Final Results

The electron impact ionisation experiments have been repeated using an axial magnetic field of no less than 600 G to collimate the electron beam. Interference effects in the measurement of the positive ion current from elastic scattering of electrons are expected to be negligible. All lens, chamber and electron collector potentials are the same as those used in the previous experiments. The chamber pressure is monitored with a 0.05 torr full scale baratron and for the low 10^{-4} torr pressures used in these experiments this is more accurate than the 10 torr head baratron used for the earlier experiments.

The maximum ionisation cross sections have been measured for the inert gases, CH_4 and a range of symmetric top alkyl halides [Vallance, 1997b]. The results are listed in Table 6.2 and compared to results from the literature. The uncertainties for the experimental data are quoted as one standard deviation. For the gases used here, the ionisation cross sections all peak near 70 eV. Comparing this experimental data to the previous experiments at 70 eV it can be seen that there is very little difference in the ionisation cross sections measured for the inert gases. However, the cross sections measured here for CH_4, CH_3F, CH_3Cl and CCl_3H are substantially higher. The difference is not unexpected and is accounted for by the magnetic collimation. The elastically scattered electrons that would reach the chamber wall in the absence of the axial magnetic field are instead forced back to the axis by the field. Therefore, the measured positive ion current will be larger as it is not reduced by scattered electrons and the resulting ionisation cross sections will increase.

The maximum ionisation cross section measurements have been extended by Claire Vallance who measured ionisation efficiency curves for Ar, CH_4, CH_3F, CH_3Cl and CH_3Br [Vallance, 1997b]. The results including the literature ionisation potentials [Lias, 1988] are graphed in Figs. 6.10-6.14 and tabulated in appendix B. Examination of the results shows that a smooth curve drawn through the experimental data points will intersect the electron energy axis at an energy roughly 10 eV above the literature ionisation potential. This difference is accounted for by the energy change the electron

beam experiences passing through the ionisation chamber, which is illustrated in Fig. 6.9. The average electron energy is calculated to be 10 eV below the nominal value, which matches the energy offset the experimental data shows from the ionisation potentials.

Species	Ionisation cross section ($Å^2$)	
	Experimental	Literature
He	0.39 ± 0.05	0.37[a,b], 0.38[e]
Ne	0.62 ± 0.03	0.72[b], 0.74[e], 0.78[a]
Ar	2.81 ± 0.03	2.54[b], 2.70[d,e], 2.86[a]
Kr	3.50 ± 0.10	3.70[e], 3.72[b], 4.26[a]
Xe	5.10 ± 0.13	4.59[c], 4.98[e], 5.46[a]
CH_4	4.24 ± 0.03	3.70[a]
CH_3F	3.72 ± 0.08	-
CH_3Cl	6.91 ± 0.08	-
CH_3Br	8.02 ± 0.03	-
CH_3I	10.3 ± 0.3	-
CCl_3H	12.25 ± 0.29	-

Table 6.2. Maximum ionisation cross sections compared with the literature values. [a] [Rapp, 1965b], [b] [Stephan, 1980], [c] [Stephan, 1984], [d] [Straub, 1995], [e] [Wetzel, 1987].

Lampe *et al* [Lampe, 1957] noticed a linear relationship existed between their ionisation cross sections measured at 75 eV and the polarisability of the ionised species. More recently Bartmess and Georgiadis [Bartmess, 1983] also noticed a similar correlation. A simple model based on the coulombic potential established between the incoming ionising electron and the target molecule was proposed by Harland *et al* [Aitken, 1995b; Vallance, 1997a] to account for the correlation between polarisability and ionisation cross section. As the electron approaches the molecule an electric field will be established at the molecule. It is assumed that when the coulombic potential reaches the ionisation potential for the molecule there will be enough energy available from the field to excite an ionising transition of the molecule.

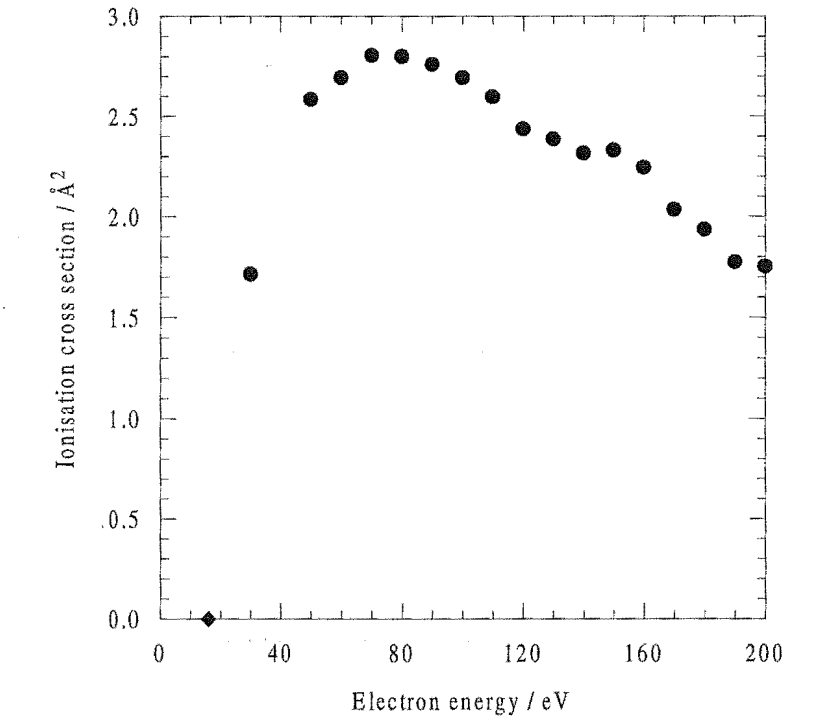

Fig. 6.10. Ar ionisation efficiency curve (●) [Vallance, 1997b]. The ionisation potential (◆) is shown [Lias, 1988].

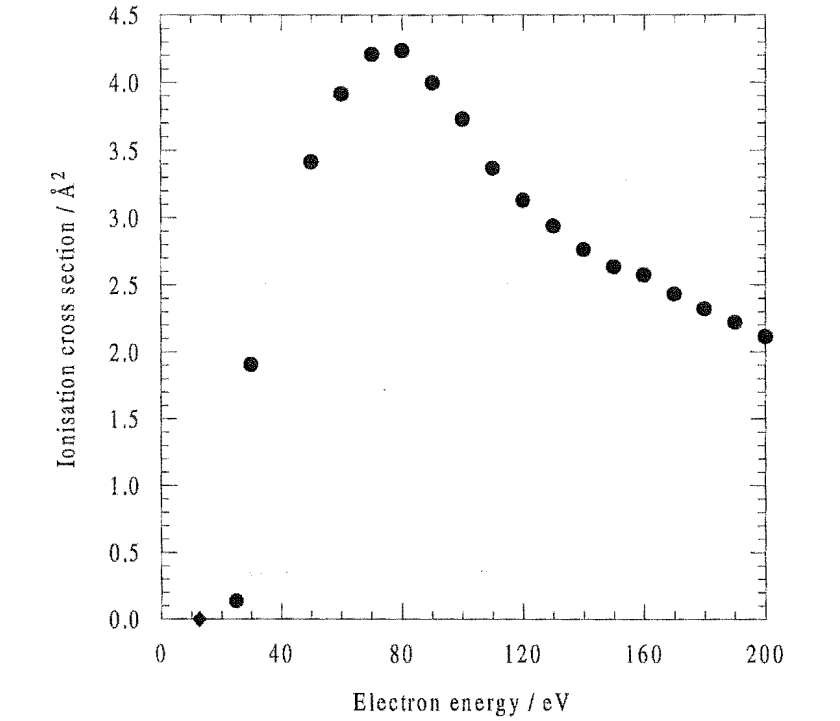

Fig. 6.11. CH_4 ionisation efficiency curve (●) [Vallance, 1997b]. The ionisation potential (◆) is shown [Lias, 1988].

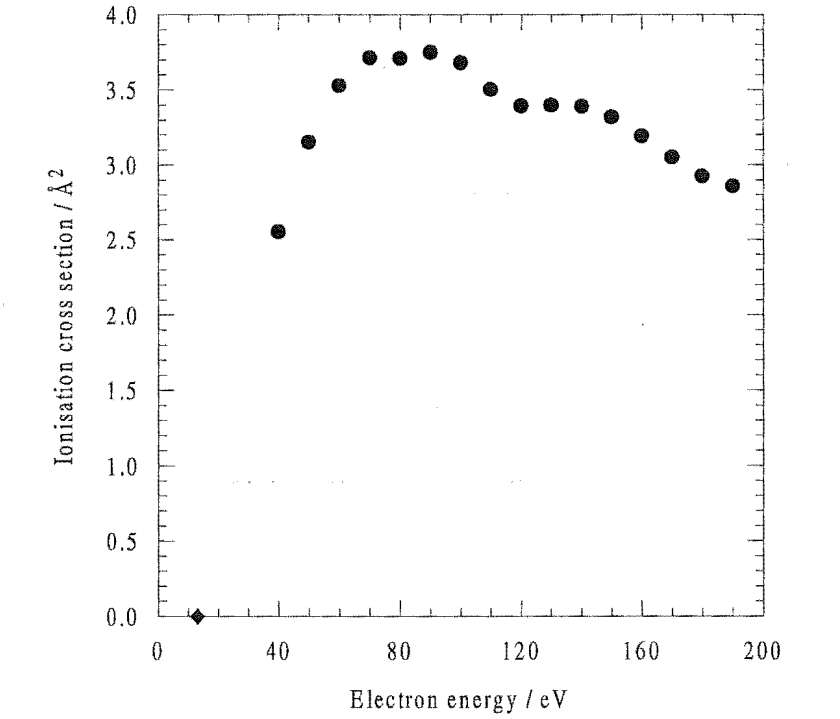

Fig. 6.12. CH_3F ionisation efficiency curve (●) [Vallance, 1997b]. The ionisation potential (◆) is shown [Lias, 1988].

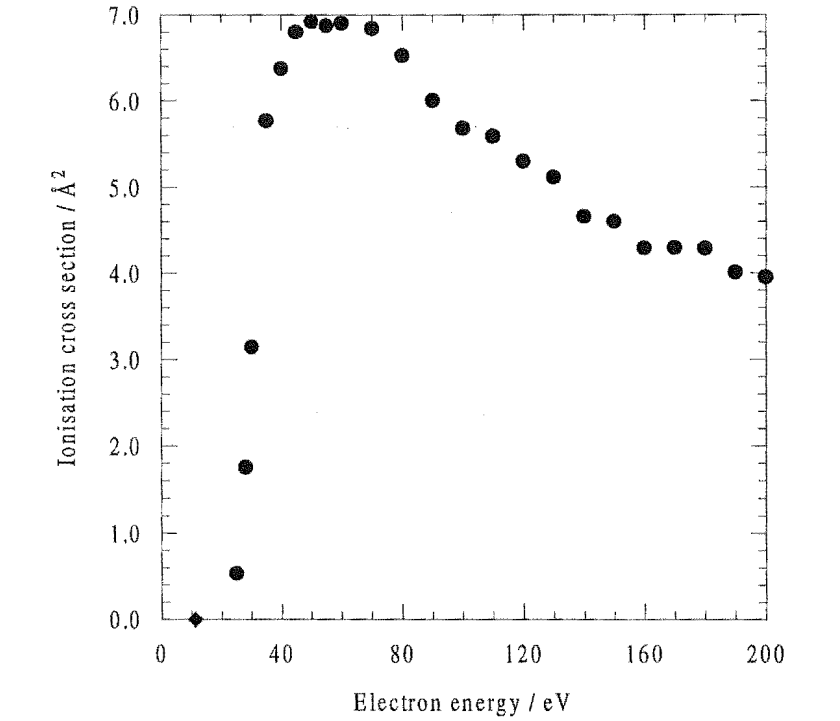

Fig. 6.13. CH_3Cl ionisation efficiency curve (●) [Vallance, 1997b]. The ionisation potential (◆) is shown [Lias, 1988].

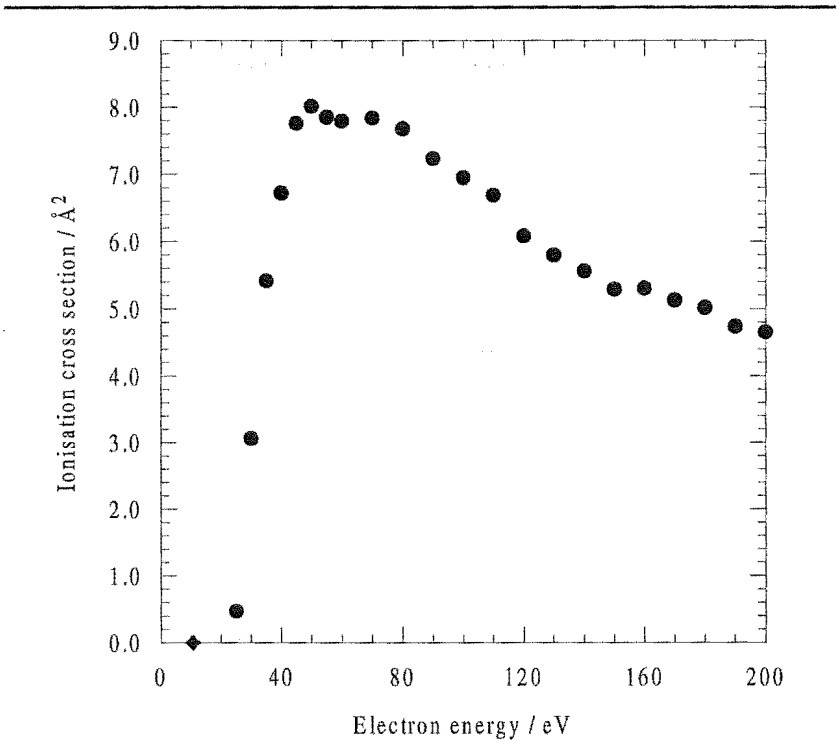

Fig. 6.14. CH_3Br ionisation efficiency curve (●) [Vallance, 1997b]. The ionisation potential (◆) is shown [Lias, 1988].

The electric field E established by an electron approaching a molecule will induce an electric dipole in the molecule's charge distribution. The magnitude of the induced dipole μ is proportional to the field and is given by

$$\mu = \alpha E \tag{6.1}$$

where the proportionality constant α is the polarisability of the molecule. The electrical potential ϕ at some point r at an angle θ to the induced dipole is

$$\phi = \frac{\mu \cos\theta}{4\pi\varepsilon_0 r^2}. \tag{6.2}$$

Because the induced dipole will point directly towards the approaching electron the angle θ is equal to zero so

$$\phi = \frac{\mu}{4\pi\varepsilon_0 r^2}. \tag{6.3}$$

The potential energy U of the ionising electron of charge $-e$ at point r will be

$$U = -\frac{\mu e}{4\pi\varepsilon_0 r^2} \tag{6.4}$$

and using equation 6.1

$$U = -\frac{\alpha E e}{4\pi\varepsilon_0 r^2}. \tag{6.5}$$

The electric field E generated by the electron is

$$E = -\frac{e}{4\pi\varepsilon_0 r^2} \tag{6.6}$$

and substituting this into equation 6.4 gives

$$U = \frac{\alpha e^2}{(4\pi\varepsilon_0 r^2)^2}. \tag{6.7}$$

When the potential U reaches the ionisation potential IP the molecule can absorb enough energy from the field to ionise. The cross section σ for the ionisation by the electron at position r is given by

$$\sigma = \pi r^2. \tag{6.8}$$

Substituting for r^2 in equation 6.6 gives

$$\sigma = \frac{e}{4\varepsilon_0}\left(\frac{\alpha}{IP}\right)^{1/2}. \tag{6.9}$$

Hence from equation 6.9 the ionisation cross section is predicted to be proportional to the square root of the ratio of the polarisability to the ionisation potential. Fig. 6.15 shows the experimental cross sections graphed as a function of $(\alpha/IP)^{1/2}$ compared to the results calculated using equation 6.9. The calculated results will apply to the cross sections at the maximum in the ionisation efficiency curves so the

experimental values used in Fig. 6.15 are the maximum values taken from Table 6.2. The graph shows there is a good linear correlation between the experimental ionisation cross sections and $(\alpha/IP)^{1/2}$. The cross sections calculated from the simple electrostatic model match the experimental cross sections reasonably well, but in general are slightly too high.

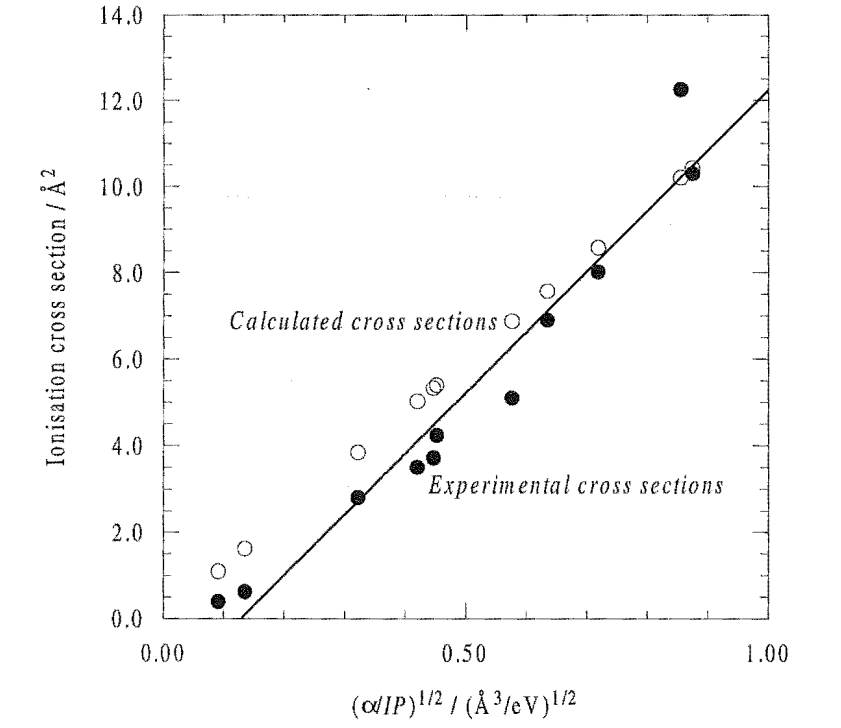

Fig. 6.15. Experimental maximum ionisation cross sections as a function of $(\alpha/IP)^{1/2}$. The linear least squares fit of the experimental data and the cross sections calculated using equation 6.9 are also shown.

6.3 Improvements

The ionisation efficiency curves measured here are limited in their accuracy by the very broad energy distribution of the electron beam which is a consequence of the axial electric field in the ionisation chamber. The energy spread can be reduced by decreasing the chamber potential but this will be at the cost of incomplete collection of the ion current leading to incorrect values for the ionisation cross sections. The only

option to improve the accuracy of the experiment is to replace the cylindrical chamber with a parallel plate setup similar to that first used by Jones [Jones, 1927] and used by Rapp *et al* {4.3.1}. The ionisation chamber is of the same design shown in Fig. 4.1. The positive ions formed in the chamber by ionisation with the electron beam aligned along the axis of the parallel plates, are attracted towards the negative collector plates by the perpendicular electric field across the chamber. In the centre of the chamber the field will be perpendicular to the parallel plates so the energy of the electron beam will not be affected by the field. The ion current is monitored only on the central of the three plates so that ions sampled will only be those that are produced along an electron path length equal in length to the central plate from the area of zero axial electric field. Fig. 6.16 shows the equipotential contours running parallel between the plates together with Ar^+ ion trajectories from ions produced along the length of the region. With -10 V on the collection plates and +10 V on the lower plate the ion trajectories are essentially perpendicular to the axis away from the ends of the chamber. An axial magnetic field ensures the electron beam does not diverge in the field and hit the lower plate.

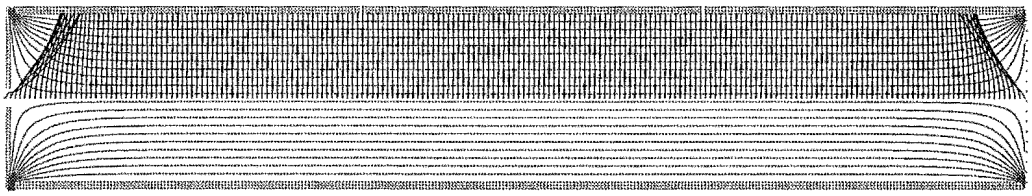

Fig. 6.16. The equipotential contours for the parallel plate ionisation cell. At the centre of the cell the electric field is perpendicular to the cell axis. The Ar^+ ion trajectories which follow the electric field are shown. Ions collected on the central plate are formed from a path equal in length to the plate.

Further improvements to this design have been made recently by Straub *et al* [Straub, 1995]. They used a pulsed electron beam to generate a burst of ions in a gas chamber in field free conditions, thus ensuring the electron energy is totally free from any effects from chamber electric fields. The application of a powerful perpendicular electric field fractionally after the passage of the electron pulse out of the chamber ensured that all of the ions produced within an accurately defined path length were collected.

Chapter 7

Rotationally State Selected Molecular Beams

Experiments have been carried out to measure the cross sections for rotationally inelastic collision processes. A molecular beam produced by a supersonic nozzle expansion is passed through an inhomogeneous hexapole electric field. The attenuation of the hexapole focused upper Stark state beam molecules through inelastic collisions with quenching gas species admitted to the hexapole region, is measured in order to determine the cross sections.

The main features of the attenuation experiment:

- Molecular beam formation
- Hexapole state selection
- Collision cross sections

will be discussed here to provide an understanding of the processes occurring.

7.1 Molecular Beam Formation

The formation of molecular beams is a fundamental technique in modern physical chemistry. The collision free nature of the beams allows chemical and physical processes to be studied at the level of the primary interaction without the interfering effects of multiple collisions modifying the reactant and product state distributions. Intersecting the molecular beam with laser radiation, other particle beams or a combination of the two allows highly resolved spectroscopic and dynamic information to be determined for reactive and energy transfer events.

Molecular beams are formed by allowing a gas to pass from a source at high pressure through a narrow slit or small circular orifice into a region of lower pressure. The properties of the resulting beam depend on the nature of the expansion through the orifice. If the mean free path λ of the gas in the source is greater than the diameter d of the orifice then the probability of a molecule undergoing a collision as it passes through the orifice is small and the resulting beam is said to be effusive. Whereas if the mean free path is small compared to the orifice diameter molecules can undergo many collisions in the expansion leading to the formation of a supersonic molecular beam. The ratio of mean free path to orifice diameter is the Knudsen number K_n

$$K_n = \frac{\lambda}{d}, \tag{7.1}$$

where $K_n > 1$ defines an effusive source and $K_n < 1$ defines a supersonic source.

7.1.1 Effusive Sources

The earliest molecular beams were produced using effusive sources [Ramsey, 1956]. As $K_n > 1$ molecules passing through the source orifice are unlikely to collide with other molecules. This means the energy partitioning and velocities of the escaping molecules will remain unmodified by the effusive expansion. The number of molecules

exiting the source per second dN into a solid angle dω at an angle θ to the normal to source orifice is

$$dN = \frac{n\bar{v}A\cos\theta}{4\pi}d\omega \tag{7.2}$$

where n is the particle density in the source, $\bar{v}$ is the mean velocity $(8kT/\pi m)^{1/2}$ for molecules of mass m in the source and A is the area of the orifice. Using $d\omega = 2\pi\sin\theta d\theta$ equation 7.2 can be integrated over the solid angle 2π from $\theta = 0$ to $\pi/2$ to give

$$N = \frac{n\bar{v}A}{4} \tag{7.3}$$

where N is the total number of molecules leaving the source per second. The distribution of molecular velocities within the source is given by the Maxwell-Boltzmann distribution $f_s(v)$

$$f_s(v) = \frac{4}{\sqrt{\pi}\,\alpha^3}v^2e^{-v^2/\alpha^2} \tag{7.4}$$

where α is the most probable velocity $(2kT/m)^{1/2}$. The velocity distribution of the beam $f_b(v)$ should match the distribution in the source as the expansion is collision free. However, the probability of a molecule passing through the orifice in a given time is proportional to the velocity of the molecule. Hence the beam distribution is the source distribution multiplied by the velocity. Renormalising to the total beam intensity gives

$$f_b(v) = \frac{2}{\alpha^4}v^3e^{-v^2/\alpha^2} = \left(\frac{v}{\bar{v}}\right)f_s(v). \tag{7.5}$$

While the internal energy partitioning and velocity distribution of the effusive beam will be easy to characterise in terms of the source conditions, the low intensity, broad velocity distribution and high number of populated internal energy states of the effusive beam means it will be unsuitable in applications such as the current experiments where quantum state resolution and a narrow velocity distribution are required.

7.1.2 Supersonic Sources

To overcome the limitations of the effusive beam, the use of supersonic beams was developed [Scoles, 1988]. If the Knudsen number of the source is less than one (K_n < 1) particles exiting the source can undergo many collisions with other molecules passing through the orifice. This isentropic continuum expansion rapidly converts the internal energy and random thermal motion of the source molecules into directed flow of the expanding beam. The stagnation state of the source is defined by the temperature T_0 and pressure P_0. For expansion into a region with background pressure P_b, if the pressure ratio P_0 / P_b exceeds a critical value $G = ((\gamma + 1)/2)^{\gamma/(\gamma - 1)}$ where γ is the ratio of heat capacities for the source gas, the flow will reach a velocity u equal to the local speed of sound a. That is the Mach number M for the flow will be 1, where

$$M = \frac{u}{a} \tag{7.6}$$

and

$$a = \left(\frac{\gamma kT}{m}\right)^{1/2}. \tag{7.7}$$

As the pressure at the nozzle will be greater than P_b under these conditions the flow is said to be underexpanded and it will expand further to meet the boundary condition imposed by P_b. As the expansion develops, further collisions raise the flow velocity above the local speed of sound, that is $M > 1$. As the flow is expanding at a rate faster than the boundary conditions can respond, a series of shock waves are established at the boundary. The shock waves are nonisentropic regions of large density, temperature, pressure and velocity gradients. The structure of the supersonic expansion is shown in Fig. 7.1. The isentropic core of the expansion is known as the zone of silence as it is unaware of the boundary conditions imposed by P_b.

With increasing distance from the nozzle the Mach number increases in the isentropic region and the random motion of the flow is rapidly decreased by further

collisions. When the collision frequency reaches zero the internal energy and velocity distributions of the flow will freeze out at characteristic temperatures much lower than the stagnation temperature T_0. To extract a beam from the expansion a skimmer must be

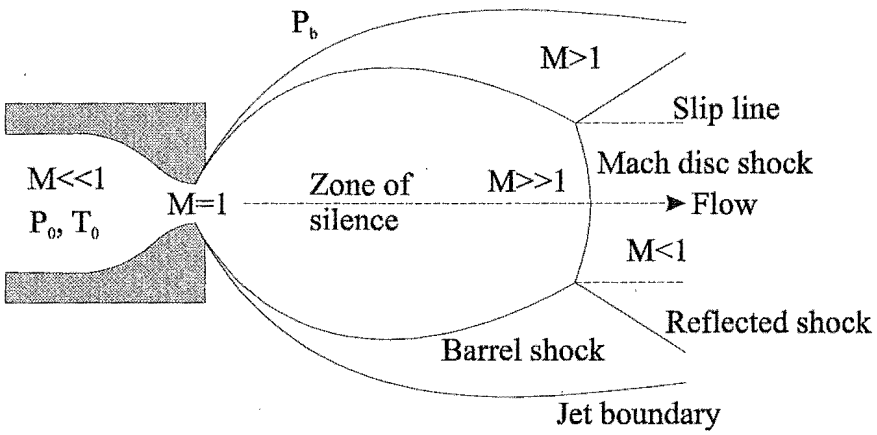

Fig. 7.1. The supersonic beam expansion.

positioned on axis with its tip within the zone of silence. The skimmer is shaped to minimise the reflection of scattered molecules back into the axial path of the expansion. The mean free path of the molecules in the part of the expansion sampled by the skimmer will be very large hence the resultant beam will be characterised by free molecular flow. That is the collision frequency within the beam will essentially be zero. However, due to the finite width of the velocity distribution of the beam there is a small probability of collisions within the beam. The form of the velocity distribution for the supersonic molecular beam is not well understood but it is assumed to be approximated by a three dimensional Maxwell-Boltzmann distribution characterised by the parallel ($T_{\|}$) and perpendicular ($T_{\perp}$) temperatures of the beam superimposed on the flow velocity u. For the axial direction the velocity distribution $f_b(v)$ is given by

$$f_b(v) = Av^2 e^{-m(v-u)^2/2kT_{\|}} \tag{7.8}$$

where A is a normalisation constant. A comparison between the effusive and supersonic beam velocity distributions is shown in Fig. 7.2. For an ideal gas the thermodynamic limiting flow velocity u_∞ where all internal and translational energy is converted to the flow velocity is

$$u_\infty = \left(\frac{\gamma}{\gamma - 1}\right)^{1/2} \left(\frac{2kT_0}{m}\right)^{1/2} \tag{7.9}$$

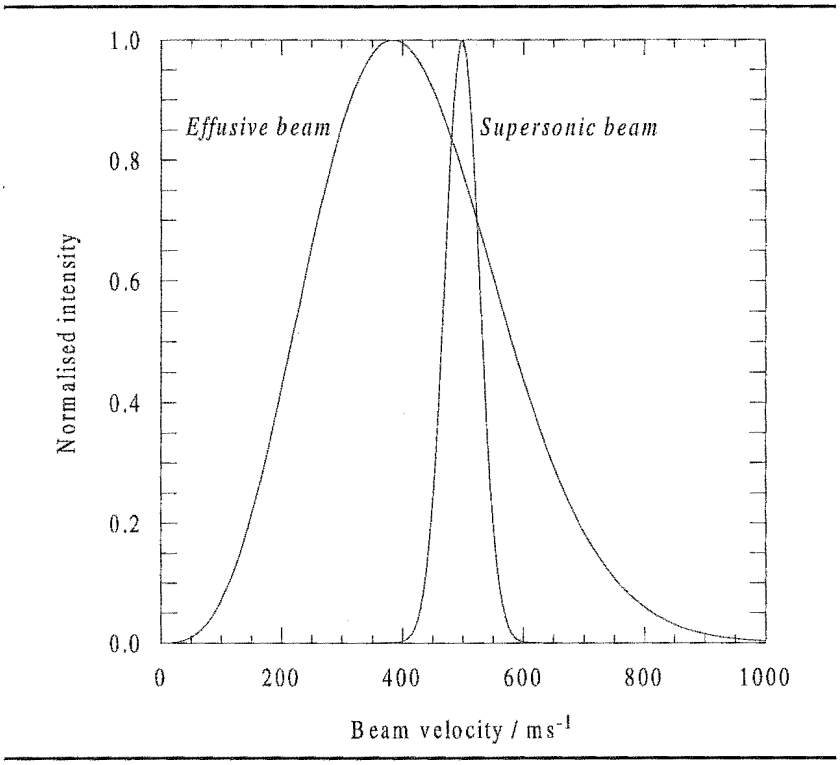

Fig. 7.2. The velocity distributions for effusive and supersonic molecular beams.

The major advantages of the supersonic source over the effusive source are the directed flow and the cooling of the beam. Due to the efficient transfer of random energy in the supersonic expansion to the flow velocity perpendicular to the nozzle orifice the expanding material will be favourably focused in the axial direction. This means the beam intensity on axis for the supersonic expansion will be much greater than the cosθ intensity angular distribution exhibited for the effusive beam. The rate of collisional relaxation of the translational and internal energy characterised by the source stagnation temperature is not a statistical process. Translational, vibrational, rotational and electronic energies will be cooled at different rates dependent on the number of collisions experienced in the supersonic expansion. In a typical expansion a molecule may undergo 10^2 to 10^3 collisions. Hence only processes that will come to equilibrium for this number of collisions will be relaxed in the expansion. For instance, vibrational relaxation of diatomics may require 10^4 collisions, hence the vibrational modes will not be cooled in the expansion. However rotational relaxation for most diatomics requires

10 to 100 collisions and will therefore be efficiently cooled. In general for the symmetric top molecules used in this work translational energy is cooled more rapidly than internal energy and the rotational states are cooled more efficiently than the vibrational states.

7.1.3 Seeded Beams

The energy distribution of a species in a supersonic molecular beam can be modified by using the technique of seeding [Scoles, 1988]. If a small percentage of a seed species is mixed with either a lighter or heavier buffer gas the resulting flow velocity of the binary mixture will closely match the velocity of an expansion of the pure buffer. That is the seed gas and the buffer gas will attain the same velocity distribution, hence seeding in a heavy gas will decrease the velocity of the seed and using a light gas will increase the velocity of the seed gas. Furthermore the properties of the binary expansion are dependent on the mole fraction of the two species in the mixture, hence the flow velocity will be modified by variation of the fraction of the seed present. Another result of the seeded technique is the preferential axial focusing of the heavier component in the supersonic beam. Since both components of the binary mixture are characterised by a single perpendicular temperature $T_\perp$, the perpendicular velocity $v_\perp$ is given by

$$v_\perp = \left(\frac{2kT_\perp}{m}\right)^{1/2} \tag{7.10}$$

which will be greatest for small mass. That is, the divergence of the light component in the seeded beam will be greater than for the heavier component.

7.2 Hexapole State Selection

7.2.1 Symmetric Top Molecules

The hexapole inhomogeneous electric field filters symmetric top molecules according to their first order Stark energy W_1 [Bernstein, 1982] which is defined by

$$W_1 = -\boldsymbol{\mu}.\mathbf{E} = -\mu\varepsilon\cos\theta \tag{7.11}$$

where $\boldsymbol{\mu}$ is the dipole moment vector of the molecule and $\mathbf{E}$ is the electric field vector. The negative sign arises as the electric field is defined from positive to negative and the dipole is defined from negative to positive. θ is the angle between the field and the dipole. Hence the necessary requirement for a molecule to have a Stark effect is the presence of a permanent electric dipole moment. The rotational period for a molecule is orders of magnitude less than the flight time of the molecule through the hexapole field. Hence the rotation averaged dipole moment of the molecule must be non-zero in the hexapole field for there to be a net Stark effect. That is, the angular momentum vector and dipole moment of the molecule must not be perpendicular. For ground vibrational state polar diatomics the electric dipole is perpendicular to the angular momentum vector hence there will be no net first order Stark effect. However, for symmetric top molecules where the total angular momentum vector is not perpendicular to the electric dipole there will be a net Stark effect in the hexapole electric field.

7.2.2 Symmetric Top Rotation

The rotational energy W_0 of a molecule free to rotate in three dimensions will be

$$W_0 = \frac{J_a^2}{2I_a} + \frac{J_b^2}{2I_b} + \frac{J_c^2}{2I_c} \tag{7.12}$$

were $J_a = I_a\omega_a$ is the classical angular momentum about the a axis, I_a is the moment of inertia about the a axis and ω_α is the angular velocity [Atkins, 1990]. For symmetric top molecules $I_x = I_y \neq I_z$ where z is the figure axis (principle axis) of the molecule. There are two classes of symmetric top molecules. If $I_x = I_y < I_z$ then the molecule is an oblate symmetric top and the principle axis is denoted c ($I_z = I_c$) as the convention is $I_a < I_b < I_c$ and if $I_x = I_y > I_z$ then the molecule is a prolate symmetric top and the principle axis is denoted a ($I_z = I_a$). CH_3Cl is an example of a prolate symmetric top and CCl_3H is an example of an oblate symmetric top.

Since the magnitude of the total angular momentum is $|\mathbf{J}| = (J_a^2 + J_b^2 + J_c^2)^{1/2}$ and $I_a < I_b = I_c$ then the rotational energy for a prolate top will be

$$W_0 = \frac{\mathbf{J}^2}{2I_b} + J_a^2\left(\frac{1}{2I_a} - \frac{1}{2I_b}\right). \tag{7.13}$$

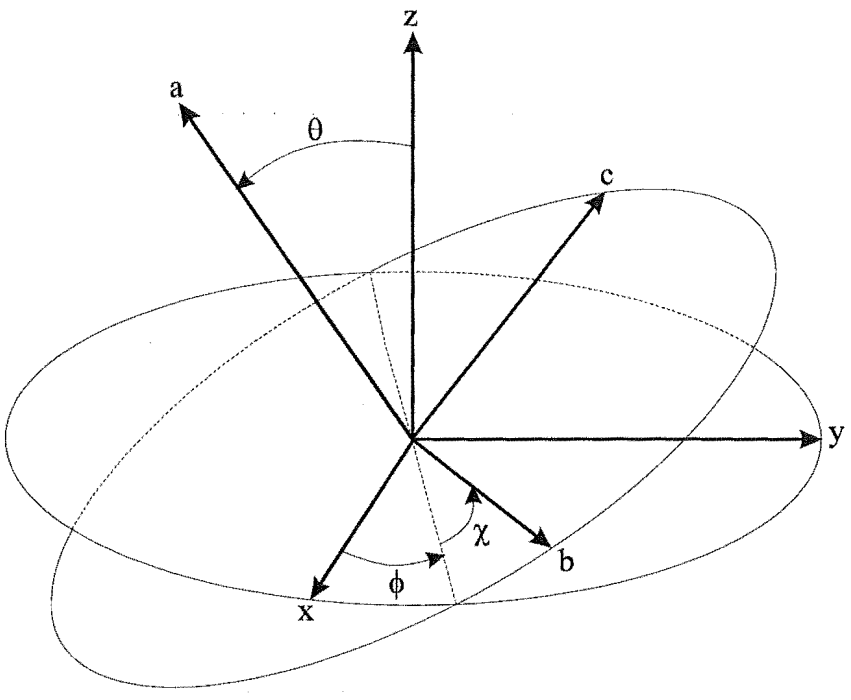

Fig. 7.3. Euler's angles for transformation from the space fixed axes *xyz* to the molecular axes *abc*.

When the molecule is placed is an external electric field a set of space fixed coordinates *xyz* defined by the field may be used in place of the molecular axes *abc*.

The fixed axis system is transformed to the molecular axes by Euler's angles $\theta\phi\chi$ [Townes, 1955] shown in Fig. 7.3. The transformation from fixed to molecular axes consists of rotation about the z axis by angle ϕ, rotation about the line of nodes by angle θ (the angle between **E** and μ) and rotation about the molecular axis c by angle χ. In terms of Euler's angles, the total rotational energy W of a prolate symmetric top in an electric field will be

$$W = W_0 + W_1 = \frac{I_a}{2}\left(\dot{\chi} + \dot{\phi}\cos\theta\right)^2 + \frac{I_b}{2}\left(\dot{\theta}^2 + \dot{\phi}^2\sin^2\theta\right) - \mu\varepsilon\cos\theta. \qquad (7.14)$$

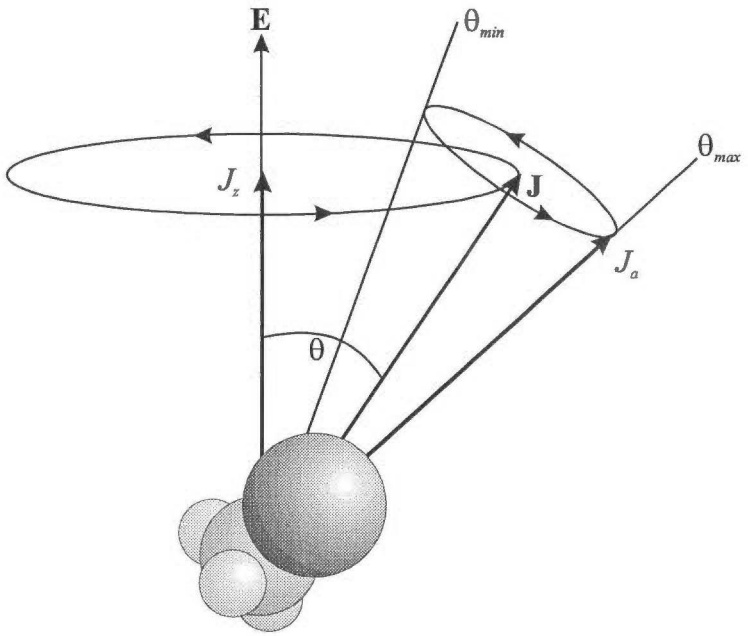

Fig. 7.4. Rotation of a symmetric top molecule in an electric field.

The important properties of the solutions to the above equation illustrated in Fig. 7.4 are found to be:

- J_z, the component of angular momentum in the field (**E**) direction is constant.
- J_a, the component of angular momentum along the symmetry axis of the molecule is constant.

- J_a precesses about the angular momentum vector **J** with a frequency $\mathbf{J}/2\pi I_b$, hence the angle θ between the electric field **E** and the electric dipole **μ** along the axis *a* will vary between two limiting values.
- The field **E** exerts a torque on the dipole **μ** causing the dipole to precess about the field direction.

To determine the average value of θ in equation 7.11, a quantum mechanical treatment of the symmetric top rotation must be made [Townes, 1955]. In zero external field the rotational Hamiltonian $\mathbf{H}_0$ for a prolate symmetric top in terms of Euler's angles will be

$$\mathbf{H}_0 = \frac{-h^2}{8\pi^2 I_b}\left(\frac{1}{\sin\theta}\frac{\partial}{\partial\theta}\left(\sin\theta\frac{\partial}{\partial\theta}\right) + \frac{1}{\sin^2\theta}\frac{\partial^2}{\partial\phi^2}\right) + \left(\frac{\cos^2\theta}{\sin^2\theta} + \frac{I_b}{I_a}\right)\frac{\partial^2}{\partial\chi^2} - \frac{2\cos\theta}{\sin^2\theta}\frac{\partial^2}{\partial\chi\partial\phi}. \tag{7.15}$$

To solve the wave equation

$$\mathbf{H}_0\Psi = W_0\Psi \tag{7.16}$$

the variables in 7.15 may be separated and the solutions to 7.16 will be of the form

$$\Psi = \Theta(\theta)e^{iM\phi}e^{iK\chi} \tag{7.17}$$

where M and K are necessarily the integers 0, ±1, ±2,... in order to make the wave function Ψ single valued. Solving the wave equation 7.16 using equation 7.17 amounts to finding the function Θ(θ) that satisfies

$$\frac{8\pi^2 I_b}{-h^2}W_0\Theta = \frac{1}{\sin\theta}\frac{\partial}{\partial\theta}\left(\sin\theta\frac{\partial\Theta}{\partial\theta}\right) - \left(\frac{1}{\sin^2\theta}M^2 + \left(\frac{\cos^2\theta}{\sin^2\theta} + \frac{I_b}{I_a}\right)K^2 - \frac{2\cos\theta}{\sin^2\theta}KM\right)\Theta. \tag{7.18}$$

The function Θ(θ) is found from the solutions of the hypergeometric equation which will have the eigenvalues

$$W_0 = BJ(J + 1) + (A - B)K^2 \tag{7.19}$$

where J is a positive integer greater than or equal to K and M. A and B are the rotational constants $\hbar^2/2I_a$ and $\hbar^2/2I_b$ respectively. The total angular momentum **J** is then given by $\hbar(J(J + 1))^{1/2}$ and the projection of **J** on to the molecular symmetry axis a is $\hbar K$, where K = 0, ±1, ±2,... ±J. In the presence of an external electric field **E** the projection of **J** on to the field is $\hbar M$, where M = 0, ±1, ±2,... ±J.

For a molecule in an electric field the Hamiltonian defined in equation 7.15 will be modified to incorporate the Stark energy according to

$$\mathbf{H} = \mathbf{H}_0 - \mu\varepsilon\cos\theta. \tag{7.20}$$

Since the first order Stark energy W_1 is small compared to the field free rotational energy W_0, perturbation theory can be used to calculate the Stark energy using the wave functions defined in equation 7.17. That is

$$W_1 = -\varepsilon\int\Psi^*\mu\cos\theta\Psi d\tau. \tag{7.21}$$

The solutions to the integral in 7.21 are

$$W_1 = -\mu\varepsilon\frac{KM}{J(J + 1)} = -\mu\varepsilon\langle\cos\theta\rangle = -\mu\varepsilon\rho \tag{7.22}$$

where $\langle\cos\theta\rangle$ is the average value of $\cos\theta$ which varies as the molecule precesses about its angular momentum vector **J**. Hence if the product KM is less than 0, the molecule will be in an upper Stark state and will be repelled by the electric field, therefore the total energy is increased. For the opposite case where KM is greater than zero, the molecule is in a lower Stark state and will be attracted by the field, hence the total energy is lower. The change in trajectory of a molecule passing through an electric field as a result of the Stark energy is the basis for the state selection properties of the hexapole electrostatic filter.

7.2.3 Hexapole Electric Field

An ideal hexapole electric field is generated by six rods of hyperbolic cross section of alternating electric potential U_0 arranged about the points of a regular hexagon with inscribed radius r_0 [Kramer, 1965]. In practice however as for the quadrupole described in {2.5.1} the rods are more usually of circular cross section. If the curvature of the circular rods closely match the ideal hyperbolic rods at r_0 then the approximation to the hyperbolic rods will be good. The electric potential U of the hexapole field is given by

$$U(r,\phi) = U_0\left(\frac{r}{r_0}\right)^3 \cos(3\phi) \tag{7.23}$$

where the cylindrical coordinates r and ϕ describe the radial and angular position in the field shown by Fig. 7.5.

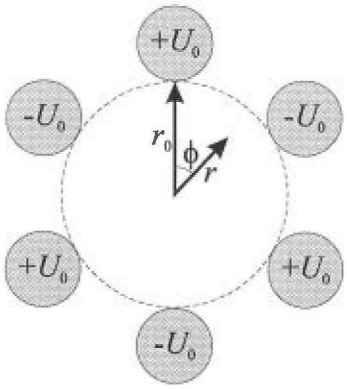

Fig. 7.5. The coordinates $r\phi$ defined for the hexapole electric field.

The electric field vector **E** is given by the negative gradient of the potential

$$\mathbf{E} = -\nabla U(r,\phi) \tag{7.24}$$

where the gradient operator is defined in cylindrical coordinates (r,ϕ,z) as

$$\nabla = \frac{\partial}{\partial r}\zeta_r + \frac{\partial}{\partial \phi}\zeta_\phi + \frac{\partial}{\partial z}\zeta_z \tag{7.25}$$

and ζ_r, ζ_ϕ and ζ_z are the unit vectors describing the cylindrical coordinates. Hence combining 7.25 and 7.23 gives the electric field

$$\mathbf{E} = 3U_0\left(\frac{r^2}{r_0^3}\right)\cos(3\phi)\zeta_r - 3U_0\left(\frac{r^2}{r_0^3}\right)\sin(3\phi)\zeta_\phi \tag{7.26}$$

and the electric field strength ε as

$$\varepsilon = (\mathbf{E}.\mathbf{E})^{1/2} = 3U_0\frac{r^2}{r_0^3}. \tag{7.27}$$

The radial force $\mathbf{F}_r$ exerted by the field on the molecular dipole is

$$\mathbf{F}_r = -\frac{\partial W_1}{\partial r} \tag{7.28}$$

where W_1 is the Stark energy of the molecule in the hexapole field given by equation 7.22. Hence using equations 7.22 and 7.27 the radial force will be

$$\mathbf{F}_r = -\frac{\partial W_1}{\partial \varepsilon}\frac{\partial \varepsilon}{\partial r} = \frac{6U_0\mu}{r_0^3}\frac{\mathrm{MK}}{\mathrm{J(J+1)}}r = m\frac{\mathrm{d}^2 r}{\mathrm{d}t^2}. \tag{7.29}$$

Hence the equation of motion will be

$$\frac{\mathrm{d}^2 r}{\mathrm{d}t^2} = \frac{6U_0\mu}{mr_0^3}\frac{\mathrm{MK}}{\mathrm{J(J+1)}}r = \omega^2 r \tag{7.30}$$

where the angular frequency ω of the molecular trajectories in the hexapole field is

$$\omega = \left(\frac{6U_0\mu}{mr_0^3}\frac{\mathrm{MK}}{\mathrm{J(J+1)}}\right)^{1/2}. \tag{7.31}$$

The solutions to 7.30 fall into three classes. For lower Stark states where MK/J(J + 1) > 0 the trajectories are

$$r(t) = Ae^{\omega t} + Be^{-\omega t} \tag{7.32}$$

which are divergent and will be lost from the field axis. For upper Stark states where MK/J(J + 1) < 0 the solutions are

$$r(t) = A\cos(\omega t) + B\sin(\omega t) \tag{7.33}$$

which are convergent and will be focused to the hexapole electric field axis. For those states where MK/J(J + 1) = 0 the hexapole field will have no effect on the trajectories and the molecules will pass through the hexapole field without suffering any deflection. The upper and lower Stark state trajectories for a molecular beam passing through the hexapole are shown in Fig. 7.6.

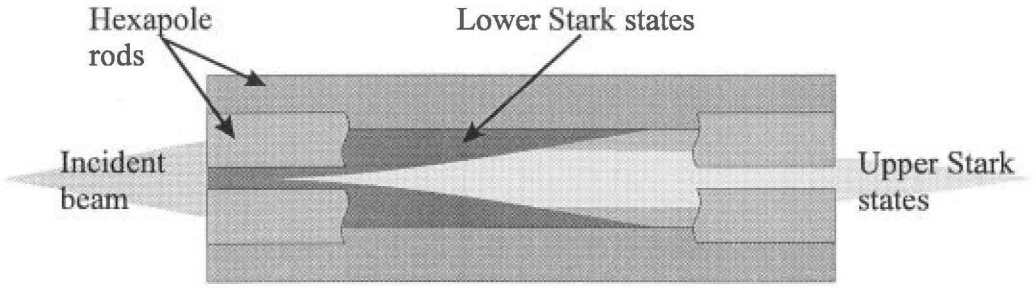

Fig. 7.6. The divergent lower Stark state and convergent upper Stark state trajectories for symmetric top molecules passing through a hexapole electric field.

7.2.4 Hexapole Transmission of |JKM⟩ States

To find the explicit equation of motion for upper Stark states in a molecular beam traversing the hexapole, the constants A and B in equation 7.33 must be determined from the initial conditions. At $t = 0$ the maximum displacement $r(0)$ from the field axis is given by the maximum divergence α of the collimated molecular beam.

The maximum initial displacement is $l_1\tan\alpha$ where l_1 is the distance from the beam source to the hexapole. At $t = 0$ equation 7.33 reduces to $r(0) = A = l_1\tan\alpha$. Because α is very small $\tan\alpha \approx \alpha$, therefore $A = l_1\alpha$. The maximum radial velocity at $t = 0$ for a molecule with velocity v is $v\sin\alpha$. Differentiating equation 7.33 gives $dr(0)/dt = B\omega = v\sin\alpha$, and since $\sin\alpha \approx \alpha$, $B = v\alpha/\omega$. Hence the equation of motion becomes

$$r(t) = l_1\alpha\cos(\omega t) + \frac{v\alpha}{\omega}\sin(\omega t). \tag{7.34}$$

For an upper Stark state molecule to be successfully transmitted by the hexapole [Brooks, 1969] three conditions must be met:

- The molecule must enter the field
- The axial displacement of the molecule must always be less than the inscribed radius of the hexapole
- The molecule must be able to exit the hexapole.

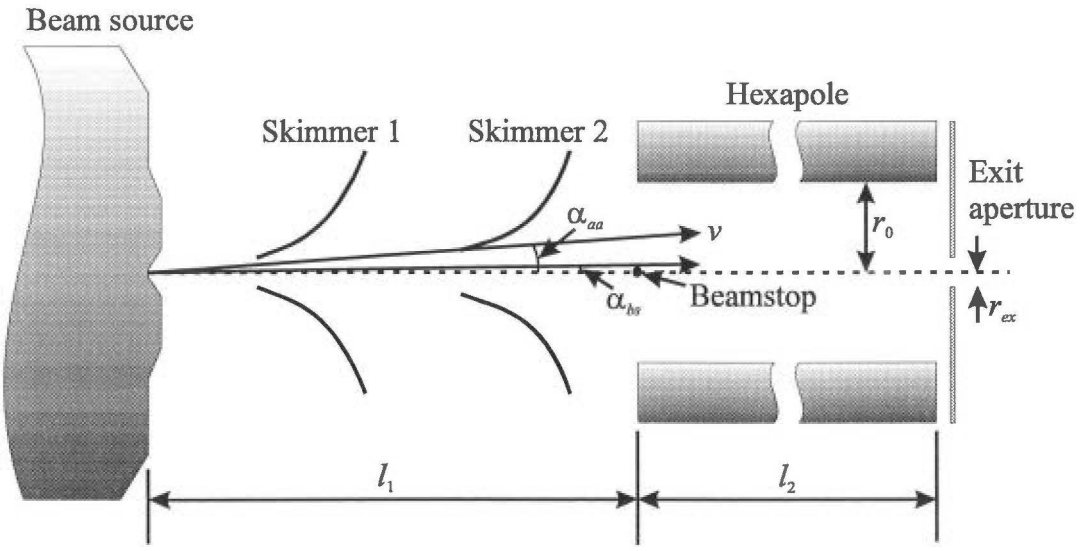

Fig. 7.7. The defining conditions for successful transmission through the hexapole.

The defining conditions which must be met for successful transmission of an upper Stark state through the hexapole are shown in Fig. 7.7. For a molecular beam aligned axially with the hexapole, the divergence α_{in} of a molecular trajectory from the

beam axis must be less than the acceptance angle α_{aa} defined by the skimmer used to collimate the beam if the molecule is to successfully enter the hexapole. If a beam stop is used to prevent non-focusable rotational states from exiting the hexapole, the divergence of the incoming molecules must be greater than the minimum angle α_{bs} defined by the beamstop. Hence the condition for a molecule to enter the hexapole is

$$\alpha_{bs} < \alpha_{in} < \alpha_{aa} \ . \tag{7.35}$$

The maximum axial displacement $r(t)$ of a molecule traversing the hexapole must always be less than the inscribed radius r_0 of the hexapole for the molecule to be transmitted by the rods. At the point of maximum displacement of a trajectory from the axis the radial velocity will be zero, that is

$$\frac{dr(t)}{dt} = -\omega l_1 \alpha \sin(\omega t) + v\alpha \cos(\omega t) = 0$$

$$\frac{v}{\omega l_1} = \frac{\sin(\omega t)}{\cos(\omega t)} = \tan(\omega t)$$

$$\omega t = \tan^{-1}\left(\frac{v}{\omega l_1}\right). \tag{7.36}$$

Hence for $r(t) = r_0$

$$r_0 = l_1 \alpha \cos\left(\tan^{-1}\left(\frac{v}{\omega l_1}\right)\right) + \frac{v\alpha}{\omega} \sin\left(\tan^{-1}\left(\frac{v}{\omega l_1}\right)\right)$$

$$r_0 = l_1 \alpha \frac{\omega l_1}{\left(v^2 + \omega^2 l_1^2\right)^{1/2}} + \frac{v\alpha}{\omega} \frac{v}{\left(v^2 + \omega^2 l_1^2\right)^{1/2}}$$

$$r_0 = \frac{v\alpha}{\omega}\left(1 + \frac{\omega^2 l_1^2}{v^2}\right)^{1/2}$$

$$r_0 = \frac{v\alpha}{\omega}\left(1 + \beta_1^2\right)^{1/2} \tag{7.37}$$

where $\beta_1 = \omega l_1/v$. Since the maximum displacement must be less than r_0 the maximum angle of incidence α_{tr} for which an incoming molecule will be transmitted by the hexapole rods will be

$$\alpha_{tr} = \frac{r_0\omega}{v}\frac{1}{\left(1+\beta_1^2\right)^{1/2}}. \tag{7.38}$$

To be successfully transmitted through the hexapole exit aperture the axial displacement $r(t)$ of the molecule at the end of the hexapole must be less than the radius of the exit aperture r_{ex}. Since the molecule will exit the hexapole at a time $t_{ex} = l_2/v$, the displacement $r(t_{ex}) = r_{ex}$ is given by

$$r_{ex} = l_1\alpha\cos\left(\frac{\omega l_2}{v}\right) + \frac{v\alpha}{\omega}\sin\left(\frac{\omega l_2}{v}\right)$$

$$r_{ex} = l_1\alpha\cos\beta_2 + \frac{l_1\alpha}{\beta_1}\sin\beta_2 \tag{7.39}$$

where $\beta_2 = \omega l_2/v$. Hence the maximum angle of incidence α_{ex} which will allow an incoming molecule to pass through the hexapole exit aperture is

$$\alpha_{ex} = \frac{r_{ex}\omega}{v}\frac{1}{\beta_1\cos\beta_2 + \sin\beta_2}. \tag{7.40}$$

Therefore, the maximum angle of incidence α_{mx} for a molecule entering the hexapole if it is to be transmitted through the field and exit aperture, will be the smaller of the limiting angles α_{tr} and α_{ex}. The fraction of the beam impinging on the hexapole that will be transmitted at a particular hexapole rod voltage U_0, orientation ρ (= MK/J(J + 1)) and velocity v, is

$$A(U_0, v, \rho) = \frac{\alpha_{mx}^2}{\alpha_{in}^2} \tag{7.41}$$

where it is assumed there is no beamstop so that the minimum angle for transmission is zero. The transmitted intensity $F_{JKM}(U_0)$ for a $|JKM\rangle$ state at a particular voltage U_0, can

then be found by integrating $A(U_0, v, \rho)$ over the velocity distribution of the beam $f_b(v)$ given in equation 7.8 and multiplying by the partition function q_{JK}

$$F_{JKM}(U_0) = q_{JK}\int_0^\infty A(U_0, v, \rho) f_b(v)dv. \tag{7.42}$$

The partition function q_{JK} [Townes, 1955] for a rotational quantum state $|JK\rangle$ in electric field free conditions is given by

$$q_{JK} = \frac{S(I, K)(2J + 1)e^{-W_0/kT_r}}{\sum_{J=0}^{\infty}\sum_{K=-J}^{J} S(I, K)(2J + 1)e^{-W_0/kT_r}} \tag{7.43}$$

where T_r is the rotational temperature of the molecular beam and the factor 2J + 1 is the statistical weight due to the degenerate M states. The statistical weight function S(I, K) takes into account the degeneracy of K levels caused by the nuclear spin I. For a symmetric top molecule the statistical weights are:

- $S(I, K) = 2(4I^2 + 4I + 3)$ for K a multiple of 3 and $K \neq 0$
- $S(I, K) = 4I^2 + 4I + 3$ for $K = 0$
- $S(I, K) = 2(4I^2 + 4I + 3)$ for K not a multiple of 3.

The total transmitted beam intensity $T(U_0)$ at a particular hexapole voltage is then the sum of the intensities $F_{JKM}(U_0)$ for each $|JKM\rangle$ state

$$T(U_0) = \sum_{JKM} F_{JKM}(U_0). \tag{7.44}$$

A comparison between an experimental hexapole focusing curve and a theoretical curve calculated using equation 7.44 for the experimental conditions, is shown in Fig. 7.8.

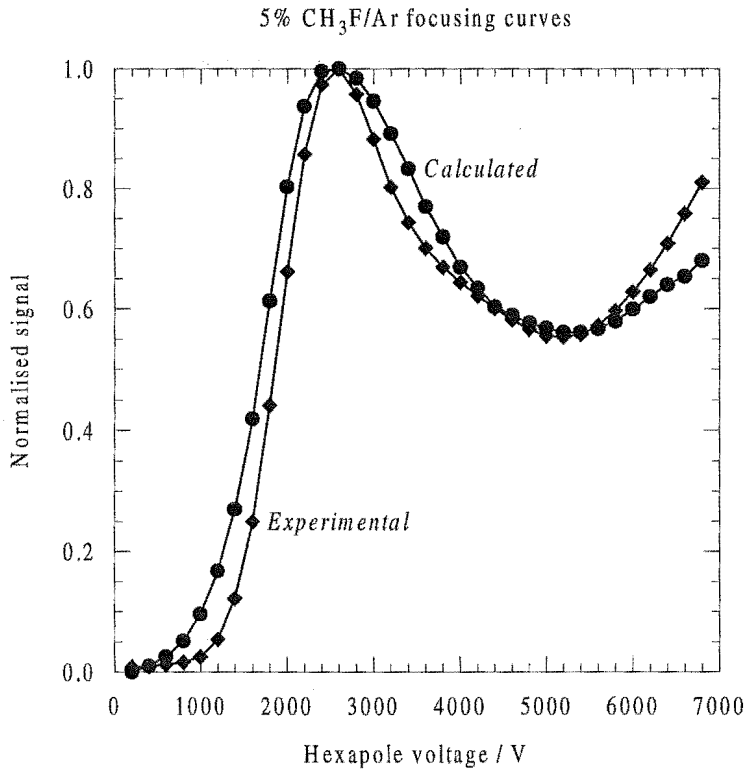

Fig. 7.8. Comparison between calculated and experimental focusing curves.

7.3 Collision Cross Sections

Molecular beams are ideally suited to the study of scattering processes as the single collision conditions that exist in the interaction region ensure the measurement of the collision cross sections are free of multiple collision and relaxation events which can modify the product state distributions. Collisions between molecular and atomic species can lead to reactive and non reactive outcomes. Where there is no reactive modification of the reactants there can be elastic or inelastic energy transfer in the collision. For elastic collisions only the translational energy distributions of the collision partners are changed, whereas there is energy transfer between internal modes such as vibration and rotation for inelastic collision events.

Scattering experiments fall into two areas; those where the differential cross section is measured and those where the integral cross section is determined. The differential cross section $d\sigma/d\omega$ is defined as the number of molecules dN scattered into the solid angle $d\omega$ per unit time dt divided by the incident beam intensity I_0 [Scoles, 1988],

$$\frac{d\sigma}{d\omega} = \frac{dN}{d\omega dt}\frac{1}{I_0} \tag{7.45}$$

and is related to the integral cross section σ by integration over the complete solid angle

$$\sigma = \int \frac{d\sigma}{d\omega} d\omega. \tag{7.46}$$

The integral cross section is determined from the attenuation of a molecular beam by a background scattering gas. For a beam intensity I_0 incident on a scattering region of length L pressurised to a particle density n, the ratio of the attenuated beam intensity I to the incident beam is

$$\ln\frac{I}{I_0} = -nL\sigma \tag{7.47}$$

where σ is the total cross section for scattering out of the beam. In the ideal experiment the cross section is determined from

$$\sigma = \frac{-1}{nL}\ln\frac{I}{I_o} \tag{7.48}$$

but in a real experiment several departures from ideality must be accounted for. The major factors being:

- The velocity distributions of the beam and target molecules
- n not constant over the scattering path length L
- The angular resolution of the apparatus.

To account for the above problems equation 7.48 is replaced by

$$\sigma_{eff}(\bar{g}) = \frac{-1}{(nL)_{eff}} \ln \frac{I}{I_o} \tag{7.49}$$

where $(nL)_{eff}$ is the product of the path length L and the density n_{eff} averaged over the entire path length. The cross section $\sigma_{eff}(\bar{g})$ is the experimentally measured cross section averaged over the relative velocity distribution $f_r(g)$, where $g = |\mathbf{v}_b - \mathbf{v}_s|$. $\mathbf{v}_b$ is the velocity of the beam with a distribution $f_b(\mathbf{v}_b)$ and $\mathbf{v}_s$ is the velocity of the scattering gas with a distribution $f_s(\mathbf{v}_s)$. As the beam is highly directional the velocity distribution $f_b(\mathbf{v}_b)$ can be replaced by the speed distribution $f_b(v_b)$. The reference velocity for the cross section is $\bar{g}$ the average relative velocity. The experimental cross section is related to the actual velocity averaged cross section $\sigma(\bar{g})$ by

$$\sigma_{eff}(\bar{g}) = \sigma(\bar{g}) - \Delta\sigma(\bar{g}) \tag{7.50}$$

where $\Delta\sigma(\bar{g})$ is the correction for the finite angular resolution of the experiment. The velocity averaged cross section is found by integration of the integral cross section $\sigma(g)$ over the velocity distributions of the beam and scattering gas according to

$$\sigma(\bar{g}) = \int_{v_b} \int_{\mathbf{v}_s} f_b(v_b) f_s(\mathbf{v}_s) \frac{g}{v_b} \sigma(g) d\mathbf{v}_s dv_b \tag{7.51}$$

and the angular resolution correction is determined from

$$\Delta\sigma(\bar{g}) = \int_{v_b} \int_{\mathbf{v}_s} \int_{\Omega} f_b(v_b) f_s(\mathbf{v}_s) \frac{g}{v_b} \frac{d\sigma}{d\omega}(g, \theta) Y(\Theta) \frac{d\omega}{d\Omega} d\mathbf{v}_s dv_b d\Omega. \tag{7.52}$$

$d\sigma/d\omega(g, \theta)$ is the differential scattering cross section for scattering to the centre of mass angle θ at relative velocity g. $Y(\Theta)$ is the angular resolution function for the laboratory scattering angle Θ, $Y(\Theta)$ will be 1 for $\Theta = 0$ and decreases to 0 for Θ greater than the angular resolution of the apparatus. $d\omega/d\Omega$ is the Jacobian for transformation from the centre of mass solid angle ω to the laboratory solid angle Ω.

To accurately measure a state to state inelastic collision cross section the quantum state of the molecule must be defined before and after the collision. The cross sections measured in this work are due to the attenuation of focused upper Stark state symmetric top molecules in a hexapole electric field. Therefore the initial rotational state of the attenuated molecules is known within the resolution of the hexapole and rotationally inelastic cross sections can be determined for the attenuation of the focused upper Stark states. The spectroscopic selection rules for rotational state transitions of symmetric top molecules [Townes, 1955] are $\Delta J = 0, \pm 1$; $\Delta K = 0$; and $\Delta M = 0, \pm 1$. In the absence of any literature evidence for other selection rules for the rotationally inelastic collisions, the spectroscopic selection rules are assumed to apply. Since only the attenuation of the focused upper Stark states in the hexapole electric field can be measured, the product JKM must be non zero and KM must be negative. Hence the possible transitions allowed by the selection rules leading to defocusing of upper Stark states $|JKM\rangle$ in the hexapole are

- $\Delta J = 0$; $\Delta M = \pm 1$, where $J > 0$ and $|M| < J$
- $\Delta J = \pm 1$; $\Delta M = 0, \pm 1$, where $J > 0$ and $|M| < J$.

The Dirac notation used to describe an upper Stark state, by convention omits the negative sign which should be present for either the K or M quantum number for the product KM to be less than zero as required for an upper Stark state. That is $|JKM\rangle$ is used instead of $|J\text{-}KM\rangle$ or $|JK\text{-}M\rangle$. As an example the $|111\rangle$ state can be attenuated by allowed transitions to form the $|110\rangle$, $|210\rangle$, $|211\rangle$ and $|212\rangle$ states. The first two states are unaffected by the hexapole electric field and will not be focused back to the hexapole exit aperture. The second pair of states are upper Stark states but as their $\cos\theta$ values are 1/6 and 1/3 respectively compared to 1/2 for the $|111\rangle$ state they will focus at different hexapole voltages and will not be transmitted at the peak hexapole voltage for focusing of the $|111\rangle$ state.

The rotational energy levels $W(JKM)$ of a prolate symmetric top in a hexapole field are given by

$$W(\mathrm{JKM}) = BJ(J+1) + (A-B)K^2 - \mu\varepsilon\frac{KM}{J(J+1)} \qquad (7.53)$$

which are shown for selected states for CH_3Cl in Fig. 7.9. The Stark energies are dependent on the hexapole electric field strength which varies from a maximum near the hexapole rods to zero at the axis. The electric field strength at the median displacement from the axis, $r_0/2$, was used to calculate the Stark energies in Fig. 7.9.

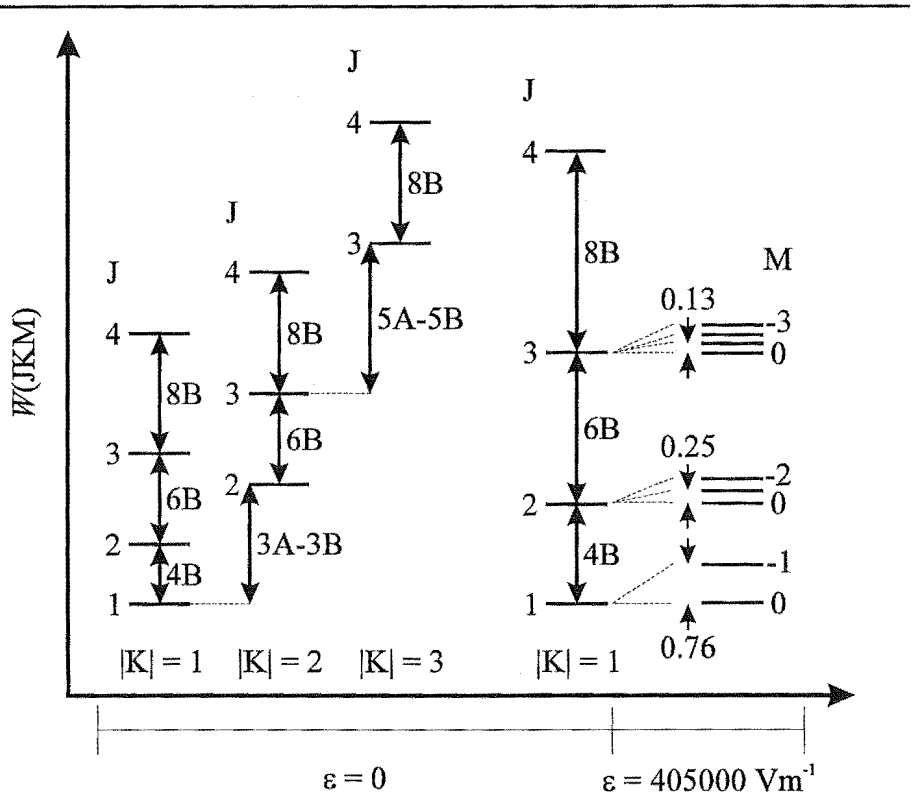

Fig. 7.9. Low lying energy levels of a prolate symmetric top. The upper Stark state energies due to the electric field are shown on the right.

The cross sections for the defocusing collisions involving ΔJ, ΔM or ΔJ ΔM transitions involve the transfer of very small amounts of energy. In terms of the interaction potential governing the collision process, the energy for the rotational transitions would be available from the long range attractive part of the interaction potential. At these intermolecular distances the potential is dominated by the attractive van der Waals interactions $V(r)$ which result from the dynamic polarisation of the electron charge distributions about each of the colliding partners. The strength of the

van der Waals attraction between gas phase molecules [Atkins, 1990] depends on the separation r according to

$$V(r) = -\frac{C}{r^6} \tag{7.54}$$

where C accounts for the various multipole and polarisation attractive interactions. C can be split up into the sum of each contributing van der Waals interaction

$$C = C_{dip-dip} + C_{dip-ind} + C_{disp} \tag{7.55}$$

where $C_{dip\text{-}dip}$ is due to the dipole-dipole interaction, $C_{dip\text{-}ind}$ is due to the dipole-induced dipole interaction, and C_{disp} is due to the induced dipole-induced dipole or dispersive interaction. Higher order multipole terms to account for quadrupole and octopole interactions are omitted as these are inherently shorter range attractive forces.

The dipole-dipole term arises from the orientation averaged interaction of the permanent electric dipoles (μ_1, μ_2) of the colliding molecules and is given by

$$C_{dip-dip} = \frac{2}{3kT_{rot}}\left(\frac{\mu_1\mu_2}{4\pi\varepsilon_0}\right)^2 \tag{7.56}$$

where T_{rot} is the effective rotational temperature of the two molecules with rotational temperatures T_1 and T_2

$$T_{rot} = \frac{2T_1T_2}{T_1 + T_2}. \tag{7.57}$$

The dipole-induced dipole term arises from the induced polarisation of one molecule by the permanent dipole of another. Therefore the dipole and induced dipole will always be aligned so averaging over the mutual orientation of the dipoles is not required, hence the interaction is independent of temperature. The term is given by

$$C_{dip-ind} = \frac{\mu_1^2\alpha_2}{4\pi\varepsilon_0} \tag{7.58}$$

where α_2 is the polarisability of the molecule without the permanent dipole. The final term is due to the instantaneous polarisation of one molecule by a transient dipole on the other. Since the two instantaneous dipoles are correlated the effect does not average to zero and is known as the dispersive or London interaction. The term is given by

$$C_{disp} = \frac{3}{2}\alpha_1\alpha_2\frac{I_1 I_2}{I_1 + I_2} \tag{7.59}$$

where α_1 and α_2 are the polarisabilities and I_1 and I_2 the ionisation potentials for the two molecules.

As an example consider the defocusing $|111\rangle \rightarrow |110\rangle$ and $|111\rangle \rightarrow |211\rangle$ transitions of CH_3Cl for scattering with Ar. The dipole-dipole term in the interaction potential is zero and the sum of the other two terms (equations 7.58 + 7.59) is 12.275 x 10^{-78} Jm^6. For the first transition, $\Delta M = 1$ and the transition energy is 0.76 $Jmol^{-1}$ from Fig. 7.9. Using equation 7.54 with $V(r) = 0.76$ $Jmol^{-1}$, the maximum separation r_{mx} for which the transition can occur is 14.6 Å. Similarly, for the ΔJ transition $V(r) = 20.7$ $Jmol^{-1}$ and the maximum separation is found to be 8.4 Å. Since the cross section σ for the interaction is defined at the largest separation for which the transition can occur then

$$\sigma = \pi r_{mx}^2 . \tag{7.60}$$

This gives cross sections for the above rotationally inelastic collisions of 670 $Å^2$ ($\Delta M = 1$) and 222 $Å^2$ ($\Delta J = 1$). Comparison with experimental cross sections of around 280 $Å^2$ for the CH_3Cl/Ar system suggest that the defocusing of the upper Stark states in the hexapole is dominated by collisions inducing ΔM and ΔJ ΔM changes rather than just ΔJ changes.

Chapter 8

Molecular Beam Machine

The molecular beam apparatus [Aitken, 1995a; Blunt, 1995] used to study the rotationally inelastic collision cross sections of symmetric top alkyl halide molecules is described here. The major components of the experiment to be discussed are:

- Vacuum system
- Gas handling
- Supersonic beam source
- Collimation
- Hexapole
- Detection
- Computer Interfacing.

8.1 Vacuum System

The vacuum system comprises a modular series of stainless steel vacuum chambers for the production, hexapole focusing and detection of supersonic molecular beams (Fig. 8.1). The supersonic beam is produced in the nozzle chamber and is differentially pumped by a buffer chamber before entering the two hexapole chambers.

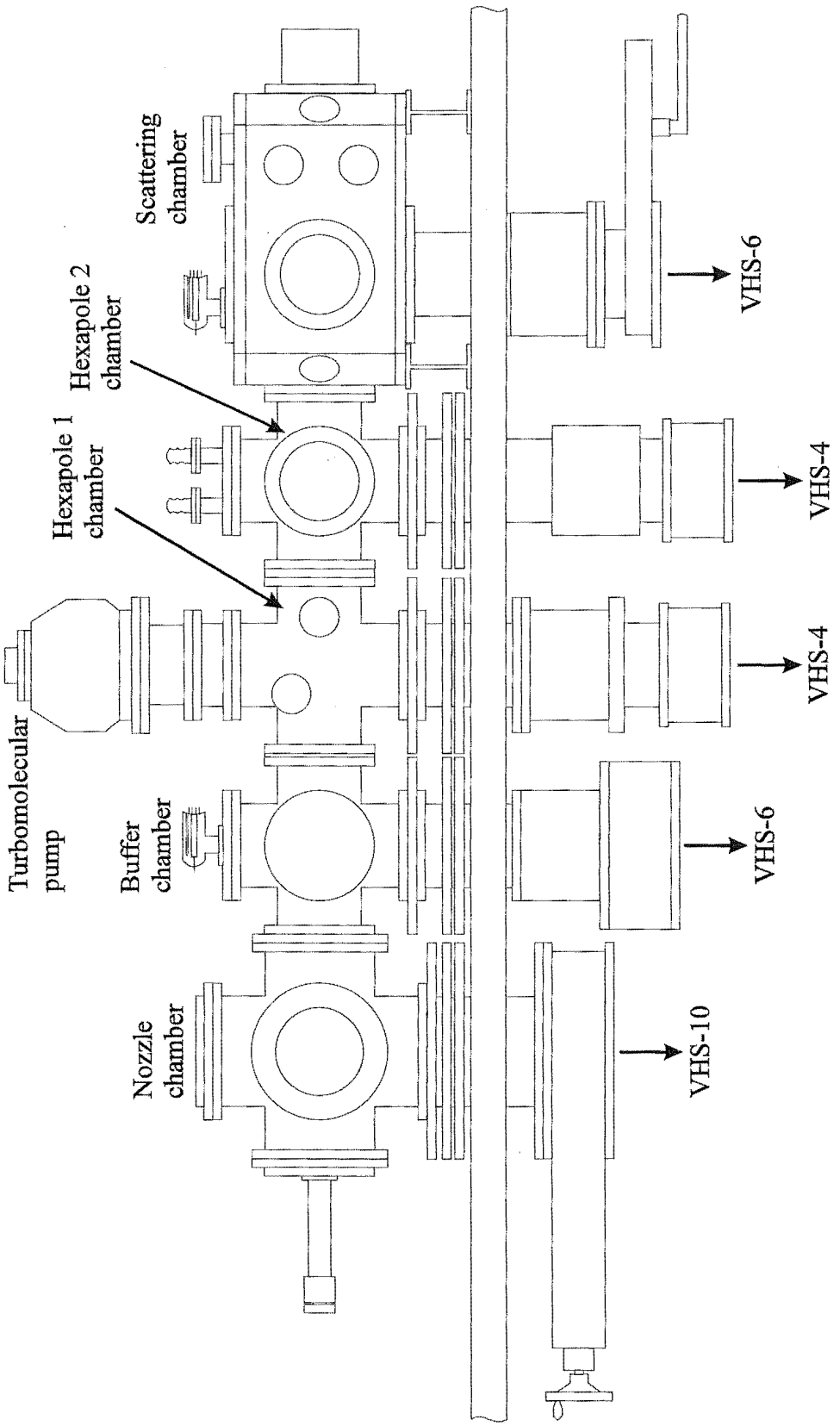

Fig. 8.1. Molecular beam machine, scale 1:12.

The beam is detected in the scattering chamber which has been designed for the study of crossed beam interactions. The nozzle, buffer and hexapole 1 and 2 chambers are each supported by carriage mounts in turn mounted on twin rails designed to allow the easy alignment and modification of the experimental components. All vacuum seals for the system are made with Viton o-rings or conflat knife edge flanges with copper gaskets.

8.1.1 Nozzle Chamber

The supersonic beam source is housed in a Huntington laboratories 10" OD flange stainless steel 6 way cross. The beam source support flange is mounted to the axial chamber flange and is sealed with a Viton o-ring for ease of removal. On the top flange of the cross a 10" OD to 8" OD adapter flange is used to mount a liquid nitrogen trap for cryogenic pumping of the chamber. Attached to the trap is a copper baffle which drops down below the beam source to prevent diffusion pump backstreaming. Another 10" to 8" adapter flange is used to connect the nozzle chamber to the smaller 8" buffer chamber. The adapter also serves as a mounting point for the alignment rods which are used to align the source, skimmers and hexapole. Attached to the bottom flange is a spacing spool that is used to mount a large 10" gate valve. The gate valve seals the chamber from a 7020 Ls^{-1} Varian VHS-10 oil diffusion pump which is capable of pumping the large gas load resultant from the supersonic source operation. The diffusion pump is backed by a 1080 $Lmin^{-1}$ Alcatel 2063C mechanical pump which is connected to the diffusion pump with $1^{7}/_{8}$" stainless steel flexible tubing through an Airco Temescal 3" Fig 5121 gate valve which isolates the diffusion pump from the mechanical pump. A $1^{3}/_{8}$" flexible stainless steel line is connected to the nozzle chamber by a Huntington Laboratories ES-150 high vacuum bellows valve which allows the diffusion pump to be bypassed for rough pumping of the vacuum chambers. The chamber pressure is monitored with a Bayard-Alpert type twin filament ion gauge mounted on a side flange. Typical pressure in the chamber during the operation of the pulsed supersonic beam source is 10^{-4}-10^{-5} torr.

8.1.2 Buffer Chamber

The buffer chamber is used to differentially pump the high pressure nozzle region to prevent pressure increases in the hexapole and scattering chambers. The chamber is a 6 way 8" OD cross (Huntington laboratories). A 6" OD stainless steel plate mounted on the alignment rods in the front arm of the chamber effectively seals the buffer chamber off from the nozzle chamber. A conical skimmer with a central hole of 1 mm diameter is mounted on a top hat in the centre of the plate and serves to allow the formation of the supersonic molecular beam. Another plate, this time with a skimmer of 1.5 mm diameter hole mounted to it is used in the same way to prevent gas flow between the buffer and hexapole 1 chamber. On the top 8" flange in the chamber an ion gauge is mounted to monitor the pressure which is typically 10^{-6} torr during beam operation. Also on the top flange is a micrometer feedthrough which is attached via a flexible spring to a beamstop which can be used to cut out the central core of the molecular beam. A baffled liquid nitrogen trap is mounted in the lower arm of the chamber leading to the pumping system. The isolation gate valve (NRC 77871) seals off a 3000 Ls^{-1} Varian VHS-6 diffusion pump which is backed by a 700 $Lmin^{-1}$ Edwards E2M40 mechanical pump. A Varian 951-5091 bellows valve seals the diffusion pump from the mechanical pump.

8.1.3 Hexapole Chambers

Because of its length the hexapole is housed in two chambers, a Varian 8" OD 4 way cross and a Huntington laboratories 8" OD 6 way cross. The pressure in the chambers is monitored by an ion gauge mounted on a $2^3/_4$" flange in the side of the 4 way cross. Without quencher gas present in the hexapole region background pressures of 10^{-8} torr are attained. For the scattering experiments gas is admitted to the hexapole chambers via a Leybold Heraeus 283-41 DN 10 KF variable leak valve. The valve is mounted on a $2^3/_4$" flange on the side of the 4 way cross. An 8" interface flange between the buffer chamber and the first hexapole chamber (4 way cross) holds the alignment

rods and supports the front end of the hexapole. A pneumatically operated Alcatel CF 150 gate valve is mounted on the top flange of the 4 way cross and leads to a 540 Ls^{-1} Alcatel 5900CP turbomolecular pump. The turbo is backed by a 373 $Lmin^{-1}$ Alcatel 2020A mechanical pump which is connected to the turbo pump by a long $1^3/_8$" flexible stainless steel tube through a MKS 160 high vacuum valve. The turbo is used to pump the system overnight and retains a vacuum of 10^{-5}-10^{-6} torr. The second hexapole chamber (6 way cross) is connected to the first through an 8" interface flange on which is mounted a half round liquid nitrogen trap. A further liquid nitrogen trap is mounted in the top hat attached to one of the side arms of the 6 way cross and two more baffled traps lie above the pumping system for the chambers. On the other side arm a 8" to $2^3/_4$" adapter flange is connected to a $2^3/_4$" flange which in turn is connected to a 690 absolute MKS baratron via flexible $^1/_4$" stainless steel tubing. The baratron is used to record the operating pressure down to 1 x 10^{-6} torr in the scattering experiments. The baratron can be sealed off from the hexapole chamber with a brass Nupro HK $^1/_4$" bellows valve. Two Huntington laboratories ceramic high voltage feedthroughs on $2^3/_4$" flanges are mounted on the top flange of the 6 way cross. The feedthroughs are for the hexapole high voltage supplies. The chamber is connected to the scattering chamber by an 8" interface flange to which the back end of the hexapole is mounted. The hexapole chambers are both isolated from 1500 Ls^{-1} Varian VHS-4 diffusion pumps by Airco Temescal 5010 gate valves. The first chamber's diffusion pump is backed by a 345 $Lmin^{-1}$ Alcatel 2021 mechanical pump through a Veeco high vacuum bellows valve. The diffusion pump can be bypassed through a Varian 951-5091 bellows valve attached to the side port on the Airco gate valve. The second diffusion pump is backed by a 75 $Lmin^{-1}$ Alcatel 2004A mechanical pump through a high vacuum valve.

8.1.4 Scattering Chamber

The stainless steel scattering chamber was custom designed as a versatile crossed beam reaction region. The body of the chamber incorporates many 8" and $2^3/_4$" flanges and seals on Viton o-rings against a base and lid. The lid can be removed with a hoist for easy access to the chamber interior. The base and lid contain numerous $2^3/_4$", 4" and

10" flanges. For the current experiment an Extranuclear 4-270-9 quadrupole mass spectrometer is mounted axially on an 8" flange for beam detection. A further mass spectrometer, a Vacuum Generators SXP300, is also mounted in the chamber but is used solely to operate an electron impact ion source mounted on the Extranuclear quadrupole. A Bayard-Alpert type ion gauge mounted on the chamber lid monitors the chamber vacuum. Typical operating pressures are 10^{-7}-10^{-8} torr. A 1000 torr head MKS 221B differential baratron is mounted in the chamber to monitor the pressure when venting the vacuum system. Further flanges are blanked or contain electrical feedthroughs for connection to various components in the chamber. The chamber is pumped through a Vacuum Research Manufacturing Company gate valve attached to a spool on the chamber base with a Varian VHS-6 diffusion pump. A baffled liquid trap to prevent backstreaming is mounted in the spool and another liquid nitrogen trap is mounted in the chamber lid to improve the vacuum in the detector region. The diffusion pump is backed by a 726 $Lmin^{-1}$ Varian SD700 mechanical pump and is isolated from the mechanical pump with a high vacuum valve. The chamber can be rough pumped through a Huntington laboratories EV-150 bellows valve.

8.1.5 Extension Detector Chamber

For experiments using a hexapole extended through the scattering chamber, a further chamber was added to the system to house the beam detector. The custom made stainless steel vacuum chamber was designed in a similar manner to the scattering chamber. In this case the chamber base is fixed but the lid is sealed to the body with a Viton o-ring as with the scattering chamber. For this purpose the chamber is mounted sideways so the bottom spool could be attached to the scattering chamber. A Huntington laboratories PM-600 xyz translator mounted axially in the lid is used to position a nude channeltron electron multiplier for the detection of the beam. A linear motion feedthrough on an 8" flange is mounted in the side of the chamber as an adjustment for the hexapole exit aperture. The pressure in the chamber is monitored with an ion gauge and typically is 10^{-7} torr during experiments. The chamber is pumped through a pneumatic Alcatel CF-150 gate valve by the 5900CP Alcatel turbomolecular

pump taken from the hexapole 1 chamber and replaced with a 300 Ls^{-1} 5400 Alcatel turbomolecular pump. The turbo is backed by a 373 $Lmin^{-1}$ Alcatel 2020A mechanical pump also taken from the hexapole 1 chamber and replaced with a 342 $Lmin^{-1}$ Edwards EDM20 mechanical pump.

8.1.6 Protection System

The vacuum protection system is designed to protect the diffusion pumps and sensitive electronics from damage in case of vacuum failure. The protection is triggered by any one of three events:

- Cooling water failure
- Foreline pressure increase
- Loss of high vacuum.

All diffusion pump temperatures are monitored by sensors attached to the sides of the pumps. If the cooling water to the diffusion pumps fails, the rise in temperature of any of the diffusion pumps above the preset maximum will cause all diffusion pumps to shut down. Once the temperature has dropped and the problem rectified the pumps may be restarted manually. 531 Thermocouple gauges are used to monitor all diffusion pump foreline pressures using MKS 286 control and readout units connected to the protection system. In the event of any pressure trip points being exceeded on the MKS controllers, the appropriate diffusion pump is shut down. When the foreline pressure has dropped the diffusion pump will automatically switch back on. The pressure is monitored in the vacuum chambers by Bayard-Alpert type ion gauges connected to MKS 290 controllers. The output from one of the controllers is taken to the protection unit. In the event of a vacuum failure the 290 controller set points will be exceeded and power will be cut to the electronics attached to the protection unit. Usually the hexapole power supplies and mass spectrometer are protected in this fashion. Once the vacuum has been re-established, power will automatically be restored to the protected electronics.

8.2 Gas Handling

A schematic of the gas handling system is shown is Fig. 8.2. The gas lines are $^1/_4$" stainless steel and copper tubing. All connections are made with Swagelok fittings and brass Nupro JN valves are used throughout. Custom made stainless steel gas reservoirs were made to hold the various gas mixtures prepared for the experiments. For the upper Stark state cross section experiments one half of the gas line system is used to pressurise the hexapole chamber with the scattering gas via a Leybold Heraeus variable leak valve. A long flexible $^1/_4$" stainless steel tube ensures stress free connection to the various gas cylinders used. The pressure is monitored by a 130 psi dial gauge. The other half of the line is used to supply the supersonic molecular beam source. The pressure is monitored with a 5000 torr MKS 122 baratron reading out on an MKS PDR-C controller. The two halves of the gas line can be pumped independently with a 100 $Lmin^{-1}$ Edwards Speedivac ES-100 mechanical pump.

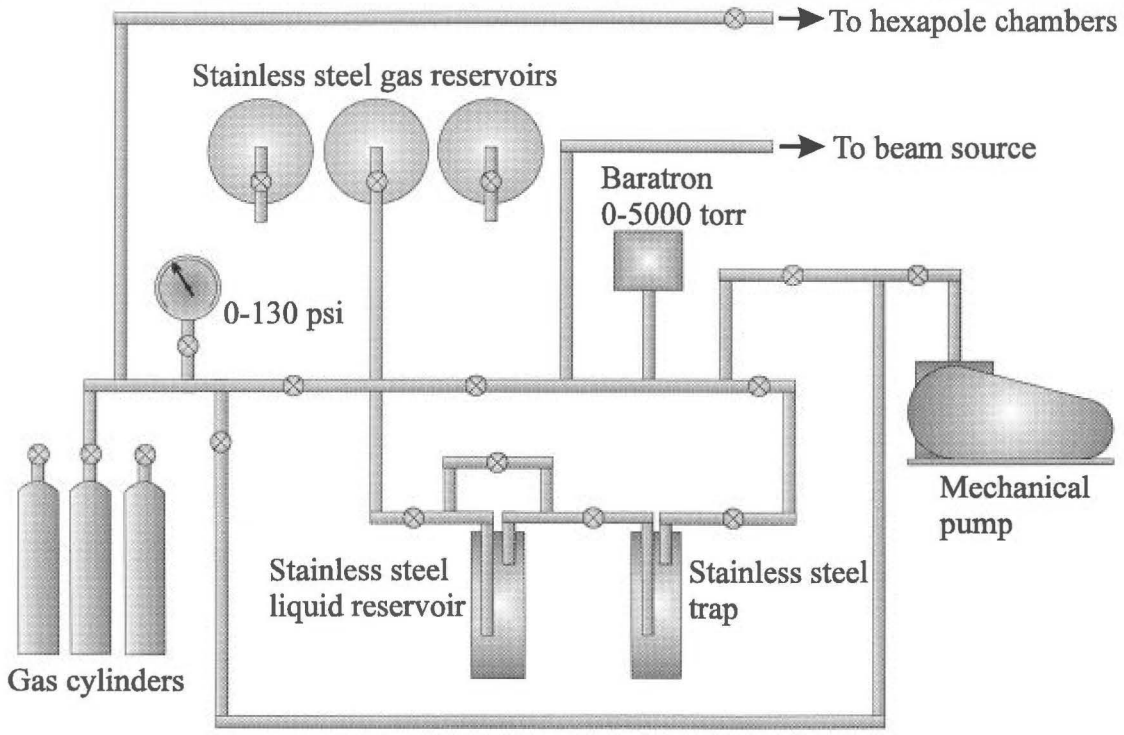

Fig. 8.2. The gas handling system.

Two further $^1/_4$" copper tubing gas lines, independent of the sample lines are connected to nitrogen cylinders. One line is used to pressurise the pneumatic gate valves used with the turbomolecular pumps. The other is used to vent the system through a Nupro HK $^1/_4$" bellows valve in the nozzle chamber and to supply the necessary gas purge to the Alcatel 5400 turbomolecular pump when it is used.

8.3 Supersonic Beam Source

Over the course of the experiments the original General Valve Corporation 9-181 solenoid valve was replaced with a P-286.20 piezoelectric valve. Both will be described here.

8.3.1 Solenoid Valve

A cross section of the solenoid valve is shown in Fig. 8.3. A spring loaded teflon poppet seals against the front plate of the valve in the power off configuration. The 300 μm orifice in the front plate is stepped down to 70 μm or 120 μm with drilled molybdenum discs clamped over the 300 μm aperture. The two piece body and front plates of the valve are made from stainless steel and at the rear a $^1/_4$" Swagelok connector is machined in the body for connection to the valve gas supply. The valve is connected to $^1/_4$" flexible stainless steel bellows tubing which in turn is connected to the gas handling system via Swagelok o-ring face sealing connectors in the valve support flange. The solenoid connections to the valve are made through an Amphenol electrical feedthrough. Wires in the vacuum are insulated with fibreglass sheath. The valve is mounted on a carriage that fits over the alignment rods {8.3.3} to allow the beam source to be positioned accurately on axis. The carriage is attached to a Huntington laboratories VF-156 linear motion feedthrough mounted on the 8" support flange which allows the valve nozzle to be positioned to within 2 mm of the first collimating skimmer

(Fig. 8.4). The nozzle-skimmer distance is optimised by adjusting the feedthrough to maximise the supersonic molecular beam intensity which varies as shown in Fig. 8.4. The pulsed waveform necessary for the operation of the valve is supplied by a custom designed beam source driver. The pulse length, height, frequency and delay are controlled by this. The voltage for the valve is supplied by a Goldstar 5P-503 50 V, 3 A power supply. Typical operating conditions for the valve are 2.0 ms open time at 10 Hz frequency.

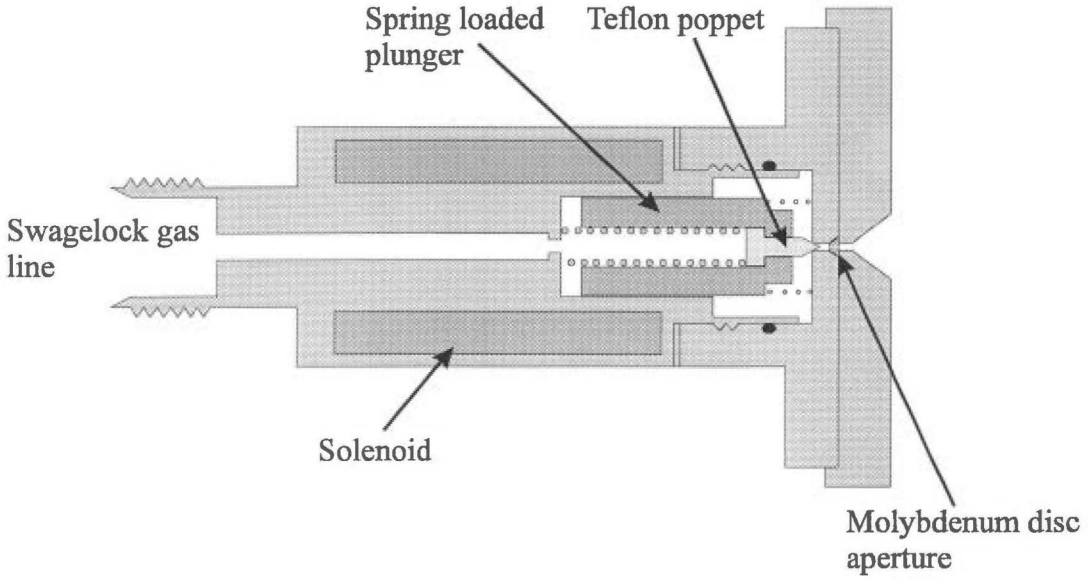

Fig. 8.3. The solenoid valve, scale 2:1.

8.3.2 Piezoelectric Valve

To improve the velocity resolution of the supersonic molecular beam for the scattering experiments without resorting to using velocity selectors which would reduce the beam intensity, the solenoid nozzle was replaced by a piezoelectric valve (constructed at: Physikalisch-Chemisches Institut, der Universität Zürich) shown in Fig. 8.5. The P-286.20 piezoelectric crystal (Physik Instrumente) is mounted in the stainless steel body of the valve and has a plunger mounted in the centre of the piezoelectric disc. The plunger has a Viton o-ring on the tip which seals against the nozzle plate attached to the front of the valve body. The nozzle size is easily adjusted by replacing the front

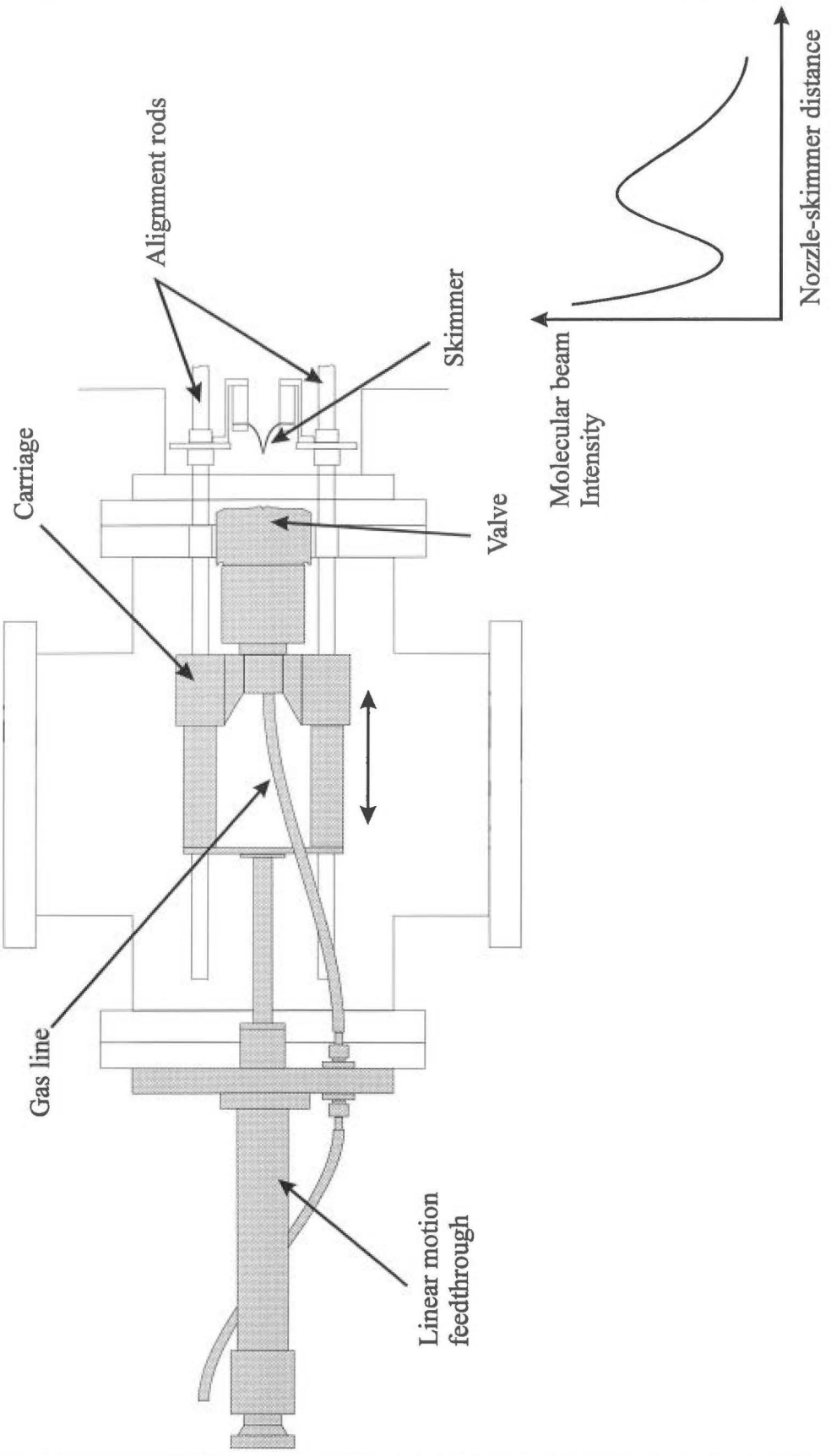

Fig. 8.4. The beam source mounting system, scale 1:5. The graph shows the downstream beam intensity as a function of the nozzle-skimmer distance.

plate with a plate with the desired orifice drilled through it. Adapters were made so the valve could be mounted on the existing carriage support and attached to the Swagelok gas line. The valve is operated by its accompanying electronics and is typically pulsed at 100 Hz with an open time of 0.1 ms.

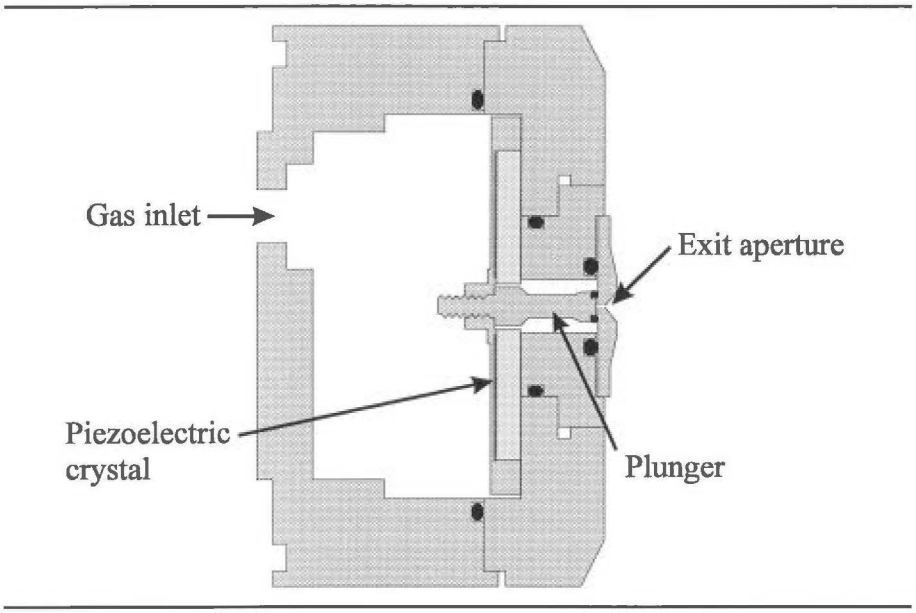

Fig. 8.5. The piezoelectric valve, scale 1:1.

8.4 Beam Collimation

The molecular beam is formed by positioning the supersonic nozzle such that the core of the expansion is sampled by a 1 mm diameter electroformed nickel skimmer. As previously mentioned {8.1.1, 8.1.2} the skimmer is mounted inside a top hat which is attached to the plate mounted on to the alignment rods. A second skimmer of 1.5 mm diameter hole is mounted in a similar manner with the skimmer tip 41 mm from the front end of the hexapole. The skimmers and alignment rods are shown in Fig. 8.6.

For the purposes of alignment of the skimmers, hexapole and detector to the molecular beam axis, the beam source is removed and replaced with an Applied Laser Systems 670 nm 5 mW He-Ne laser mounted on to the alignment rods. The front end of the hexapole is fixed to the beam axis, so by using the laser beam aligned to the front of

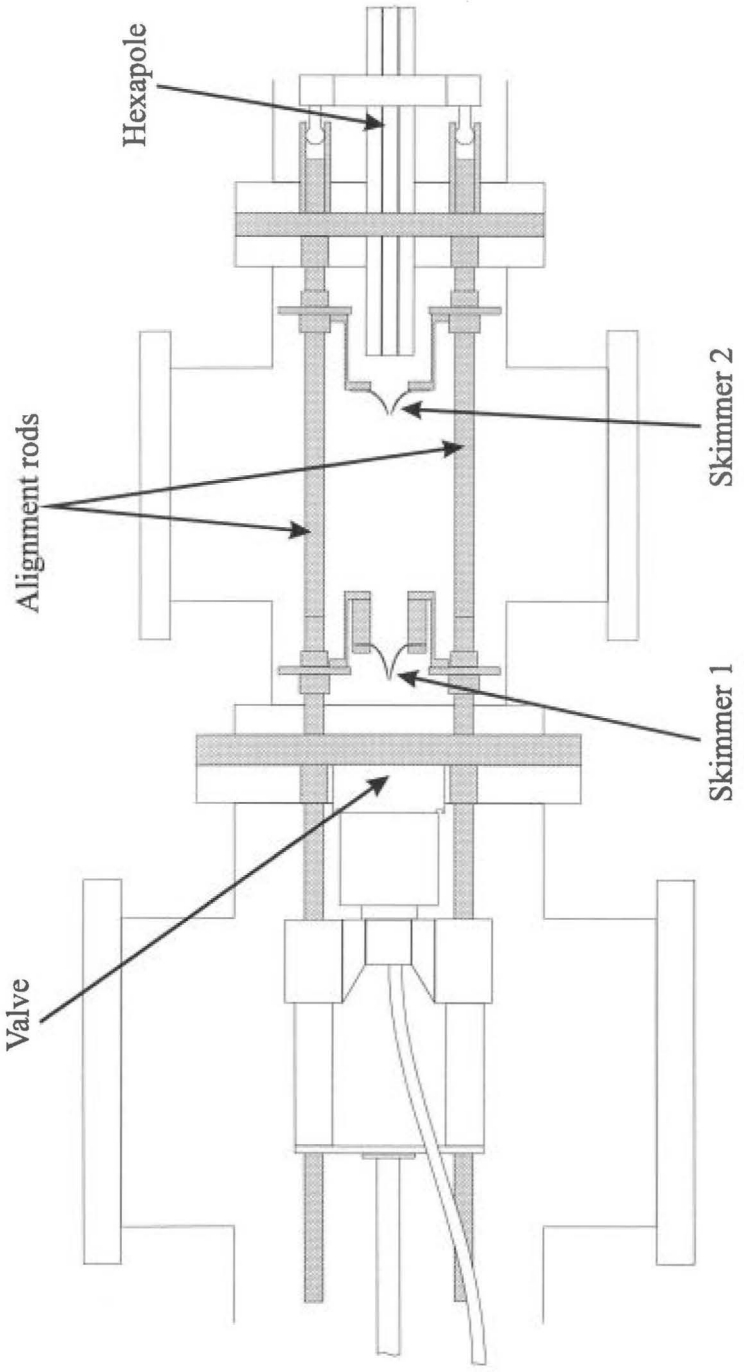

Fig. 8.6. The alignment rods used to mount and ensure correct alignment of the beam source, skimmers and hexapole, scale 1:5.

the hexapole the skimmers, rear end of the hexapole and detector can be moved in their mounts so they lie exactly on the laser beam defined axis.

8.5 Hexapole

The hexapole is constructed of six 10 mm diameter 833 mm long centreless ground stainless steel rods held on an inscribed radius of 5.88 mm by two ceramic mounts (Fig. 8.7). The ceramic mounts are designed with large keyhole slots cut out between the rod attachment points to minimise surface discharging. The alignment rods extend into the hexapole chamber and are terminated by metal sleeves. Ball joints attached to the front hexapole mount are pushed into the sleeves to provide a pivoting support so the back end of the hexapole can be aligned to the beam axis. The rear mount of the aligned hexapole is clamped against an 8" interface flange between the hexapole 2 and scattering chambers. Electrical connections to the rods are made by short copper rods pressed into holes drilled in the hexapole rods. The copper rods of like polarity are linked by copper wire and then to braided copper leads attached to the high voltage ceramic feedthroughs mounted on the top flange of the hexapole 2 chamber. Voltage is supplied to the hexapole rods by two oppositely biased computer controlled Glassman EH high voltage supplies. The supplies are capable of delivering up to ±30 kV at 3 mA but are only used up to ±7.5 kV as above this voltage electrical discharging across the hexapole mounts is a problem. A number of different exit apertures were used for the hexapole. An externally adjustable iris is used which allowed the exit aperture diameter to be set from 1.5-8.0 mm, but the final aperture used is a simple 1 mm diameter hole drilled in stainless steel shim mounted to a top hat pressed into the flange opening to the scattering chamber. An extension was made to the hexapole to allow states which focus above the 7.5 kV limit of the standard hexapole to be accessed at lower voltage. The extension which passes through the scattering chamber measures 594 mm long and is mounted in perspex hexapole mounts. The front of the extension has cuffs welded to the outside of the rods so the extension can be aligned exactly with the end of the standard hexapole. Holes are drilled in the end of the

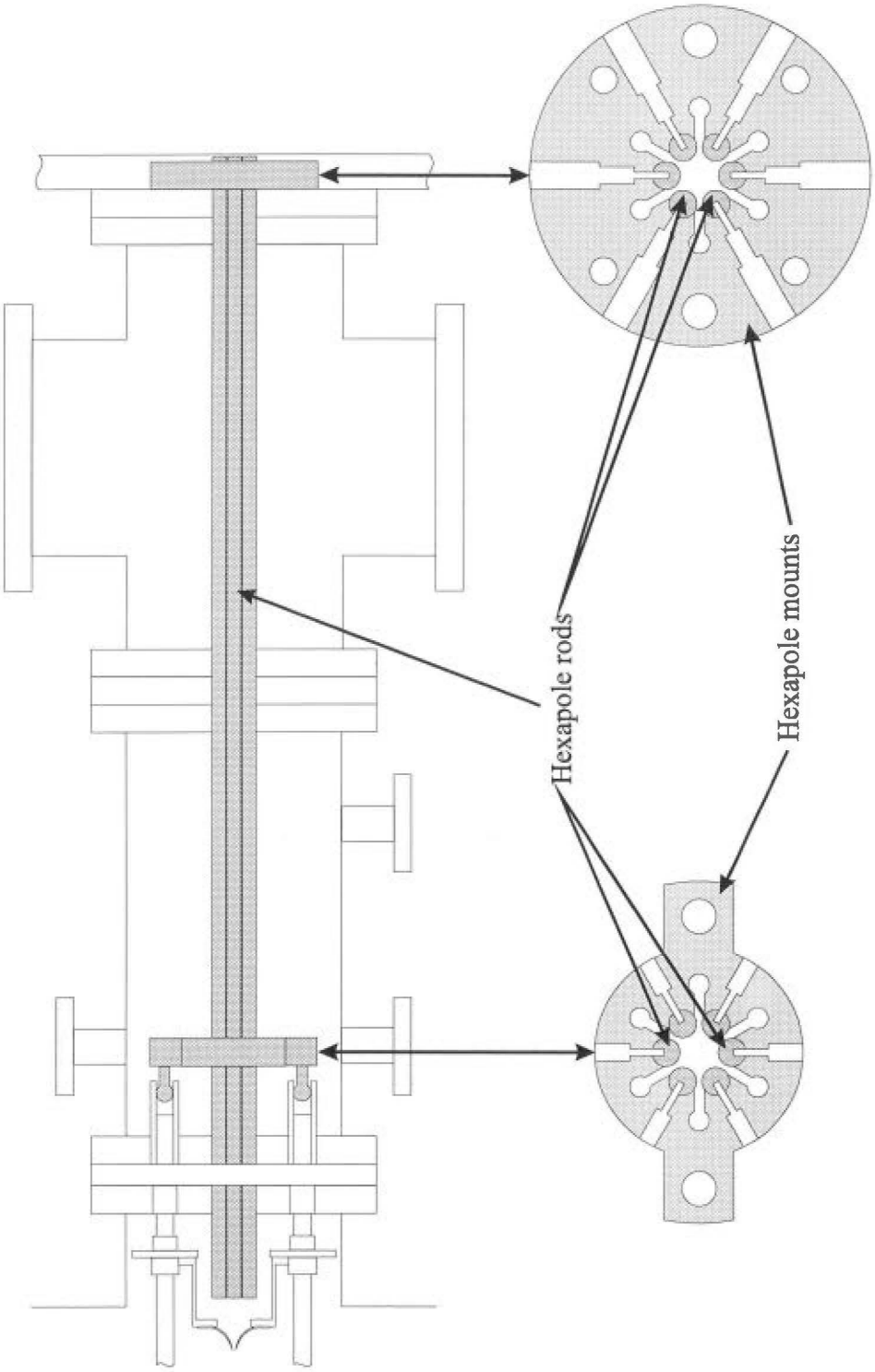

Fig. 8.7. The hexapole, scale 1:5, and ceramic hexapole mounts, scale 1:2.5.

extension rods and springs placed inside the holes ensure a good electrical connection is made to the standard rods. The rear end of the extension is supported by two brackets screwed into the inside of the scattering chamber, which allows the back end of the hexapole extension to be correctly aligned. The exit aperture arrangement is the same as that mentioned for the standard hexapole.

8.6 Detection

Two different detectors have been used, a mass insensitive channeltron electron multiplier and an Extranuclear 4-270-9 quadrupole mass spectrometer. The mass insensitive detector (Fig. 8.8) consists of a Galileo 4816 channeltron electron multiplier mounted on a ceramic block attached to a stainless steel sheet support. The support is attached to the shaft of a Huntington laboratories PM-600 xyz translator which allows the detector to be scanned horizontally and vertically through the molecular beam profile and hence to be accurately positioned on the beam axis. The electron impact ion source from the Vacuum Generators SXP300 mass spectrometer is mounted in front of the CEM to ionise the molecular beam. The ion source leads are sheathed in resin free fibreglass insulation and are attached to the SXP300 ion source electrical feedthroughs so that the ion source can be controlled by the mass spectrometer electronics. The high voltage and signal lines to the CEM are connected to vacuum BNC feedthroughs. The silver wire signal line is insulated with fibreglass, twisted together with an earthed lead and shielded within a braided earthed shield. The high voltage and earth electrical connections to the CEM are made with nickel tabs clamped to the CEM which are connected to copper leads attached to the ceramic mount.

To overcome the lack of mass discrimination with the CEM detector it was replaced with an Extranuclear 4-270-9 quadrupole mass spectrometer. The mass spectrometer has been used previously {2.5} and the only modification here is the addition of the SXP300 ion source to the front of the Einzel lens (Fig. 8.9). The mass spectrometer is mounted in the end of the scattering chamber on an 8" flange such that

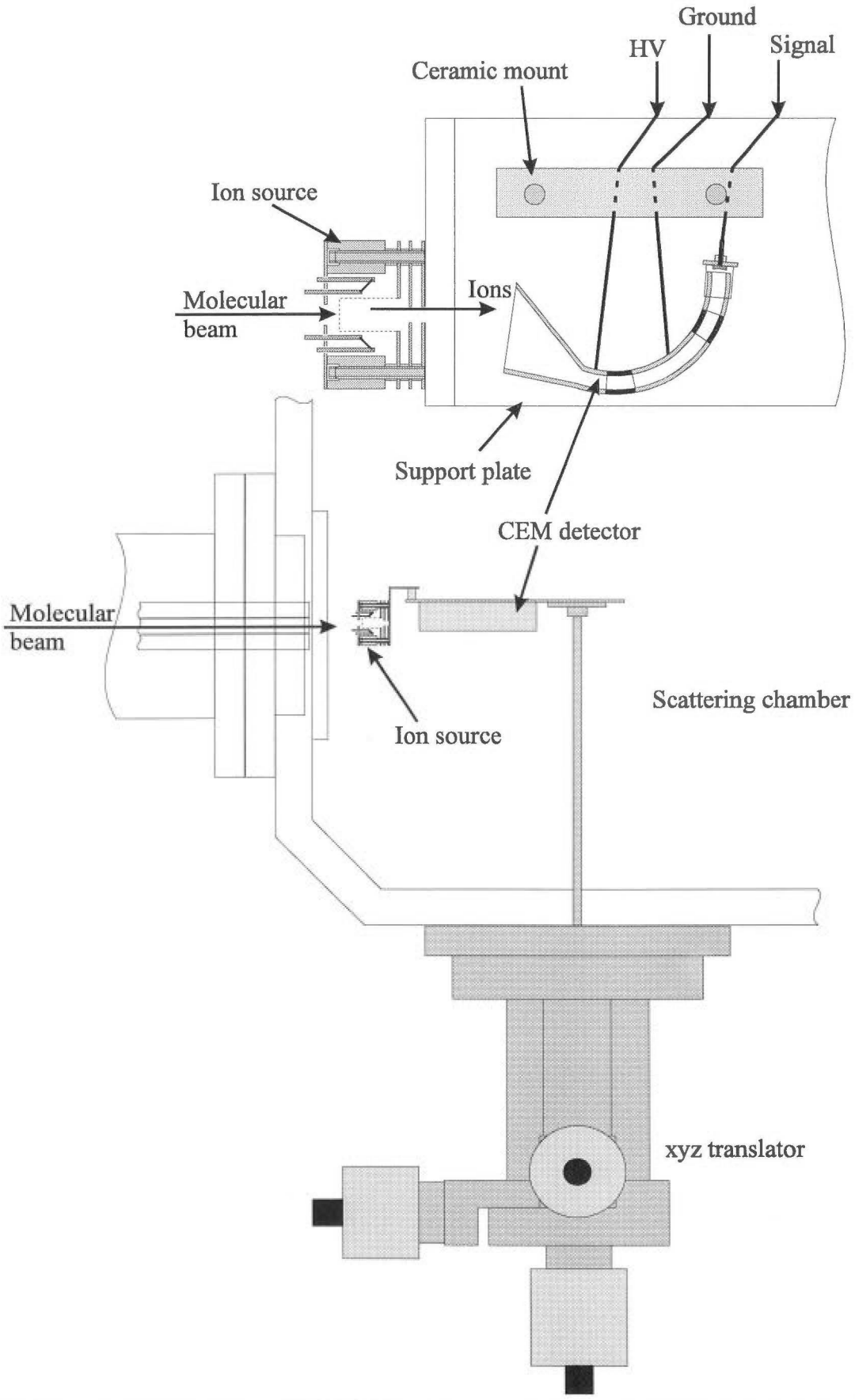

Fig. 8.8. The CEM detector, scale 1:5, with enlarged view, scale 1:1.25.

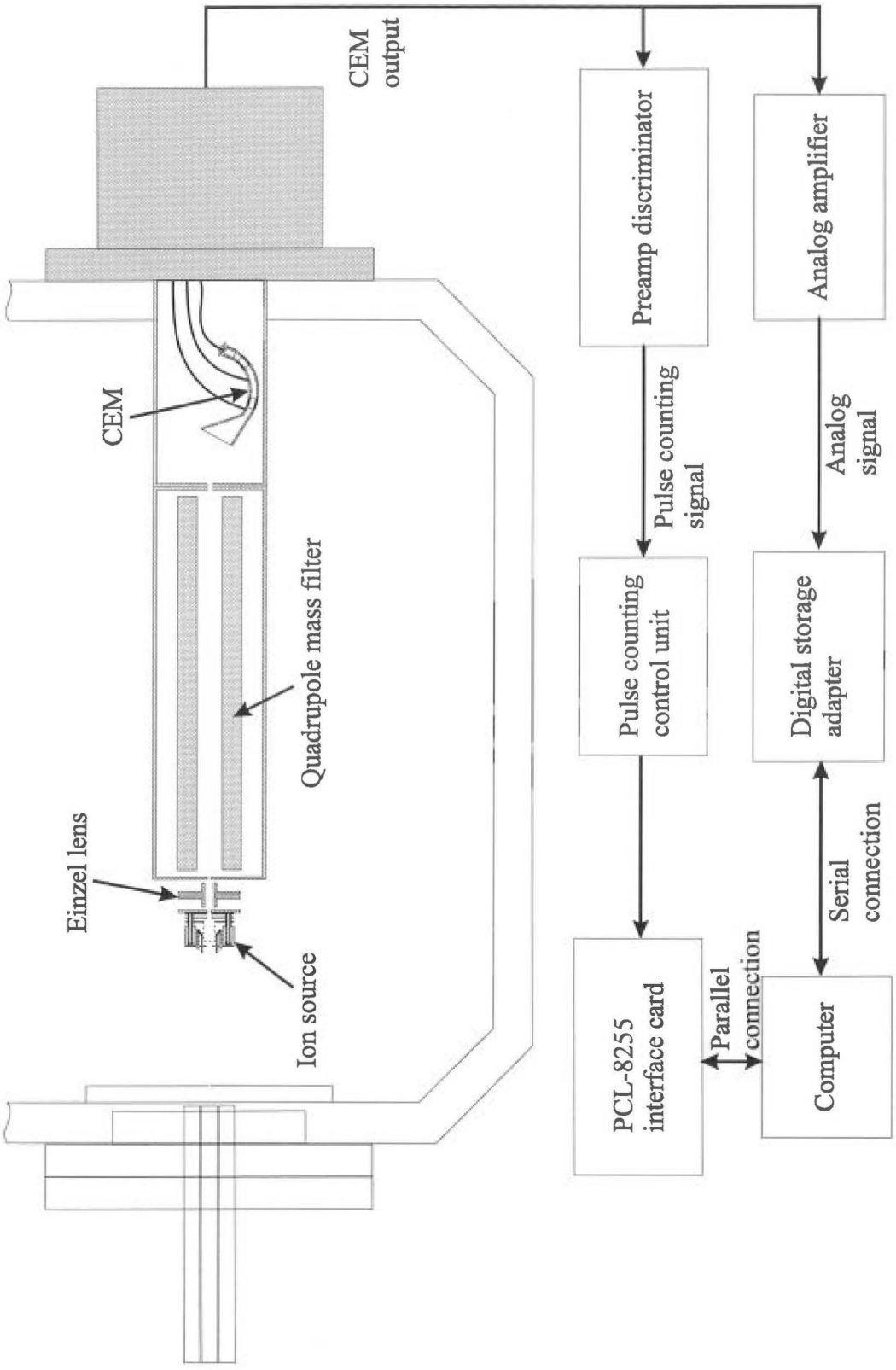

Fig. 8.9. Mass spectrometer, scale 1:4. The signal processing is also shown.

the front face of the ion source lies 108 mm from the end of the hexapole. The adjustable quadrupole housing ensures the mass spectrometer is centred on the molecular beam axis and a threaded support prevents the quadrupole from sagging out of alignment.

For both detectors the pulse counting signal from the CEM is passed through an Extranuclear 032-3 pulse counting preamplifier/discriminator which converts the current pulses from the CEM to 5 V voltage pulses and removes the background electrical noise. Voltage pulses from the preamplifier are passed to a custom built pulse counting control unit and subsequently to a computer via a PCL-8255 lab card for recording and analysis. For analog signal analysis the CEM signal is passed directly to the SXP300 analog amplifier, then to a Thurlby DSA524 digital storage adapter and finally via serial interface to a computer.

8.7 Computer Interfacing

8.7.1 Leak Valve Stepping Motor

The pressure of the scattering gas for the upper Stark state attenuation experiments in the hexapole chambers is controlled by a Leybold Heraeus variable leak valve which is operated by a stepping motor interfaced to a 486 computer. The stepping motor is a Howard industries 1-19-4307 motor and it is connected to a Crystalap STD-206 driver unit. The STD-206 receives pulse and direction signals for the operation of the stepping motor from a PCL-7388 lab card which is controlled by program commands from the computer.

8.7.2 Baratron

The pressure of the scattering gas in the hexapole chambers is monitored by a 690 MKS baratron mounted on the side of the second hexapole chamber. The baratron is connected to a 670A MKS controller which communicates with the computer via an RS-232 serial interface. While most functions of the 670A unit can be controlled from the computer, only the acquisition of averaged pressure signals is of concern here.

8.7.3 Hexapole

The Glassman EH high voltage hexapole power supplies are operated by a 0-10 V signal from a single 12 bit digital to analog converter. The DAC is interfaced to the computer through a PCL-8255 lab card. The 12 bit DAC allows the hexapole voltage to be set with a resolution of 7 V.

8.7.4 Pulse Counting Signal

The pulsed molecular beam is detected by collecting the pulse counting signal output from the Extranuclear preamplifier/discriminator. To remove the background contribution from the beam signal the pulse counting control unit places two counting gates over the time dependent signal. One gate is positioned in time such that it records the signal when the beam pulse arrives at the detector and the other when the beam is not at the detector. The difference in the two counts is therefore due to the beam only. The pulse counting control unit controls the timing for the experiment. A trigger output from the unit is used to control the beam source pulsed operation and with this trigger as the reference time the counting gates are positioned appropriately. Typically the system is run at 100 Hz with 0.5 ms wide counting gates. The signal voltage pulses are passed to the PCL-8255 lab card where they are counted by three 8253 multi-mode 8 bit

counters. The counters are continually latched by the computer and the results transferred to the computer.

8.7.5 Analog Signal

The raw output from the CEM is passed to the SXP300 analog amplifier where the CEM current pulses are integrated and amplified to an analog voltage output. The signal from the SXP300 is passed to a Thurlby DSA524 which is triggered by the pulse counting control unit. The Thurlby digitises the analog signal and converts it to 1024 8 bit words. Repeated acquisitions are averaged by the Thurlby and transferred by serial interface to the computer.

Chapter 9

Upper Stark State Defocusing Cross Section Results

9.1 Introduction

In this work the rotationally inelastic collisional attenuation of hexapole focused upper Stark state symmetric top molecules has been studied as a function of scattering gas density in the hexapole assembly. A collision between a beam molecule following a focusing upper Stark state trajectory in the hexapole with a background molecule can result in the beam molecule being effectively lost from the transmitted beam intensity. The attenuation of the focused beam has been attributed to rotationally inelastic collisions in which a beam molecule in a focusing upper Stark state $|JKM\rangle$ is converted by a ΔJ and/or ΔM transition to a non-focusing rotational state which will not be transmitted by the hexapole. It is assumed that the spectroscopic selection rules [Townes, 1955] hold for the changes in rotational quantum state of the focused beam molecules bought about by the molecule-molecule(atom) interaction. The magnitude of the defocusing cross sections suggests the collision process is a long range interaction, occurring at intermolecular separations up to 15 Å.

State resolved rotationally inelastic scattering of molecules was first studied by Toennies in the early 1960's [Toennies, 1962; Toennies, 1965: Toennies, 1966]. He used a velocity selected effusive beam of TlF which was rotationally state selected with an electrostatic quadrupole field. The quadrupole field focused a particular TlF rotational state $|JM\rangle$ into a gas filled scattering chamber and a second quadrupole selector placed 1° off axis was used to analyse the state distribution of the scattered TlF. The cross sections measured for the $|20\rangle \rightarrow |30\rangle$ transition ($\Delta J = 1$) ranged from 2 $Å^2$ for collisions with He up to 375 $Å^2$ for collisions with NH_3. The total cross section for loss of the $|20\rangle$ state through all channels (inelastic and elastic) was 152 $Å^2$ for the He collisions up to 2140 $Å^2$ for NH_3. For the collisions involving the inert gas atoms the dominant term in the interaction potential was the quadrupole induction potential, but for the symmetric top NH_3 the dipole-dipole interaction term was dominant and the large cross sections were rationalised by the possibility of dipole locking of the TlF and NH_3 molecules. It should be noted that TlF has a very large dipole moment; 4.23 D and polarisability; 6.7 $Å^3$ and is used in these experiments as it will produce good focusing with the quadrupole field. Because of the large dipole moment and small separation of adjacent J rotational levels in TlF, the energy for the rotational transitions will be available from the quadrupole induction and dipole-dipole terms in the interaction potential at long range, and will therefore lead to large cross sections.

More recently, inelastic cross sections have been measured for CsF in supersonic Xe seeded beams [Borkenhagen, 1976; Borkenhagen, 1979]. Again the CsF is chosen as it has a large dipole moment and will give good focusing in the quadrupole. The scattering chamber of the earlier experiments has been replaced with a crossed beam of the scattering species to reduce the averaging effect of the broad velocity distribution of the gas in the scattering chamber on the cross sections. The gases chosen for the inelastic scattering experiments with the CsF beam included the inert gases, small molecules such as N_2, CO_2, CH_4 and SF_6 as well as symmetric top alkyl halides such as CH_3Cl, CH_3Br, CF_3H, CF_3Cl and CF_3Br. Cross sections for $\Delta M = 1$ and $\Delta J = 1,2$ transitions of CsF are reported. They range in magnitude from 0.5 $Å^2$ for the $|30\rangle \rightarrow |10\rangle$ transition with Kr gas, up to 620 $Å^2$ for the $|20\rangle \rightarrow |30\rangle$ transition with CF_3H.

9.2 Experimental

The cross sections σ for the attenuation of the symmetric top molecular beam in the hexapole filter are calculated using the Beer-Lambert law [Scoles, 1988]

$$\sigma = \frac{-1}{nL} \ln \frac{I}{I_0} \tag{9.1}$$

where L is the length of the scattering region in cm and n is the density of the scattering gas species over this path length in cm^{-3}. I is the measured beam intensity and I_0 is the beam intensity in the absence of any scattering gas

The overall path length of the molecular beam through the hexapole region is defined at the front end by the second beam collimating skimmer and at the back end by the hexapole exit aperture. This distance is 88.4 cm (Fig. 9.1). The path length for the attenuation of the focused upper Stark state beam molecules is therefore taken as 88.4 cm.

The molecular beam is attenuated by admitting scattering gas to the hexapole region using a Leybold Heraeus variable leak valve {8.1.3}. The pressure within the hexapole rods is considered to be the same as the pressure in the surrounding vacuum chambers and is measured with a high accuracy 690 MKS baratron with a 0.1 torr full scale head. To ensure that this is the case the gate valves leading to the diffusion pumps on the two hexapole chambers are partially closed to reduce the throughput to the pumps and hence the pumping speed. With suitable signal averaging the 690 baratron is capable of measuring the chamber pressure with an accuracy of around $\pm 3 \times 10^{-7}$ torr down to 1×10^{-7} torr although the chamber pressure is typically 5×10^{-7} torr with the supersonic beam running in the absence of scattering gas. The pressure of the scattering gas introduced to the hexapole chambers is limited by the need to keep the pressure low enough to prevent electrical discharging between the hexapole rods at high voltage. Scattering gas pressures from 1×10^{-6} torr to 5×10^{-5} torr were found to be satisfactory. The leakage of the scattering gas through the skimmer and exit aperture into the buffer

chamber and scattering chamber respectively will effectively increase the scattering path length. However, the leakage is effusive and falls off rapidly with distance from the aperture. Compared to the long hexapole region, the increase in path length due to this end effect will be negligible.

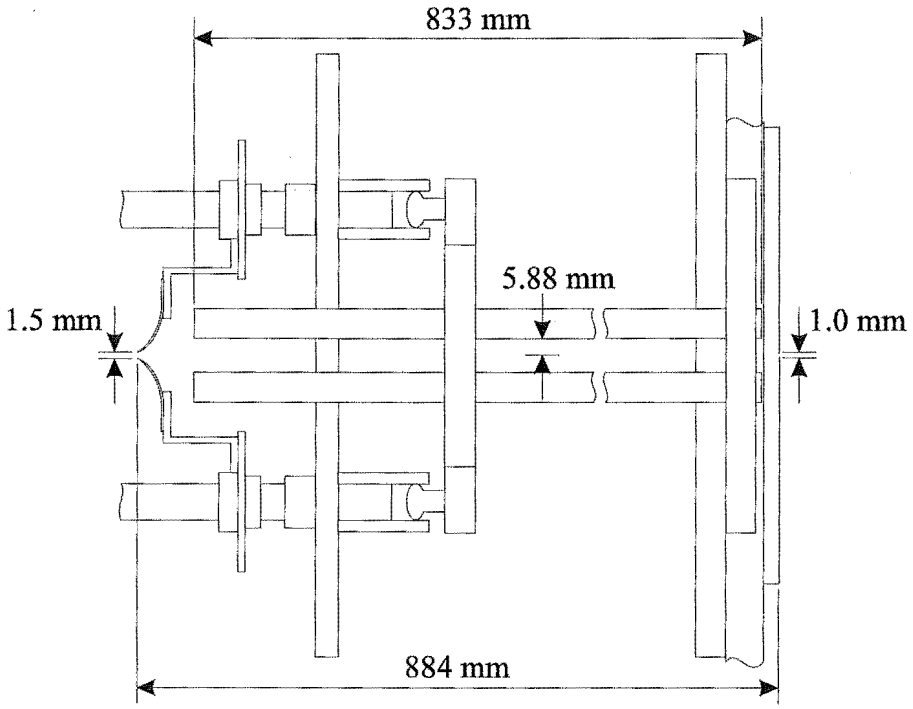

Fig. 9.1. Dimensions of the hexapole assembly.

From equation 9.1 the scattering gas particle density is required to calculate the collision cross sections. The baratron pressure P measured in torr is converted to particle density n using the ideal gas law by

$$n = \frac{N_a}{V_m}\frac{P}{760}\frac{273.15}{T} \tag{9.2}$$

where N_a is the Avogadro constant and V_m is the molar volume at standard temperature and pressure of an ideal gas in cm^3. P and T are the pressure and temperature of the scattering gas in the hexapole chambers. Hence for ambient temperatures around 25°C the particle density is given by

$$n = 3.241 \times 10^{16} P. \tag{9.3}$$

The beam intensity transmitted by the hexapole was originally detected by ionising the beam and pulse counting with a channeltron electron multiplier. The signal to noise with this detection method is poor, typically 1:10, due to the mass insensitivity and low beam intensity compared to the background signal. This introduces large uncertainties in the determination of the beam signal. To improve this the CEM was removed and replaced with a quadrupole mass spectrometer {8.6}. Using the mass selectivity of the quadrupole the background count rate is of the order of the beam signal so the signal to noise is vastly improved.

In order to maximise the beam signal the factors controlling the beam generation and detection must be optimised. The formation of the pulsed supersonic molecular beam depends on the background pressure in the nozzle chamber being low enough to ensure the nozzle expansion is supersonic. Hence the duty cycle of the beam source must be kept low enough so the pumping system can cope with the gas load. Early experiments using the solenoid beam source were run with a nozzle open time of 2.0 ms at 10 Hz and later experiments using the piezoelectric nozzle used an open time of 0.1 ms at 100 Hz. In both situations the beam signal is degraded for longer open times or higher frequency operation.

The intensity of a supersonic beam shows a strong dependence on the distance between the beam source and the skimmer positioned within the supersonic expansion which defines the beam. If the source to skimmer distance is too short the resultant beam will be effusive in behaviour as free molecular flow has not been attained. As the distance increases the beam intensity will decrease and then pass through a maximum before falling away (Fig. 8.4). The position of the maximum is the optimum nozzle-skimmer distance and it is typically 50-100 nozzle diameters from the source nozzle. Further loss of the beam can be minimised by ensuring the system is correctly aligned and background pressure along the beam path is kept low to prevent losses by scattering. Also since beam intensity falls off as the square of the beam path length this should be kept as short as possible.

The beam that successfully reaches the detector is ionised by electron impact, focused with an Einzel lens, mass selected by the quadrupole mass spectrometer and detected by the CEM. Hence the signal is optimised by the ionising, focusing and resolution conditions of the overall detection system. The extent of ionisation and dissociative ionisation of the beam is controlled by varying the energy of the ionising electron current produced in the ion source. The ions produced in the ion source are attracted into the three element Einzel lens by an extraction voltage where they are focused into the entrance aperture of the quadrupole housing. The intensity of the signal transmitted by the quadrupole depends on the required mass resolution. For this application high resolution is not important so the signal to noise can easily be optimised as required. Typical experimental settings for the beam source and detector are given in Table 9.1.

Beam source frequency	$10^{a}/100^{b}$ Hz
Nozzle open time	$2.0^{a}/0.1^{b}$ ms
Mach space ratio	$1{:}50^{a}/1{:}100^{b}$
Nozzle-skimmer distance	30 mm
Electron energy	100 eV
Electron current	0.3 mA
Ion energy	23 eV
Einzel lens 1	-185 V
Einzel lens 2	55 V
Einzel lens 3	-80 V
CEM high voltage	2.2 kV
Beam signal count rates	50-1000 counts s^{-1}

Table 9.1. Typical beam source, ion source, lens and CEM settings. Values labelled [a] refer to the solenoid valve and values labelled [b] refer to the piezoelectric valve.

9.3 Analysis

The experimental determination of the cross sections for defocusing of the upper Stark states amounts to measuring the upper Stark state signal transmitted by the hexapole for various pressures of scattering gas in the hexapole region. If equation 9.3 is substituted into equation 9.1, the result

$$\ln I = -3.241\times10^{16} PL\sigma + \ln I_0 \tag{9.4}$$

shows that a least squares fit to a plot of pressure verses the natural log of the signal will yield a slope -3.241 x $10^{16} L\sigma$, from which the experimental cross section can be found.

To use equation 9.4 to calculate upper Stark state defocusing cross sections the transmitted beam signal due to hexapole focused upper Stark states with scattering gas present at pressure P must be found. This is done by subtracting the signal recorded at zero hexapole voltage, $I_{off,P}$, from the signal recorded with the hexapole on, $I_{on,P}$. The difference

$$I_{uss,P} = I_{on,P} - I_{off,P} \tag{9.5}$$

is then due to those upper Stark states which are focused by the hexapole at that particular hexapole voltage. Since the determination of the cross section requires upper Stark states to be focused by the hexapole, the cross sections will only be defined for hexapole voltages greater than the threshold upper Stark state transmission voltage. The threshold voltage is given by [Chakravorty, 1982]

$$U_{th} = \frac{\pi^2 r_0^3}{6l_1^2}\frac{mv^2}{\mu} \tag{9.6}$$

where r_0 and l_1 are the inscribed radius and length of the hexapole respectively and m, v and μ are the mass, velocity and electric dipole moment of the beam molecule in the hexapole field.

An actual experiment may involve the determination of cross sections at a single hexapole voltage or at a range of hexapole voltages so the cross section dependence on the Stark state population can be examined. Typically an experiment will be carried out at 4-8 different scattering gas pressures, with the pressure incremented in steps of 1 x 10^{-6} to 5 x 10^{-6} torr up to a maximum pressure of 3 x 10^{-5} torr. At each pressure the transmitted beam signal is recorded with the hexapole off and then at each hexapole voltage as required. Usually the hexapole voltage is stepped from the threshold voltage for upper Stark state focusing up to 7000 V in 200 V increments. Then putting the differences calculated using equation 9.5 into equation 9.4 the upper Stark state defocusing cross sections can be determined at each hexapole voltage. A typical example of upper Stark state attenuation is shown in Fig. 9.2 and an example of the variation in cross section with hexapole voltage is given in Fig. 9.3.

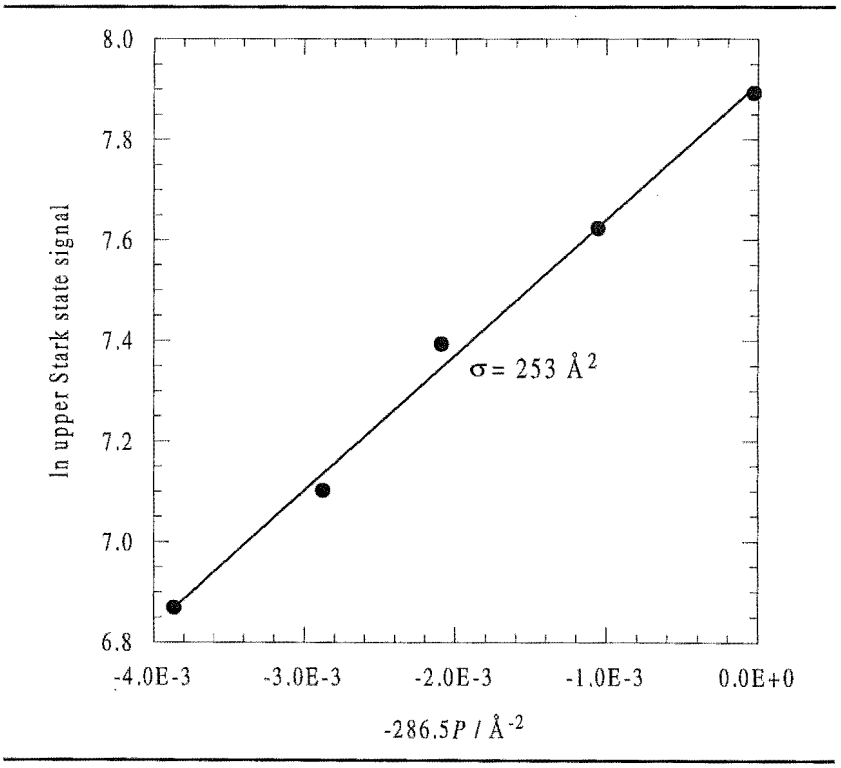

Fig. 9.2. The upper Stark state attenuation for a CH_3Cl beam with Ar. The slope of the linear least squares fit is the upper Stark state defocusing cross section.

In any scattering experiment there will be a certain minimum angular resolution inherent in the apparatus because of the finite size of all beam collimating apertures. Any scattered beam molecules that are deflected through an angle smaller than the

acceptance angle defined by the detector aperture will therefore still be detected and the measured cross section $\sigma_{eff}(\bar{g})$ will be the so called incomplete integral cross section [Scoles, 1988]. To extract the complete integral cross section $\sigma(\bar{g})$ a correction must be made for the angular resolution as given in equations 7.50 and 7.52.

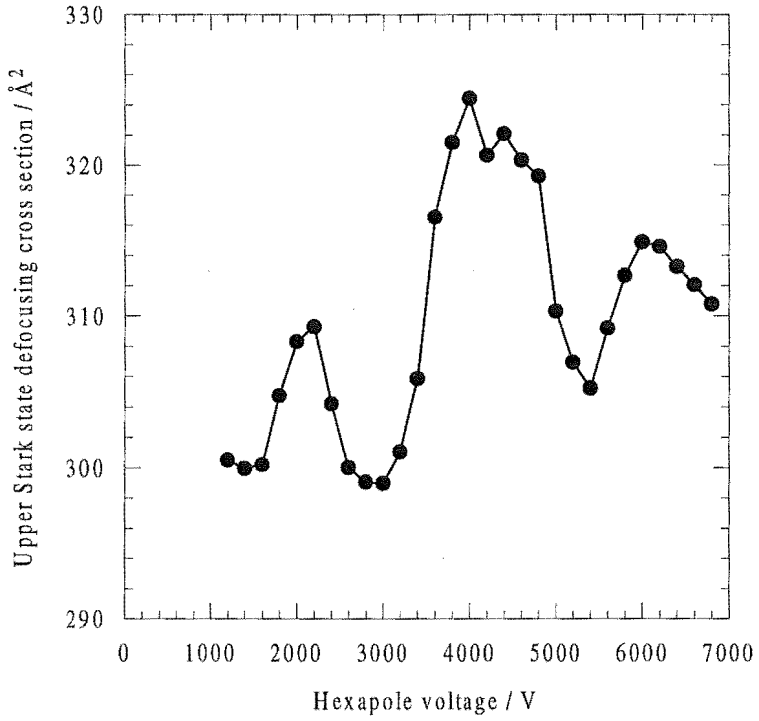

Fig. 9.3. Variation of the upper Stark state defocusing cross section for a 5% CH_3Cl/Ar beam with Ar.

In this work the hexapole used is 833 mm long, has a 5.88 mm inscribed radius and an exit aperture of 1.0 mm diameter. The angular resolution for the convergent upper Stark state beam molecules can be found by averaging the exit aperture acceptance angle as seen from all points within the length and radial distance of the hexapole. From this the angular resolution is found to be 0.4°. In reality however the angular resolution will be much less than this because of the focusing effect of the hexapole electric field. That is, any rotationally inelastic collision of a focused upper Stark state beam molecule will produce a rotational state that will not be favourably focused by the hexapole field. Therefore the scattered product will be effectively scattered through an angle greater than the initial scattering angle and this will be proportional to the change in ρ (= KM/J(J + 1)) for the beam molecule in the collision.

This further reduces the likelihood of the beam molecule being successfully transmitted through the hexapole exit aperture. Under these conditions the angular resolution correction will be small and it will vary for each upper Stark state $|JKM\rangle$. For a focused beam molecule that suffers a collision accompanied by a small change in ρ there is a greater probability that the scattered beam molecule will still be detected than if the molecule undergoes a transition that brings about a large change in ρ. Hence the cross sections that are measured here will be incomplete cross sections although the difference from the complete integral cross sections is expected to be small.

For an attractive interaction potential of the form

$$V(r) = -\frac{C}{r^s} \tag{9.7}$$

the cross sections $\sigma(g)$ are expected to show a velocity dependence [Landau, 1958; Massey, 1933; Massey, 1934] such that

$$\sigma(g) \propto g^{-2/(s-1)} \tag{9.8}$$

where g is the relative velocity of the collision partners. For the van der Waals attractive forces considered here, $s = 6$ in the above equations so the velocity dependence of the upper Stark state cross sections will be proportional to $g^{-0.4}$.

Because of the velocity distributions of the supersonic molecular beam and the scattering gas, the experimental cross sections measured for the defocusing of upper Stark states $\sigma(\bar{g})$ will be the result of averaging the integral cross sections $\sigma(g)$ over the relative velocity distribution $f_r(g)$ where $g = |\mathbf{v}_b - \mathbf{v}_s|$ and $\mathbf{v}_b$ and $\mathbf{v}_s$ are the beam and scattering gas velocities {7.3}. Hence the chosen reference velocity for the upper Stark state cross sections is the average relative velocity $\bar{g}$ which is given by

$$\bar{g} = \left(v_b^2 + v_s^2\right)^{1/2} \tag{9.9}$$

where v_b is the most probable beam velocity determined from arrival time distributions of the beam and v_s is the most probable velocity of the scattering gas at the temperature of the hexapole collision region.

The most probable velocity v_s is calculated from the thermal Maxwell-Boltzmann distribution function for the scattering gas as

$$v_s = \left(\frac{2kT}{m}\right)^{1/2}. \tag{9.10}$$

The beam velocity v_b can either be estimated as the thermodynamically limiting value as given in equation 7.9 or it can be measured from the experimental time of flight analysis (TOF) of the beam. Beam arrival time distributions (ATD's) are measured by digitising and averaging the analog signal output from the detector CEM using a Thurlby digital storage adapter {8.7.5}. From the time corresponding to the maximum in the ATD, t_{mx}, the beam velocity is found from d/t_{mx} where d is the flight path length of the molecular beam from source to detector. From a comparison of the experimental Ar flight time with the velocity determined with this equipment in earlier studies [Cameron, 1991], an effective distance from nozzle to detector can be found. This will take into account the response time of the electronics and the piezoelectric nozzle opening function. From this the effective distance is found to be 1.57 m and beam velocities are calculated using

$$v_b = \frac{1.57}{t_{mx}} \tag{9.11}$$

where t_{mx} is in units of s and the beam velocity v_b is in ms^{-1}.

In the case of the pure symmetric top beams the beam velocity will be substantially slower than the limiting velocity due to the incomplete cooling of the rotational and vibrational modes in the molecules. Hence the limiting velocity will be a poor estimate of the experimental velocity. However, for the 5% symmetric top-inert gas seeded mixtures that have been used, the thermodynamic limiting velocity should be a good approximation to the experimental velocity. This is due to the large excess of

the atomic inert gas whose random thermal motion will be efficiently converted to the beam flow velocity.

9.4 Results

9.4.1 Voltage Dependence for Upper Stark State Defocusing Cross Sections

The attenuation of focused upper Stark state beam molecules in a hexapole electric field by collisions with a background scattering gas, has been attributed to the production of non-focused rotational states of the beam molecules by inelastic collisions. The measured cross sections are therefore the result of averaging over the rotational state distribution of the beam transmitted by the hexapole for all allowed rotational transitions that lead to defocusing of the beam.

For the pure symmetric top molecular beams used in this work the rotational state resolution of the hexapole is not adequate to isolate and transmit individual $|JKM\rangle$ states of the beam. The translational and rotational temperatures of the molecular beam established in the supersonic expansion ensure that the focusing curves for individual $|JKM\rangle$ states are broad leading to overall hexapole focusing curves characterised by a general increase in transmitted intensity with voltage but with very little quantum state structure (Fig. 9.4). However, since the defocusing cross section at a particular hexapole voltage is dependent on the ensemble of focused $|JKM\rangle$ states there should be variation in the cross section as a function of the hexapole voltage. To improve the resolution of the hexapole the translational and rotational temperatures of the beam must be reduced. If the molecular beam is velocity selected a small range of velocities will be presented to the hexapole region which will reduce the width of the focusing curves for each $|JKM\rangle$ state and hence improve the resolution. However, since the rotational temperature is still high there will be a large number of highly populated rotational

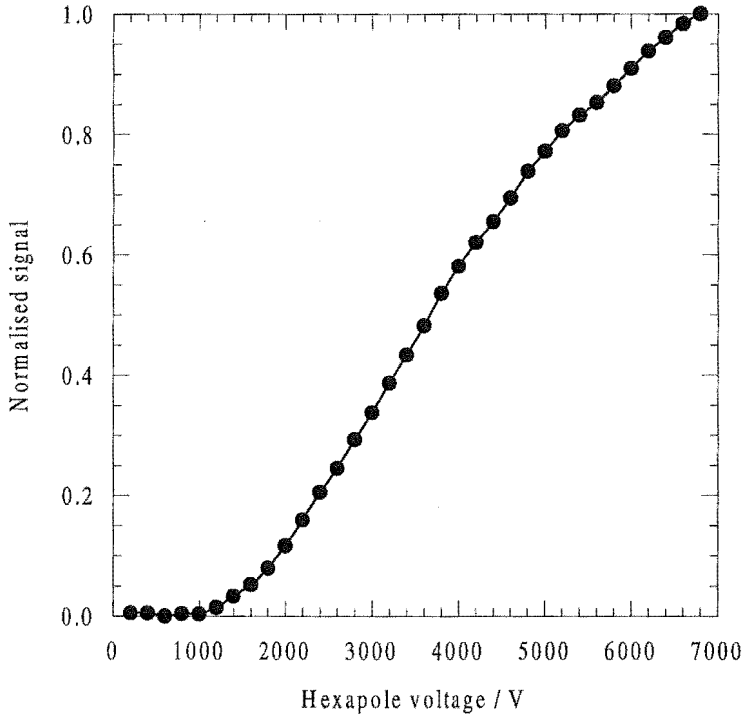

Fig. 9.4. Hexapole focusing curve for the CH_3Cl beam.

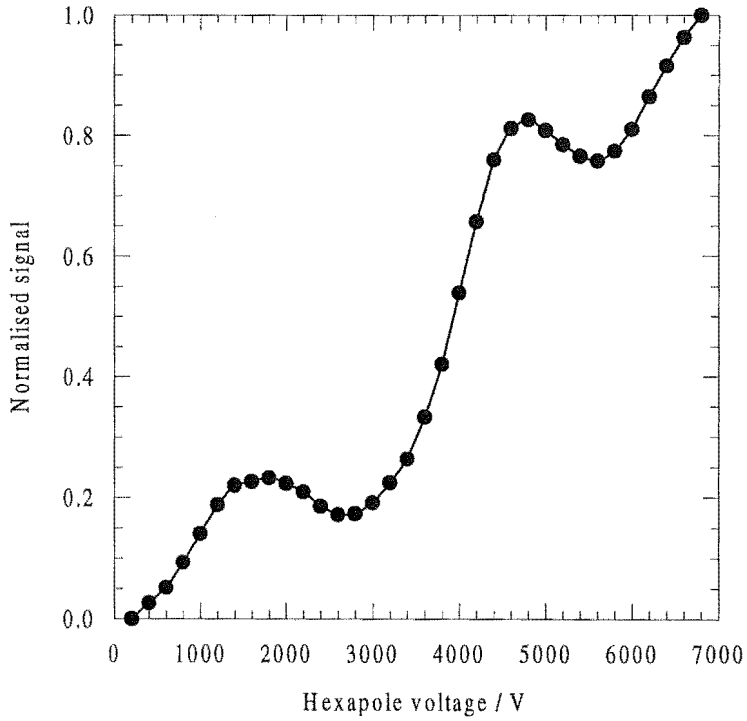

Fig. 9.5. Hexapole focusing curve for the 5% CH_3Cl/Xe seeded beam.

states present in the focusing range of the hexapole so the state resolution will still be poor due to the superposition of different $|JKM\rangle$ states with the same or similar values

of ρ (=KM/J(J+1)). Instead, the technique of seeding {7.1.3} is used to reduce the translational and rotational temperatures of the symmetric top molecules by expanding them in a dilute mixture with an inert gas buffer. The success of this approach is illustrated by Fig. 9.5 which shows the experimental hexapole focusing curve for a seeded mixture of 5% CH_3Cl in Xe. While the state resolution is by no means absolute it is a vast improvement on the pure beams that have been used. Hence for the seeded beams the defocusing cross section is expected to show a greater dependence on the hexapole voltage due to the improved $|JKM\rangle$ state resolution. The combination of mechanical velocity selection with the seeded beam technique should provide even greater resolution albeit at the expense of signal intensity, this has not been implemented as yet.

The molecular beam scattering gas combinations that have been studied here are:

- CH_3Cl beam with He, Ne, Ar, Kr, Xe and N_2
- 5% CH_3Cl/Ar seeded beam with He, Ne, Ar, Kr, Xe and N_2
- 5% CH_3Cl/Kr seeded beam with He, Ne, Ar, Kr, Xe and N_2
- 5% CH_3Cl/Xe seeded beam with He, Ne, Ar, Kr, Xe and N_2
- 5% CH_3F/Ar seeded beam with He, Ne, Ar, Kr, Xe and N_2
- 5% CH_3F/Kr seeded beam with He, Ne, Ar, Kr, Xe and N_2
- CF_3H beam with He, Ne, Ar, Kr, Xe and N_2
- 5% CF_3H/Kr seeded beam with He, Ne, Ar, Kr, Xe and N_2.

The seeded mixtures were chosen to take advantage of the hydrodynamic focusing of the different weight components in the mixtures {7.1.3}. Since the use of the hexapole to focus upper Stark states requires a divergent beam, it was found that using heavier buffer gases in the seeded beam mixtures produced a greater hexapole focusing effect than for lighter buffers. For example, CH_3Cl seeded in He or Ne produced poor focusing curves as the heavy CH_3Cl was preferentially focused to the beam axis. For the heavier buffers Kr and Xe the buffer is heavier than the CH_3Cl component so the situation is reversed and the hexapole focusing is enhanced.

The upper Stark state defocusing cross sections are determined by running hexapole focusing curves with and without the scattering gas present and recording the transmitted upper Stark state beam signal as a function of hexapole voltage from the threshold voltage up to 7000 V in 200 V steps. Results below the threshold voltage are ignored as the upper Stark states are not focused at these low voltages and differences calculated using equation 9.5 will be due to noise only. The defocusing cross sections are determined from equations 9.4 and 9.5. Because long counting times were needed at each voltage/pressure data point the experiments were lengthy so only two focusing curve were measured, one without scattering gas and one with scattering gas in the hexapole region. Each experiment was repeated at least five times and the results averaged. The experimental uncertainty due to the measurement of the upper Stark state signal at a particular hexapole voltage is typically 1% and this leads to a 2% uncertainty in the determination of the defocusing cross sections. Hence the shape of the defocusing cross section verses hexapole voltage curves are highly reproducible. However, due to the uncertainties associated with measuring the pressure, which does not affect the shape of the defocusing cross section curves, the absolute uncertainty for the curves is around ±5-15%. The upper Stark state defocusing cross section results for all of the beam-scattering gas combinations listed above are shown in Figs. 9.6-9.13 and the data is tabulated in appendix C. The cross sections are for the attenuation of upper Stark states only and are therefore only defined above the hexapole threshold voltage, as below this point there is no hexapole focusing and hence no upper Stark states transmitted by the hexapole. Because of the three point averaging used to smooth the experimental data the position of the features in the upper Stark state cross section curves are expected to have an uncertainty in hexapole voltage position of ±100 V.

It is clear from comparison of the upper Stark state cross section curves measured for a particular beam, that the general variation in cross section with hexapole voltage is reproduced for all of the scattering gases used and is therefore not due to random experimental uncertainty. Hence the cross section for attenuation of the hexapole focused beam must be due to the loss of focused upper Stark states from the beam by rotationally inelastic processes. If the attenuation was due to any other collision process then no variation in the cross section with hexapole voltage would be expected.

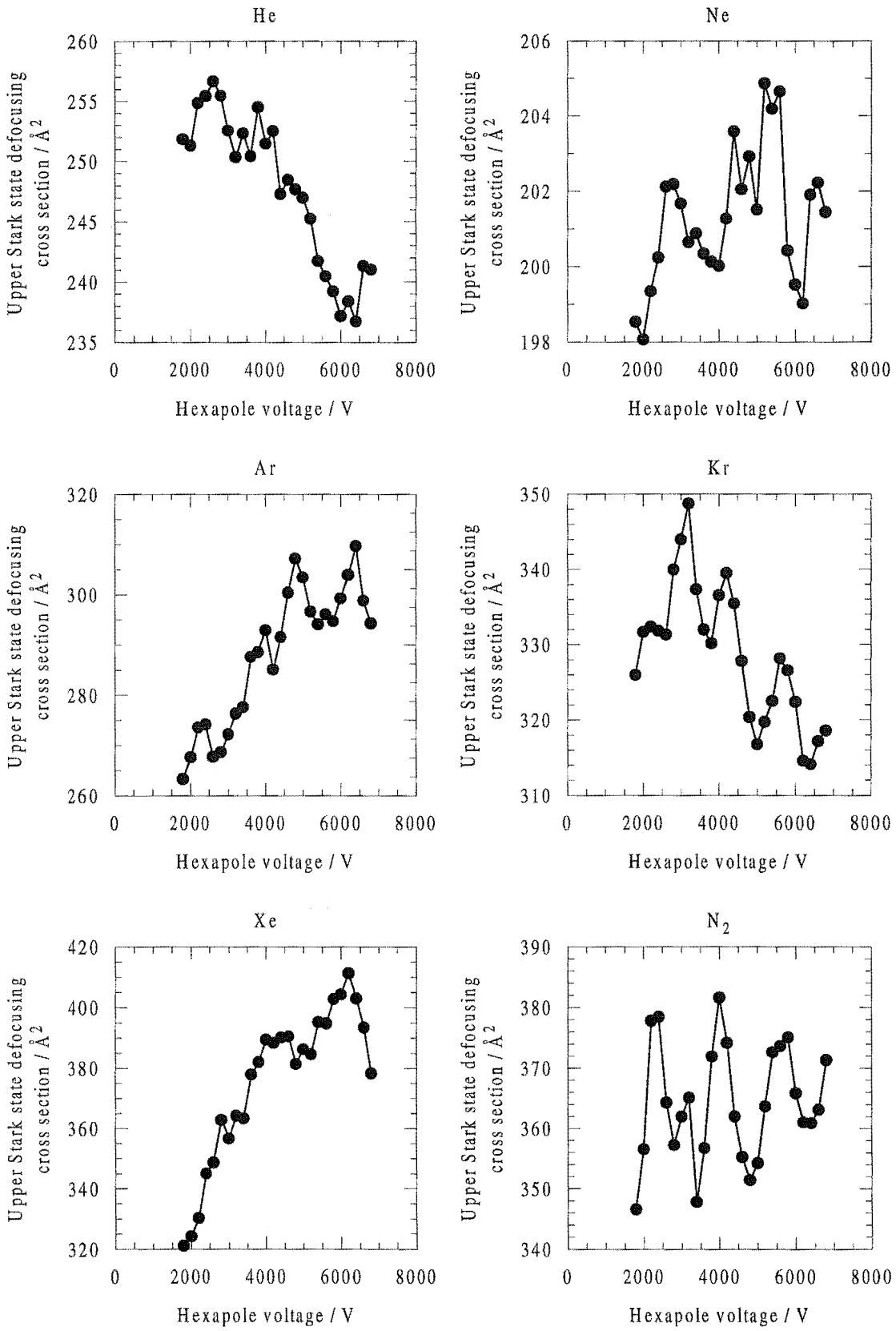

Fig. 9.6. Upper stark state defocusing cross sections for the CH_3Cl beam.

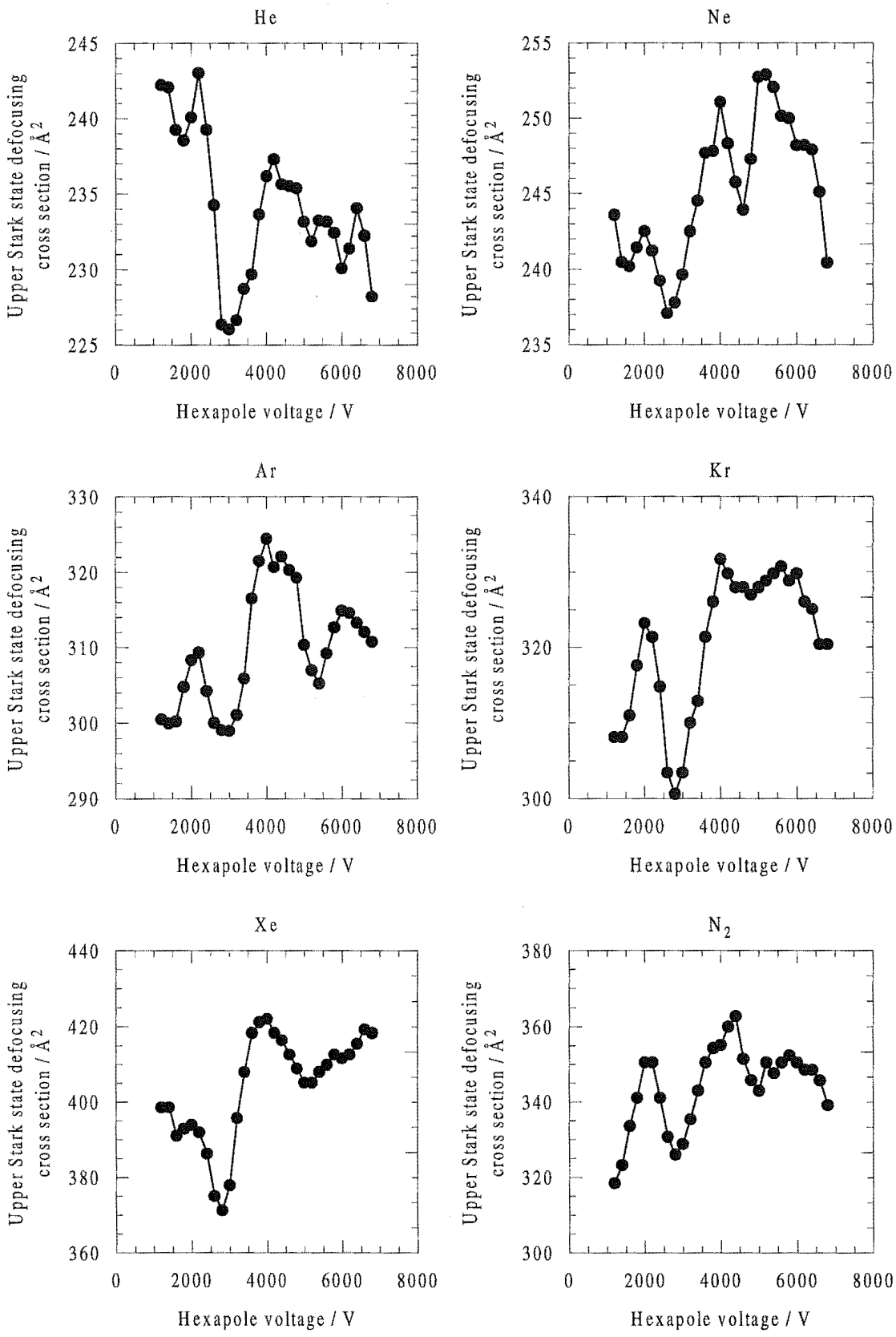

Fig. 9.7. Upper stark state defocusing cross sections for the 5% CH_3Cl/Ar beam.

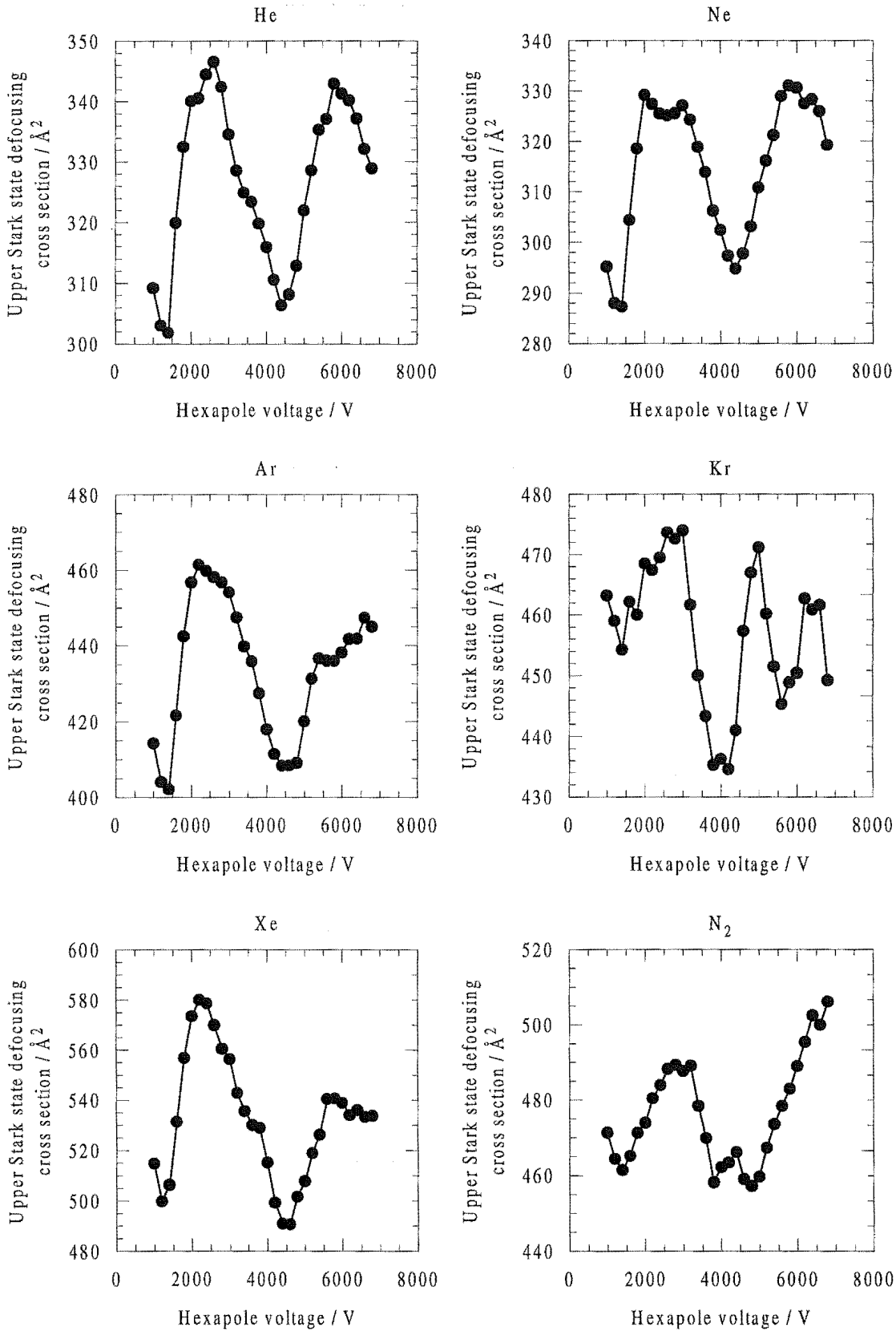

Fig. 9.8. Upper stark state defocusing cross sections for the 5% CH_3Cl/Kr beam.

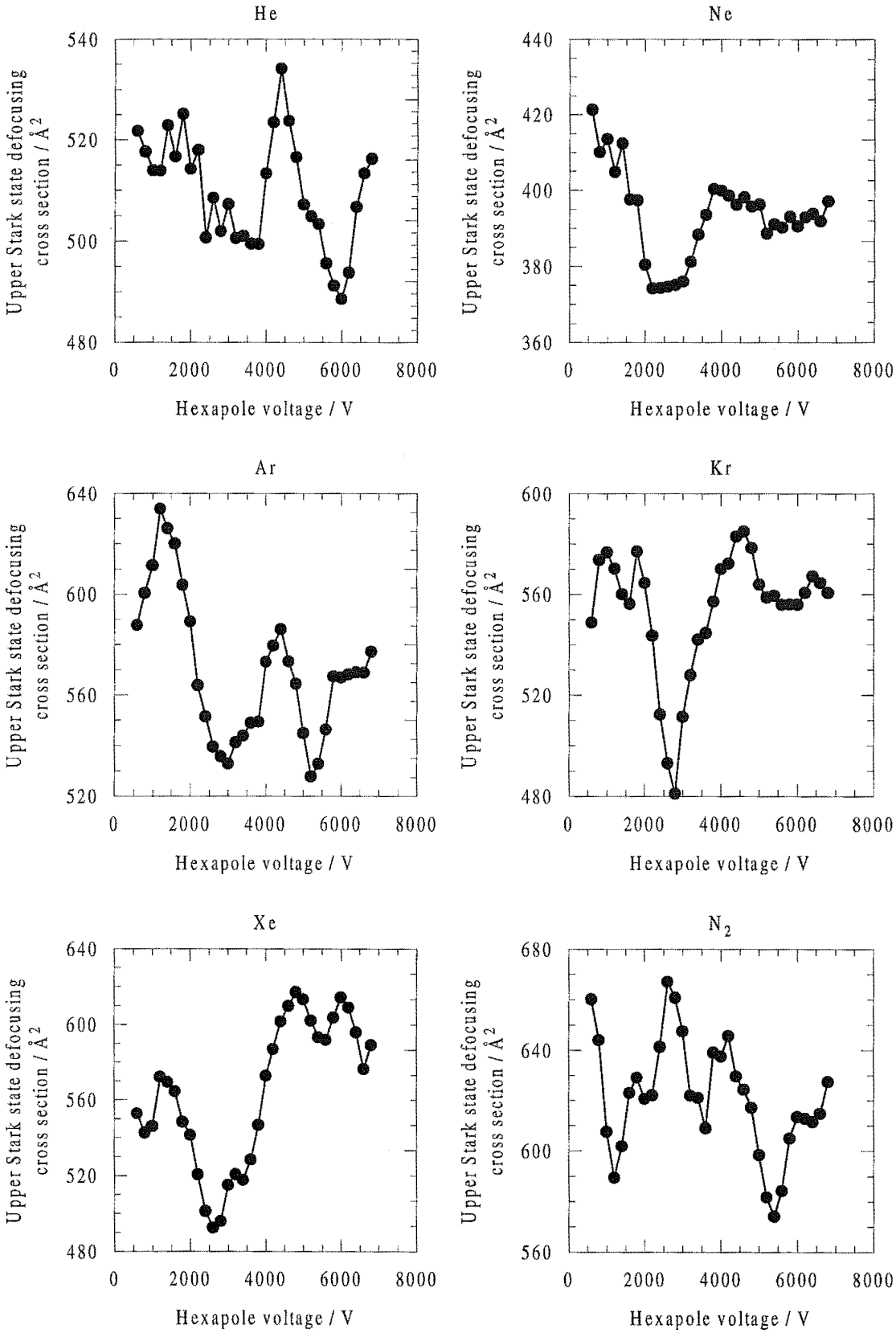

Fig. 9.9. Upper stark state defocusing cross sections for the 5% CH_3Cl/Xe beam.

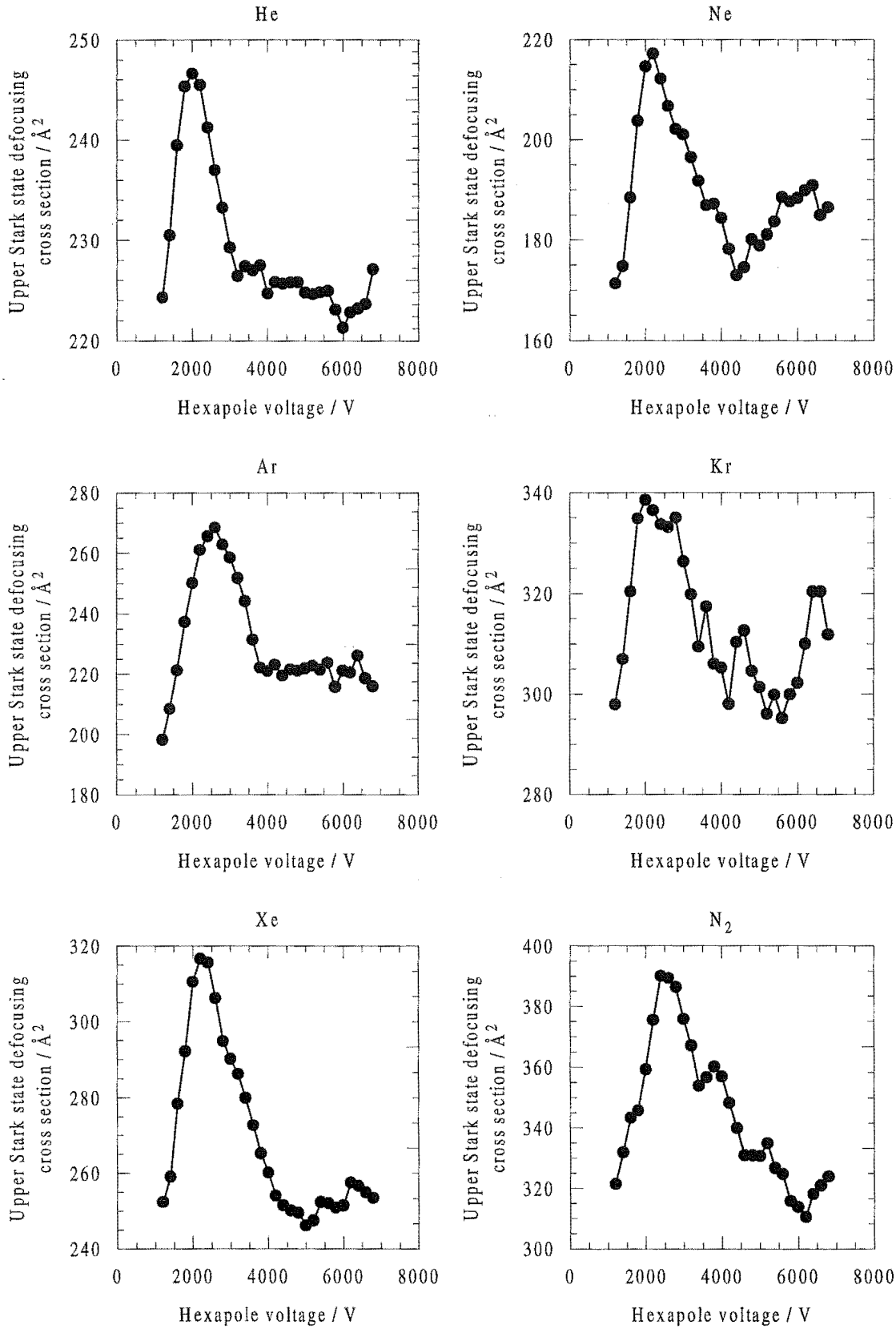

Fig. 9.10. Upper stark state defocusing cross sections for the 5% CH_3F/Ar beam.

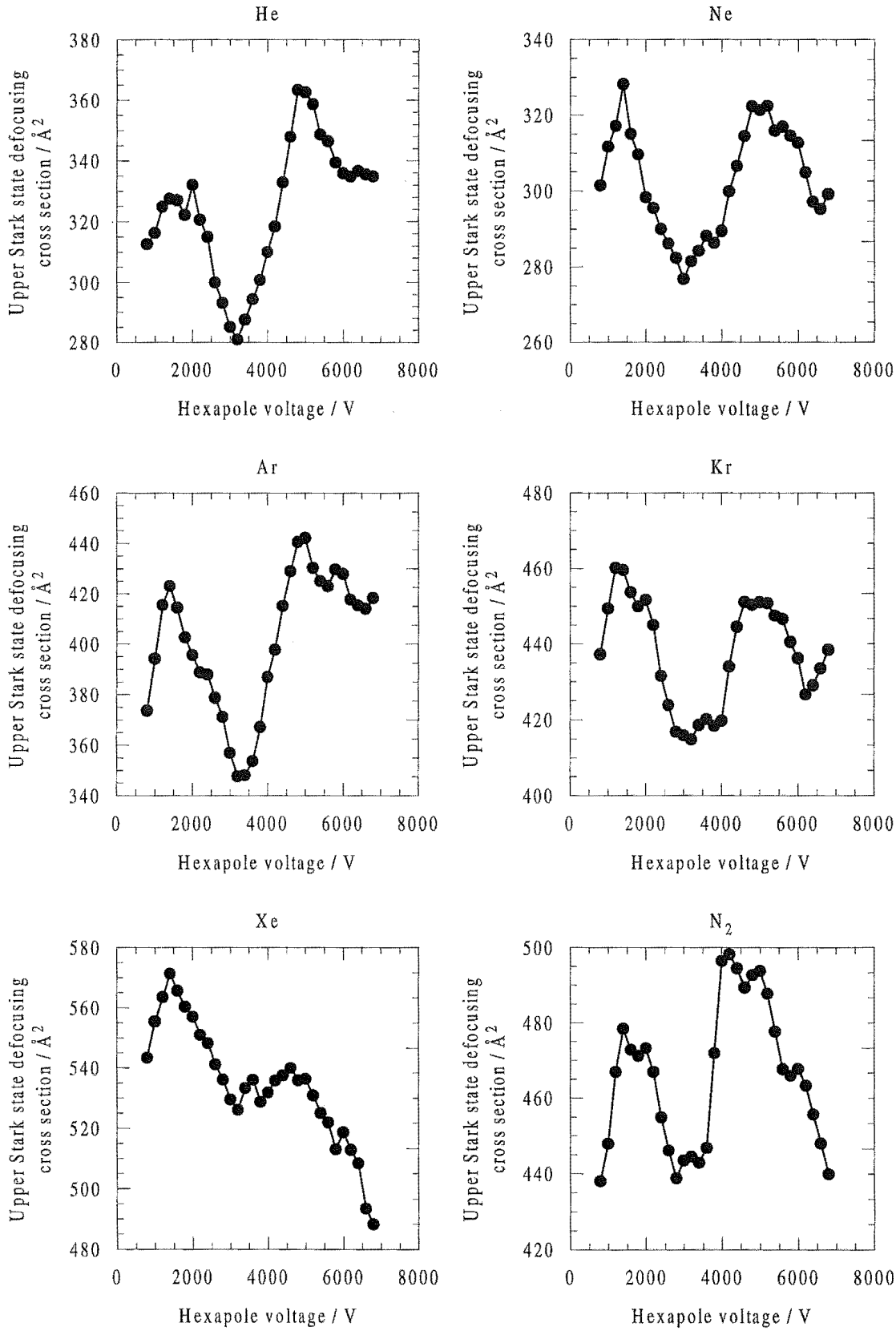

Fig. 9.11. Upper stark state defocusing cross sections for the 5% CH_3F/Kr beam.

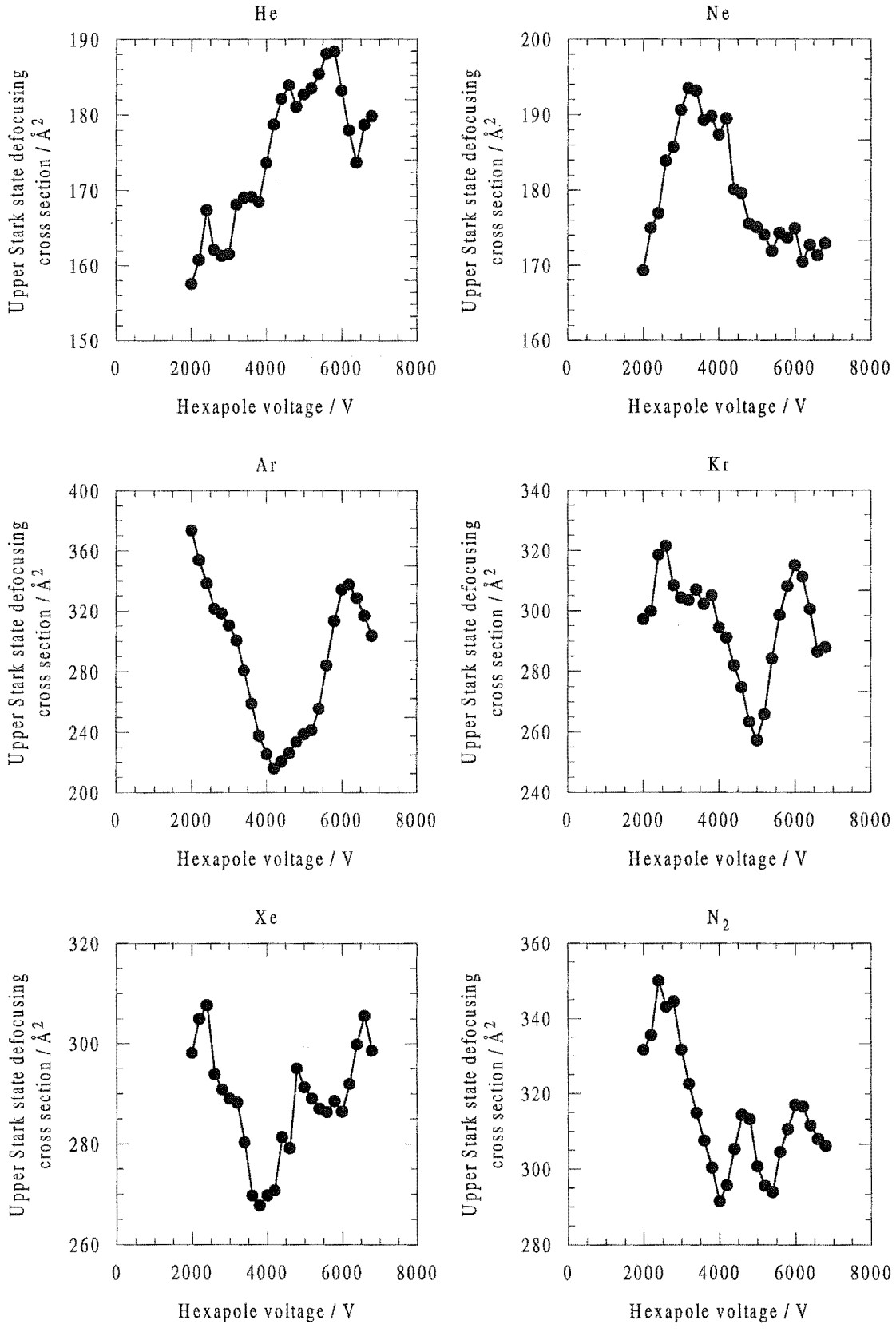

Fig. 9.12. Upper stark state defocusing cross sections for the CF_3H beam.

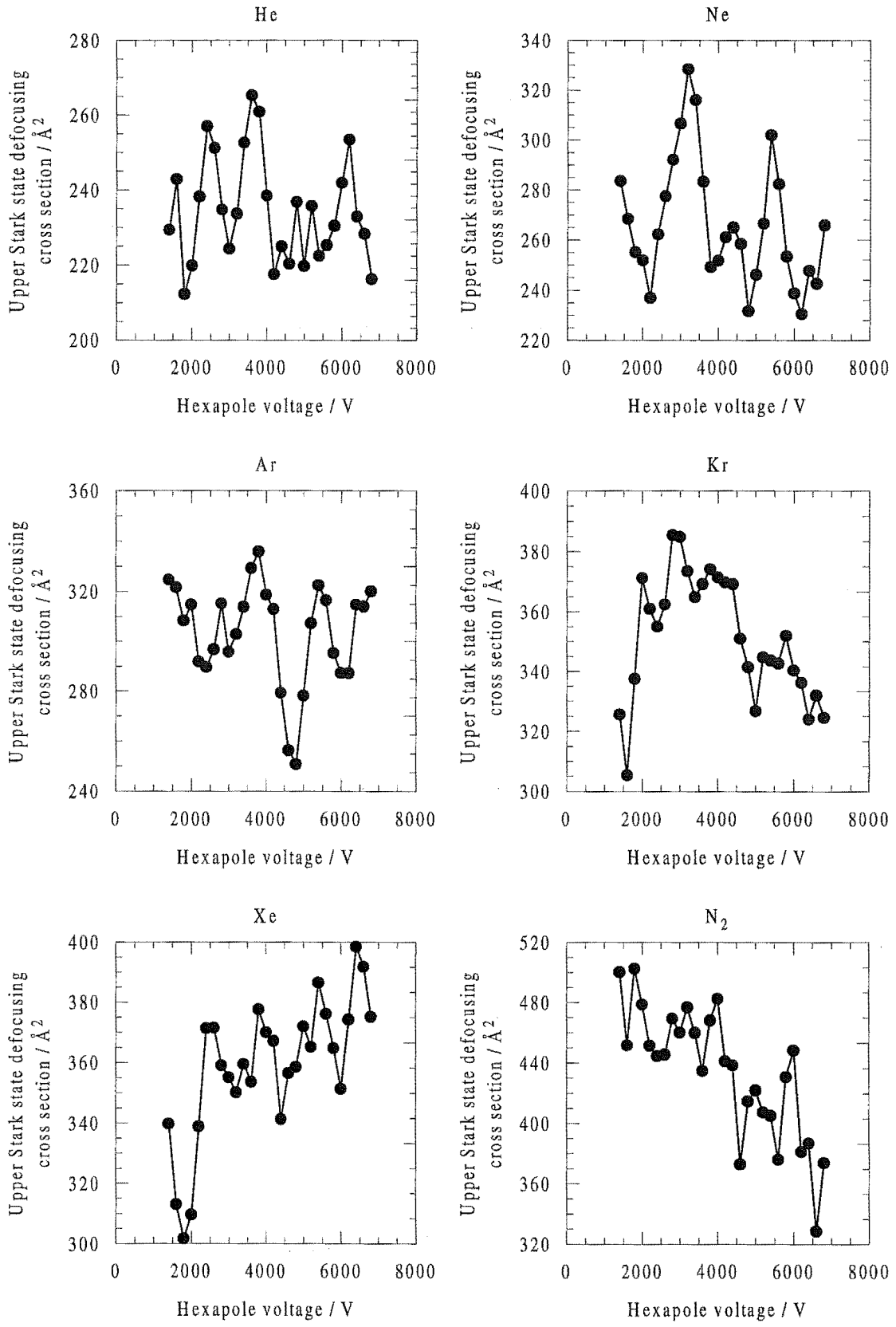

Fig. 9.13. Upper stark state defocusing cross sections for the 5% CF_3H/Kr beam.

A discussion of the upper Stark state cross section data as a function of hexapole voltage requires knowledge of the focusing curves for the beams transmitted by the hexapole so |JKM⟩ states can be located and compared to features in the cross section curves. Experimental focusing curves have been measured for all of the beams used and calculated focusing curves matched to the experimental curves are used to find the focusing voltages for the various rotational states. Furthermore the magnitude and velocity dependence of the upper Stark state cross sections will be examined using the van der Waals interaction potential {7.3}. A discussion of the rotationally inelastic collision processes responsible for the upper Stark state defocusing will be made.

9.4.2 Experimental Hexapole Focusing Curves

The upper Stark state focusing behaviour of the hexapole has been examined for each of the molecular beams used for the cross section experiments. The transmitted beam intensity is measured as a function of hexapole voltage from 0-7000 V in 100 V increments for each beam in the absence of any scattering gas in the hexapole region. Typically 3-6 focusing curves are averaged to reduce noise in the final curve. The results for each of the beams are graphed in Figs. 9.14-9.21. It is apparent from each of the focusing curves that the |JKM⟩ rotational state resolution varies for the different molecular beams used. For instance the CF_3H focusing curve shown in Fig. 9.20 shows a smooth increase in signal from threshold up to 7000 V. There are no features corresponding to the individual |JKM⟩ states. However, for the seeded beams the smooth increase is absent, instead the upper Stark state signal rises and falls with voltage as various |JKM⟩ states are focused by the hexapole. Because the resolution is not high, it is difficult to make an absolute comparison in the position of the focusing curve maxima (|JKM⟩ state focusing voltages) with the corresponding maxima in the upper Stark state cross section curves shown in Figs. 9.6-9.13. However, an examination of the general features shows there is a correlation in position between the cross section and focusing curves. In order to determine the |JKM⟩ state focusing

distributions in the experimental focusing curves, theoretical focusing curves must be calculated.

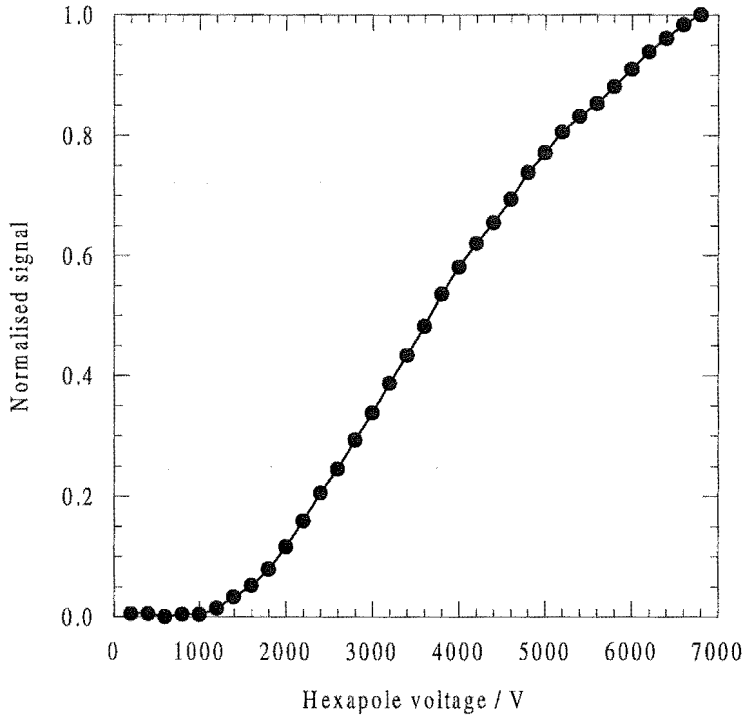

Fig. 9.14. Hexapole focusing curve for the CH_3Cl beam.

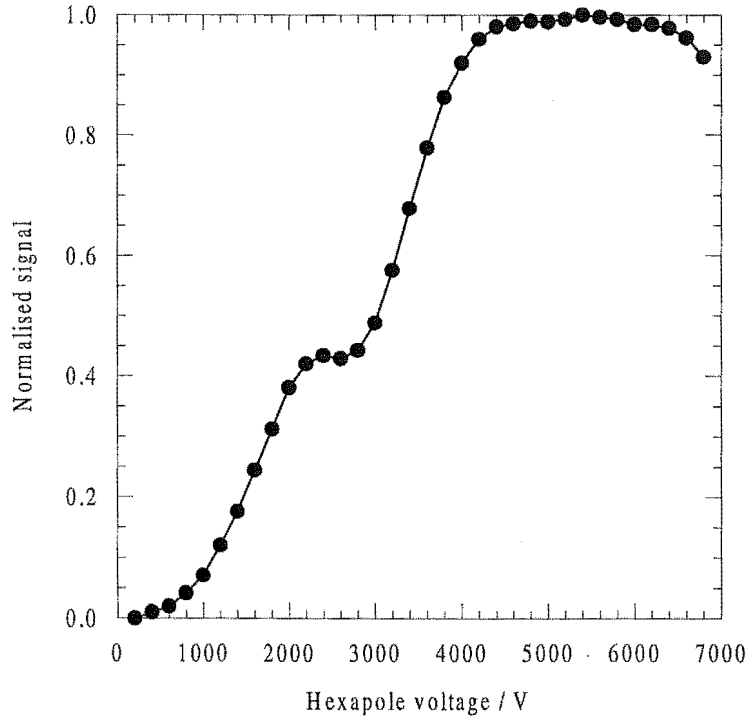

Fig. 9.15. Hexapole focusing curve for the 5% CH_3Cl/Ar beam.

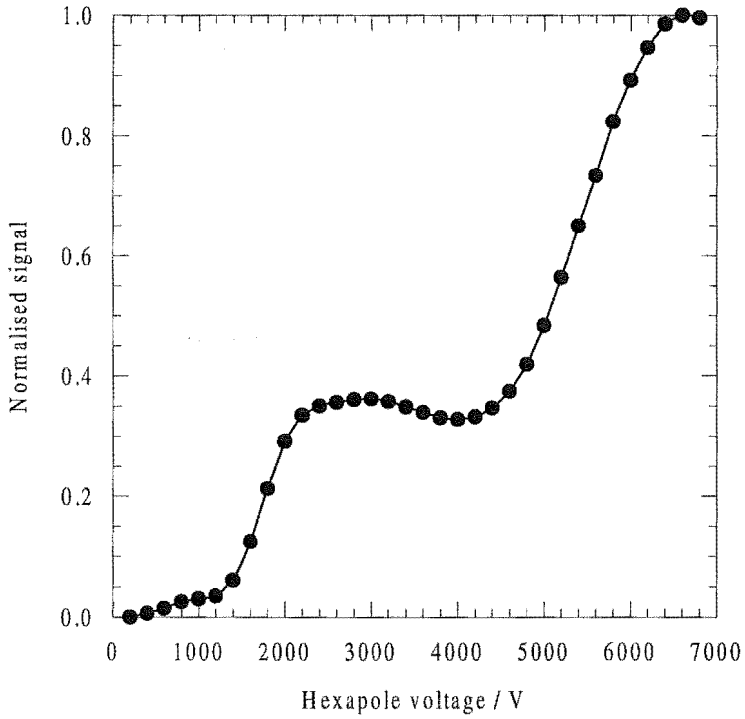

Fig. 9.16. Hexapole focusing curve for the 5% CH_3Cl/Kr beam.

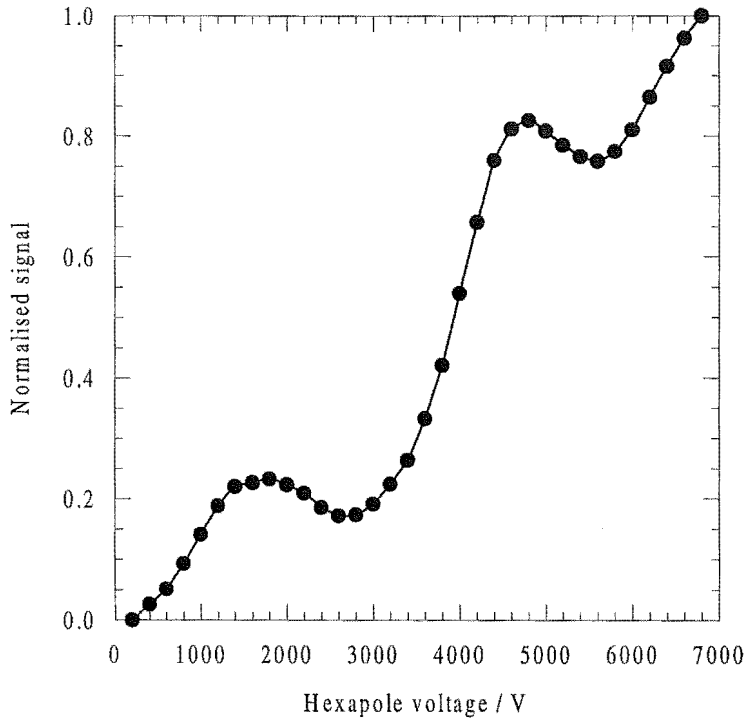

Fig. 9.17. Hexapole focusing curve for the 5% CH_3Cl/Xe beam.

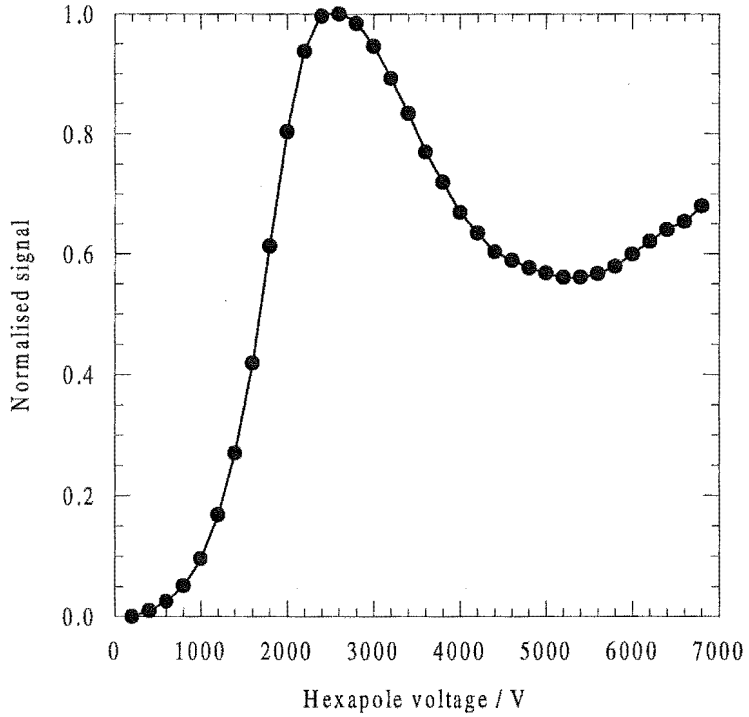

Fig. 9.18. Hexapole focusing curve for the 5% CH_3F/Ar beam.

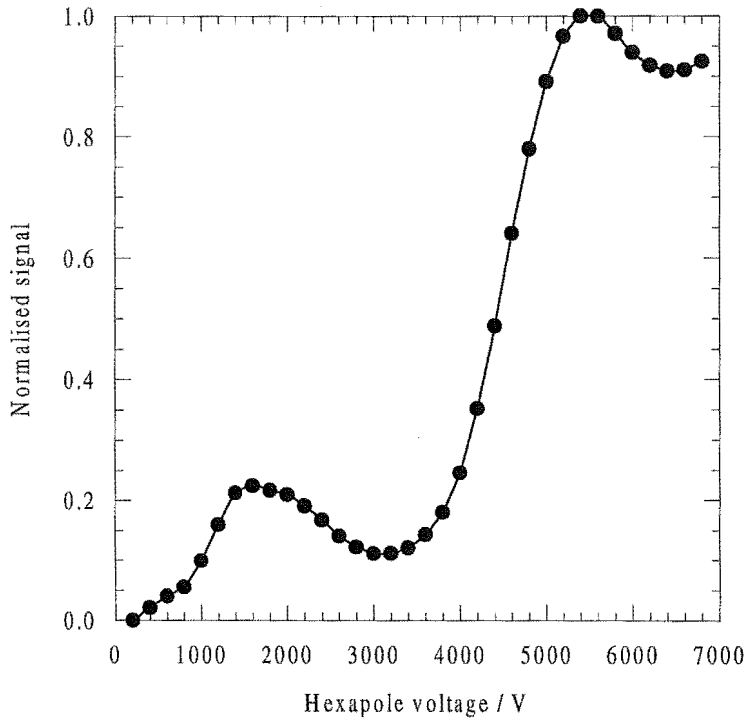

Fig. 9.19. Hexapole focusing curve for the 5% CH_3F/Kr beam.

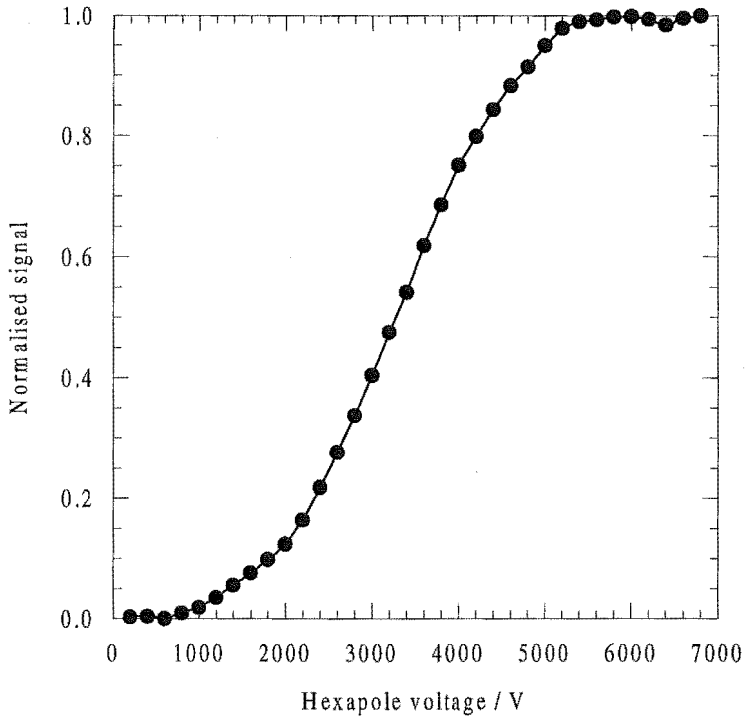

Fig. 9.20. Hexapole focusing curve for the CF_3H beam.

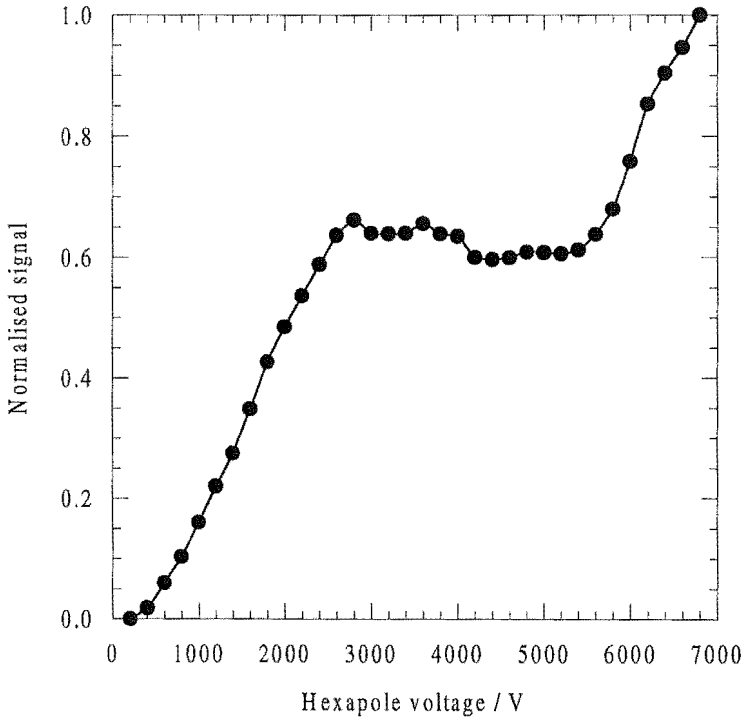

Fig. 9.21. Hexapole focusing curve for the 5% CF_3H/Kr beam.

9.4.3 Theoretical Hexapole Focusing Curves

The trajectories of upper Stark state symmetric top beam molecules traversing a hexapole electric field depend on the angle θ between the molecule electric dipole and the hexapole field direction. For a rotational state |JKM⟩ the angle θ is found from the expectation value for cosθ [Bernstein, 1982]

$$\langle \cos\theta \rangle = \frac{KM}{J(J+1)} = \rho. \tag{9.12}$$

The transmission of the upper Stark states |JKM⟩ by the hexapole can be calculated for the geometry of the hexapole used. In the limit of infinitesimally small entrance and exit apertures to the hexapole region and infinitely narrow velocity distribution for the beam, the calculated hexapole focusing curve will consist of a series of lines of varying intensity. Each line is due to a single |JKM⟩ state and is positioned at the hexapole focusing voltage U_{JKM} for the state given by

$$U_{JKM} = \frac{\pi^2 r_0^3}{6l^2} \frac{mv^2}{\mu} \frac{J(J+1)}{KM} \tag{9.13}$$

where r_0 and l are the inscribed radius and length of the hexapole and m, v and μ are the mass, velocity and electric dipole respectively of the focused beam molecule in the upper Stark state |JKM⟩.

In reality however, the beam velocity distribution and finite size of the entrance and exit apertures ensure the |JKM⟩ peaks are not infinitely narrow and hence the resolution of the hexapole is very much reduced. The resolution is reduced even further as there is a finite probability of finding the molecular dipole oriented between 0-180° with respect to the field. The angle θ determined using equation 9.12 is simply the average value of the range of possible orientations which is dependent on the |JKM⟩ state.

The hexapole focusing curves are determined by calculating the transmission probabilities $A(U_0, v, \rho)$ (equation 7.41) at each hexapole voltage, beam velocity and orientation ρ. The beam velocity distribution $f_b(v)$ used is given in equation 7.8 and it is normalised using Simpson's rule. The transmission probabilities are reduced by integration over the beam velocity distribution to give the transmission probabilities $A(U_0, \rho)$ as a function of hexapole voltage and orientation ρ

$$A(U_0, \rho) = \int_0^\infty A(U_0, v, \rho) f_b(v) dv. \tag{9.14}$$

The focusing curve for a state |JKM⟩ is then found by determining the value of ρ for the state and multiplying the appropriate probabilities $A(U_0, \rho)$ by the partition function q_{JK} (equation 7.43). The resulting transmitted state intensity $F_{JKM}(U_0)$

$$F_{JKM}(U_0) = q_{JK} A(U_0, \rho) \tag{9.15}$$

is then plotted as a function of the hexapole voltage. Finally the total transmitted intensity $T(U_0)$ (equation 7.44) is determined by summing the intensities $F_{JKM}(U_0)$ over all populated |JKM⟩ states in the molecular beam.

The focusing curve calculations require a range of known parameters to be input, from the physical dimensions of the hexapole apparatus to molecular properties such as dipole moments and rotational constants as well as the beam velocity and translational and rotational beam temperatures. The computer programs used to calculate the focusing curves were developed by Professor Philip Brooks of Rice University, Texas.

The beam velocities v_b used in the calculations have been determined from time of flight analysis {9.3} for each of the molecular beams under investigation. The beam velocities are calculated using equation 9.11 and listed in Table 9.2. Since no attempt has been made to velocity select the molecular beam or to deconvolute the supersonic nozzle opening function from the ATD, it is expected that the velocities calculated in Table 9.2 will be approximate only. Even so they do provide a good starting point for fitting the calculated focusing curves to the experimental data.

Beam	Beam Velocity (ms^{-1})
CH_3Cl	579
5% CH_3Cl/Ar	525
5% CH_3Cl/Kr	372
5% CH_3Cl/Xe	310
5% CH_3F/Ar	612
5% CH_3F/Kr	387
CF_3H	502
5% CF_3H/Kr	388

Table 9.2. Experimental beam velocities measured from time of flight analysis.

The translational temperature $T_{\|}$ of the beam does not need to be known accurately. Larger values of $T_{\|}$ serve only to broaden the individual state focusing curves which will smooth any features in the total focusing curve. Previous work with this experimental apparatus has shown that the translational beam temperatures for supersonic beams of inert gases and small diatomics typically lie in the range 1-15 K [Cameron, 1991]. From this a translational temperature of around 10 K seems to be a suitable estimate for the initial temperature to use in the calculations. It has also been found that the rotational temperature of the beam tends to reduce at a slower rate than the translational temperature in the supersonic expansion. From comparison between calculated and experimental focusing curves, 15 K appears to be a reasonable choice for the rotational temperature.

Using the initial conditions for the calculations, the beam velocity and temperatures were slowly varied until the best match could be made between the experimental and calculated focusing curves. The beam velocities determined from this fitting procedure vary somewhat from the approximate experimental values and are listed in Table 9.3. Under these conditions the individual $|JKM\rangle$ state focusing curves were calculated and the peak voltages recorded for comparison to the features in the upper Stark state defocusing cross section curves. Only the focusing curves for $|JKM\rangle$ states which focus below 7000 V and which are significantly populated were calculated.

For the prolate CH_3F and CH_3Cl molecules used, the difference between the rotational constants about the symmetry and perpendicular axes are large. This ensures $|JKM\rangle$ states with high K quantum number will not be highly populated. For the rotational temperatures used in the focusing curve calculations of less than 20 K, the maximum K considered for focusing $|JKM\rangle$ states is K = 3. For these low K states the maximum J quantum number that gives reasonable state populations is J = 5. For the slightly oblate CF_3H however, the magnitude of the J and K quantum numbers have a similar magnitude effect on the $|JKM\rangle$ state populations and for a given J the state population increases with K. In this case the maximum J,K considered for the focusing states is J = K =10 and for the high J states only those with high K are included. The calculated focusing voltages for the major $|JKM\rangle$ states focused below 7000 V are summarised for each of the molecular beams used in Tables 9.4-9.5.

Beam	Beam Velocity (ms^{-1})
CH_3Cl	610
5% CH_3Cl/Ar	520
5% CH_3Cl/Kr	470
5% CH_3Cl/Xe	370
5% CH_3F/Ar	635
5% CH_3F/Kr	470
CF_3H	535
5% CF_3H/Kr	450

Table 9.3. Calculated beam velocities from fitting of calculated hexapole focusing curves to the experimental data.

The focusing voltages listed in Tables 9.4-9.5 are the voltages where the $|JKM\rangle$ states focus in the limit of infinitely small hexapole entrance and exit apertures and infinitely narrow velocity distribution of the beam. However, because the beam is characterised by a random translational temperature and the defining apertures at each end of the hexapole reduce the resolution, the focusing voltages should be replaced by $|JKM\rangle$ state focusing curves centred about the voltages in Tables 9.4-9.5. The widths of

|JKM⟩	CH_3Cl	CH_3Cl/Ar	CH_3Cl/Kr	CH_3Cl/Xe	CH_3F/Ar	CH_3F/Kr
222	2600	1800	1400	900	1800	1000
111	3400	2300	2000	1200	2400	1400
424	4200	2800	2400	1400	3000	1700
212	5200	3600	3000	1800	3800	2100
423	5600	3800	3200	2000	4000	2200
524	6400	4400	3800	2200	4700	2600
313	-	4800	4000	2400	5100	2800
414	-	5800	4800	3000	6100	3400
211	-	-	6100	3700	-	4200
413	-	-	-	4200	-	4800
514	-	-	-	4900	-	5600
412	-	-	-	5900	-	-

Table 9.4. Calculated |JKM⟩ state focusing voltages.

|JKM⟩	CF_3H	CF_3H/Kr
555	2300	1600
444	2400	1700
333	2600	1800
222	3000	2100
111	3900	2700
442	4800	3400
221	6000	4200
432	6400	4500
542	-	5200
331	-	5600

Table 9.5. Calculated |JKM⟩ state focusing voltages.

the individual state focusing curves increase with increasing aperture size and increasing beam translational temperature and hence reduce the |JKM⟩ state resolution of the

hexapole. Fig. 9.22 shows the calculated focusing curve for the 5% CH_3F/Ar beam with the individual |JKM⟩ focusing curves for the highly populated states. Summation of the individual |JKM⟩ curves over all states will reproduce the full focusing curve.

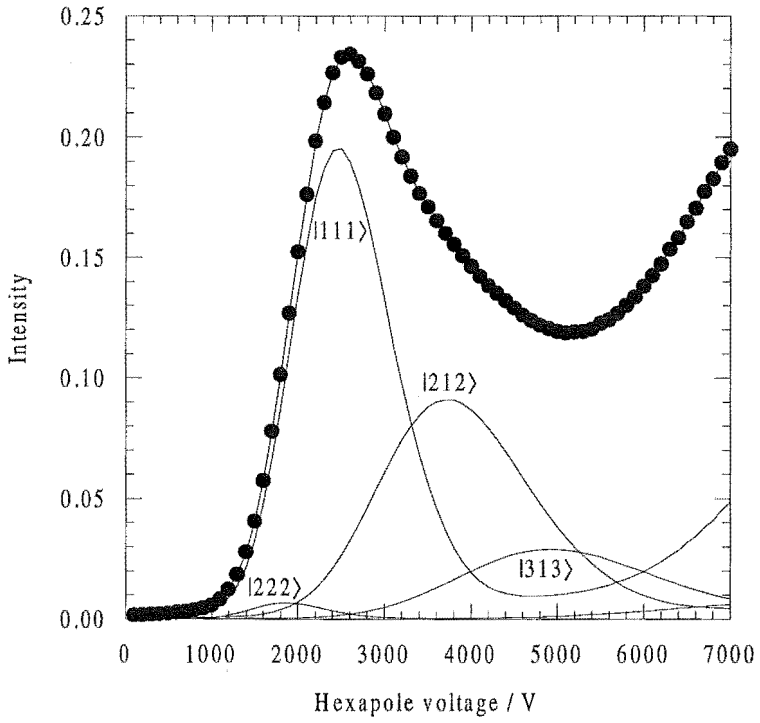

Fig. 9.22. Calculated focusing curve for the 5% CH_3F/Ar beam with individual |JKM⟩ state focusing curves.

9.4.4 Correlation Between Upper Stark State Cross Section and |JKM⟩ State Focusing

It has already been shown that the position of the general features present in the upper Stark state cross section curves (Figs. 9.6-9.13) for each beam are independent of the scattering gas used to attenuate the hexapole focused beam. Hence to simplify the comparison of the upper Stark state cross section curves with the hexapole focusing curves, the cross section curves averaged over all of the scattering gases for each beam will be used. The resulting normalised cross section and focusing data, together with

the calculated |JKM⟩ focusing curves are collated in Figs. 9.23-9.30. Since the calculated focusing curves {9.4.3} do not fully reproduce the experimental focusing curves, the individual calculated |JKM⟩ curves are intended as a guide only to the focusing position and intensity of the upper Stark states present in the transmitted beam. The focusing curves shown are those for the highly populated |JKM⟩ states only. Because of the width of the individual |JKM⟩ state focusing curves, the features shown in the upper Stark state cross section curves are the result of overlap between |JKM⟩ states focused at similar voltages.

It is clear from Figs. 9.23-9.30 that the variation in the upper Stark state cross sections with hexapole voltage match the features present in the focusing curves. This is especially apparent for the seeded beams where the rotational temperature is lower and hence fewer rotational states are populated giving improved state resolution. For the CH_3Cl series the beam velocity is greatest for the pure CH_3Cl beam and slowest for the CH_3Cl/Xe seeded mixture. The state resolution shown by the upper Stark state cross section curves is expected to increase with increasing beam velocity, as the |JKM⟩ focusing positions shift to higher voltage and are therefore more widely spaced according to equation 9.13.

For the pure CH_3Cl beam, Fig. 9.23, the cross section peaks around 3600 V which is within the calculated uncertainty of the position of the |111⟩ focusing voltage at 3400 V. Below this voltage the cross section generally decreases as |JKM⟩ states with $J = K = M > 1$ are focused by the hexapole. As hexapole voltage is increased above 3600 V there is a decrease in the cross section to a minimum at 4600 V and then increase again to another peak around 5200 V corresponding to focusing of the |212⟩ and |423⟩ states. At 4600 V there are no highly populated states focused. Above 5200 V the cross section decreases with a small peak at the |524⟩ focusing voltage of 6400 V. Moving to the Ar seeded beam, Fig. 9.24, this pattern is repeated at lower voltage. The cross section peaks around the |111⟩ focusing voltage at 2300 V, decreases down to 2800 V and then peaks again at 4000 V where the |212⟩, |423⟩ and |524⟩ states are focused. Above this voltage the cross section again decreases to a minimum at 5000 V and then

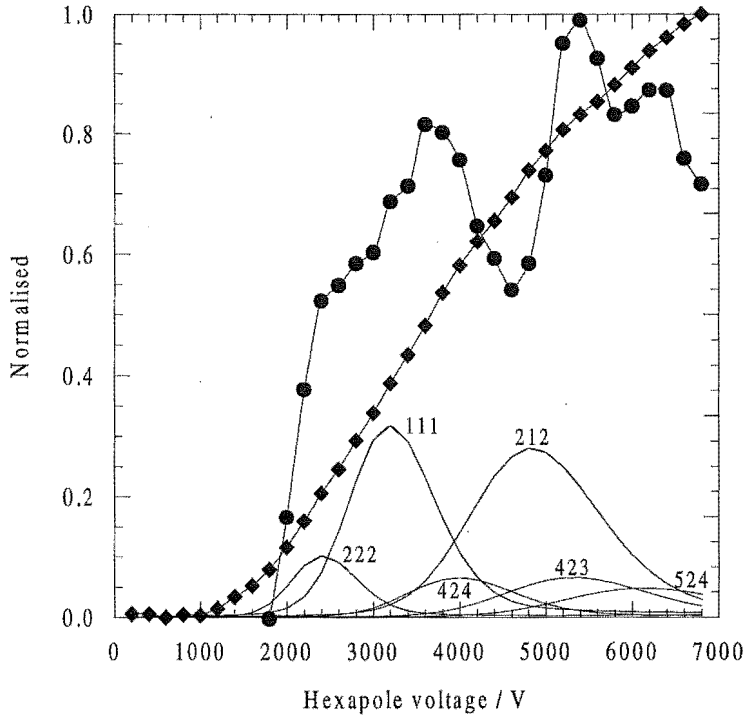

Fig. 9.23. Defocusing cross sections averaged over all scattering gases (●) compared to the focusing curve (◆) and calculated |JKM⟩ state voltages for CH_3Cl.

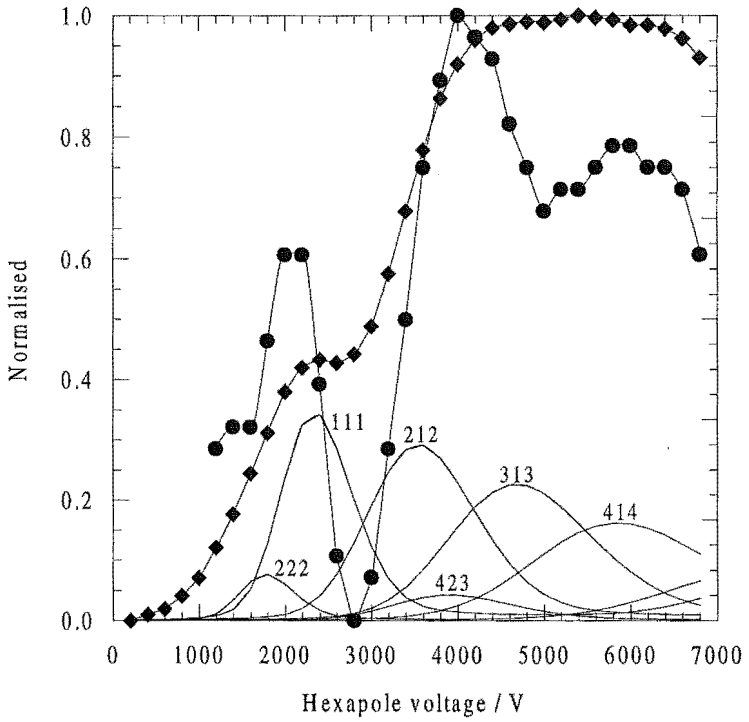

Fig. 9.24. Defocusing cross sections averaged over all scattering gases (●) compared to the focusing curve (◆) and calculated |JKM⟩ state voltages for 5% CH_3Cl/Ar.

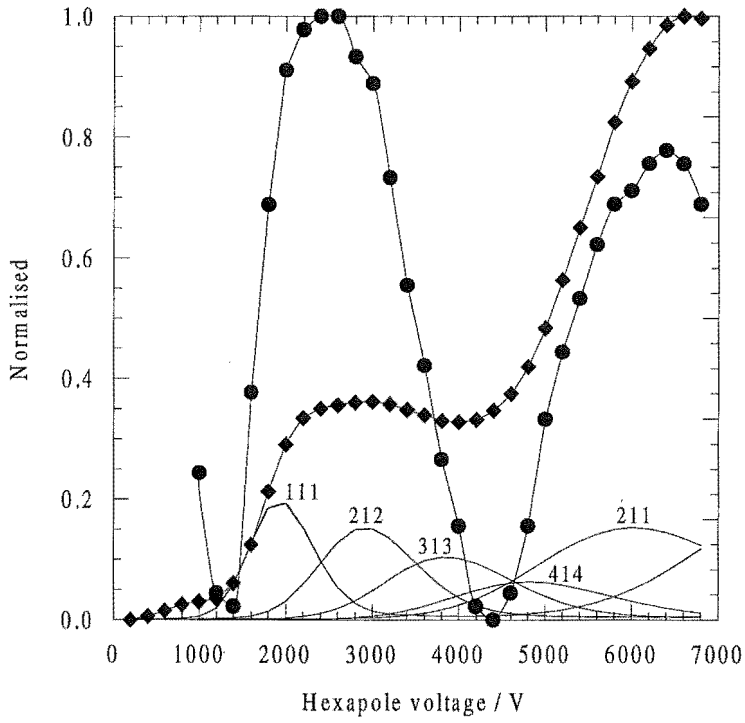

Fig. 9.25. Defocusing cross sections averaged over all scattering gases (●) compared to the focusing curve (◆) and calculated |JKM⟩ state voltages for 5% CH_3Cl/Kr.

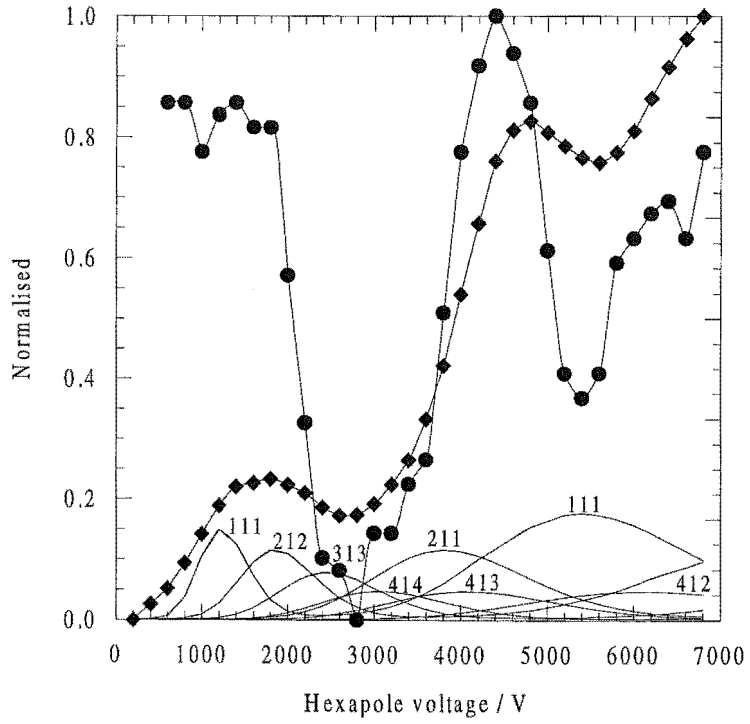

Fig. 9.26. Defocusing cross sections averaged over all scattering gases (●) compared to the focusing curve (◆) and calculated |JKM⟩ state voltages for 5% CH_3Cl/Xe.

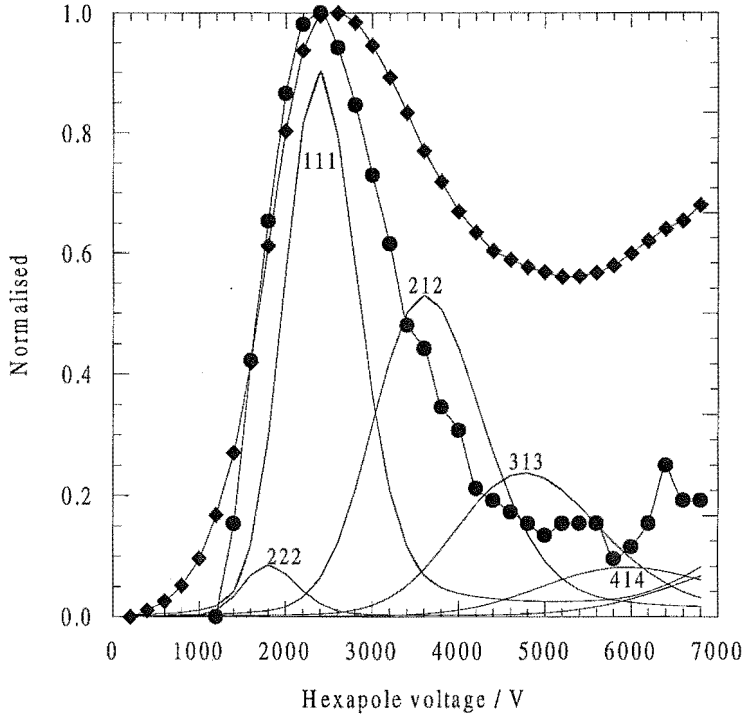

Fig. 9.27. Defocusing cross sections averaged over all scattering gases (●) compared to the focusing curve (◆) and calculated |JKM⟩ state voltages for 5% CH_3F/Ar.

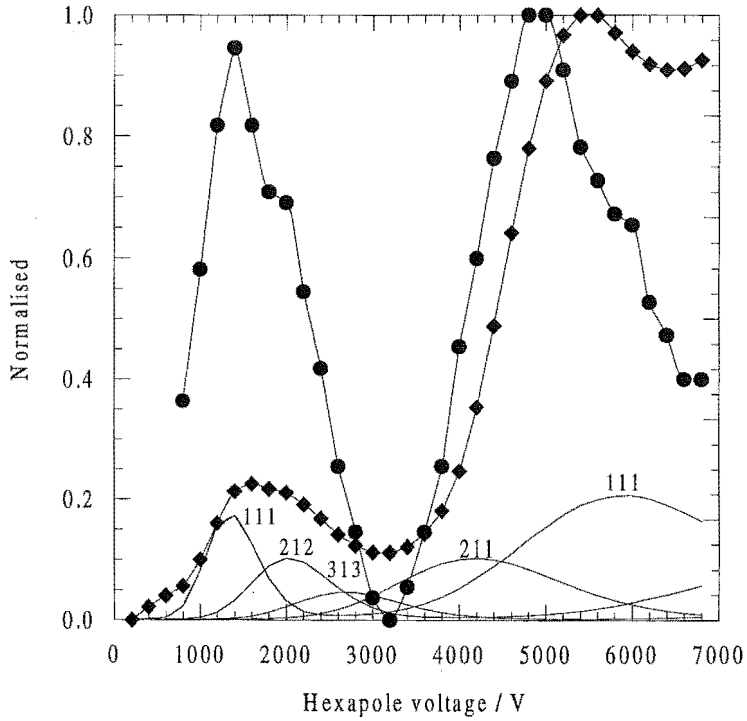

Fig. 9.28. Defocusing cross sections averaged over all scattering gases (●) compared to the focusing curve (◆) and calculated |JKM⟩ state voltages for 5% CH_3F/Kr.

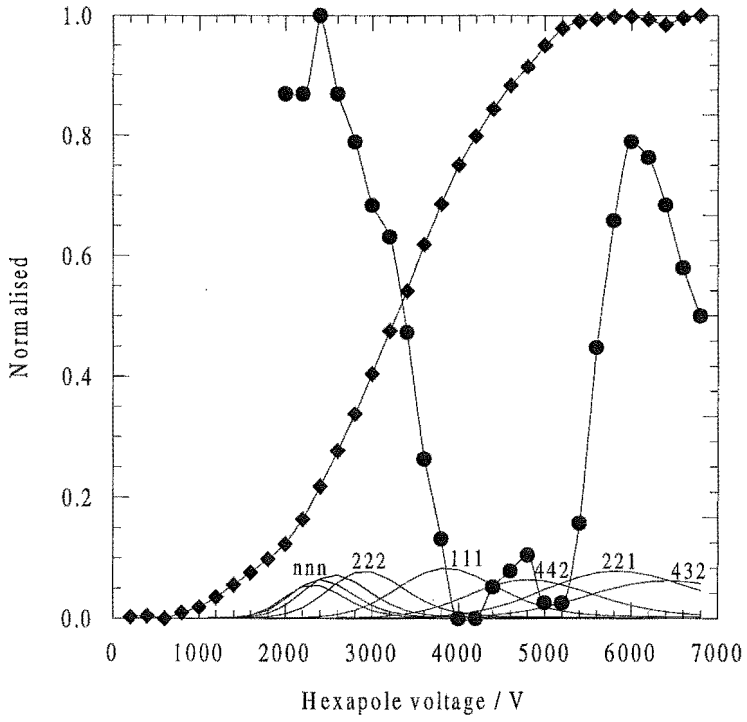

Fig. 9.29. Defocusing cross sections averaged over all scattering gases (●) compared to the focusing curve (◆) and calculated |JKM⟩ state voltages for CF_3H.

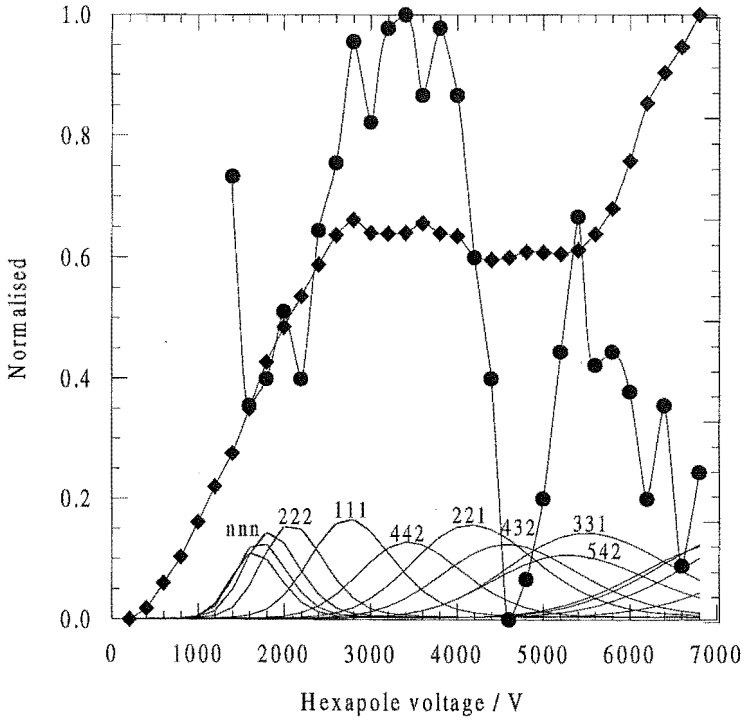

Fig. 9.30. Defocusing cross sections averaged over all scattering gases (●) compared to the focusing curve (◆) and calculated |JKM⟩ state voltages for 5% CF_3H/Kr.

peaks again at 5800 V where the |414⟩ state is focused. Changing to the Kr seeded beam, Fig. 9.25, produces some slight differences. At low voltage the state resolution is no longer good enough to differentiate between the |111⟩ and |212⟩ peaks. The minimum between these states present for the CH_3Cl and CH_3Cl/Ar beams, is lost as the rotational states are closer together and hence cannot be resolved. The high hexapole voltage behaviour shown for the Ar seeded beam is extended however with the highest voltage peak for the Kr seeded beam occurring at 6400 V corresponding to the |211⟩ rotational state. The |414⟩ state now lies on the shoulder of the |211⟩ peak. Finally for the Xe seeded beam, Fig. 9.26, the trend shown for the Kr seeded beam is continued. At low voltage the |111⟩, |212⟩ peak dominates and at higher voltage the next major peak is at 4400 V where the |413⟩ state is focused. The |211⟩ state shifts to the shoulder of this peak and the |414⟩ to a small shoulder at 3000 V. That is, the peak shifts towards lower ρ from the |414⟩ state to the |211⟩ state to the |413⟩ state as the beam changes from the Ar seed to the Kr seed to the Xe seed. This is due to the decreasing resolution as the beam velocity is decreased causing overlap between the states. At higher hexapole voltage for the Xe seeded beam the cross section passes through another minimum at 5400 V and then peaks again at 6400 V near the |412⟩ state focusing voltage.

The variation of the upper Stark state cross section with hexapole voltage for the seeded CH_3F beams shows a similar correlation with |JKM⟩ state focusing voltages as seen for the CH_3Cl beams. For the CH_3F/Ar beam, Fig. 9.27, the cross section peaks at 2400 V which is the calculated focusing voltage for the |111⟩ state. Towards lower hexapole voltage the cross section generally decreases down to the threshold voltage. Towards higher voltage there are no more peaks in the cross section curve, the states |424⟩, |212⟩ and |423⟩ form shoulders on the main |111⟩ peak. The cross section decreases to a minimum at 5800 V between the |313⟩ and |414⟩ state focusing voltages as is the case for all of the CH_3Cl beams. Above 5800 V the cross section increases again as the focusing voltage for the 211 state is approached. The CH_3F/Kr seeded beam, Fig. 9.28, reproduces the cross section behaviour shown for the CH_3F/Ar beam. The cross section peak at the |111⟩ state position is shifted down to 1400 V and the minimum after the |313⟩ state is at 3200 V. Above this point the cross section curve

peaks again at 4900 V corresponding to the |413⟩ focusing voltage. The |211⟩ and |514⟩ states form shoulders on each side of this peak. Above 4900 V the cross section decreases through the |514⟩ focusing voltage to a minimum at 7000 V.

For the oblate symmetric top CF_3H, Fig. 9.29, the relationship between the upper Stark state cross section and the |JKM⟩ focusing voltages differs from that shown for the prolate CH_3Cl and CH_3F beams. The cross section curve initially shows a general decrease with increasing hexapole voltage as successive |JKM⟩ states where J = K = M are focused. The cross section decreases to a minimum at 4000 V near the |111⟩ focusing voltage. Above this point a small peak at 4800 V corresponds to the |442⟩ state and a further peak at 6000 V is due to the |221⟩ and |432⟩ states. For the CF_3H/Kr seeded beam mixture, Fig. 9.30, the cross section increases with increasing voltage for the states where J = K = M to a peak at 2800 V near the |111⟩ state. Above this voltage is another small peak due to the |442⟩ state at 3400 V and following this a general decrease in the cross section through the |221⟩ and |432⟩ states to a minimum at 4600 V. At higher voltage the cross section peaks again at 5400 V near the |542⟩ and |331⟩ states and then generally decreases again as the voltage increases further.

Because of the finite angular resolution of the hexapole there is a possibility that collisions of focused beam molecules near the exit aperture of the hexapole that result in small changes in ρ (and hence a small change in θ, as $\rho = \cos\theta$) will not prevent the beam molecule from reaching the detector. Hence the cross section for the loss of upper Stark states by a ΔM transition that has a small change in angle θ will be smaller than those for which the change in θ is large {9.3}. For loss of the |111⟩ state, a ΔM transition results in a change in angle of 30° which is large and therefore the upper Stark state cross section is expected to be large due to the high angular resolution. This is shown in Figs. 9.23-9.28 for the CH_3Cl and CH_3F beams where the |111⟩ state always focuses at the lowest voltage peak in the cross section curves. On the other hand the |JKM⟩ states that fall between the peaks in the cross section curves such as the |424⟩ state for the high velocity beams (Figs. 9.23-9.24) and the |313⟩ and |414⟩ states are lost from the focused beam by ΔM transitions that produce a change in the angle θ of 7°, 4°

and 3° respectively. These angle changes are much smaller than for the |111⟩ state, hence the angular resolution is poorer and the upper Stark state cross sections are smaller. Generally, the upper Stark state defocusing cross section is higher for |JKM⟩ states where M is small and lower where M is large.

The same sort of correlation between the upper Stark state cross section and |JKM⟩ state is not as obvious for the CF_3H beam cross section curves. For the rotational temperatures of around 10 K for the CF_3H beams the most highly populated J levels are J = 3 and 4. Therefore there will be a lot of highly populated |JKM⟩ states which focus in the voltage region accessible by the hexapole. Because of this large number of |JKM⟩ states the resolution will be low and attributing the trends in the cross section curves to particular states is difficult. Further investigation of the CF_3H system using different seeded mixtures is required to clarify any real trends.

9.4.5 Upper Stark State Cross Section Velocity Dependence

The defocusing of upper Stark states in the hexapole electric field by rotationally inelastic collisions with a scattering gas, has been attributed to the long range van der Waals attractive interaction {7.3}. Using this interaction potential, the upper Stark state defocusing cross sections are expected to vary with velocity with a dependence of $g^{-0.4}$, where g is the average relative velocity of the beam scattering gas combination. The calculated relative velocities for each beam scattering gas pairing using the beam velocities determined from the calculated focusing curves (Table 9.3) are shown in Table 9.6.

For the four different CH_3Cl gas mixtures used here the velocity dependence for the upper Stark state cross sections measured at the focusing voltages for the |111⟩ state are examined. The linear least squares fits for the graphs of cross section verses $g^{-0.4}$ resulted in fitting coefficients ranging from around 0.93 up to 0.98. So within the

experimental uncertainties associated with the cross section measurements the $g^{-0.4}$ velocity dependence is reproduced by the data. The linear fit for the cross sections measured using Ne scattering gas is shown in Fig. 9.31.

	He	Ne	Ar	Kr	Xe	N_2
CH_3Cl	1269	787	704	657	640	741
CH_3Cl/Ar	1228	720	628	574	555	669
CH_3Cl/Kr	1208	685	587	529	508	631
CH_3Cl/Xe	1173	620	511	443	418	560

Table 9.6. Calculated relative velocities g (ms^{-1}) for each beam scattering gas pair.

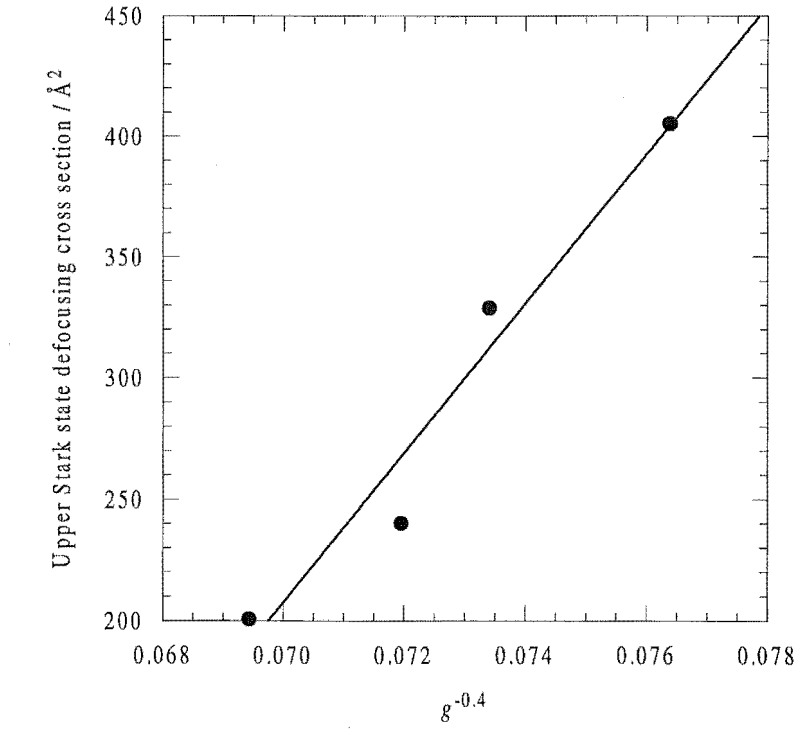

Fig. 9.31. $|111\rangle$ state defocusing cross sections for CH_3Cl with Ne scattering gas for all of the CH_3Cl pure and seeded beams as a function of the average relative velocity.

9.4.6 Correlation with the van der Waals Interaction

The large upper Stark state defocusing cross sections (> 200 Å^2) suggest the defocusing interaction between the focused beam and scattering gas is occurring for separations in excess of 8 Å. At these distances the interaction potential is dominated by the attractive van der Waals interaction $V(r)$ {7.3}. From equations 7.54 and 7.60 it is apparent that the cross section for inducing a defocusing rotational transition of some state $|JKM\rangle$ in the hexapole focused beam is proportional to the cube root of the van der Waals constant. However for each beam scattering gas combination used the relative velocity varies and a comparison of the upper Stark state defocusing cross sections must also take into account the $g^{-0.4}$ velocity dependence which exists for the van der Waals interaction potential.

The upper Stark state defocusing cross sections measured at the calculated hexapole focusing voltages for the $|111\rangle$ state for each of the CH_3Cl molecular beams used are graphed in Fig. 9.32 against $C^{1/3}g^{-0.4}$. The van der Waals constants C are determined using equations 7.55, 7.58 and 7.59 from consideration of the dipole-induced dipole and dispersion van der Waals forces. Fig. 9.32 shows that a linear correlation does exist between the upper Stark state defocusing cross sections and $C^{1/3}g^{-0.4}$, which suggests that the van der Waals interaction potential describes the energy transfer mechanism for the rotationally inelastic defocusing of the hexapole focused upper Stark states.

However, the cross sections measured using He as the scattering gas do not fit well with the rest of the data. The most likely reason for this is due to the low mass and high velocity of the He. This means the pumping speed of the He gas will be much larger than for the other gases used and this could result in pressure gradients being established within the hexapole vacuum chamber. This would manifest as an underestimation of the hexapole region pressure by the baratron and therefore produce cross sections too large. Also the conductance of gas from the hexapole chamber through the hexapole entrance and exit apertures will be greatest for He. Hence the

increase in the scattering length will be most serious for He and again this would result in the cross sections being overestimated.

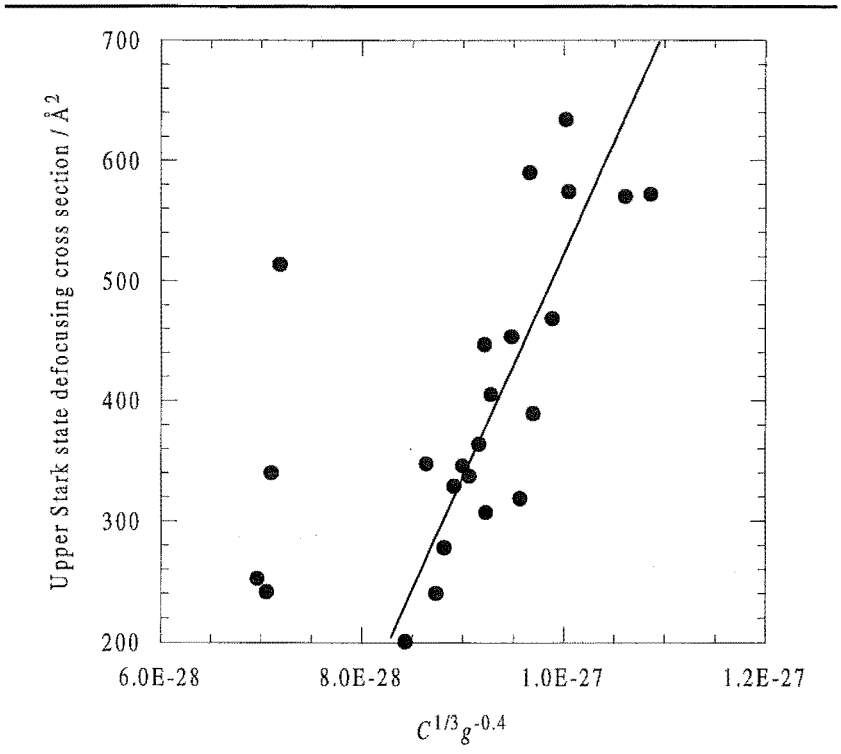

Fig. 9.32. $|111\rangle$ state defocusing cross sections for all of the pure and seeded CH_3Cl beams with all of the scattering gases, as a function of the calculated van der Waals constant and relative velocity dependence. The least squares fit includes all the experimental cross sections except for the four outlying points on the left hand side of the graph due to the cross sections measured with He scattering gas.

9.4.7 Upper Stark State Defocusing Processes

In order to determine what rotational transitions are responsible for the defocusing of the upper Stark states, the maximum separation at which the transition energy can be lost to or absorbed from the interaction potential must be considered. For collisions between CH_3Cl and Ar the energy difference for a $\Delta J = 1$ transition from $|111\rangle$ to $|211\rangle$ is equal to 20.7 $Jmol^{-1}$. For the van der Waals potential this energy is available at a separation of 8.4 Å which corresponds to a cross section of 222 $Å^2$. Similarly for

the spectroscopically forbidden $\Delta K = 1$ transition from $|111\rangle$ to $|101\rangle$ the energy change is 56.4 $Jmol^{-1}$ which requires closer approach to 7.1 Å and gives a cross section of 158 $Å^2$. For the $\Delta M = 1$ transition the energy is much smaller as it is simply due to the Stark energy in the hexapole electric field. For the hexapole field strength at a point halfway from the hexapole axis to the rods the energy change for the transition $|111\rangle$ to $|110\rangle$ is 0.76 $Jmol^{-1}$. This is a very small amount of energy compared to the ΔJ and ΔK transitions and hence it will occur at large separation, 14.6 Å in this case. This gives a cross section of 670 $Å^2$. The experimental cross section for defocusing at the $|111\rangle$ hexapole focusing voltage by Ar varies from 278 $Å^2$ for the pure CH_3Cl beam up to 634 $Å^2$ for the slower CH_3Cl/Xe seeded beam. The calculated cross sections assume zero relative velocity in the collision and are therefore upper limits for the true cross section. From these considerations the process by which the upper Stark states are defocused from the beam must be due to M changing transitions. The separations at which ΔK transitions would become important appear to be too small to have any part in the defocusing processes here. However, ΔJ transitions for low J states produce cross sections comparable to the experimental values and hence could contribute to the defocusing of the upper Stark states.

9.5 Conclusions

The cross section for defocusing of upper Stark states focused by a hexapole electric field have been measured for a variety of symmetric top alkyl halide molecular beams by attenuation with a range of scattering gases. The cross sections have been shown to be dependent on the $|JKM\rangle$ upper Stark state population of the focused beam and therefore have been attributed to rotationally inelastic collisions changing the focused upper Stark state to a non focused rotational state. The variation is accounted for from consideration of the change in angle θ that accompanies the change in $|JKM\rangle$ rotational state for the defocused beam molecules. The upper Stark state defocusing cross section is large when the change in angle is large and small when the change is

small. This is due to the lower angular resolution of the hexapole for defocusing of $|JKM\rangle$ states where the rotational transition results in a small change in angle θ. Generally, $|JKM\rangle$ states where M is small will give large defocusing cross sections and states with larger M will lead to smaller cross sections.

The long range attractive van der Waals interaction has been used to model the defocusing collisions and this accounts for the velocity dependence and magnitude of the cross sections. From consideration of the separation at which the rotational transition energy is available from the interaction potential, the defocusing cross sections of the upper Stark states must be due to ΔM changes with the possibility of ΔJ changes for states with low J. In order to gain more experimental evidence in support of this, the rotational state distribution of the attenuated beam must be examined with a further hexapole field. Two new hexapoles have recently been made to investigate this in the near future.

Chapter 10

Future Directions

Of the three separate experiments described in this thesis, work is continuing on the upper Stark state defocusing cross section measurements, and crossed beam experiments involving the alkali metal ions and spatially oriented alkyl halides are planned.

Presently, the hexapole used in the upper Stark state defocusing cross section measurements has been removed and replaced by two shorter hexapoles separated by a region containing both dc and radio frequency (rf) electric fields. The first hexapole is used to state select the upper Stark states in the molecular beam, the centre dc-rf field region is used to resonate rotational transitions of the upper Stark state molecules, and the final hexapole field is used to analyse the upper Stark state population of the beam. In the limit of no rf field in the centre region and a dc field of suitable magnitude to ensure the upper Stark states undergo adiabatic transitions moving from the first hexapole to the dc orienting field to the second hexapole field, the overall arrangement will act as a single hexapole. However, when a rf field is applied in the centre region, rotational transitions in resonance with ν/E ($\propto K/J(J+1)$), the ratio of the rf frequency to the dc field strength, can be excited and the upper Stark state population will be modified. For dc fields around 100 Vcm^{-1} and a rf frequency around 1 MHz, $\Delta M = \pm 1$ transitions will be excited. The upper Stark state signal transmitted by the second

hexapole can then be recorded as a function of the rf-dc ratio and state resolved information on the |JKM⟩ upper Stark state populations can be gained.

If a scattering gas is introduced to the first hexapole region, the upper Stark states in the beam can undergo rotationally inelastic collisions with the gas thus modifying the state distribution of the focused beam. The state resolved rotationally inelastic cross sections for these collisions can therefore be measured using the dc-rf field and second hexapole to analyse the changes in the transmitted upper Stark state populations.

The ion molecule chemistry observed for the K^+ ion with CH_3X and tertiary C_4H_9X {3.4.2, 3.4.3, 3.5}, where X = Cl or Br, is to be studied in crossed ion molecule beams. Furthermore, the orientation dependence of the reactions will be studied by spatially orienting the symmetric top alkyl halide beam using a hexapole and a dc orienting field in the crossed beam collision region. It is hoped that variations in reactivity will be observed as a function of the relative spatial orientation of the symmetric top alkyl halides to the alkali ion beam. Further reactions involving other alkali metal ion beams and investigation of the orientation dependence of the S_N2 reaction mechanism using halide ion beams are also proposed.

Since there will be appreciable momentum transfer involved in the reactive ion molecule collisions, the angular dependence of the products scattered from the interaction will need to be determined. Therefore a position sensitive detector is required. A simple option is to mount a CEM such that it can be rotated about the scattering centre in the plane of the beams. If the detection of neutral products is desired then an ionisation source can be attached to the front of the CEM. In order to identify the products arriving at the detector, the CEM will need to be replaced by a rotatable quadrupole mass spectrometer so the scattered products can be mass filtered. It is hoped that in the near future an Ion Imaging detection system will be acquired which will allow the scattered products from the ion molecule reactions to be detected in far less time than is required for the rotatable detectors.

Appendix A

Alkali Ion Emitters

A.1 Thermionic Alkali Metal Ion Emitters

A.1.1 Alumino-Silicates

The thermionic emission of ions from heated surfaces has been known for some time [Richardson, 1916]. Early work by Blewett and Jones [Blewett, 1936] investigated the use of various lithium alumino-silicates coated on tungsten or platinum filaments to produce beams of positive lithium ions. Of the compounds they studied the best ion emitters they found were β-eucryptite; $Li_2O.Al_2O_3.2SiO_2$, followed by spodumene; $Li_2O.Al_2O_3.4SiO_2$, both naturally occurring minerals. Emission of Li^+ ions from β-eucryptite was observed for filament temperatures around 1000°C up to the reported melting point for β-eucryptite of 1306°C. Li^+ beam currents up to 1 mA per cm^2 of emitter surface were readily obtained at 1150°C. The lifetime for a filament made up of 250 mg of β-eucryptite running at an emission current of 100 μA was estimated at a few hundred hours. In this time 90% of the lithium present in the filament is emitted as Li^+ ions with only negligible amounts released as neutral Li atoms or LiO.

The excellent emission characteristics of β-eucryptite led to the preparation of analogues of β-eucryptite for the other alkali metal ions [Allison, 1961; Blewett, 1936; Heinz, 1968; Wizemann, 1986], that is $X_2O.Al_2O_3.2SiO_2$ where X = Na, K, Rb, Cs. The alkali ion emission from these was enhanced by the addition of excess X_2O in the preparation of the material. Mass spectrometric analysis of the synthetic compounds $X_2O.Al_2O_3.2SiO_2$ for all five alkali ions showed pure emission of the appropriate ion with only 1-2% impurity from other alkali ions.

A.1.2 Zeolites

Weber and Cordes [Weber, 1966] proposed the use of Linde type A zeolite [Breck, 1956], a synthetic sodium alumino-silicate as a sodium ion source. Type A zeolite has the formula $Na_{12}(AlO_2)_{12}(SiO_2)_{12}.27H_2O$ and structurally consists of a three dimensional network of AlO_4 and SiO_4 tetrahedra. The interstices in the lattice are filled by the Na^+ ions and the water molecules. Each unit cell consists of 24 AlO_4 and SiO_4 tetrahedra forming cavities of 11.4 Å diameter separated by openings of 4.2 Å diameter and smaller cavities of 6.6 Å diameter separated by 2.0 Å diameter openings. Ion exchange has been used to successfully produce the Li^+, Na^+, K^+ and Cs^+ forms of the type A zeolite [Beck, 1989; Freeman, 1961; Satoh, 1987; Weber, 1966]. Satoh *et al* [Satoh, 1987] measured ion beam currents of up to 100 μA for Li^+, Na^+, K^+ and Cs^+ type A zeolites.

Pargellis and Seidl [Pargellis, 1978] investigated the Na^+ form of type Y zeolite; $Na_2O.Al_2O_3.5SiO_2$ and the zeolite Na-mordenite; $4Na_2O.4Al_2O_3.40SiO_2$. The Na-mordenite was exchanged for K^+, Rb^+ and Cs^+ but the Li^+ form was not able to be made. Ion currents were of the same magnitude as those observed for the type A zeolite emitters. Operating the ion sources in pulsed mode led to beam current densities two orders of magnitude greater than the currents measured under continuous operation. This was also shown by Satoh *et al* [Satoh, 1987] for K^+ type A zeolite.

The emission of neutral material from the zeolites was investigated by Pargellis and Seidl [Pargellis, 1978]. This is important as the purity of the ion beam and the lifetime of the ion source will be decreased if alkali ions are emitted in a neutral state as either atoms or molecules. They measured the ion signal produced by ionising the neutral species desorbing from the zeolite surface. Mass spectrometric detection was used to check that the ion current was due to desorbing neutral alkali fragments. Ratios of neutral signal to ionic signal were found to vary from 10^{-3} for continuous emission down to 10^{-6} for high voltage pulsed operation, that is in any situation neutral emission accounts for only a fraction of a percent of the total alkali ion emission.

This work utilised the readily available type A zeolite (Linde 4A) molecular sieve as a source for Li^+, Na^+ and K^+ ion beams as well as type Y zeolite as a source for Na^+ ions.

A.2 Preparation

Two approaches can be taken to produce the desired alkali ion emitter. Commercially available zeolites can be ion exchanged in solutions containing the alkali ion to be used [Beck, 1989; Freeman, 1961; Pargellis, 1978; Satoh, 1987; Weber, 1966], or alkali alumino-silicates can be made by heating appropriate stoichiometric amounts of alkali salts with Al_2O_3 and SiO_2 [Allison, 1961; Blewett, 1936; Heinz, 1968; Wizemann, 1986].

A.2.1 Ion Exchange

Ion exchange [Helfferich, 1962] is the process whereby solid insoluble materials exchange cations or anions with a solution in which they are mixed. Materials which can exchange cations with a solution are known as cation exchangers and similarly for

anions. This work is concerned only with zeolites a subgroup of the cation exchangers. Zeolites consist of a negatively charged rigid three dimensional lattice of AlO_4 and SiO_4 tetrahedra forming a series of cavities and channels containing water, other small molecules and the positive alkali counter ions. When a zeolite in Na^+ form (NaX) is added to an aqueous solution containing K^+ the following equilibrium is reached

$$NaX + K^+_{(aq)} \rightleftarrows KX + Na^+_{(aq)}. \qquad (A.1)$$

The mechanism of ion exchange is simply interdiffusion of the zeolite Na^+ counter ions with the K^+ ions from the solution through the channels of the zeolite lattice. As well as exchange of ions the zeolite can absorb solvent, usually water, or other molecules of a small enough size to pass through the lattice channels. This can result in the unwanted presence of ionic species in the zeolite other than the desired alkali ions. Uptake of solvent can result in swelling of the zeolite framework, the degree of which is governed by the structural forces of the lattice. Swelling can have an effect on the ion exchange properties of the zeolite by changing the diffusion coefficients of the alkali ions in the zeolite and hence modifying the kinetics of diffusion through the channels.

The ion exchange equilibria is not just a statistical redistribution of counter ions between the ion exchanger and the solution. Usually the ion exchanger will have a preference for one or the other of the competing counter ions. The selectivity of the ion exchanger is based on the following effects:

- Counter ion charge
- Counter ion solvated volume
- Counter ion polarisability
- Counter ion interactions with fixed ionic groups in the lattice
- Counter ion interactions with other components in the solution
- Degree of crosslinking of the ion exchanger
- Concentration of the solution
- Temperature.

In general the ion exchanger prefers the counter ion of highest charge. This can be explained using the Donnan potential [Helfferich, 1962]. The Donnan potential attracts ions into the ion exchanger lattice. The force of this attraction is dependent on the ionic charge and hence the counter ion of highest charge is favoured.

Swelling of the ion exchanger matrix by solvent uptake leads to high strain in the lattice. This strain can be decreased by the ion exchanger losing ions of large solvated volume for ions of smaller solvated size. Furthermore large solvated cations may be excluded by the sieve action of the ion exchanger. This occurs in zeolites where channels may be too small to allow passage of large cations hence preventing diffusion into the zeolite. A consequence of this in zeolites containing channels of different sizes, is the larger cation may be able to pass into the larger channels but is prevented from entering the smaller channels. This means the smaller cation can never be totally removed by the larger leading to a zeolite containing a mixture of counter ions.

The strength of the electrostatic interaction between fixed ionic groups in the lattice and the counter ion is dependent on the ionic charge and the distance between the charged lattice sites and the ion. Ion's with high polarisability are more strongly attracted by the lattice and will be favoured over ions of a similar size but lower polarisability.

In some instances counter ions can form ion pairs or even covalent chemical bonds with the fixed ionic groups in the ion exchanger lattice. The removal of the labile counter ions from the ion exchanger matrix by bonding, forces the ion exchange equilibrium to shift and displaces the non bonded counter ions in favour of the counter ions that can form strong bonding interactions with the lattice.

The removal of counter ions by complexation with other ions or neutral species in the solution, causes the ion exchange equilibrium to act to remove more of the complexing counter ion from the ion exchanger. This means the ion exchanger favours the counter ion having the least tendency to bind in the solution. Selective precipitation of one of the counter ions with anions in the solution also has the same effect.

An increased degree of crosslinking of the ion exchanger results in a more rigid lattice. The ability of a highly crosslinked matrix to swell is reduced so the uptake of highly solvated counter ions is disfavoured and the selectivity of the ion exchanger is increased.

The concentration of the solution also affects the selectivity. The Donnan potential increases with decreasing solution concentration thus favouring the counter ion of greatest charge density.

Interactions between the counter ions and the solution or the lattice fixed ionic sites, are disfavoured by increasing temperature. Hence the selectivity is increased for decreasing temperature.

For zeolites the rigid lattice means the swelling capacity of the matrix is very minimal. Selectivity factors based on swelling are relatively unimportant for zeolites, counter ion size and lattice interactions are the most important properties. The sieve action of the zeolites has already been mentioned, a result of the regular and rigid structure of the lattice. The overall selectivity of the zeolites is greater than for the resin type ion exchangers.

Experimental ion exchange methods fall into two areas, the column and batch techniques. The batch technique is very simple. A solution containing the required alkali cation is stirred together with the zeolite and allowed to come to equilibrium. The zeolite is finely ground to increase the surface area presented to the solution and hence to increase the rate of ion exchange. Because the system is closed and the overall composition does not change as equilibrium is reached, the initial conditions of the mixture fully determine the extent of the ion exchange of the desired alkali ions into the zeolite. For this reason complete ion exchange of the zeolite may not be attained in a single batch equilibration. Multiple steps involving filtering the zeolite and remixing with fresh solutions may be needed to produce full ion exchange of the zeolite.

Breck *et al* [Breck, 1956] used the batch method to ion exchange the Na^+ form of type A zeolite with the alkali metal ions as well as other alkali earth and transition metal ions. At room temperature in solutions containing an amount of exchanging cation equivalent to the amount of Na^+ present in the zeolite sample, the degree of exchange ranged from 88% for Ag^+ down to 31% for Cs^+. Increasing the initial amount of exchanging ion in the solution led to increased conversion of the zeolite to the new form. The poor degree of exchange for Rb^+ and Cs^+ ions are an example of the sieve properties of the type A zeolite. The large ions can only move into the larger cavities present in the zeolite matrix, Na^+ is retained in the smaller cavities.

Weber and Cordes [Weber, 1966] also used the Na^+ form of type A zeolite. They produced sources for Na^+, K^+ and Cs^+. The zeolite was added to a solution containing a four fold excess of the exchanging alkali cation, sealed in a Pyrex tube and heated in a water bath at 95°C for two days. The solution was constantly stirred to keep the zeolite well mixed. After two days the zeolite was filtered and placed in fresh solution for further exchange. Again after two days the zeolite was filtered, washed with distilled water and dried in an oven at 100°C. The zeolite was then ground back to a fine powder ready for use.

Beck *et al* [Beck, 1989] exchanged Na^+ type A zeolite with a three fold excess of alkali ions for 24 hours in a room temperature stirred solution. Exchange was carried out for K^+ and Cs^+. Mass spectrometric analysis of the emission from the resulting ion sources showed the exchange was in excess of 99%. No more exchange was observed when the zeolite was stirred in fresh solution for any further period.

In the column method the powdered zeolite is packed into a column and the solution containing the cation to be exchanged into the zeolite matrix is allowed to percolate slowly down through the finely ground zeolite. The immediate advantage of this technique over the batch method is the flow of the alkali ion solution through the zeolite bed continually exposes the zeolite to fresh solution rich with the desirable alkali ions and devoid of the counter ions from the zeolite. Thus the flow through the column can be regarded as a series of incomplete equilibrations successively resulting in the

complete ion exchange of the zeolite with the alkali ions from the solution. Initially the top of the column will undergo ion exchange with the feed solution. As time passes the top will be totally converted to the exchanged form and the zone where ion exchange occurs will be displaced down the column. Eventually the entire zeolite column will be converted (Fig. A.1).

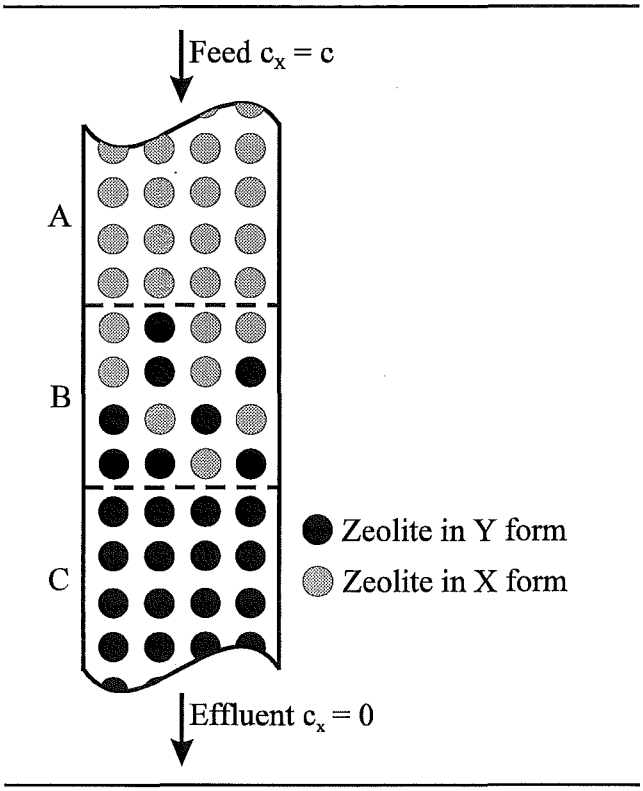

Fig. A.1. The feed solution containing the cation X^+ (concentration $c_X = c$) is passed through the zeolite in the Y form. In zone A exchange of X^+ for Y^+ has completely converted the zeolite to the X form. B is the ion exchange zone where the zeolite is in both X and Y forms. In zone C the zeolite is still in the Y form. When the ion exchange zone has shifted down to the bottom of the column the effluent will contain X^+ ions for the first time, that is $c_X > 0$.

The major factors improving the efficiency of the column exchange are:

- Preference of the ion exchanger for the cation from the feed solution
- Small, uniform particle size
- High temperature

- Low flow rate
- Low concentration of the cation in the feed
- High column length or aspect ratio.

Any small volume of solution will be in contact with a given layer of the zeolite for a short time. This is usually too short to allow complete ion exchange equilibrium to be established, therefore any factors which tend to increase this contact time and hence slow the rate at which the zone of exchange moves down the column will improve the efficiency of the ion exchange in the column. Running the column at high temperature to enhance the diffusion of ions through the zeolite and using a finely ground zeolite will promote a high rate of ion exchange. On the other hand the elevated temperature may cause a decrease in selectivity of the column and the small particle size will produce a large resistance to the flow of the feed solution. Low flow rates of the feed coupled with low concentration of the exchanging cation in the solution will reduce the rate of motion of the exchanging zone allowing more time for equilibrium to be reached. Increasing the length of the zeolite column or increasing the aspect ratio of length to diameter will improve the utilisation of the zeolite but will result in greater flow resistance.

Freeman and Stamires [Freeman, 1961] used the Na^+ forms of types A, X ,Y zeolites and exchanged them with various cations including the alkali metals the alkaline earths and silver. They found all three Na^+ zeolites could be completely exchanged for Ag^+. In situations where ion exchange with the Na^+ zeolite was unfavourable the Ag^+ was used instead. Use of the thiocynate or chloride salt of the exchanging cation provided a driving force for the ion exchange equilibrium with the Ag^+ zeolites. Formation of the soluble silver thiocynate complex or the insoluble silver chloride forces the ion exchange equilibrium in the required direction. Near 100% conversion was attained for all the type A zeolites that were prepared. Pargellis and Seidl [Pargellis, 1978] ion exchanged the Na^+ form of mordenite for K^+, Rb^+ and Cs^+ in a column at room temperature. They were unable to produce the Li^+ form.

Satoh *et al* [Satoh, 1987] ion exchanged type A zeolite for Li^+, Na^+, K^+ and Cs^+. They used the powdered commercial molecular sieve form which is initially in the Na^+ form. The exchange was carried out in a Pyrex column with flow rates of around 0.5 mL min^{-1}. The chloride salt of the alkali metals was used and the concentration of the feed solution was 1 mol L^{-1}. Ion exchange was carried out at 80°C for Li^+ and room temperature for the other ions. Full exchange was attained for the Li^+, Na^+ and K^+ ions but because of the sieve effect of the zeolite only the larger cavities could be occupied by Cs^+. The longest exchange time was 75 hours for the Li^+ ions. The exchanged zeolites were washed and dried before use. Examination of the emission from the Cs^+/Na^+ zeolite showed Cs^+ but no Na^+ in the beam. The ionic work function for the removal of Cs^+ ions from the zeolite is 1.3 eV, significantly lower than the Na^+ work function of 2.8 eV, hence the ion source can be run at lower temperature where there is only enough energy to emit Cs^+ from the zeolite matrix giving the exclusive emission of Cs^+ ions.

A.2.2 Synthesis

Blewett and Jones [Blewett, 1936] synthesised various lithium alumino-silicates to study the effect of composition on the alkali ion emission. The compounds were made by mixing stoichiometric quantities of Li_2CO_3, $Al(NO_3)_3.9H_2O$ and pure powdered quartz at 1400°C. The resultant melt was powdered and melted again to ensure reaction was complete. The compositions prepared are listed in Table A.1 from the best emitter at the top to the least successful at the bottom.

Synthesis of the alumino-silicates of the other alkali metals was based on the β-eucryptite structure; $X_2O.Al_2O_3.2SiO_2$, where X = Li, Na, K, Rb, Cs. The compounds were enriched with X_2O until no further enhancement of the emission was observed. The potassium source $3K_2O.Al_2O_3.2SiO_2$ was prepared which showed good emission.

Allison and Kamegai [Allison, 1961] have also produced β-eucryptite. They mixed finely powdered Li_2CO_3, Al_2O_3 and SiO_2 together and compressed it into a die at 16000-18000 lb in^{-2}. The tablets are melted inside a platinum crucible in an induction furnace at temperatures up to 1800°C. The melt must be kept at this high temperature for 10 minutes to ensure all CO_2 liberated from the Li_2CO_3 is evolved. If any CO_2 is retained it can result in the emitter material flaking off the filament during use in an ion source.

Li_2O	Al_2O_3	SiO_2	Compound
1	1	2	(β-eucryptite)
1	1	4	(spodumene)
1	1	6	
2	1	5	
3	1	3	
1	0.12	1.6	
1	0	1	

Table A.1. Composition of the lithium alumino-silicates prepared by Blewett and Jones [Blewett, 1936]. The emissivity of the compounds decreases down the table.

A somewhat simpler approach was taken by Wizemann and Gaukler [Wizemann, 1986]. Using the same starting materials as Allison and Kamegai, they immersed a double loop of tungsten wire into the powdered mix and heated the wire up to 1500°C under vacuum using an electron microscope cathode supply. A current of about 2.6 A was required to initiate the reaction and this was maintained until the evolution of CO_2 from the melt ceased. When removed, the wire loop contained a glassy pellet of the β-eucryptite ready for use in an ion source.

A.3 Ion Sources

An ion source is required to deliver an alkali metal ion beam of up to 100 μA intensity for use in crossed beam reactions with spatially oriented symmetric top molecules. The alkali ions are to be produced by thermionic emission from synthetic alumino-silicates or zeolites mounted on heated filaments and focused into beams by appropriate ion optics. Both the stability of the ion source intensity over the course of an experiment and the useful emission lifetime are important factors to be considered. Alkali ion sources can be designed with a large reservoir of emitting material to increase the lifetime of the source. The emission current from the source is limited by the diffusion of the alkali metal ions in the emitting matrix so the intensity should remain constant until the emitter becomes heavily depleted of alkali ions. Hence the use of a reservoir should retain the emission stability for longer.

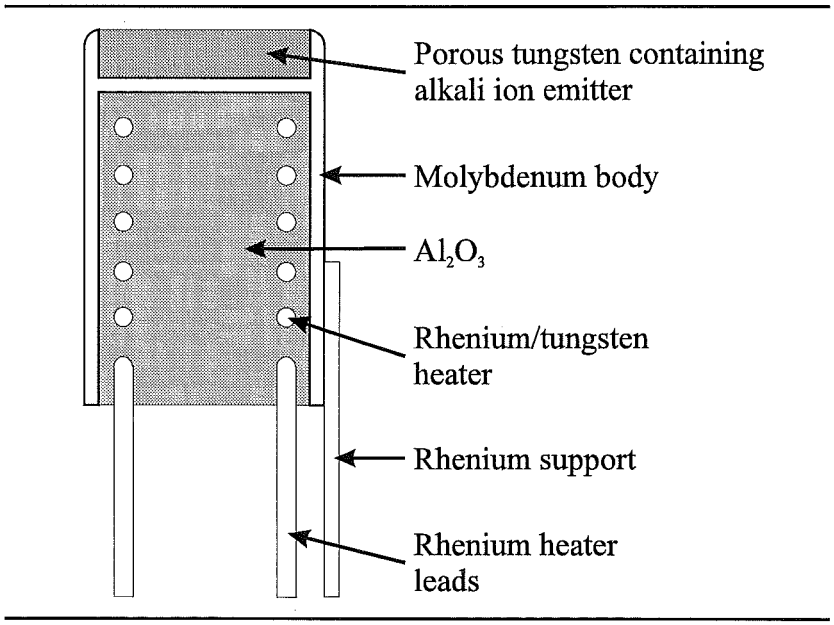

Fig. A.2. Spectra-mat 250 ion source, scale 5:1.

Fig. A.2 shows the commercial 250 alkali ion source available from Spectra-mat inc. They are available as lithium 6, lithium 7, sodium, potassium, rubidium or cesium emitters. The lithium emitter has been described by Heinz and Reaves [Heinz, 1968]. They used an indirectly heated porous tungsten disc into which β-eucryptite had been

melted (Fig. A.2). Emission currents up to a few hundred microamps were attained with lifetimes of 200 hours without any signs of deterioration of the emission. Initial operation revealed a small fraction of other alkali ion impurities present. These diminished rapidly to a fraction of a percent within a few hours of ageing of the source. The sources are recommended for low energy emission; <100 eV, and are capable of producing an energy spread of less than 0.5 eV.

Beck *et al* [Beck, 1989] used a source with a reservoir for the zeolite. A small stainless steel cylinder is used to contain the zeolite. At one end a rhenium filament is embedded in the zeolite to provide the necessary heat for emission. The zeolite is ground with water to form a paste before being packed into the reservoir in a layered manner allowing drying between layers. Upon heating the zeolite solidifies encapsulating the filament. The extraction of ions and formation of a beam is handled by two electrodes mounted on the front of the reservoir cylinder. The source is shown in Fig. A.3. Beam currents of a few microamps at energies up to 5 keV were maintained for over 300 hours of operation with less than 5% drift in the emission intensity.

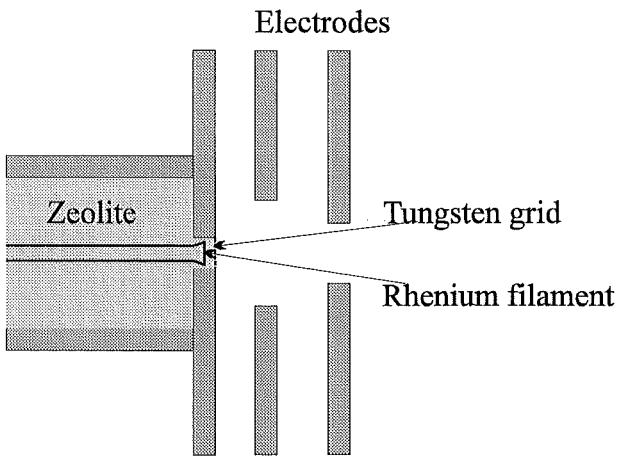

Fig. A.3. Ion source used by Beck *et al* [Beck, 1989].

Appendix B

Ionisation Efficiency Curves

The experimental electron impact ionisation cross section data graphed in Figs. 6.10-6.14 is tabulated below [Vallance, 1997b].

Electron energy (eV)	Ionisation cross section ($Å^2$)	Electron energy (eV)	Ionisation cross section ($Å^2$)
15.76	0	120	2.44
30	1.71	130	2.39
50	2.59	140	2.32
60	2.7	150	2.33
70	2.81	160	2.25
80	2.8	170	2.04
90	2.76	180	1.94
100	2.7	190	1.78
110	2.6	200	1.75

Table B.1. Ar ionisation cross sections as a function of the electron energy.

Electron energy (eV)	Ionisation cross section (Å^2)	Electron energy (eV)	Ionisation cross section (Å^2)
12.6	0	120	3.13
25	0.14	130	2.94
30	1.91	140	2.76
50	3.42	150	2.64
60	3.92	160	2.57
70	4.21	170	2.43
80	4.24	180	2.32
90	4	190	2.22
100	3.73	200	2.11
110	3.37		

Table B.2. CH_4 ionisation cross sections as a function of the electron energy.

Electron energy (eV)	Ionisation cross section (Å^2)	Electron energy (eV)	Ionisation cross section (Å^2)
12.85	0	120	3.39
40	2.55	130	3.4
50	3.15	140	3.39
60	3.53	150	3.32
70	3.72	160	3.19
80	3.71	170	3.05
90	3.75	180	2.92
100	3.68	190	2.86
110	3.5		

Table B.3. CH_3F ionisation cross sections as a function of the electron energy.

Electron energy (eV)	Ionisation cross section (Å^2)	Electron energy (eV)	Ionisation cross section (Å^2)
11.22	0	90	6.01
25	0.54	100	5.69
28	1.75	110	5.59
30	3.15	120	5.3
35	5.77	130	5.12
40	6.37	140	4.66
45	6.8	150	4.6
50	6.92	160	4.29
55	6.88	170	4.29
60	6.9	180	4.29
70	6.84	190	4.01
80	6.53	200	3.95

Table B.4. CH_3Cl ionisation cross sections as a function of the electron energy.

Electron energy (eV)	Ionisation cross section (Å^2)	Electron energy (eV)	Ionisation cross section (Å^2)
10.54	0	100	6.95
25	0.47	110	6.69
30	3.06	120	6.09
35	5.42	130	5.8
40	6.72	140	5.56
45	7.76	150	5.29
50	8.02	160	5.3
55	7.85	170	5.13
60	7.8	180	5.02
70	7.84	190	4.74
80	7.68	200	4.66
90	7.24		

Table B.5. CH_3Br ionisation cross sections as a function of the electron energy.

Appendix C

Upper Stark State Defocusing Cross Sections

The upper Stark state defocusing cross sections graphed in Figs. 9.6-9.13 are tabulated below.

Hexapole / V	He	Ne	Ar	Kr	Xe	N_2
1800	252	199	263	326	321	347
2000	251	198	268	332	324	357
2200	255	199	274	332	330	378
2400	255	200	274	332	345	378
2600	257	202	268	331	349	364
2800	255	202	269	340	363	357
3000	253	202	272	344	357	362
3200	250	201	276	349	364	365
3400	252	201	278	337	363	348
3600	250	200	288	332	378	357
3800	254	200	289	330	382	372
4000	251	200	293	337	390	382
4200	253	201	285	339	388	374
4400	247	204	292	335	390	362
4600	248	202	300	328	391	355
4800	248	203	307	320	381	351
5000	247	202	303	317	386	354
5200	245	205	297	320	385	364
5400	242	204	294	323	395	373
5600	240	205	296	328	395	374
5800	239	200	295	327	403	375
6000	237	200	299	322	404	366
6200	238	199	304	315	411	361
6400	237	202	310	314	403	361
6600	241	202	299	317	393	363
6800	241	201	294	319	378	371

Table C.1. Upper Stark state defocusing cross sections for CH_3Cl.

Hexapole / V	He	Ne	Ar	Kr	Xe	N_2
1200	242	244	301	308	399	319
1400	242	240	300	308	399	323
1600	239	240	300	311	391	334
1800	239	241	305	318	393	341
2000	240	243	308	323	394	351
2200	243	241	309	321	392	351
2400	239	239	304	315	386	341
2600	234	237	300	303	375	331
2800	226	238	299	301	371	326
3000	226	240	299	303	378	329
3200	227	242	301	310	396	335
3400	229	245	306	313	408	343
3600	230	248	317	321	418	351
3800	234	248	321	326	421	354
4000	236	251	324	332	422	355
4200	237	248	321	330	418	360
4400	236	246	322	328	417	363
4600	236	244	320	328	413	351
4800	235	247	319	327	409	346
5000	233	253	310	328	405	343
5200	232	253	307	329	405	351
5400	233	252	305	330	408	348
5600	233	250	309	331	410	351
5800	232	250	313	329	413	352
6000	230	248	315	330	412	351
6200	231	248	315	326	413	349
6400	234	248	313	325	416	349
6600	232	245	312	320	419	346
6800	228	240	311	320	418	339

Table C.2. Upper Stark state defocusing cross sections for 5% CH_3Cl/Ar.

Hexapole / V	He	Ne	Ar	Kr	Xe	N_2
1000	309	295	414	463	515	471
1200	303	288	404	459	500	464
1400	302	287	402	454	506	461
1600	320	304	422	462	531	465
1800	332	319	442	460	557	471
2000	340	329	457	468	574	474
2200	340	327	461	467	580	480
2400	344	326	460	470	579	484
2600	347	325	458	474	570	488
2800	342	326	457	473	561	489
3000	335	327	454	474	556	488
3200	329	324	447	462	543	489
3400	325	319	440	450	536	478
3600	323	314	436	443	530	470
3800	320	306	427	435	529	458
4000	316	302	418	436	515	462
4200	311	297	411	435	499	464
4400	306	295	408	441	491	466
4600	308	298	408	457	491	459
4800	313	303	409	467	502	457
5000	322	311	420	471	508	460
5200	329	316	431	460	519	467
5400	335	321	437	451	526	474
5600	337	329	436	445	540	478
5800	343	331	436	449	541	483
6000	341	331	438	450	539	489
6200	340	328	442	463	534	495
6400	337	328	442	461	536	503
6600	332	326	447	462	533	500
6800	329	319	445	449	534	506

Table C.3. Upper Stark state defocusing cross sections for 5% CH_3Cl/Kr.

Hexapole / V	He	Ne	Ar	Kr	Xe	N_2
600	522	421	588	549	553	660
800	518	410	600	574	543	644
1000	514	413	611	577	546	608
1200	514	405	634	570	572	589
1400	523	412	626	560	570	602
1600	517	398	620	556	565	623
1800	525	397	604	577	548	629
2000	514	380	589	565	542	621
2200	518	374	564	544	521	622
2400	501	374	552	512	501	641
2600	509	375	539	493	493	667
2800	502	375	536	481	496	661
3000	507	376	533	511	515	648
3200	501	381	541	528	521	622
3400	501	388	544	542	518	621
3600	499	394	549	545	529	609
3800	499	400	549	557	547	639
4000	513	400	573	570	573	638
4200	523	399	580	572	587	646
4400	534	396	586	583	602	630
4600	524	398	573	585	610	624
4800	517	396	564	578	617	617
5000	507	396	545	564	613	598
5200	505	389	528	559	602	582
5400	503	391	533	559	593	574
5600	496	390	546	556	592	584
5800	491	393	567	556	604	605
6000	489	391	567	556	614	614
6200	494	393	568	561	609	613
6400	507	394	569	567	596	612
6600	513	392	569	565	577	615
6800	516	397	577	561	589	627

Table C.4. Upper Stark state defocusing cross sections for 5% CH_3Cl/Xe.

Hexapole / V	He	Ne	Ar	Kr	Xe	N_2
1200	224	171	198	298	252	321
1400	230	175	209	307	259	332
1600	239	188	221	320	278	343
1800	245	204	237	335	292	346
2000	247	215	250	339	311	359
2200	245	217	261	336	317	376
2400	241	212	266	334	316	390
2600	237	207	269	333	306	389
2800	233	202	263	335	295	386
3000	229	201	259	326	290	376
3200	226	196	252	320	286	367
3400	227	192	244	309	280	354
3600	227	187	232	317	273	357
3800	228	187	222	306	265	360
4000	225	184	221	305	260	357
4200	226	178	223	298	254	348
4400	226	173	220	310	252	340
4600	226	175	222	313	250	331
4800	226	180	221	305	250	331
5000	225	179	222	301	246	331
5200	225	181	223	296	247	335
5400	225	184	221	300	252	327
5600	225	189	224	295	252	325
5800	223	188	216	300	251	316
6000	221	188	221	302	251	314
6200	223	190	221	310	258	311
6400	223	191	226	320	257	318
6600	224	185	219	320	255	321
6800	227	186	216	312	254	324

Table C.5. Upper Stark state defocusing cross sections for 5% CH_3F/Ar.

Hexapole / V	He	Ne	Ar	Kr	Xe	N_2
800	313	301	374	437	543	438
1000	316	312	394	449	555	448
1200	325	317	416	460	564	467
1400	327	328	423	460	571	478
1600	327	315	414	454	566	473
1800	322	310	403	450	560	471
2000	332	298	396	452	557	473
2200	321	296	389	445	551	467
2400	315	290	388	432	548	455
2600	300	286	379	424	541	446
2800	293	282	371	417	536	439
3000	285	277	357	416	529	444
3200	281	282	348	415	526	445
3400	288	284	348	419	533	443
3600	294	288	354	420	536	447
3800	301	286	367	418	529	472
4000	310	289	387	420	532	496
4200	318	300	398	434	536	498
4400	333	307	415	444	538	494
4600	348	314	429	451	540	489
4800	363	322	440	450	536	493
5000	363	321	442	451	536	494
5200	359	322	430	451	531	488
5400	349	316	425	447	525	478
5600	346	317	423	447	522	468
5800	339	315	430	440	513	466
6000	336	313	428	436	519	468
6200	335	305	418	427	513	463
6400	337	297	415	429	508	456
6600	336	295	414	433	493	448
6800	335	299	418	438	488	440

Table C.6. Upper Stark state defocusing cross sections for 5% CH_3F/Kr.

Hexapole / V	He	Ne	Ar	Kr	Xe	N_2
2000	158	169	373	297	298	332
2200	161	175	354	300	305	336
2400	167	177	338	319	308	350
2600	162	184	322	322	294	343
2800	161	186	318	308	291	344
3000	162	191	310	304	289	332
3200	168	193	300	303	288	323
3400	169	193	281	307	280	315
3600	169	189	259	302	270	308
3800	168	190	237	305	268	300
4000	174	187	225	294	270	292
4200	179	189	216	291	271	296
4400	182	180	220	282	281	305
4600	184	180	226	275	279	314
4800	181	176	233	263	295	313
5000	183	175	238	257	291	301
5200	183	174	241	266	289	296
5400	185	172	256	284	287	294
5600	188	174	284	299	286	305
5800	188	174	313	308	288	311
6000	183	175	334	315	286	317
6200	178	170	337	311	292	317
6400	174	173	328	301	300	312
6600	179	171	317	286	306	308
6800	180	173	303	288	299	306

Table C.7. Upper Stark state defocusing cross sections for CF_3H.

Hexapole / V	He	Ne	Ar	Kr	Xe	N_2
1400	229	284	325	326	340	500
1600	243	269	322	305	313	452
1800	212	255	308	338	302	503
2000	220	252	315	371	310	479
2200	238	237	292	361	339	451
2400	257	262	290	355	371	445
2600	251	277	297	363	372	446
2800	235	292	315	385	359	469
3000	224	307	296	385	355	460
3200	234	328	303	374	350	477
3400	253	316	314	365	360	460
3600	265	283	329	369	354	435
3800	261	249	336	374	378	468
4000	238	252	319	372	370	483
4200	217	261	313	370	367	441
4400	225	265	279	369	341	439
4600	220	258	256	351	357	373
4800	237	232	251	341	359	415
5000	220	246	278	327	372	422
5200	236	267	307	345	365	408
5400	222	302	323	344	387	405
5600	225	283	316	343	376	376
5800	230	253	295	352	365	431
6000	242	239	287	340	352	449
6200	253	231	287	336	374	381
6400	233	248	315	324	398	387
6600	228	243	314	332	392	329
6800	216	266	320	325	375	374

Table C.8. Upper Stark state defocusing cross sections for 5% CF_3H/Kr.

References

Aitken, 1994 — C. G. Aitken, D. A. Blunt, P. W. Harland, *J. Chem. Phys.* **101**, 11074, (1994)

Aitken, 1995a — Craig George Aitken, *Ph.D. Thesis*, University of Canterbury, Christchurch, N.Z. (1995)

Aitken, 1995b — Craig G. Aitken, David A. Blunt, Peter W. Harland, *Int. J. Mass Spectrom. Ion. Proc.* **149/150**, 279, (1995)

Allison, 1961 — Samuel K. Allison, M. Kamegai, *Rev. Sci. Instrum.* **32**, 1090, (1961)

Allison, 1979 — J. Allison, D. P. Ridge, *J. Am. Chem. Soc.* **101**, 4998, (1979)

Asundi, 1963a — R. K. Asundi, *Proc. Phys. Soc.* **82**, 372, (1963)

Asundi, 1963b — R. K. Asundi, J. D. Craggs, M. V. Kurepa, *Proc. Phys. Soc.* **82**, 967, (1963)

Atkins, 1990 — P. W. Atkins, *Physical Chemistry* 5th edition, Oxford University Press (1990)

Bartmess, 1983 — J. E. Bartmess, J. E. Georgiadis, *Vacuum* **33**, 149, (1983)

Beck, 1989 — Scott T. Beck, Doug W. Warner, Ben A. Garland, Fred V. Wells, *Rev. Sci. Instrum.* **60**, 2653, (1956)

Bernstein, 1982 — Richard B Berstein, *Chemical Dynamics via Molecular Beam and Laser Techniques,* Oxford University Press, (1982)

Bleakney, 1929 — W. Bleakney, *Phys. Rev.* **29**, 157, (1929)

Blewett, 1936 — J. P. Blewett, Ernest J. Jones, *Phys. Rev.* **50**, 464, (1936)

Blunt, 1995 — David Alan Blunt, *Ph.D. Thesis*, University of Canterbury, Christchurch, N.Z. (1995)

Borkenhagen, 1976 — U. Borkenhagen, H. Malthan, J. P. Toennies, *Chem. Phys. Lett.* **41**, 222, (1976)

Borkenhagen, 1979 — U. Borkenhagen, H. Malthan, J. Peter. Toennies, *J. Chem. Phys.* **71**, 1722, (1979)

Boyd, 1958 R. L. F. Boyd, G. W. Green, *Proc. Phys. Soc. (London)* **71**, 351, (1958)

Breck, 1956 D. W. Breck, W. G. Eversole, R. M. Milton, T. B. Reed, T. L. Thomas, *J. Am. Chem. Soc.* **78**, 5963, (1956)

Briglia, 1965 Donald D. Briglia, Donald Rapp, *J. Chem. Phys.* **42**, 3201, (1965)

Brook, 1978 E. Brook, M. F. A. Harrison, A. C. H. Smith, *J. Phys. B* **11**, 3115, (1978)

Brooks, 1969 Philip R. Brooks, Eugene M. Jones, Ken Smith, *J. Chem. Phys.* **51**, 3073, (1969)

Cameron, 1991 Brett R. Cameron, Peter H. Harland, *J. Chem. Soc. Faraday Trans.* **87**, 1069, (1991)

Chakravorty, 1982 K. K. Chakravorty, D. H. Parker, R. B. Bernstein, *Chem. Phys.* **68**, 1, (1982)

Compton, 1925 K. T. Compton, C. C. Van Voorhis, *Phys. Rev.* **26**, 436, (1925)

Creasy, 1985 W. R. Creasy, J. M. Farrar, *J. Phys. Chem.* **89**, 3952, (1985)

Creasy, 1986 W. R. Creasy, J. M. Farrar, *J. Chem. Phys.* **85**, 162, (1986)

Creasy, 1987a William R. Creasy, James M. Farrar, *Faraday Discuss. Chem. Soc.* **84**, 281, (1987)

Creasy, 1987b W. R. Creasy, J. M. Farrar, *J. Chem. Phys.* **87**, 5280, (1987)

Dahl, 1995 David A. Dahl, *SIMION 3D Version 6.0*, (1995)

Dawson, 1976 Peter H. Dawson, *Quadrupole Mass Spectrometry and its Applications*, Elsevier Scientific Publishing Company, (1976)

Ellis, 1976 H. W. Ellis, R. Y. Pai, E. W. McDaniel, *Atomic Data and Nuclear Data Tables* **17**, 177, (1976)

Fite, 1958 W. L. Fite, R. T. Brackmann, *Phys. Rev.* **112**, 1141, (1958)

Freeman, 1961 Donald C. Freeman Jr., Dennis N. Stamires, *J. Chem. Phys.* **35**, 799, (1961)

Harland, 1984 P. W. Harland, B. J. McIntosh, *Int. J. Mass Spectrom. Ion Proc.* **57**, 283, (1984)

Hayes, 1987 Todd R. Hayes, Robert C. Wetzel, Robert S. Freund, *Phys. Rev. A* **35**, 578, (1987)

Heinz, 1968 — O. Heinz, R. T. Reaves, *Rev. Sci. Instrum.* **39**, 1229, (1968)

Helfferich, 1962 — Friedrich Helfferich, *Ion Exchange*, McGraw-Hill Book Company Inc, (1962)

Holland, 1974 — L. Holland, W. Steckelmacher, J. Yarwood, *Vacuum Manual*, E. & F. N. Spon London, (1974)

Jones, 1927 — T. J. Jones, *Phys. Rev.* **29**, 822, (1927)

Kieffer, 1966 — L. J. Kieffer, Gordon H. Dunn, *Rev. Mod. Phys.* **38**, 1, (1966)

Kramer, 1965 — K. H. Kramer, R. B. Bernstein, *J. Chem. Phys.* **42**, 767, (1965)

Lampe, 1957 — F. W. Lampe, J. L. Franklin, F. H. Field, *J. Am. Chem. Soc.* **79**, 6129, (1957)

Landau, 1958 — L. D. Landau, E. M. Lifshitz, *Quantum Mechanics*, Pergamon Press, (1958)

Larrivee, 1990 — Mary L. Larrivee, John Allison, *J. Am. Chem. Soc.* **112**, 7134, (1990)

Lias, 1988 — Sharon G. Lias, John E. Bartmess, Joel F. Liebman, John L. Holmes, Rhoda D. Levin, W. Gary Mallard, *J. Phys. Chem. Ref. Data* **17**, Suppl. 1, (1988)

Massey, 1933 — H. S. W. Massey, C. B. O. Mohr, *Proc. Roy. Soc. A* **141**, 434, (1933)

Massey, 1934 — H. S. W. Massey, C. B. O. Mohr, *Proc. Roy. Soc. A* **144**, 188, (1934)

Massey, 1952 — H. S. W. Massey, E. H. S. Burhop, *Electronic and Ionic Impact Phenomena*, Oxford University Press, (1952)

McDaniel, 1984 — Earl W. McDaniel, L. A. Viehland, *Physics Reports* **110**, 333, (1984)

Pargellis, 1978 — A. N. Pargellis, M. Seidl, *J. Appl. Phys.* **49**, 4933, (1978)

Ramsey, 1956 — Norman F. Ramsey, *Molecular Beams*, Oxford University Press, (1956)

Rapp, 1965a — Donald Rapp, Paula Englander-Golden, Donald D. Briglia, *J. Chem. Phys.* **42**, 4081, (1965)

Rapp, 1965b — Donald Rapp, Paula Englander-Golden, *J. Chem. Phys.* **43**, 1464, (1965)

Richardson, 1916 — O. W. Richardson, *The Emission of Electricity from Hot Bodies*, Longman's Green and Company London, (1916)

Satoh, 1987 — Y. Satoh, M. Takebe, K. Iinuma, *Rev. Sci. Instrum.* **58**, 138, (1987)

Schram, 1964 — B. L. Schram, F. J. de Heer, M. J. van der Wiel, J. Kistemaker, *Physica* **31**, 94, (1964)

Scoles, 1988 — Giacinto Scoles, *Atomic and Molecular Beam Methods* Volume 1, Oxford University Press, (1988)

Smith, 1930 — Philip T. Smith, *Phys. Rev.* **36**, 1293, (1930)

Staley, 1977 — Ralph H. Staley, Robert D. Wieting, J. L. Beauchamp, *J. Am. Chem. Soc.* **99**, 5964, (1977)

Stephan, 1980 — K. Stephan, H. Helm, T. D. Märk, *J. Chem. Phys.* **73**, 3763, (1980)

Stephan, 1984 — K. Stephan, T. D. Märk, *J. Chem. Phys.* **81**, 3116, (1984)

Straub, 1995 — H. C. Straub, P. Renault, B. G. Lindsay, K. A. Smith, R. F. Stebbings, *Phys. Rev. A* **52**, 1115, (1995)

Tate, 1932 — J. T. Tate, P. T. Smith, *Phys. Rev.* **39**, 270, (1932)

Tate, 1934 — J. T. Tate, P. T. Smith, *Phys. Rev.* **46**, 773, (1934)

Toennies, 1962 — J. P. Toennies, *Faraday Discuss. Chem. Soc.* **33**, 96, (1962)

Toennies, 1965 — J. P. Toennies, *Zeitschrift für Physik* **182**, 257, (1965)

Toennies, 1966 — J. P. Toennies, *Zeitschrift für Physik* **193**, 76, (1966)

Townes, 1955 — C. H. Townes, A. L. Schawlow, *Microwave Spectroscopy*, McGraw-Hill Book Company Inc, (1955)

Vallance, 1997a — Claire Vallance, Peter W. Harland, *In Press*, (1997)

Vallance, 1997b — Claire Vallance, Sean A. Harris, James E. Hudson, Peter W. Harland, *In Press*, (1997)

Wannier, 1953 — G. H. Wannier, *Bell System Tech. J.* **32**, 170, (1953)

Weber, 1966 — Roland E. Weber, Linus F. Cordes, *Rev. Sci. Instrum.* **37**, 112, (1966)

Wetzel, 1987 — Robert C. Wetzel, Frank A. Baiocchi, Todd R. Hayes, Robert S. Freund, *Phys. Rev. A* **35**, 559, (1987)

Wieting, 1975 Robert D. Wieting, Ralph H. Staley, J. L. Beauchamp, *J. Am. Chem. Soc.* **97**, 924, (1975)

Wizemann, 1986 H. D. Wizemann, K. H. Gaukler, *Int. J. Mass Spectrom. Ion Proc.* **72**, 299, (1986)